HYDROGEN SORPTION PROPERTIES OF MAGNESIUM-BASED THIN FILMS

By

Luke J.R Hughes

A thesis submitted to the University of Birmingham
For the Degree of
Doctor of Philosophy

School of Metallurgy and Materials
College of Engineering and Physical Sciences
University of Birmingham
March 2016

Synopsis

The hydrogen sorption properties of a variety of magnesium-based thin films prepared by magnetron sputtering, were investigated. A range of methods were employed to investigate and ascertain the influence of stress on the sorption properties: deposition conditions, thickness, substrates (both rigid and flexible) and multilayers.

Film preparation conditions in a closed field unbalanced magnetron system are shown to influence microstructural and intrinsic film growth stress, examined by the use of X-Ray Diffraction (XRD) and Scanning Electron Microscopy (SEM). Mg films are shown to grow with an in plane tensile stress which is attributed to crystallite coalescence. The influence of intrinsic stress and microstructure on the resultant hydrogen sorption behaviour is discussed and it is postulated that intrinsic stress can be linked to hydrogen absorption kinetics, as well as the corresponding thermodynamic destabilisation of the MgH_2 phase.

The effect of film thickness is investigated. XRD results show a small change in intrinsic stress with thicker film growth. The resultant hydrogen sorption behaviour and stress analysis has been used to propose a theory that demonstrates how sorption behaviour in thinner versus thicker films changes from a regime dominated by grain boundary diffusion to a regime dominated by transgranular diffusion. The effects of this loading behaviour are shown to influence observed mechanical properties and suggests that additional strain energy can drive the equilibrium value according to the uptake mechanism.

The influence of a selection of substrates on the sorption behaviour of Mg films has been investigated for the first time. The results are only partially conclusive due to the complexity of many potential influential factors. The substrate has been shown to influence many factors associated with Mg films such as the film growth mode/microstructure, intrinsic stress and adhesion energy. The above factors

all translate to mechanical aspects of films, which act to alter the thermodynamics of the phase transition.

Flexible substrates have been used to tune thermodynamics by the introduction of stress due to film bending. However, bending to a radius of curvature generating an in plane stress of 3 GPa was shown to induce plastic deformation within the film and a stabilisation of the phase. Nevertheless, the flexible nature of this type of film/substrate system could be used as a mechanical hydrogen sensors as opposed to optical methods already proposed.

Finally, a multilayer system was used to investigate the influence and comparative differences of Ti and Y based multilayers. Ti multilayers show some destabilisation with thinner layers down to 10 nm which is proposed to be due to interfacial energy contributions. In comparison, it has been shown for the first time that Mg/Y based multilayers could provide a route towards MgH_2 destabilisation due to the accommodation of lattice mismatch between strained FCC Y / Mg interfaces.

Acknowledgements

I would like to thank Professor David Book for his patience, thoughts and guidance during my time in the energy storage group at the University of Birmingham. In addition, I would like to thank the energy storage group for their thoughtful discussions and support.

You don't complete a PhD without ups and downs - if you do, you're lucky! There are too many individuals to thank for helping me through the frustration but also spurring me on to finish. A particular mention to five of the best friends I've had the pleasure of meeting and working with, in alphabetical order: Jonathan Boukhobza, Craig Knaggs, Josh Vines, Dean Welton and Rich Wyse. Let's hope this work is better than our golf!

Financially, I would like to thank the EPSRC for funding the research via the DTA route in metallurgy and materials at the University of Birmingham.

A thank you to my parents and family, for all of their support. At the times I wanted to quit, you were there to help me take stock of the big picture.

Last but not least, a thank you to Jen, for putting up with me on a day to day basis, the many mood swings and late night reading – I don't know how you did it! Oh, and of course thanks to Rupert, the silent partner (apart from the occasional 'woof') who doesn't care about all of your worries, just that you're coming home to see him and feed him. I can't help but think how good a dog's life is!

Table of Contents

“THE ENERGY OF THE MIND IS THE ESSENCE OF LIFE” - *Aristotle*

1 GLOBAL ENERGY AND THE CASE FOR HYDROGEN

1.1 INTRODUCTION

Energy is ubiquitous. It surrounds and governs the very core of the existence that we know; present in many different forms – deviating from one form or another, depending on the surrounding environment; and governed by various physical laws and phenomena studied by multiple scientists around the world for centuries. To the human race, energy is possibly more important than ever to its survival and ability to thrive. All of the evidence showing the requirement for a paradigm shift to an alternative energy source, which eliminates our dependence on fossil fuels and reduces environmental damage, is well documented and acknowledged. However, the implementation of such an energy system has never been faced before. The scale of such a change is almost mind blowing. In addition, the technology required to implement the change is not yet industrialised or fully developed. This chapter aims to provide a historical overview of global energy and provide perspectives on where we should focus our efforts for future energy generation and storage. Arguments are presented which link the availability of energy to technology development, health and worldwide economics. In addition, the magnitude of energy production is analysed and a breakdown of the sectors is shown, alongside carbon emissions. An argument is made for a hydrogen based economy and the challenges that this technology still needs to overcome to be accepted, with a focus on the transportation sector.

1.2 TRENDS IN GLOBAL ENERGY DEMAND

Arguably, the most important starting point for consideration of the effects of energy is the industrial revolution. The industrial revolution started in the UK in the late 18th century and its effects took around a century to spread worldwide. The revolution spawned the age of machine-operated manufacture, often powered by steam engines from the combustion of coal. Nobel prize winner Robert E Lucas, Jr. denoted it as[1]:

"The first time in history that the living standards of the masses of ordinary people have begun to undergo sustained growth."

Since the dawn of this revolution, energy demand has risen dramatically – mainly due to increased manufacture, which has stimulated continuous economic growth. Of course, the manufacturing industry led to technological developments and ultimately a better standard of living. The effect of better living standards has led to an exponential increase in population and thus the demand for energy increases further[2]. This cycle spirals upwards, resulting in the huge energy demand and huge population (ca 7 billion) we have on earth today. The International Energy Agency (IEA) states that the current world energy consumption is in the region of 5×10^{20} J per year[3].

The bulk of the energy demand (around 80 %) has been met by fossil fuels, in what is known as a carbon-based economy (See Fig 1.1). Because of this, countries with these natural resources have, arguably, had significant advantages in terms of economic growth, stability and energy security. This has led to political instabilities in some countries, and so, one can see that energy is arguably a causal factor in the volatile nature of Middle Eastern countries[4,5]. Certainly, countries without these natural resources, which depend on oil importation are likely to be at a higher risk of energy security[6]. Countries with a high energy use per capita are more likely to be affected by changes in energy price (Fig 1.2). It follows then, that the availability of energy is linked to economic prosperity and population growth. Thus, these two factors are probably good predictors of trends in energy availability and consumption.

Moving forward to the present and over 150 years of the combustion of fossil fuels, it seems as though the culmination of the industrial revolution was in July 2008, when the price of one barrel of oil peaked at over US $140[7]. This raises questions with regards to the economic sustainability of the carbon-based economy. The price of oil should behave elastically with demand; however recent reports have indicated that oil production has reached its peak value (Fig 1.3)[7]. The fact that oil production is at its peak (around 75 million barrels/day) means that supply and demand is somewhat inelastic, leading to high volatility in oil prices. In addition to the inelastic oil market, the price of oil will continue to rise, as the cost for extraction increases due to scarcity and expenses in deeper drilling.

Although only accounting for a small percentage of total demand, renewable energy as well as nuclear sources of energy, are growing at the quickest rate. Reports from organisations including the IEA (International Energy Agency)[8] and BP (British Petroleum)[9] forecast increases in primary energy demand by up to 56 % (from 2010 to 2040)[8]. The large drivers for this appear to be non-OECD countries which are experiencing rapid economic growth (India and China in particular). The extra demand must be met in other ways. BP have predicted that renewable growth will be the highest out of all current energy sources[9]. Reasons for this may be longevity, cost and availability. However, if we consider that the total energy in terms of solar irradiation is around 5×10^{24} J (10,000 times the world energy consumption), one may start to see that moving towards a system that harnesses power from the sun would be more beneficial and not dependent on the natural resources on earth[10]. In addition, this figure demonstrates that the development of the world is sustainable, however we are somewhat involved in an energy conversion crisis, rather than production.

It becomes important here to look at which sectors are responsible for energy demand. Figure 1.4 shows the total energy demand per sector from the 1970s onwards. There is a decreasing trend in industrial energy use, possibly due to increased efficiencies or move to international manufacture and the recent recession. Domestic usage has stayed similar. Again, more heat efficient building design may counteract the increased demand. One can see that the transport sector has grown and is currently responsible for over 30 % of total energy consumption. It is clear that this is the market that is growing the most. Despite the efforts of many manufacturers promoting lower emission vehicles (UK fleet average is now around 160 gCO_2/km and still decreasing), it would seem that the build quality and reliability of used cars is increasing, meaning that the amount of cars on the roads is still increasing (32 million in 2014) [11]. It would therefore be best to tackle the problem of reducing our transport sectors dependence on fossil fuels, as this is the highest growth sector.

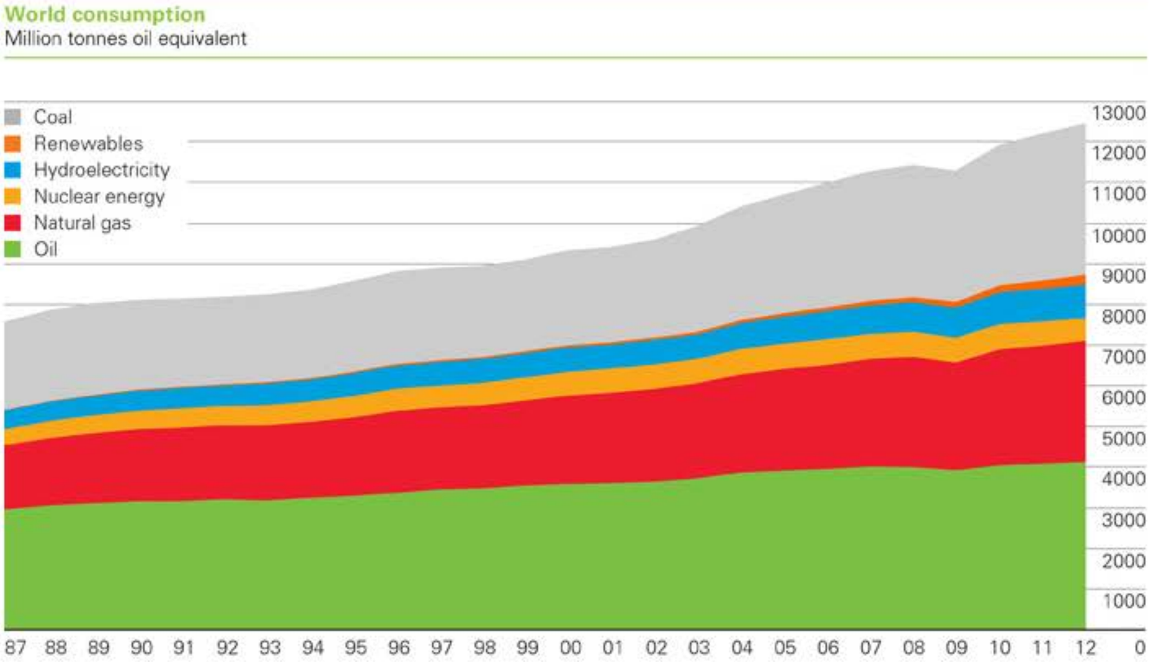

Fig 1.1. World energy consumption up to 2012. Here, the Y axis describes the quantity of energy in equivalent units of millions of tonnes of oil and the X axis is the year. (1 tonne is equivalent to around 42 GJ). Around 80 % of all energy was supplied by fossil fuels with the remainder being made up of nuclear and hydroelectric/renewables. [9]

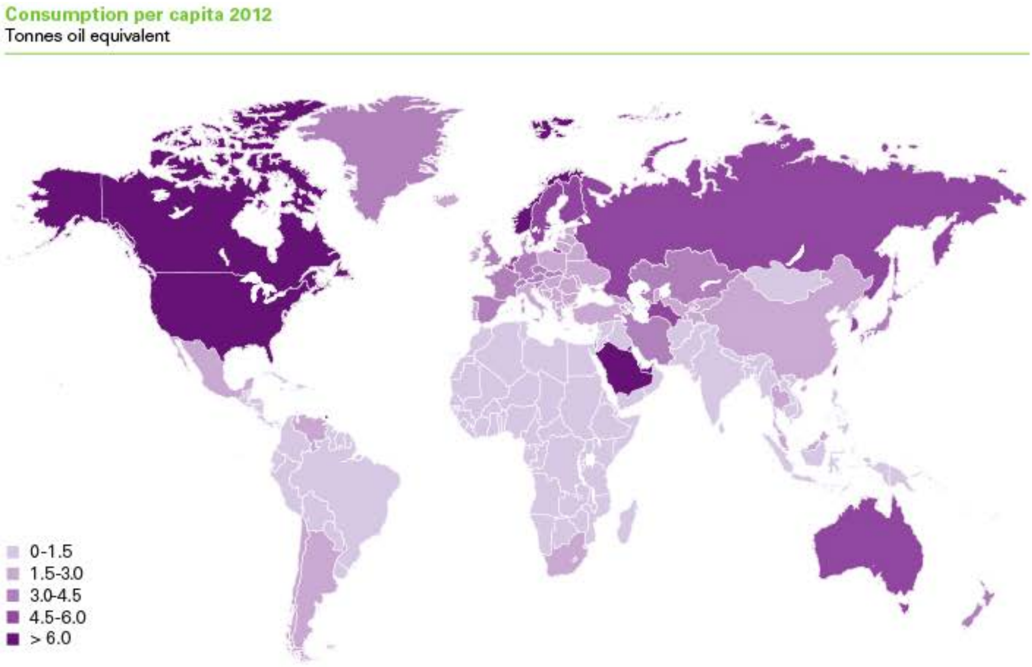

Fig 1.2. World wide energy use per capita. [9] *(Note the units of tonnes of oil equivalent - 1 tonne of oil is equivalent to around 42 GJ)*

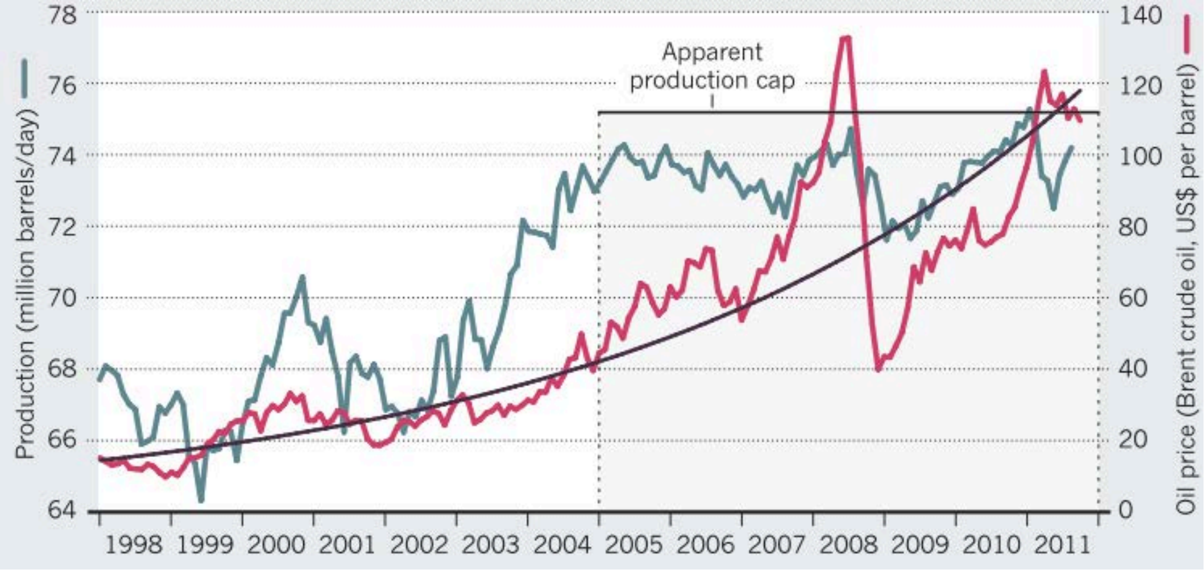

Fig 1.3. Oil production seemed to have reached a cap of ca. 75 millions barrels/day in 2005, which led to a steady rise in price per barrel. [7]

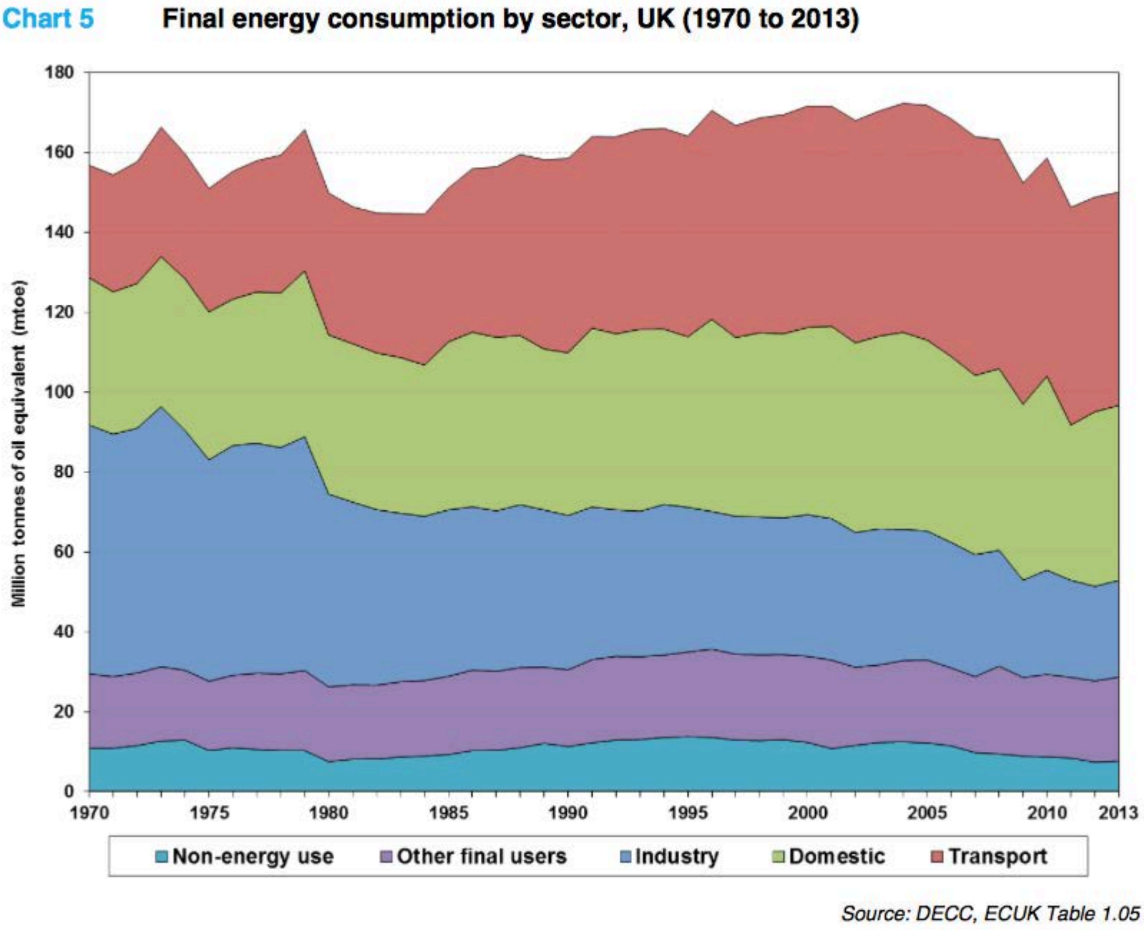
Chart 5 **Final energy consumption by sector, UK (1970 to 2013)**

Source: DECC, ECUK Table 1.05

Fig 1.4. Breakdown of the total energy demand in the UK by sector, showing the three main players: industry, domestic and transport. (1 tonne of oil is equivalent to around 42 GJ) [9]

1.3 GLOBAL WARMING AND CLIMATE CHANGE

Another important driver for a more sustainable source of energy is the risk of climate change, brought about by excessive CO_2 production. Complete combustion of hydrocarbons produces H_2O and CO_2. As a greenhouse gas, CO_2 is partially responsible for warming the surface of the earth as it has the ability to absorb and emit infrared radiation, contributing to the greenhouse effect and warming the earth.

The excessive combustion of fossil fuels has meant an increased amount of CO_2 in the atmosphere, rising from around 300 ppm in 1960 to almost 400 ppm in 2014 (Fig 1.5)[12].

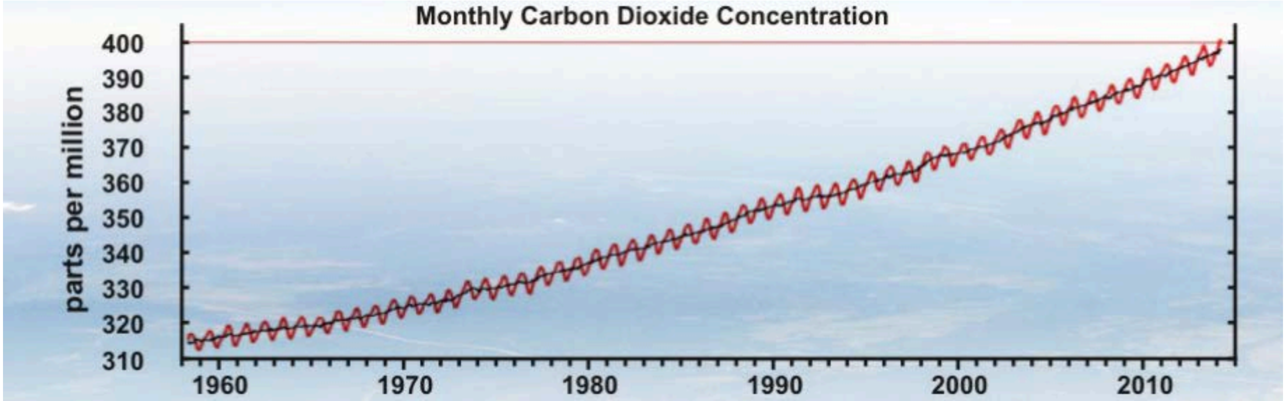

Fig 1.5. Concentration of atmospheric carbon dioxide trends from around 1960. The trend is clearly increasing. [13]

There is strong scientific evidence to suggest that an increasing amount of atmospheric CO_2 is linked to global warming, which can ultimately lead to climate change[14]. CO_2 levels recorded in ice cores dating back 800,000 years have shown a definitive relationship with climate change[15]. A rise in CO_2 has preceded the last 8 glacial ages, signifying that our current growth and pollution level will cause climate change.

In addition to this, climate change may not be a linear transition. Melting of the Greenland ice sheet and changes to the atlantic thermohaline circulation are potentially crucial 'tipping points' which will induce rapid climate change[16]. It is clear then, that if scientific evidence as to the cause of global warming is correct, then there is an urgent need for the transition to a system that does not produce CO_2. Stern predicts the cost to the global economy to be around 5 % of global GDP if no action is taken to prevent this change[17]. These costs include natural disasters that will likely increase in frequency due to climate change. In a further argument, it is demonstrated that if we invest just 1-2 % of global GDP in renewable energy technology then this could overcome this issue. These model predictions are based on a variety of assumptions leading up to the year 2100. As an alternative approach, consider the argument of taking no action: fossil fuels will run out, economies will regress and we will have no solution to our problem. Can we afford not to act now?

1.4 LEGISLATION

The energy conundrum is not a new issue. Politicians and the government have been aware of the issue for decades. There is increasing pressure to advocate more funding into research and development of primary energy users, aiming to reduce carbon emissions. This was firstly agreed internationally when in 1997, the Kyoto protocol binding targets between various governments which target a reduction in carbon dioxide emissions [18]. This not only works to guarantee future energy security for a nation, but may also support economic growth and security.

Some countries have stated more rigorous targets for the reduction in emissions. Germany for example, has aimed to reduce emissions by 95% in 2050. However, legislation in the UK (Climate Change Act, 2008) requires a carbon emission reduction of 80% by the same time, in comparison to 1990 baseline levels[19].

Of course, the targets cannot be set at simply a countrywide level. Various papers have been passed which guide certain industries to achieve certain targets. For example, the average fleet tailpipe emissions for the automotive industry in the UK should have averaged 130 g CO_2/km in 2015, with a further reduction to 120 g CO_2/km by 2020 [20].

Clearly, there is a global effort to reduce carbon emissions. However, it remains to be seen whether these targets can still be met. Managing this sort of paradigm shift in energy use at this scale has never been achieved before. Hopefully in the years to come, and in the words of Barack Obama:

> *'Someday, our children, and our children's children, will look at us in the eye and they'll ask us, did we do all that we could when we had the chance to deal with this problem and leave them a cleaner, safe, more stable world?' – Barack Obama, June 2013*

1.5 A HYDROGEN BASED ECONOMY

The previous sections provide an argument for the development of a zero carbon economy, which will provide solutions to the inelastic and finite oil market, as well as reducing the long-term effects of climate change. The development of an energy system based on renewable and universally available sources could also provide energy security to many countries and eliminate energy poverty. However, despite all of these promising qualities, there are challenges that renewable energy sources face. Aside from capital costs to build a new infrastructure, the main two problems with these methods of electricity production are the intermittent nature of production and the location (e.g. solar and wind). Therefore, the ability to meet the variety of energy demands of the population requires a form of energy storage. The requirements of the three main energy users have massive differences. Examples include scalability, mobility, reliability, efficiency, price and energy flux to name a few.

Fortunately, many types of energy storage systems exist and their respective energy densities vary on a massive scale (Fig 1.6). The energy densities in terms of volumetric and gravimetric storage capacity for fossil fuels are the highest known (apart from nuclear). The current energy densities of alternative energy storage systems are not able to match these qualities. In addition, fossil fuels have the advantage of being easily transported around the world, can be scaled, and have a developed infrastructure. For this reason, the introduction of an alternative energy carrier must make technological and economical sense for its introduction to be successful.

As an element, the specific density of hydrogen at its lower heating value (LHV) is 120 MJ/kg, which is almost 3 times as high as gasoline (45 MJ/kg). Hydrogen is therefore very attractive as a basis for an energy economy based on renewables and is carbon free, as long as the electricity used for its production comes from renewable resources. However, the energy density per unit volume for hydrogen at its lower heating value is only around 10.7 kJ/L at room temperature and pressure, which is around 3 orders of magnitude lower than what would be required practically. A potential hydrogen cycle is shown in Fig 1.7.

However, storing hydrogen for use in a variety of environments and scales is a technological barrier for the development of a so called ‘hydrogen economy’. Hydrogen storage is the main topic of this thesis and an overview of hydrogen storage technologies is given in chapter 2.

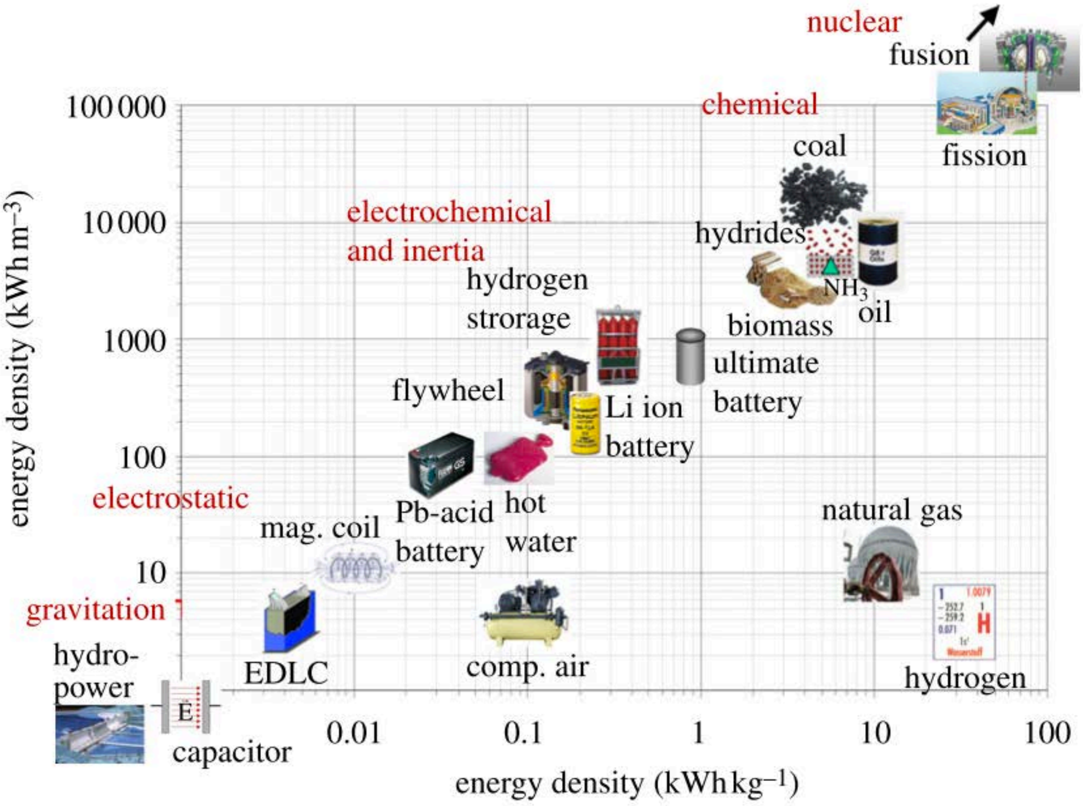

Fig 1.6. Volumetric (vertical) and gravimetric (horizontal) energy storage densities of various technologies. Hydrogen has a very high gravimetric energy density, but is very low in terms of volumetric density. [21]

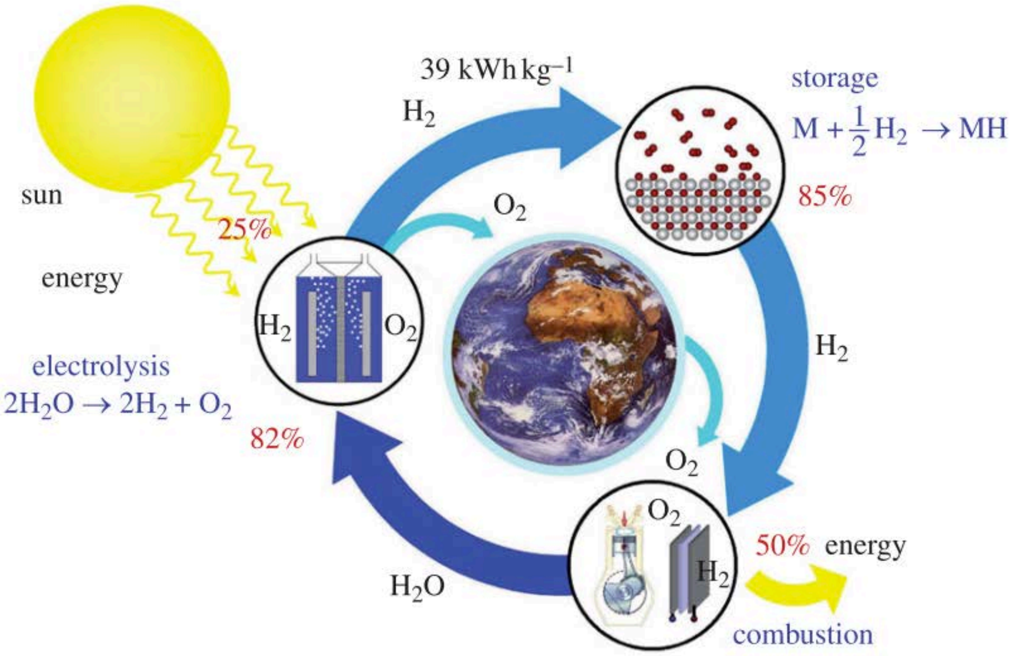

Fig 1.7. Representation of the hydrogen cycle. Solar energy is used to electrolyse water. Hydrogen is stored and then combusted when required, releasing only water as a byproduct. Therefore, the cycle is closed and the only energy input is from the sun. [21]

1.6 SUMMARY

To summarise, the key points in this introductory chapter:

- Historically, energy demand has increased from the start of the industrial revolution and is predicted to continue to rise, mainly due to large economic growth of non-OECD countries such as India and China.
- Energy availability and demand are good predictors of economic growth
- Oil production appears to have hit a ceiling, which affects world economic stability due to energy import costs. Oil and fossil fuels will not be able to support energy demand forever.
- Renewable and nuclear energy are predicted to become big growers in the energy industry
- Legislation has governed the requirement to reduce carbon emissions.
- The hydrogen economy is a viable solution to the potential problems associated with renewable energy, however it faces many technological challenges for its widespread adoption.

2 LITERATURE REVIEW

This review is split into four sections. Firstly, a broad overview of the known methods for storing hydrogen are discussed; comparing the advantages and disadvantages for each with a particular focus on metal hydrides. This is followed by a more detailed review of the properties of powdered magnesium hydride. Section three is a more detailed review of literature relating to hydrogen storage in thin films, again with a particular focus on magnesium hydride. The final section describes some of the typical properties of physical vapour deposition (PVD) systems, with an emphasis on nucleation and growth mechanisms in relation to the observed microstructure. Emphasis is placed on the use of storage technologies for application in automotive vehicles, although alternative applications for stationary storage and sensors are also discussed where relevant.

2.1 HYDROGEN STORAGE TECHNOLOGIES

2.1.1 Storage technologies

There are a variety of ways to store hydrogen. It can be stored as a molecule, H_2 or bonded to a material. The way a material is named usually follows on from its bonding nature, which will be discussed in the following sections in more detail. Fig 2.1 represents a range of hydrogen storage materials currently being considered for use as part of a system for on board storage. This list is not extensive, however it gives a good appreciation for the quantities of hydrogen one can expect to store for a given mass and volume for some of the more commonly recognised storage materials. As one can observe, the type of hydride often dictates its capacity, and they are grouped together on the graph. Firstly, storing as a gas can achieve reasonable gravimetric capacities, but volumetric capacity is severely limited. Metal hydrides (red cluster) such as $LaNi_5$ provide a very good volumetric capacity, but due to the heavy elements, sacrifice a lot of their gravimetric capacity. Purple coloured compounds are complex hydrides, where both volumetric and gravimetric storage capacity can be very good. However, their lack of reversibility means that they are currently infeasible for mobile applications. Finally, the green groups are carbon-based materials. Of course, combustion of these with oxygen produces CO_2. This graph is only a small insight into the requirements for a material that incorporates all of the necessary factors for the full realisation of a transition to a transport economy fully based on hydrogen. For example, one has to factor in the required reaction conditions for reversible storage, material cost and manufacture, longevity, toxicity and safety. A list of the US department of energy's (DOE) system based targets for 2020 is shown in Fig 2.2. When all of these factors are considered, it is easy to see why automotive manufacturers are opting towards hydrogen storage in a gas form, as currently, it is the best solution in terms of the aforementioned factors. However, there is clearly potential to study metal hydrides and other similar materials, that could one day be a better solution than high pressure hydrogen tanks.

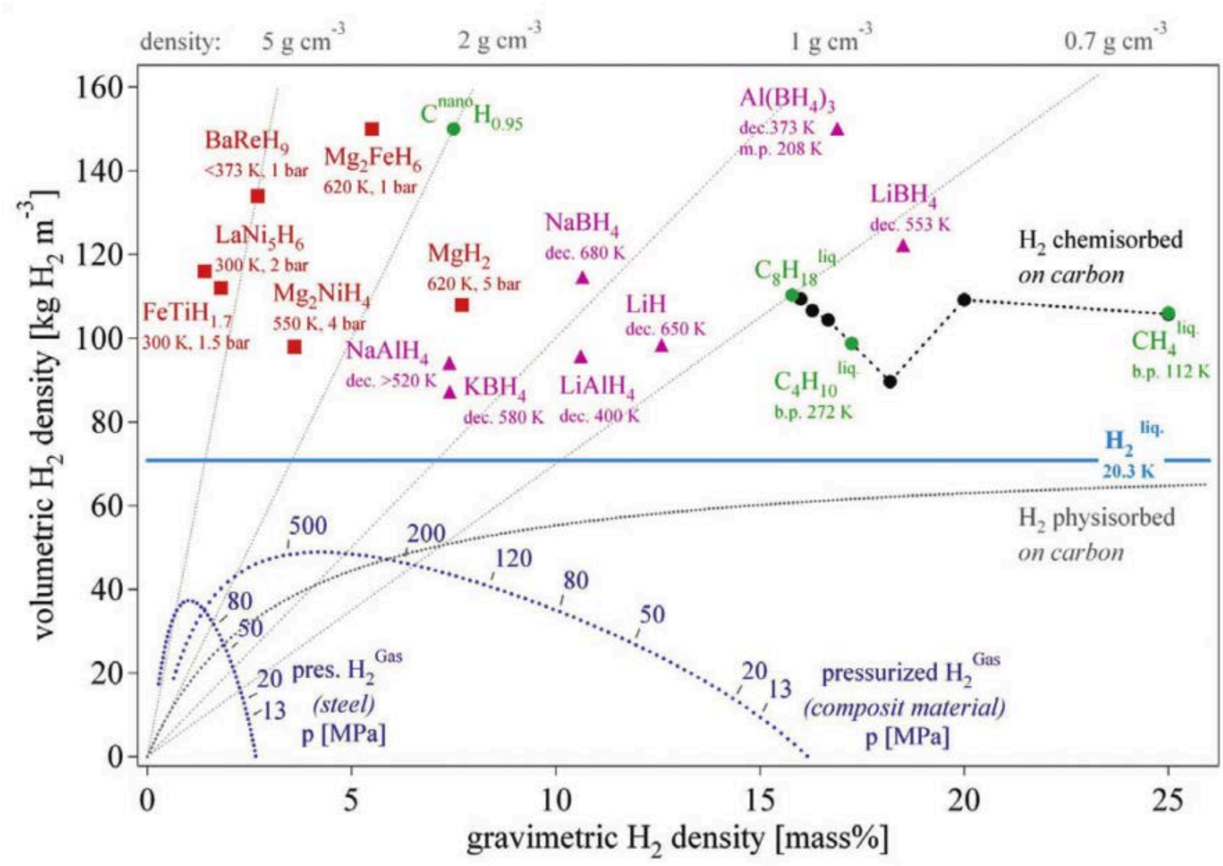

Fig 2.1. Volumetric and gravimetric energy densities of a range of selected hydrogen storage materials [22]. *Red – metal hydrides. Purple – complex hydrides. Green – carbon based hydrides. Dotted lines represent theoretical densities for a compressed gas in either a mild steel or composite container.*

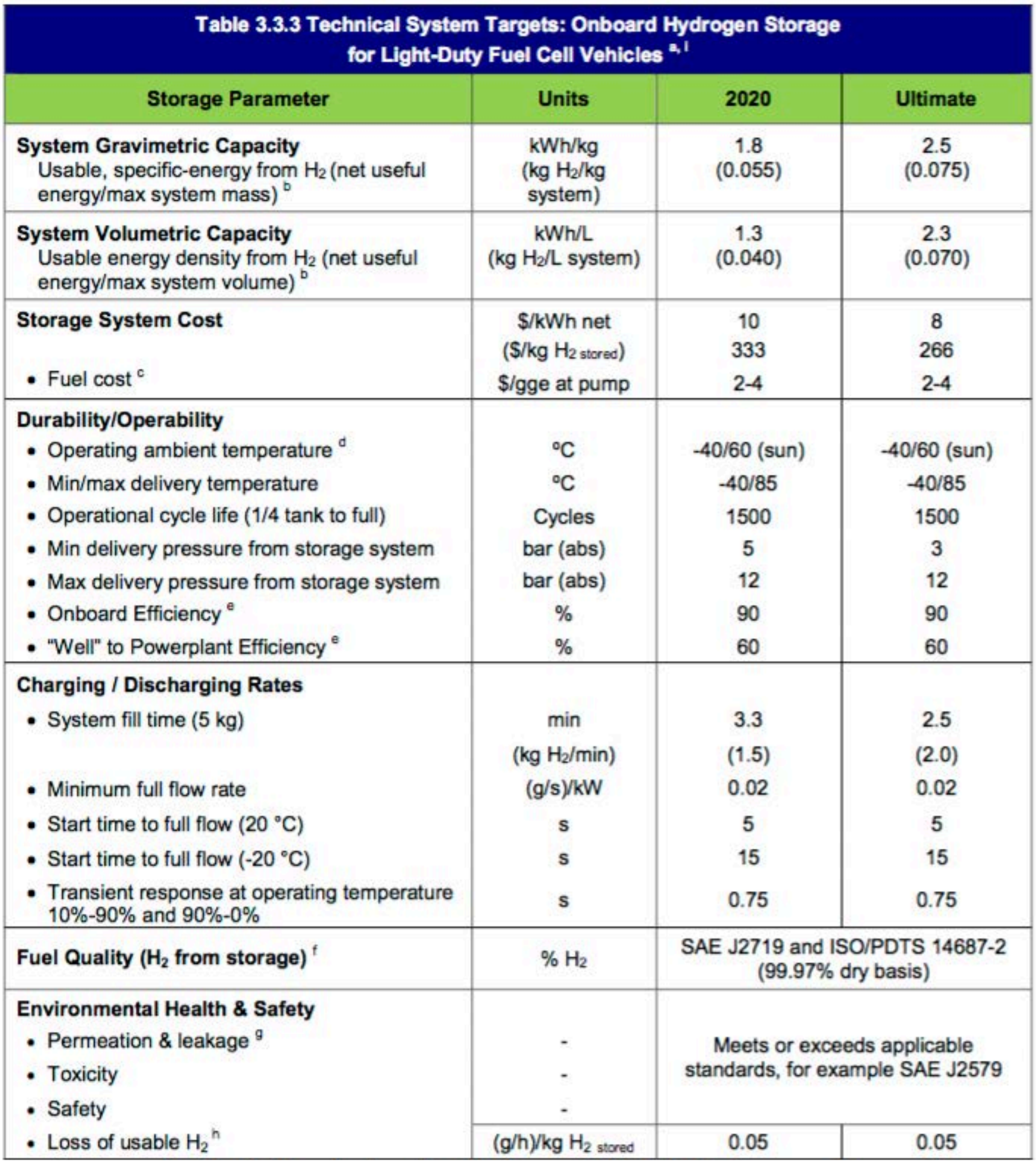

Table 3.3.3 Technical System Targets: Onboard Hydrogen Storage for Light-Duty Fuel Cell Vehicles [a, i]

Storage Parameter	Units	2020	Ultimate
System Gravimetric Capacity Usable, specific-energy from H_2 (net useful energy/max system mass) [b]	kWh/kg (kg H_2/kg system)	1.8 (0.055)	2.5 (0.075)
System Volumetric Capacity Usable energy density from H_2 (net useful energy/max system volume) [b]	kWh/L (kg H_2/L system)	1.3 (0.040)	2.3 (0.070)
Storage System Cost	\$/kWh net (\$/kg $H_{2\ stored}$)	10 333	8 266
• Fuel cost [c]	\$/gge at pump	2-4	2-4
Durability/Operability			
• Operating ambient temperature [d]	°C	-40/60 (sun)	-40/60 (sun)
• Min/max delivery temperature	°C	-40/85	-40/85
• Operational cycle life (1/4 tank to full)	Cycles	1500	1500
• Min delivery pressure from storage system	bar (abs)	5	3
• Max delivery pressure from storage system	bar (abs)	12	12
• Onboard Efficiency [e]	%	90	90
• "Well" to Powerplant Efficiency [e]	%	60	60
Charging / Discharging Rates			
• System fill time (5 kg)	min (kg H_2/min)	3.3 (1.5)	2.5 (2.0)
• Minimum full flow rate	(g/s)/kW	0.02	0.02
• Start time to full flow (20 °C)	s	5	5
• Start time to full flow (-20 °C)	s	15	15
• Transient response at operating temperature 10%-90% and 90%-0%	s	0.75	0.75
Fuel Quality (H_2 from storage) [f]	% H_2	SAE J2719 and ISO/PDTS 14687-2 (99.97% dry basis)	
Environmental Health & Safety			
• Permeation & leakage [g]	-	Meets or exceeds applicable standards, for example SAE J2579	
• Toxicity	-		
• Safety	-		
• Loss of usable H_2 [h]	(g/h)/kg $H_{2\ stored}$	0.05	0.05

Fig 2.2. US department of Energy Targets for a hydrogen storage system to be incorporated into a light duty fuel cell vehicle. [23]

2.1.1.1 Storage as a Gas

Hydrogen has the lowest atomic mass of any element. Its boiling point is -252 °C and is critical above -240 °C (See Fig 2.3). Therefore, the most convenient and common storage method for hydrogen in terms of mobile applications, is as a compressed gas. This is a common method used within industry for other gases such as argon, helium, nitrogen etc. However, considering the weight of the canister materials, the pressure of hydrogen in the system must approach 700 bar to get an estimated total gravimetric energy density approaching 5 %. Hydrogen is not an ideal gas as in equation 1. The work done to compress hydrogen isothermally is given by equation 2. For compression to 350 and 700 bar H_2, this gives energy densities of 1.05 and 1.36 kWh/kgH_2 [24]. However, it has been found in practice that this figure averages around 3.1 kWh/kgH_2 due to compressor inefficiencies and overpressure required due to non isothermal conditions [25]. Given current average energy tariff costs of ca. 10 pence per kWh this would mean around £1 charge just in compression for filling of a vehicle tank (around 10-15 % of total cost). With a production cost for high purity hydrogen of around 50-80 kWh/kg (£5 to £8), this is a significant added cost.

$$pV = nRT \qquad [1]$$

Where p is pressure in pascals, V is volume in m^3, *n* is the number of moles, R is the universal gas constant and T is temperature.

$$W = nRTln\frac{v}{v_0} \qquad [2]$$

Where W is work done, *v is the final volume and v_o is the original volume.*

Of course, one can use lower density and stronger materials with high tensile strength such as carbon fibre reinforced plastic to manufacture the tank, but it is then limited to the ability to manufacture a tank robustly and the price of the tank increases. In addition, the space available for a fuel tank in typical automotive design is usually limited to somewhere on the underbody area of the car and is frequently shaped to fit the design of the body shell. Fracture mechanics and design against failure tells us that a cylindrical shape avoids stress concentrations. To design a tank in the way that a typical fuel tank is now designed would mean it is virtually impossible to manufacture. One would have to redesign an entire underbody of a car in order to make it feasible to manufacture incorporating a tank design, a cost that most OEM's would not like to face. Even if all of the above concerns were overcome, the most important issue would be safety. Although a pressure vessel can be designed with an appropriate wall thickness so that it does not catastrophically fail, it may still leak if damaged, and if ignited by a spark, could explode.

In summary, although gravimetric and volumetric figures are reasonable for compressed gas storage, it would seem that the systems engineering and safety components would outweigh the benefits of the storage method. Recently, Toyota have launched the Mirai – a hydrogen fuel cell vehicle that uses two 700 bar cylinders, although this is in an early stage of development is not what could be called mass manufacture.

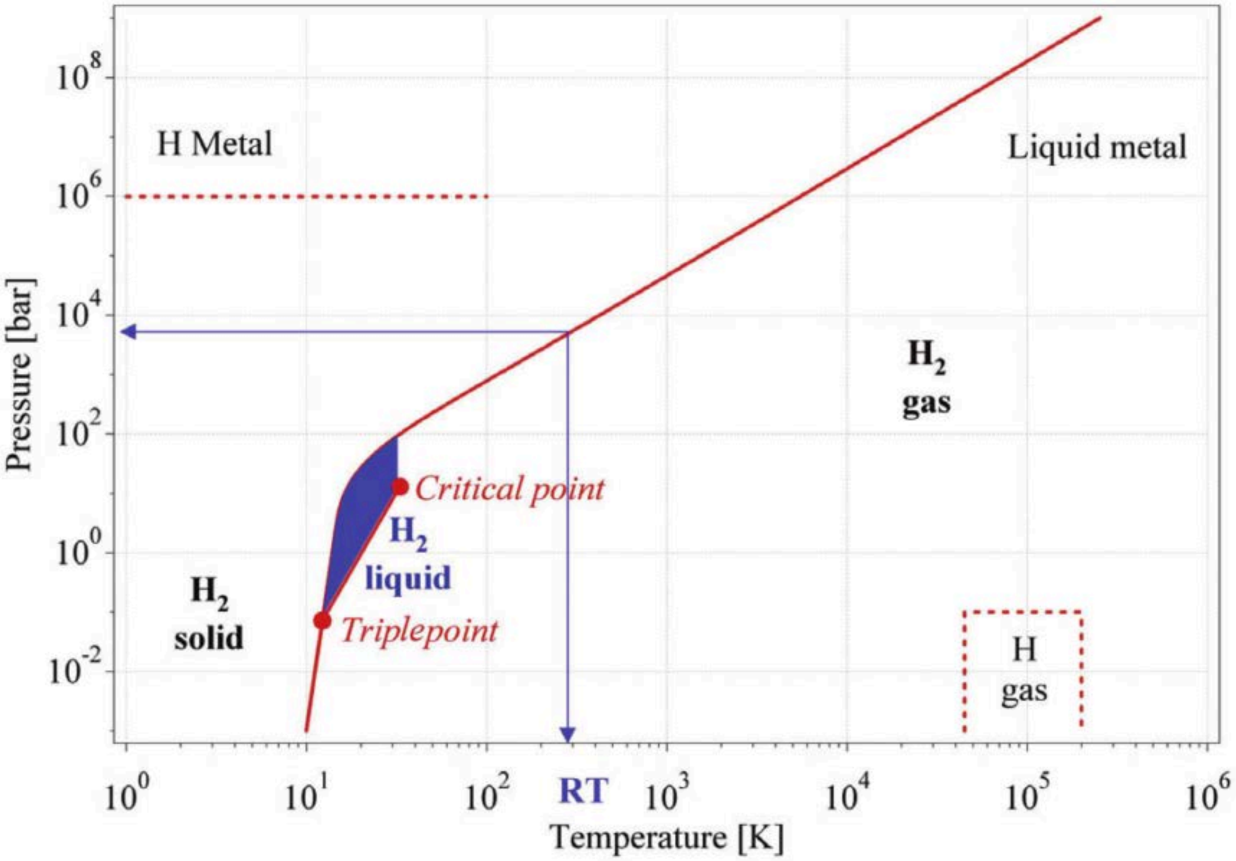

Fig 2.3. Phase diagram for hydrogen. At atmospheric pressure and temperature, hydrogen exists as a gas. The range for storage as a liquid is minimal and requires tight control of surrounding atmosphere.[22]

2.1.1.2 Liquid Hydrogen

Liquid hydrogen has been the fuel of choice for space programmes since the 1960s. However, the cryogenic temperatures required present multiple issues for the use of liquid H_2 for automotive applications.

Firstly, the energy required for liquefaction is in the order of 10 kWh/kgH_2 (figures vary from around 8 – 16 kWh/kgH_2 depending on plant scale and turbine/compressor efficiencies)[25]. This energy intensive process is at least 2-3 times more costly than for compressed air (adding around £4/tank fill).

In addition, the low temperatures required (less than -240 °C) present complications with material selection. Many metals exhibit ductile to brittle transition temperatures far above the temperatures required. In addition, liquid hydrogen can easily leak out of porosities within welded seams. The low temperatures required also require advanced insulation, which adds additional cost and weight to the system.

If there was a failure of the insulation, or the temperature inside the tank reached the critical point, pressure build up would require significant release of gas and a waste of fuel. This phenomenon is known as boil-off, and would be another large problem for on board applications that were used infrequently.

2.1.1.3 Solid state

2.1.1.3.1 Physisorption

Physisorption or adsorption describes the bonding of hydrogen molecules to the surface of a material using van der Waals attractions. This low energy bonding means that storage capacity is generally only observed at low temperatures. Hydrogen storage capacity is dependent on surface area, whereas thermodynamics are dependent on the strength of the van der Waals interactions. Some of the most common materials used for physisorption are metal organic frameworks (MOF's), activated carbons and zeolites. At the time of writing, most of the adsorption materials are capable of storing around 5-7 wt% hydrogen at temperatures around -190 °C (77 K). This capacity is significantly reduced to around 0.5 wt% H_2 at room temperature [26].

2.1.1.3.2 Complex Hydrides

Complex hydrides are a promising class of materials for hydrogen storage. They generally have very large gravimetric and reasonable volumetric hydrogen capacity but poor and not fully understood reversibility. The list of complex hydrides is extensive but some of the more commonly studied systems at the time of writing involve the $[BH_4]^-$, $[AlH_4]^-$, $[NH_2]^-$ complexes which are bonded to an electropositive ion, usually an alkaline metal (Li, Na, Mg). A good rule of thumb is that the stability of the complex is derived from the difference in electronegativity of the two main constituents [27]. Of course, this is not true for all types.

Due to the covalent nature of the bonding within the complexes, high temperatures are often needed to release hydrogen from the material. For example, $Mg(BH_4)_2$ requires temperatures between 300-400 °C to release 10 wt% H_2. The conditions for reversing this reaction are very harsh (400-500 °C and 850-950 bar H_2) [28]. However, $Mg(BH_4)_2$ can also release smaller quantities of hydrogen and form an intermediate compound $Mg(B_3H_8)_2$ when reacted at 200 °C over a 5 week period. Furthermore, this reaction is reversible at more moderate conditions (250 °C at 120 bar H_2 for 48 hours) [29]. Anion substitution with halides (LiCl into $LiBH_4$) has been reported to change the complex size, affecting the length of the hydrogen – complex bond and its stability.[30] This type of reaction opened a whole host of possibilities where adjusting the structural chemistry allows tailoring of the hydrogen storage properties is possible.

In summary, complex hydrides are an exciting class of materials that require extensive research in order to improve their properties. Their industrialisation and commercial value is probably many years away, but there is no doubt that if successful, they would provide an optimal system for reversible on board hydrogen storage.

2.1.1.3.3 Metal hydrides

Metal hydrides are another unique form of solid state hydrogen storage. Metals can absorb hydrogen into interstitial sites within a crystalline lattice. To do this, the hydrogen must dissociate at the surface of the metal before being chemisorbed into the metal lattice. This is shown schematically in Fig 2.4. Initial chemisorbed atoms sit in interstitial locations within a metal lattice (hence the common term 'interstitial hydrides'). Hydrogen to metal concentrations (H/M) of around 0.1 are usually achievable in this (solid solution) α-phase, with the addition of each hydrogen atom adding around 2-3 Å^{3} [31]. After the saturation of solid solution, the nucleation and growth of the metal hydride (β-phase) starts, often reaching values of (H/M) = 1 or higher. In the majority of cases, a co-existence of the α and β phases occurs, which is observed on a typical pressure composition isotherm (PCI) as the plateau pressure. Gathering a range of PCIs enables one to create a van't Hoff plot, giving thermodynamic quantities as shown in Fig 2.5.

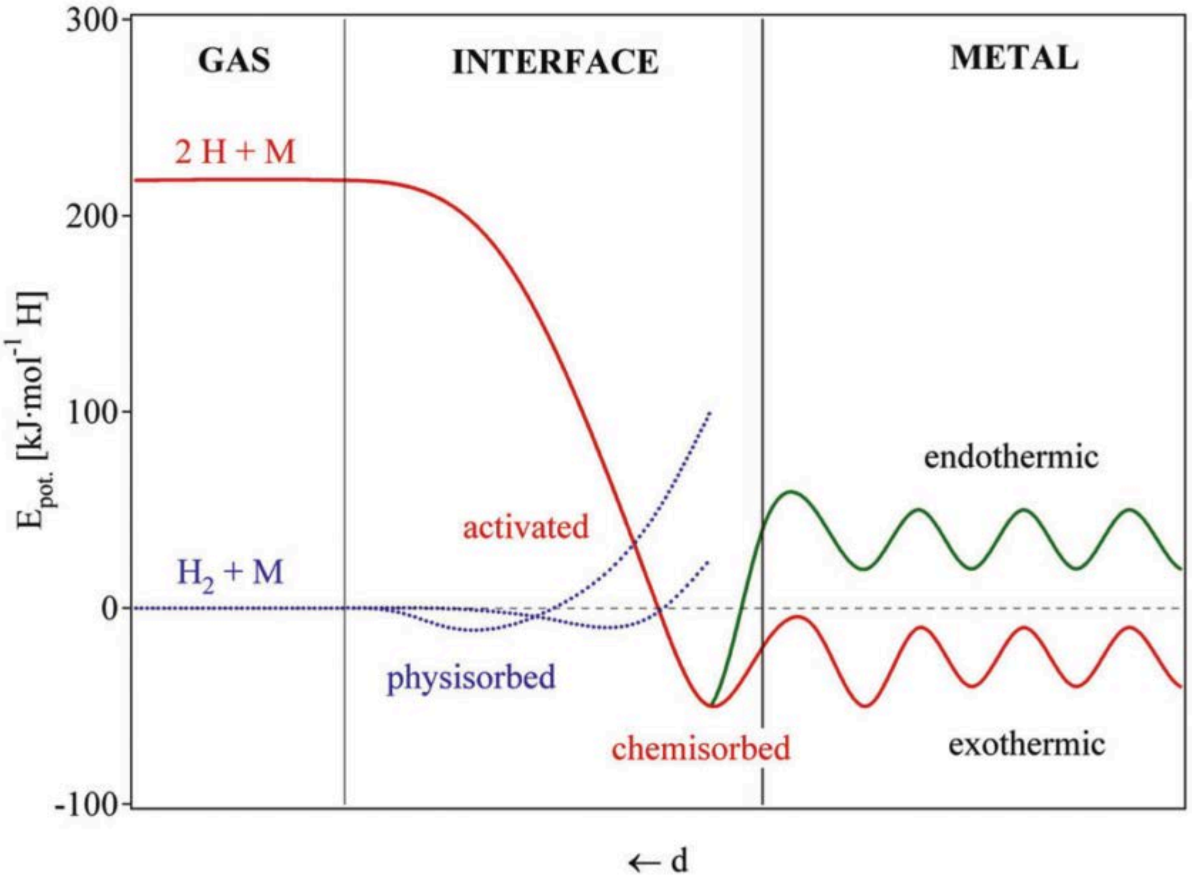

Fig 2.4. Lennard Jones Potential Energy diagram illustrating the possible interactions of hydrogen within a metal. Firstly, hydrogen can bond as a molecule, requiring only a small activation barrier (van der Waals interaction- Blue line). Or, hydrogen can dissociate and be chemisorbed into a lattice (red line) which requires overcoming a dissociation barrier (element dependent).[22]

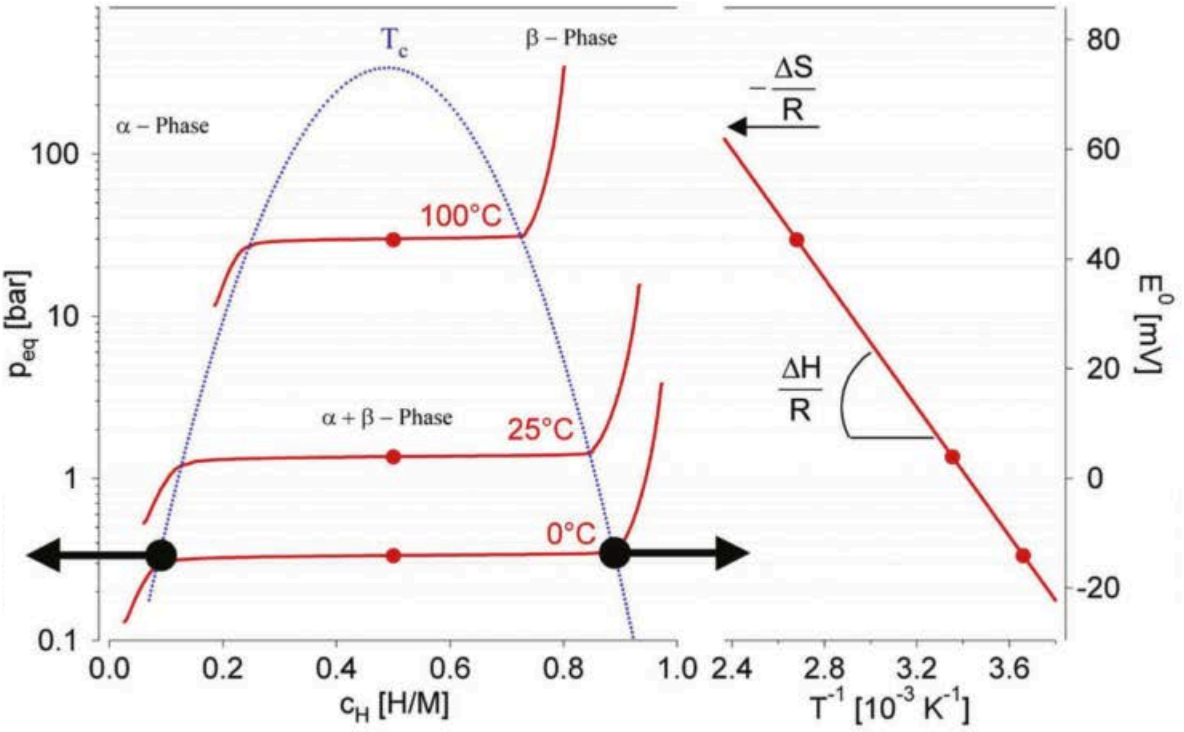

Fig 2.5. A typical pressure composition isotherm obtained from a metal hydride with the areas of α, (α+β) and β phases denoted.[22] *The construction of a van't Hoff plot is shown on the right hand side, with the gradient denoting ΔH/R and gradient ΔS/R. This is very useful in the characterisation of hydrogen storage materials.*

Derivation of the van't Hoff law comes from state functions. Gibbs free energy is denoted as ΔG. When ΔG is negative, a reaction can occur and is said to be spontaneous.

$$\Delta G = \Delta H - T\Delta S \qquad [1]$$

Where ΔH is the enthalpy change, T is temperature and ΔS is the change in entropy.

Another form of this equation is given as:

$$\Delta G = -RT \ln K \qquad [2]$$

With R being the universal gas constant and K being the chemical equilibrium constant. By equating these two we get the relation:

$$\ln K = \frac{\Delta H}{RT} - \frac{\Delta S}{R} \quad [3]$$

This is the van't Hoff equation. In the case of Metal- Hydrogen interactions, the equilibrium constant, K, is proportional to -1/T. As pressure is related to temperature, we replace the term K with the term P/P_0 where P is the reaction pressure and P_0 is atmospheric pressure. As the equation is of the form y=mx + c, a plot of ln K against 1/T will give the graphical solution of the equation where the gradient is ΔH/R and the intercept is ΔS/R, known as a van't Hoff plot. As the majority of the reactions studied are dealing with the reaction of molecular H_2 to dissolved atomic hydrogen then the entropy change should be very close to -130 J/K/mol H_2. Using this value, the ideal measured value of enthalpy for hydrogen release at 1 bar H_2 at 300 K is -39.2 kJ/mol.

Nucleation and growth of the β-phase is due to interactions between hydrogen atoms within the metal lattice (H-H interactions) [32]. When hydrogen atoms are added into a lattice, they interact with the stress field of other hydrogen atoms within a surrounding phase. The effect of this is observed in Fig 2.6, where the enthalpy of solution is altered, depending on hydrogen concentration [31]. At very low initial concentrations of hydrogen, the local lattice distortion can be considered as a local point defect (Fig 2.6). Much work has been done on this by Eshelby with his work on the force of an elastic singularity-showing that the point defect induces a lattice distortion as well as a volume expansion to keep the surface stress free. At increasing concentrations, the lattice has already been expanded at different defects, and the addition of more H atoms within the stress field of defects becomes energetically easier, enthalpy is reduced, following the trend in Fig 2.6. At higher hydrogen concentrations, the volume change reverts to normal values, probably associated with the long range order/crystal structure change becoming more obvious within the lattice and enthalpy values tend to increase.

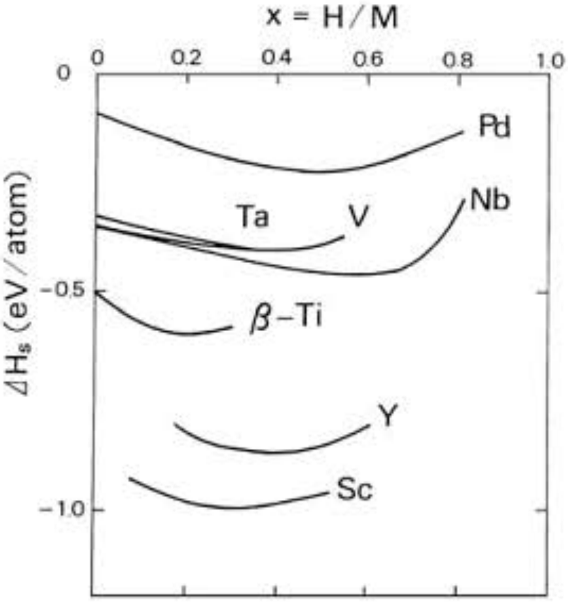

Fig 2.6. The dependence of the enthalpy of solution on hydrogen concentration for given metal hydrides.[31]

The enthalpy change can be quantified using thermodynamic relationships. The following relationships are taken from Fukai [31]. The relationship for the volume occupied by each hydrogen atom with respect to the enthalpy change for the system can be simplified approximately to:

$$v_H \approx \left(\frac{\partial \Delta H_s}{\partial p}\right)_T \tag{4}$$

Where V_H is the volume occupied by the hydrogen atom, p is pressure, T is temperature and ΔH_s is the enthalpy change per hydrogen atom. The enthalpy contribution dependent on volume is given by:

$$\frac{d\Delta H}{dx} = \left(\frac{d\Delta H}{dV}\right)_x \frac{dV}{dx} + \left(\frac{d\Delta H}{dx}\right)_v \tag{5}$$

Where x is the H/M ratio and V is the corresponding volume change. The first term on the right is the elastic contribution and is equated to:

$$\left(\frac{d\Delta H}{dV}\right)_x \frac{dV}{dx} \cong -K_0 \frac{V_H^2}{V_0} \tag{6}$$

Where K_0 is the materials bulk modulus, and V_H and V_0 are the volumes of the hydride and original material respectively.

The elastic volume expansion caused by addition of H atoms is thus directly related to enthalpy change. In powdered materials, the lattice dilatation is unrestricted; the lattice can freely expand and be free of stresses. However, in the case of a thin film, the substrate does not allow for the required expansion (at least in the x-y plane). This means that the expression is reduced in value, hence a change in the enthalpy value. The restriction of lattice dilatation due to H atom incorporation thus serves to change enthalpy values (and more usefully, the plateau pressure).

An approach that does not require the restriction of volume uptake but rather the size available for hydrogen site occupancy has been shown empirically, where the volume available for site occupancy in a metal hydride can be tuned by addition of small amounts of alloying elements. This was demonstrated by Lundin for AB_5 and AB_2 type alloys [33] and by Reilly et al for AB_5 type hydrides [34]. These examples relate the enthalpy of formation to the size of the tetrahedron within which the hydrogen atom is located. The empirical relationship is shown in Fig 2.7.

However, using this approach for magnesium may not be quite as trivial. The bonding in MgH_2 is partially covalent, with an elongated H ion[35]. The charge density map for the MgH_2 planar surfaces are shown in Fig 2.8. In general, we may not expect such a direct change in the enthalpy of formation.

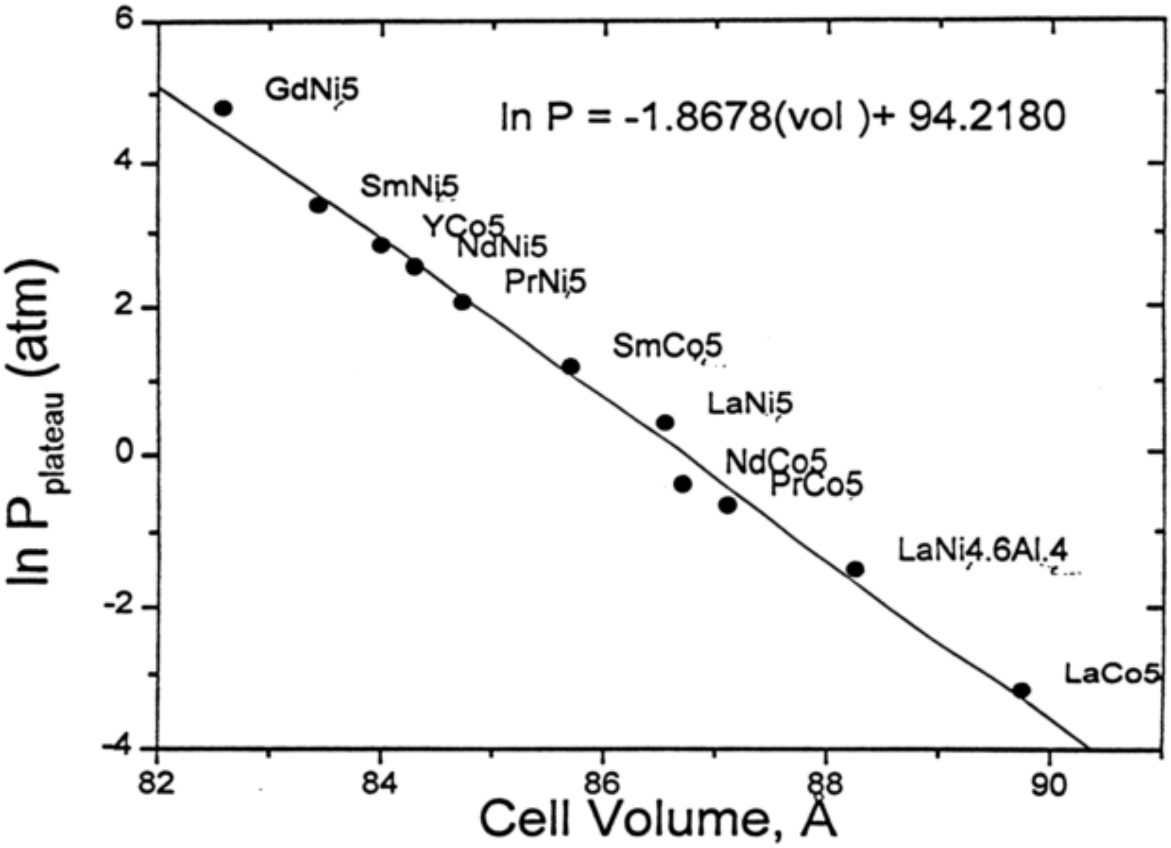

Fig 2.7. Empirical data observed which shows the relationship between plateau pressure and cell volume in AB_5 type hydrides. This shows how one can tune the thermodynamics of a given metal hydride by varying the alloy composition. [34]

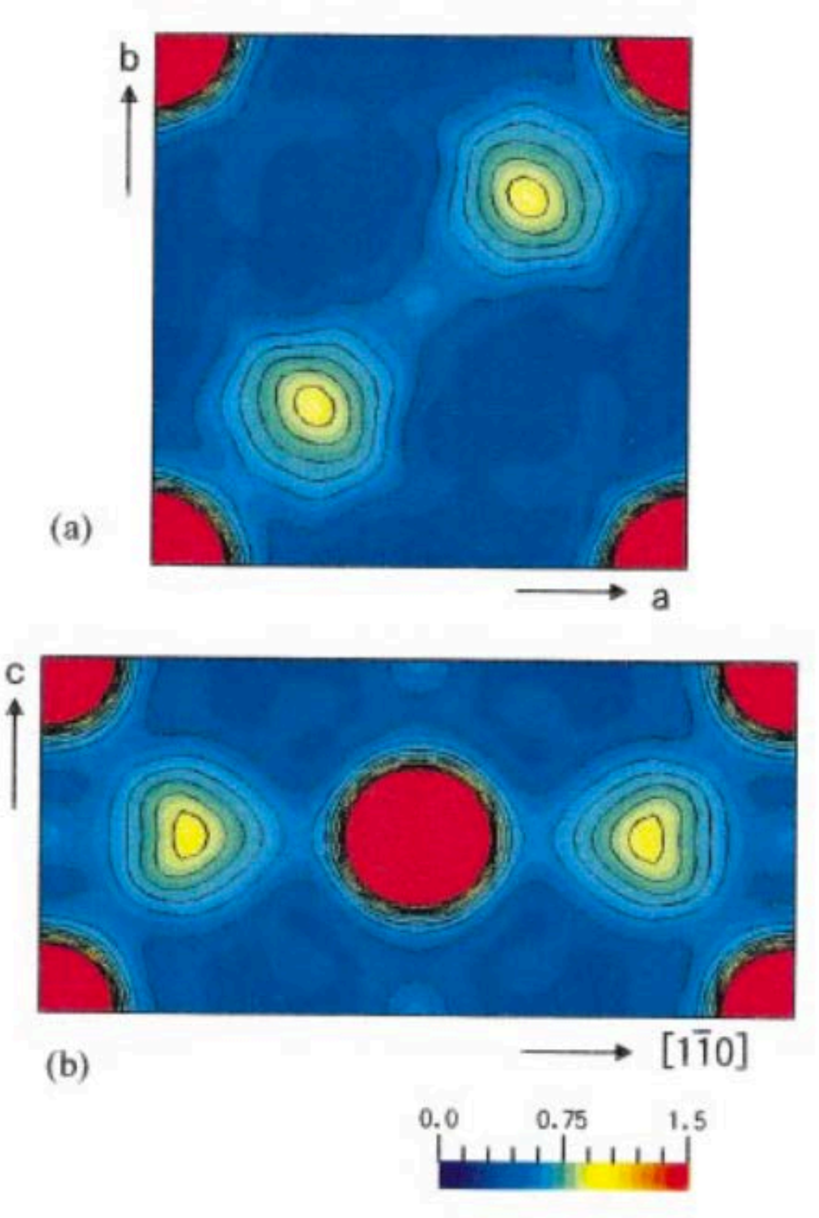

Fig 2.8. Electron charge density maps of MgH_2 planar surfaces - a) 001 projection and b) 110 projection. The scale shows the electron density surrounding Mg atoms (depicted as red) and hydrogen atoms (seen as yellow). At the bond midpoint, the electron density is around 0.26 e/A^3 which is larger than a typical Li-H ionic bond length (0.12 e/A^3) but much smaller than a typical Si covalent bond (0.7 e/A^3). The electron densities surrounding the Mg and H atoms are distorted, suggesting a degree of covalent bonding, not purely ionic character.[35]

2.2 HYDROGEN SORPTION PROPERTIES OF MAGNESIUM

2.2.1 Overview

Magnesium is one of the most promising candidates for a future hydrogen storage material. It has a gravimetric capacity of 7.6 wt% H_2 and, being a metal hydride, has very good volumetric capacity (around 110 kg H_2 m^{-3}). In addition, it is cheap and widely available. However, two main barriers to its utilisation for on board hydrogen storage media are its thermodynamic stability and its slow reaction rates. Magnesium forms the hydride, MgH_2 as a one step reaction, which is reversible:

$$Mg + H_2 \leftrightarrow MgH_2$$

Theoretical and practical thermodynamic (PCI) experiments agree that the enthalpy of formation of MgH_2 is around -75 kJ/mol H_2. In theory then, the absorption of hydrogen into magnesium should occur at room temperature and should desorb at around 300 °C at an equilibrium pressure of 1 bar H_2. The phase diagram for the entire Mg-H system at 1 bar is shown in fig 2.9. However, the ability of Mg to dissociate and recombine H_2 molecules at its surface is poor due to a lack of an anti-bonding d-orbital[36]. In addition to this, the hydrogenation of magnesium must occur through a solid state diffusion mechanism. For these reasons, the temperatures required to perform the absorption and desorption reactions are much higher than theory.

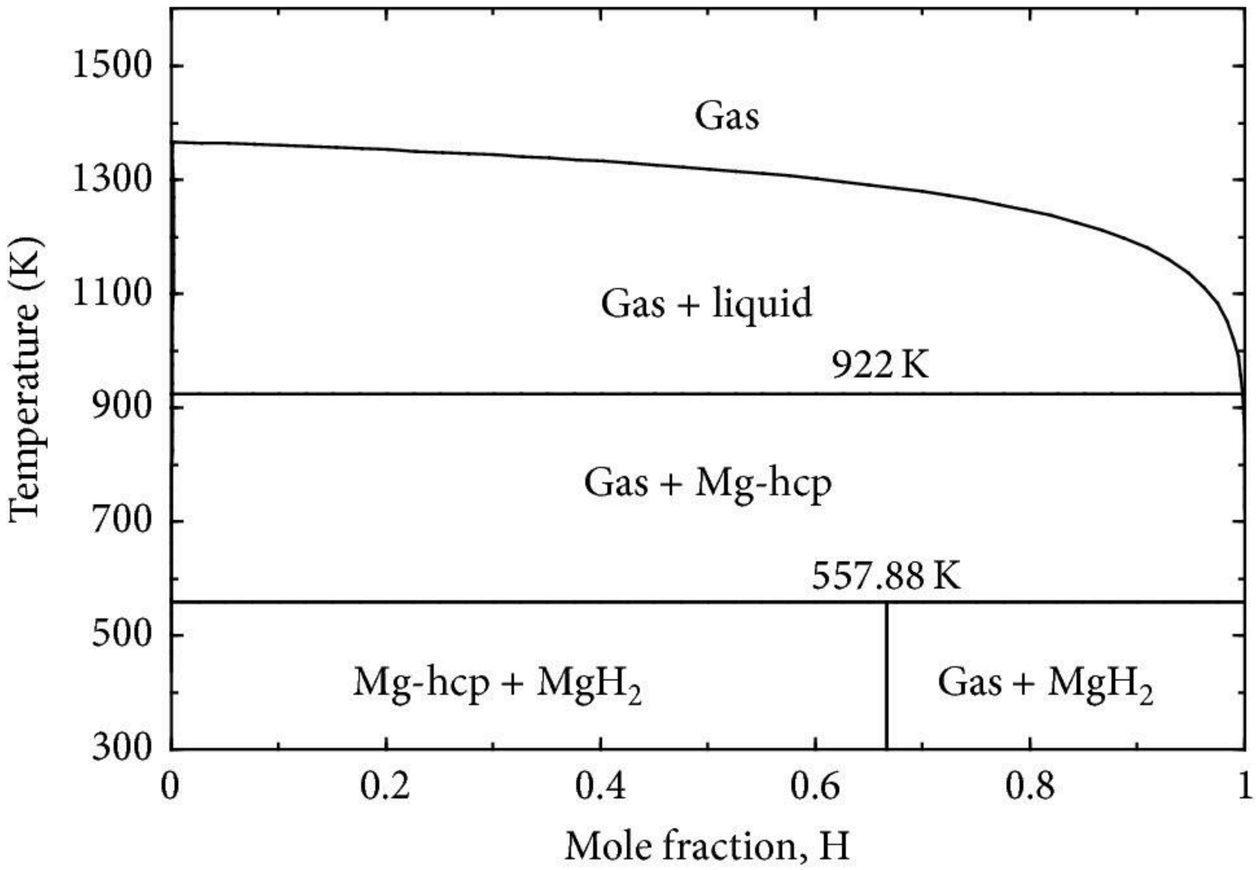

Fig 2.9. Calculated phase diagram for the Mg-H system at 1 bar H_2[37]*. The dissociation temperature of around 570 K is consistent with published literature.*

2.2.2 Kinetics

The reaction kinetics of Mg to MgH_2 and vice versa are peculiar. Early experiments by Krozer and Kasemo demonstrate a $P^{1/2}$ dependence on uptake rate in α - Mg [38]. This is to say that at H/Mg values up to 0.01, there is an influence of the loading pressure with respect to the kinetic behaviour. Around the concentration of H/Mg expected for the nucleation of the hydride phase, there is a lengthening of time required to reach equilibrium. This can be associated with the possible onset of H-H interactions required for the formation of the hydride phase. The influence of hydrogen loading pressure is important when considering practical applications, as the behaviour of the material needs to allow for rapid filling and a complete reaction. Fig 2.10 shows the potential known implications of loading at different pressures and temperatures with regards to the phase formation. The mechanisms for the reaction kinetics are clearly different for each case [39].

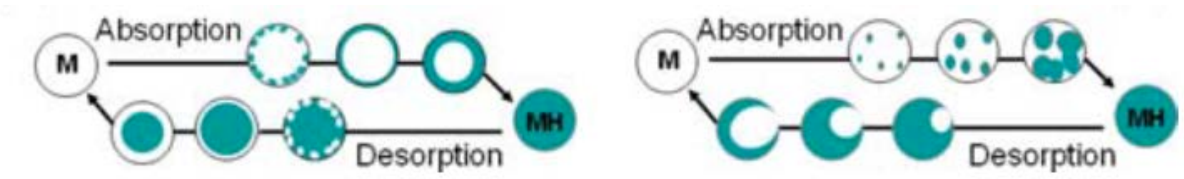

Fig 2.10. Typical microstructures that could be expected when reactions are carried out with hydrogen pressure at (Left) much higher than the equilibrium plateau pressure and (Right) very similar pressure to the equilibrium pressure. Note how the nucleation and growth behaviour differs significantly between a core-shell model and a random nucleation pattern. [36]

2.2.2.1 Microstructural Modification

As an initial starting point, we know that 'bulk' magnesium cannot be completely hydrogenated. If the thickness or particle size is above 30-50 micrometers, hydrogen cannot diffuse through the MgH_2 'shell' which is a total kinetic barrier for complete hydrogenation in practical terms[40].

By decreasing the particle size of Mg to no greater than 100 micrometers, using techniques such as ball milling, then the theoretical hydrogenation of Mg can be completed. Fig 2.11 shows the sorption behaviour of a conventional Mg powder sample with a particle size between 50-100 microns, meaning that theoretical absorption can occur. However, only after annealing at 350 °C and hydriding at 400 °C was any absorption shown in the conditions stated.

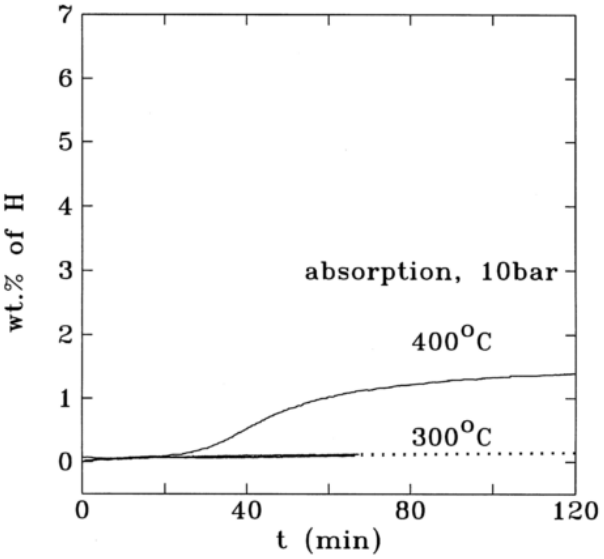

Fig 2.11. Hydrogen absorption in conventional magnesium powder at 300 and 400 °C at 10 bar H_2*.*

Absorption is limited to around 1.5 wt%, is kinetically very slow and not applicable for on board storage [40].

However, by increasing the ball milling time, the grain size can be decreased to the nanometer scale. The reduction in grain size to this scale greatly improves the absorption behaviour of the Mg and allows a much higher absorption percentage to occur, moderately quickly. This enhancement is shown to occur in proportion to the reduction in grain size with 20-30 nm proving to be optimal (Fig 2.12) [40]. The relationship between grain size and absorption kinetics is due to the modification of the microstructure. Because the transition of Mg to MgH_2 occurs via a nucleation and growth process, the increase in defects and grain boundaries at or near to the particle surface provide more nucleation sites on the Mg surface, as well as a diffusion path for hydrogen through the particle. Also, the reduced grain size limits the diffusion distance of H through the MgH_2 phase already formed, meaning the absorption is a lot less dependent on solid state diffusion mechanisms. In addition to the improvement in absorption kinetics, the improvements in desorption kinetics were also similar in this study as well as others, showing that the decrease in grain size is important for desorption behaviour.

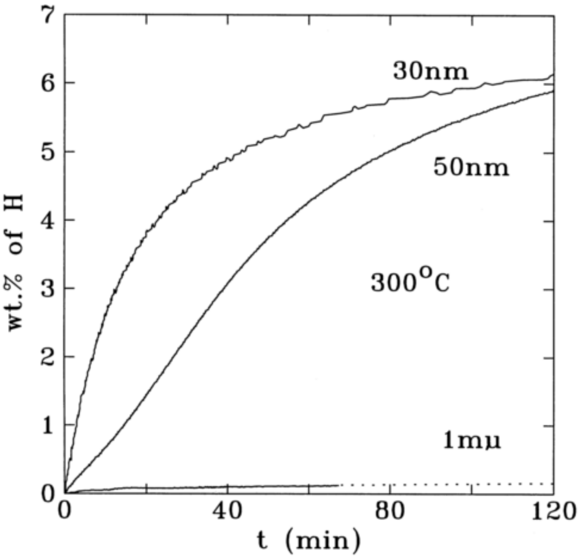

Fig 2.12. Hydrogen absorption behaviour, at 300 ℃, of ball milled Mg powder with respective average grain sizes displayed [40].

2.2.2.2 Catalysis

The previous section showed the improvement in absorption behaviour by micro structural modification of Mg. However, the improvements are not good enough to meet the demands of on board hydrogen storage, due to the high temperatures and long times required for absorption/desorption. Further kinetic improvement has been made possible with the addition of catalysts. Of these, a lot of effort has been on the use of transition metals and transition metal oxides, which are known for their catalytic properties in other industrial applications such as Haber process (Ru and Fe_2O_3). The important action of a catalytic particle in the case of hydrogen storage in metal hydrides is the ability to dissociate a hydrogen molecule which requires the presence of d orbitals which can interact with the hydrogen anti bonding orbital [36]. However, with any catalytic addition, it is important to realise that the theoretical limit of wt % is reduced.

Palladium is an example of a very effective catalyst for Mg. A fine dispersion of Pd nanoparticles on Mg particles of around 1 wt% has been shown to be very effective for catalysis. In this case, absorption/desorption occurred within 30 minutes at 300 °C (10 bar) and 330 °C (1 bar) respectively and is shown in Fig 2.13. In addition to the vast improvement in kinetics, the absorption of hydrogen could occur at lower temperatures (230 °C), which is related to the reduction in activation energy, not a thermodynamic effect. Thermodynamic effects tend to occur when there is a higher percentage of the catalyst present, which can form a Mg-alloy or a separate phase. This has been demonstrated with Mg-Y-Zn with 10at% Y and Zn. In this case, there was a marked increase in plateau pressure, similar to Mg_2NiH_4 but without such a drastic wt % decrease. The absorption temperatures could be lowered even further with the use of multiple TM's, as in the case of 4 wt% (Mn + Zr) although the mechanism for this behaviour was not discussed (Fig 2.14).

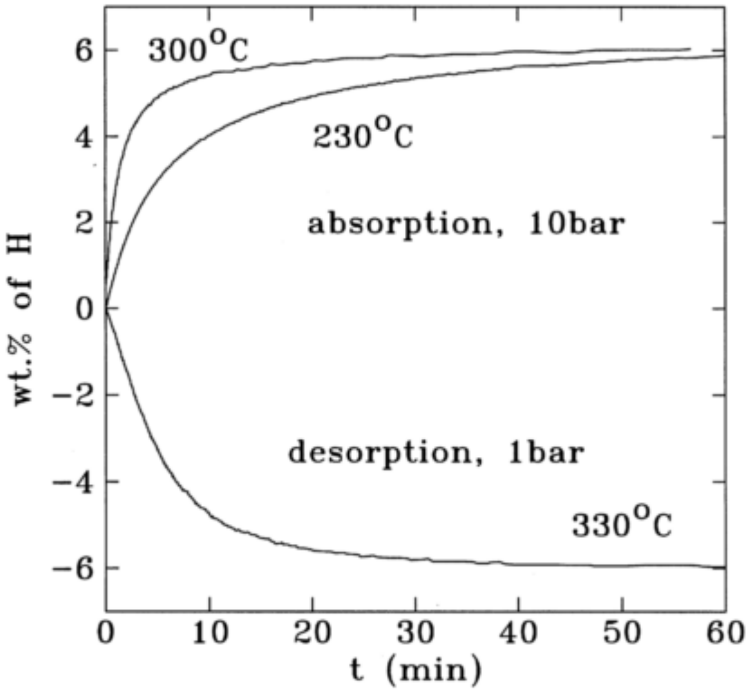

Fig 2.13. Hydrogen absorption/ desorption behaviour of Mg with a Pd nanoparticle catalyst added. Kinetics are a lot quicker in comparison to uncatalysed Mg powders with the same grain size [40]*.*

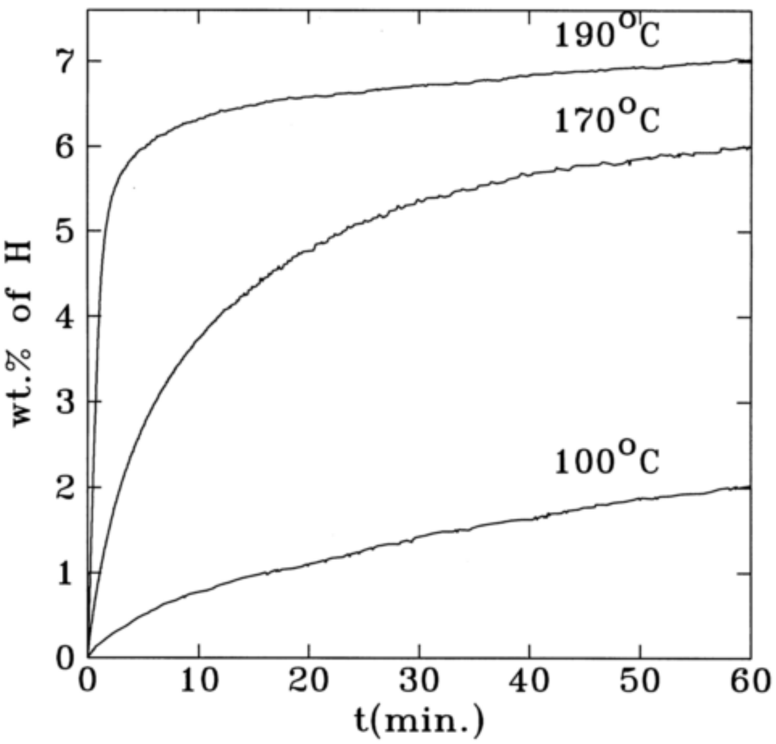

Fig 2.14. Hydrogen absorption/desorption behaviour for a Mg and 4 wt% (Mn + Zr) catalyst. Lower temperature absorption is possible due to a reduction in activation energy [40].

The ultimate aim is for room temperature absorption to occur. This would mean that refuelling at hydrogen stations would be easier and less costly. More recent research has demonstrated that room temperature (20 °C) absorption is possible with the use of 1 mol% Nb_2O_5 with 4.5 wt% achievable within 15 seconds. This is a marked improvement in comparison to earlier research and was attributed to the valence state of Nb within the Nb_2O_5 complex, which was reduced by the MgH_2 during milling [41]. This composite was later shown to desorb 5.3 wt% hydrogen at 160 °C within 100 minutes with a calculated activation energy of 71 kJ/mol H_2 (Fig 2.15) [42]. Similar effects of electron transport have been reported in MgH_2 coated with multivalence Ti-based catalysts [43]. In this instance, the coated MgH_2 particles were able to desorb 5 wt% H_2 within 15 mins at 250 °C. A new mechanism of electron transport via the Ti catalyst in the Mg^{2+} H^- desorption route was proposed. It would seem as though the valence state of the catalyst in Mg based systems is very important to aid the sorption properties. If the catalysts used mean that absorption and desorption can occur with little activation energy then the thermodynamics of the MgH_2 system are closer to what they should be in theory.

We can see then, that even if the thermodynamics are as good as we can make them in practice, they may still not be good enough to present a solution for on board hydrogen storage.

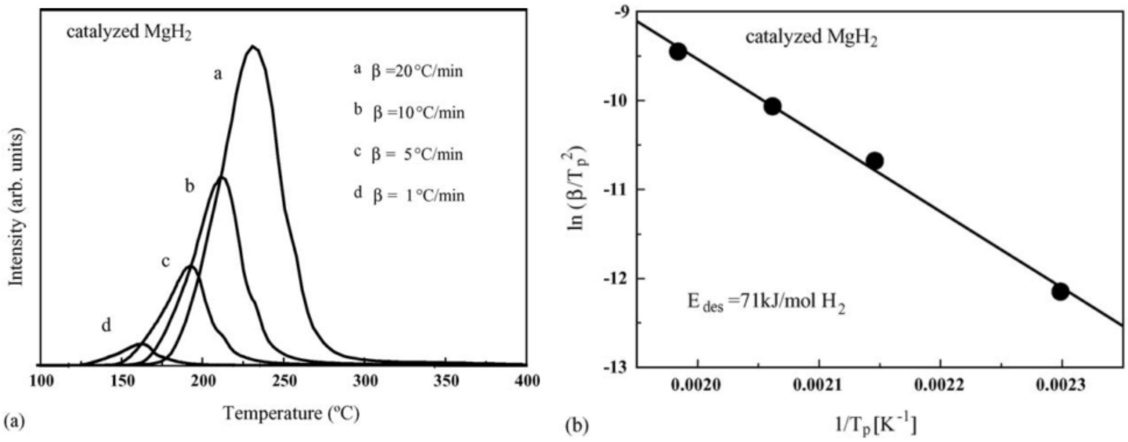

Fig 2.15. TPD profiles of (a) MgH_2-1mol% Nb_2O_5 composite and (b) corresponding Kissinger plot [42].

2.2.3 Thermodynamic destabilisation

2.2.3.1 Formation of secondary phases

As mentioned previously, thermodynamics of the Mg-H system can be altered if enough additions are added to form a different (or possibly secondary) phase. This will have the effect of destabilising the Mg-H bond and is usually done with the additional elements being non-hydride formers. An example of this is the Mg_2NiH_4 compound. This material was first reported by Reilly in 1968 and has more ideal thermodynamic properties than pure MgH_2. It has an enthalpy of formation of around -64 kJ/mol H_2 meaning that its desorption temperature is around 250 °C with a plateau pressure of around 3.4 bar at room temperature.

2.2.3.2 Nanoconfinement

There is theoretical evidence to suggest that the reduction of particle sizes to the nano scale can alter fundamental bulk quantities. Buckley et al. [44] calculated an increased desorption temperature for MgH_2 using the harmonic approximation method. This is contrary to other DFT based studies where a decrease is calculated. This demonstrates the difficulty in the modelling technique using at such finite sizes. This is known to be incorrect because there have been demonstrations by various researchers which show reduced desorption temperatures from MgH_2.

Some of the main authors who have attempted to decrease particle size experimentally have shown reduced desorption temperatures – based on their own DFT based calculations. Examples of this are by Wagemans et al [45] who calculated that particle sizes of 0.9 nm (Mg atoms <20) would give a desorption temperature of 200 °C. Experimentally, this particle size was not achieved [46]. However, the attempt at nanoconfinement did achieve particle sizes of 3-5 nm, using melt infiltration into a carbon scaffold. The desorption temperature here was not investigated.

There is more evidence for the reduction in desorption temperature where MgH_2 was embedded within a LiCl salt matrix[47]. The particle size of 7 nm showed a reduction in desorption temperature of 6 °C. Although this is smaller than expected, it shows the possibility of destabilisation (The reduced effect was shown to be due to increased entropy).

Further examples of lower temperature desorption stem from colloidal magnesium with particle sizes centred around 5 nm [48]. Here, the nanoconfined MgH_2 particles could desorb hydrogen at 80 °C. This was a massive improvement in desorption due to nano-size effects. There is speculation as to the reactions with the salt in which it was incorporated as they may have provided a better means to desorb hydrogen.

Gas phase synthesis is another experimental method which has been used to synthesise Mg nanoparticles. Particle sizes of around 10 nm have been prepared in this way[49], however their particular sorption properties were not investigated. Acetylene plasma metal reactions have been shown to produce carbon-supported Mg nanoparticles with a minimum size of 40 nm [50]. There was a reduced enthalpy quoted here, but this may be caused by the alloying with carbon frames in a similar fashion to Zinsou [48].

2.2.3.3 Thin Films

Thin films have been shown to be a very good model system for investigation of both alloying, nano-sizing or a combination of both. They are the main focus of this research and a complete review follows.

2.3 THIN FILMS

2.3.1 Overview

There are multiple definitions for a 'thin film' within the literature. However, a general consensus is that for a film to be considered as thin, it must have one dimension infinitely smaller than the other two. For the majority of the research carried out on thin films for hydrogen storage, the film thickness is sub micron.

In the search for hydrogen storage materials, thin film technology has shown many advantages in comparison to conventional bulk processing methods. The main advantages of thin film metal hydrides are reviewed by Baldi and Dam from recently published research and are as follows[51]:

- Ability to control microstructure by altering deposition parameters
- Co-deposition of normally immiscible metals creating new phases not available in bulk
- Forming wedged films and samples with a large range of compositions which can be characterised quickly using combinatorial techniques
- In depth study of metal hydride behaviour on a nanoscale (down to just a few nanometres)
- New phenomena have been observable (hysteresis/stress related)

Despite these advantages, the thin film approach suffers from a few drawbacks, namely:

- Amounts of material are usually very small (thickness <1 µm)
- Scaling up to bulk structure with the same composition and nanostructure is not always possible
- Characterisation can be difficult in comparison to powder samples

Thin film technology thus provides a model system in the search for materials for on board hydrogen storage. However, it has also been shown that thermodynamics and sorption behaviour can be different to bulk systems. This will be discussed in detail further on.

Besides their role in the search for hydrogen storage materials, thin films have other potential applications within energy related research. Hydrogen induced changes in the electronic band structure of the host metal means that optical changes are often observed, lending these films to applications as fibre optic hydrogen sensors[52–54], smart windows [55] and semiconductor devices[5657]. This was first reported for the transition of yttrium and lanthanum from YH_2 to YH_3 and LaH_2 to LaH_3 by Huiberts and colleagues[58]. Later, it was discovered that the Mg to MgH_2 phase transition also exhibits a transition from opaque and insulating metal to a transparent semiconductor. Mg-X alloys with X= (Ni, Co, Fe ; Mg:X =2)[59] and Mg-Zr-H solid solutions[60] have also shown similar behaviour. Other examples include the Mg_yTi_{1-y} ($0.1<y>0.3$) alloys which form a black state upon hydriding, lending them to applications as solar thermal absorbers[61].

The optical switching behaviour has been extensively exploited to characterise thermodynamic conditions (temperature and plateau pressure) for hydrogen absorption/desorption in thin films using 'hydrogenography' - a unique technique developed by Gremaud and colleagues based on the transmission of light through a sample[62]. This technique has led to the research and development of multiple interesting phenomena. In addition to this method, the hydrogen induced band structure changes means that metallic conductors become insulators or semiconductors, lending them to resistivity measurements.

The next sections review recent developments in the area of thin film hydrogen storage in more detail. The main focus is on the developments specific to Mg based films but other examples are also used to give a more complete overview.

2.3.2 Control of microstructure

A more complete overview of the properties of physical vapour deposition (PVD) systems is given in section 2.4. By altering some of the parameters within a deposition system such as working pressure, target/bias voltages and rotation speed, it is possible to control, at least to some extent, the microstructural features of the film. This was demonstrated by Higuchi and coworkers by altering the system base pressure and the RF target power to an Mg target[63]. The degree of preferred orientation of Mg (002) growth varied and was related to the difference in grain sizes and slight mis-oriented growth of columnar crystals within the film, affecting the diffracted intensity. Subsequent hydrogen loading revealed that films absorbed different quantities of hydrogen (from 2.9 to 6.6 wt%) and desorption occurred at different temperatures, shown by Temperature Programmed Desorption (TPD). An explanation for the difference in absorption amounts was not fully given. However, it may be that the grain size of the film plays an important role is how easily the film absorbs hydrogen. Singh et al[64] demonstrated the difference in film texture developed by pulsed laser deposition (PLD) and Sputtering, with sputtered films producing just one out of plane (002) peak and the PLD producing (002), (10-10) and (10-11) peaks. Highly textured films can have different mechanical properties in comparison to polycrystalline counterparts. The effect of column width was shown to affect the desorption temperature for pure Mg films, although the Pd capping layer serves as the main controlling factor governing sorption kinetics. In addition, a similar substrate induced change in microstructure was observed by deposition of films onto porous aluminium substrates. A more porous film structure was created by the porous substrate, which improved hydrogen absorption and allowed for stress release [65].

Clearly, this shows that the manipulation of texture and grain sizes influences the sorption kinetics and gives some insight as to thermodynamic modification through the use of thermal techniques. Examples of the microstructures obtained in these papers are shown in Fig 2.3.4.

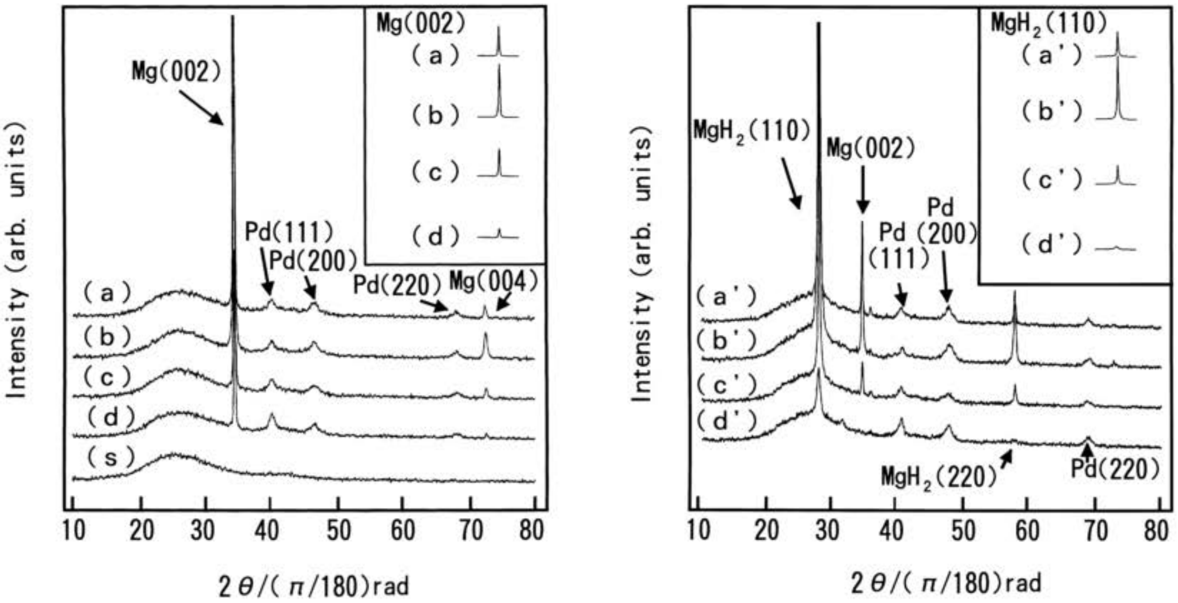

Fig 2.3.1 XRD patterns showing different diffraction intensities of Mg/Pd bilayer films as prepared (left) and after hydrogenation (right) in various conditions, suggestive of differences in texture and texture development after hydriding[63]. No consideration was given to intrinsic or hydrogenation stress.

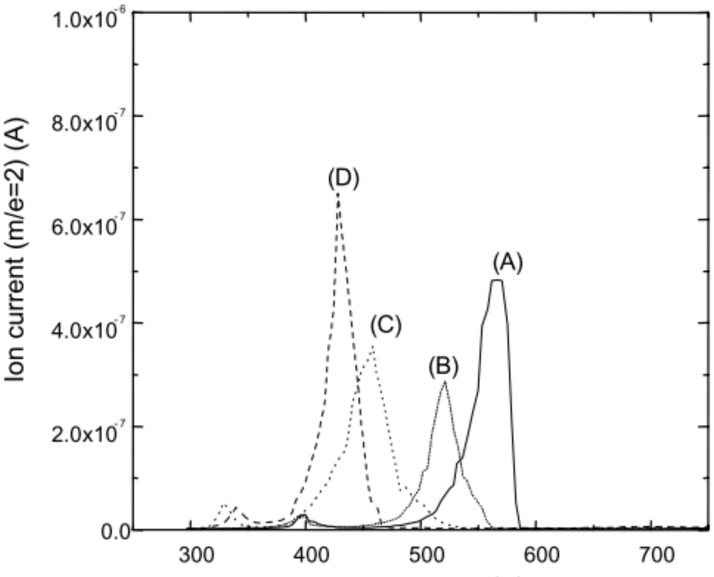

Fig 2.3.2. TPD profiles of a range Pd capped Mg films (250nm) prepared in a variety of evaporation conditions clearly showing a difference in thermodynamic stability [66].

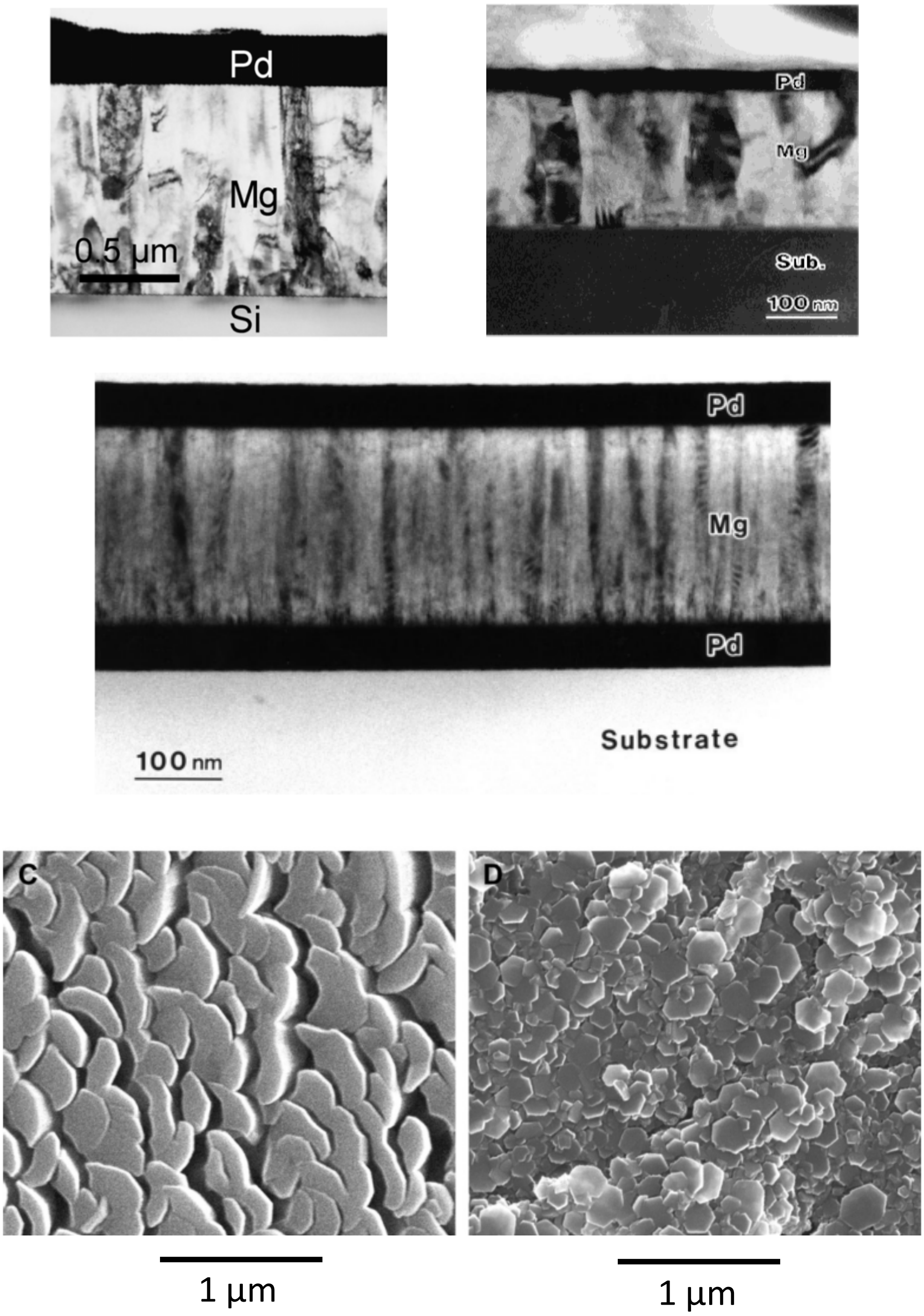

Fig 2.3.4. Typical microstructures obtained for Mg deposition from [64] *top left and* [66] *top right. Middle picture shows a Pd/Mg/Pd structure from*[67]*. Note how the column width changes dramatically for the Mg film deposited on the Pd base layer. (Bottom) Comparison of Pd/Mg/Pd films prepared on anodic aluminium oxide (AAO)showing intrinsic porosities and glass substrates* [65]*.*

For pure metals with low melting points such as magnesium, the ability to form an amorphous material is very difficult, requiring a cooling rate in the order of millions of degrees per second. However, the possibility to deposit amorphous alloys is far easier. The criterion developed by Lu et al. shows a dependence on the liquidus, crystallisation and glass transition temperature. Mg-Ni alloys, certainly those close to the eutectic composition (see Fig 2.3.5), readily deposit as amorphous if the degree of undercooling is large enough, and is often achieved by a cooled substrate holder. The large rate of undercooling serves to increase nucleation rate and limit any grain growth, either producing completely amorphous or nanocrystalline materials [68]. This allows one to investigate the properties of ordered vs disordered alloys. Chen et al[69] investigated the composition $Mg_{1.2}Ni_{1.0}$. The metastable film was found to crystallise at over 300 °C and hydrogen sorption properties revealed absorption and desorption at 150 °C under 33 bar H_2. The resulting enthalpy was calculated as -42 kJ/mol H_2 for hydrogen desorption, a significantly differently quoted value to the crystalline values (-64 kJ/mol H_2). The value was not quite as low as melt spun ribbons, with an enthalpy quoted as -39 kJ/mol, suggesting that the degree of disorder and composition are sensitive to thermodynamic changes.

Amorphous/nanocrystalline materials in either film or melt spun ribbon form is an emerging theme within hydrogen storage technology. This is due to a variety of factors. To start with, the specific binding energies for hydrogen are not as well defined in these systems. As long range order is significantly lacking, there is evidence to suggest that the occupancy energies of interstitial sites becomes much more varied (a Gaussian distribution function normally applies)[70]. As such, amorphous alloys do not often exhibit a clear plateau pressure characterised by crystal structure phase changes in crystalline alloys. This has been observed in $Zr_{50}Ni_{50}$ alloys[71] (Fig 2.3.6). It was also observed that hydrogen solubility is related in a linear fashion to hydrogen pressure- demonstrating an interesting feature of using these materials as storage tanks as the cost to fill would be proportional to hydrogen pressure. Thus, the use of thin film technology to control order within the deposited alloys serves as a way to investigate and potentially improve the hydrogen sorption properties.

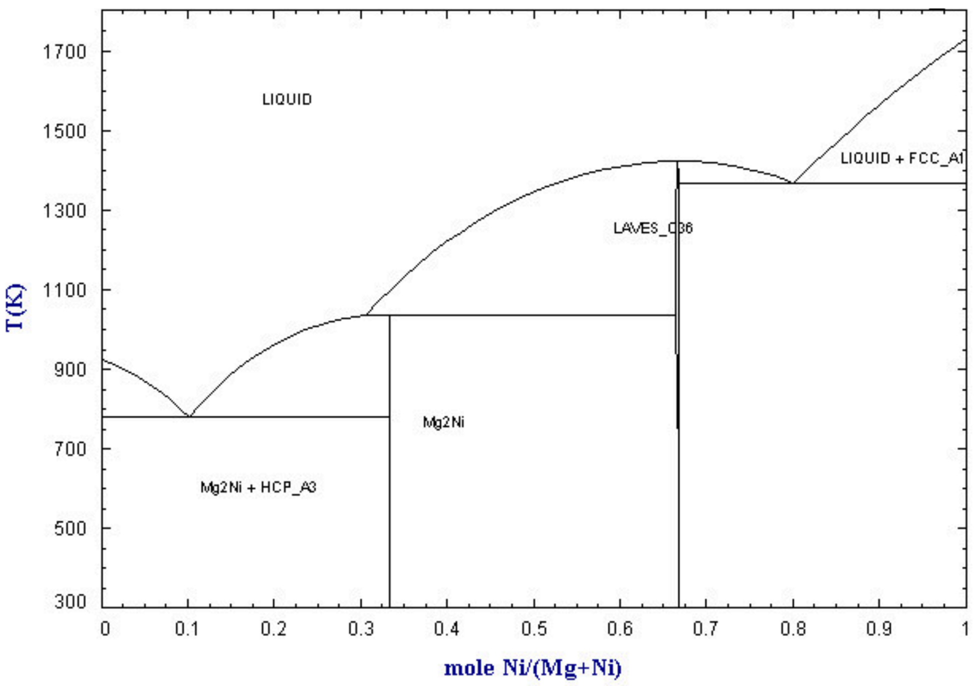

Fig 2.3.5 Mg-Ni phase diagram[72]*. The eutectic composition around* $Mg_{0.9}Ni_{0.1}$ *is favourable for forming amorphous/nanocrystalline structures.*

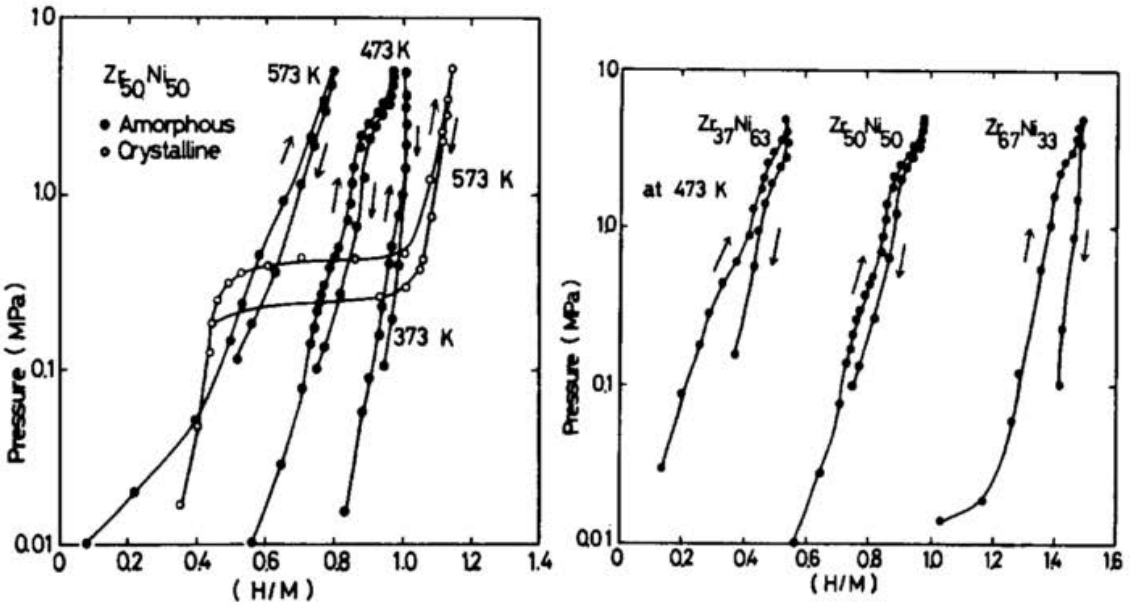

Fig 2.3.6 Hydrogen sorption isotherms of Zr_xNi_{1-x} *alloys. No plateau pressure is observed and there is negligible hysteresis, reported to be due to the different energies of binding sites for hydrogen due to short range order.*[71]

2.3.3 Formation of new phases

In PVD systems, the thermodynamic driving force in thin film systems for formation of grains is generally the degree of vapour supersaturation, which is extraordinarily high in comparison to bulk methods, meaning that films tend to have a very fine grain structure. It also means that it is possible to achieve very high levels of doping and in some cases, new crystal structures with normally immiscible elements. Demonstrations of this have successfully been shown in the Mg-Ti alloys with Mg_yTi_{1-y} (0.05<y>0.9) being prepared by both electron beam and sputter deposition[73]. Metastable Mg_yTi_{1-y} alloys have been prepared, and upon hydrogenation, form new hydride phases $Mg_yTi_{1-y}H_x$. For y values of 0.9 or greater, the HCP structure of the host Mg lattice is preserved, with Ti as a solid solution element. There is no significant improvement in thermodynamics or kinetics observed. However, adding more titanium leads to the evolution of a cubic structure.

The hydride here tends to form a FCC fluorite phase and has good kinetic properties even at room temperature, storing around 4 wt% $H_{2,}$ as measured galvanostatically[74]. The formation of a FCC phase shows the importance of crystal structure as related to sorption kinetics[75]. This structure has been formed using high-energy ball milling and a BCC phase was identified at the composition $Mg_{35}Ti_{65}$. The hydrogenation of these structures was also shown to occur (at 80 bar) without phase segregation into Mg and Ti elements, but the high temperatures required for dehydrogenation meant the Mg-Ti elements segregated[76].

Another approach to produce a variety of compositions and thicknesses using thin film systems is to block off a target using a shutter system. By positioning a shutter at a given position and keeping the substrate in the same position, it is possible to create a film with a compositional gradient (when co-sputtering with an adjacent target) or alternatively, a wedged structure can be created, so that the film has a different thickness across its length. Because of these unique properties of thin film deposition, the hydrogen sorption properties of thousands of compositions, as well as the effect of thickness, can be tested using high throughput methods such as hydrogenography. The technique of 'hydrogenography' developed by Dam and colleagues and based on the transmission of light through a sample, has been shown to be useful in characterising the Mg-Ni-Ti ternary system.[77]. The findings here revealed that there are ternary compositions of Mg-Ti-Ni which showed an ideal formation enthalpy of -40 kJ/mol (Fig 2.3.7). This material was later investigated with the use of EXAFS and it was found that although the enthalpy change was ideal, the Gibbs free energy was affected by the change in entropy related to formation of TiNi intermetallics[78].

In addition, a wedge shaped film of Mg was deposited with a thickness variation between 1-10 nm (Fig 2.3.8). The resulting isotherms were measured at different points on this film, revealing that at very small thicknesses, the interface energies from adjacent layers becomes important[79].

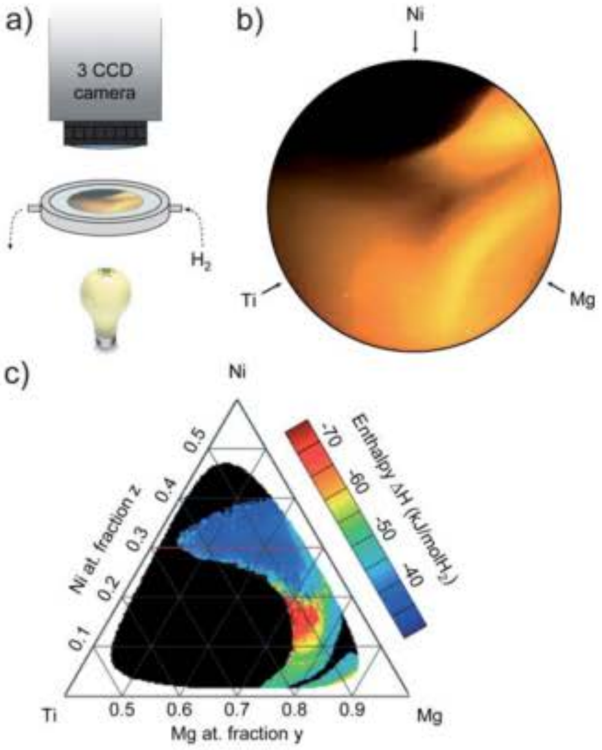

Fig 2.3.7. A) The optical set up used for the experiment. B) The physical appearance of the specimen. C) The enthalpy map of a thin film with ideal thermodynamics identified in the composition region $Mg_{69}Ni_{26}Ti_5$ *with enthalpies of around 40 kJ/mol* H_2 *and a hydrogen storage capacity around 3.2 wt% (H/M = 1.1)* [62].

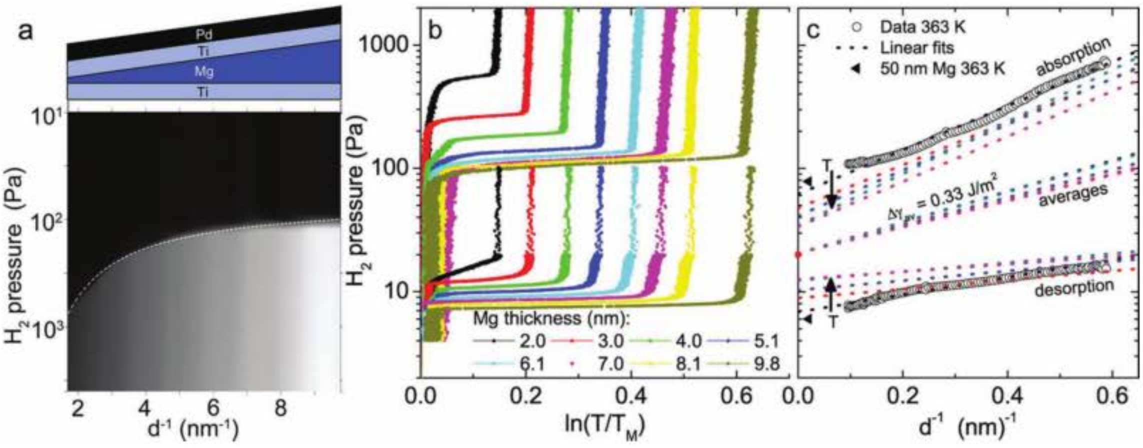

Fig 2.3.8. Example of a wedge shaped structure (a) and its effects on thermodynamics (b). The description of the hysteresis branches shows the contribution of interface energy to the destabilisation of the hydride (c).

2.3.4 Effect of stress

Thermodynamic destabilisation of MgH_2 by using mechanical methods was first reported by Fujii [67]. In the Pd/Mg/Pd layered films fabricated by sputtering, the contraction of PdH_x layers to Pd upon heating induced a large compressive stress into the lattice of MgH_2. This produced a large thermodynamic shift in the stability of the MgH_2 and reduced the sorption temperatures to just above room temperature (measured in vacuum). No values could be quoted for the enthalpy change in this case, although the effect was termed the 'co-operative phenomena'. A schematic representation is shown in Fig 2.3.9.

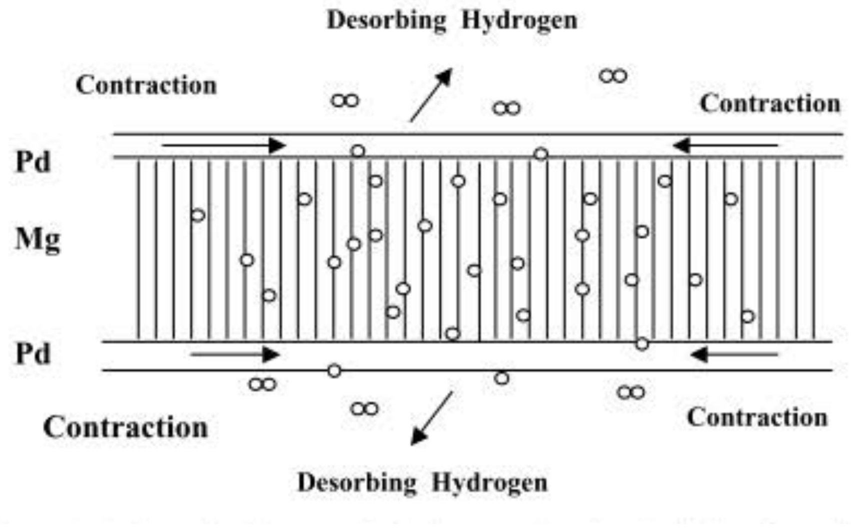

Fig 2.3.9. Schematic representation of the co-operative phenomenon. The contraction of PdH_x layers to Pd upon hydrogen desorption induces a compressive force into the MgH_2 layer, lowering the desorption temperature[62].

This effect was built upon by Baldi et al[80] who revealed that the absorption plateau pressure can be altered when very thin layers of Mg are capped with a miscible element (Fig 2.3.10). The origins of this effect were suggested to be due to 'elastic constraints', meaning that the volume change in the MgH_2 was effectively restricted due to the small layer of alloying at the interface. The fundamental reasoning for this effect is the repulsive attraction between H-H atoms within metals when volume expansion is restricted, as mentioned in section 2.1. Capping elements that do not alloy with Mg (Ti, Nb, V) show behaviour of Mg similar to bulk. Chung et al[81] argue that the observed destabilisation is of chemical origin, whereby the interfacial mixing of the Mg/Pd regions requires additional energy for the formation of MgH_2, which is exacerbated within thinner layers.

This effect has not been observed directly in powders because the metal lattice is often free to expand. However, synergistic effects have been reported for mixtures of Mg_2NiH_4/MgH_2 phases, where the hydrogen is released at different temperatures depending on the amount of phases present[82]. The desorbing phase may be surrounded by an alternative phase. The tensile/compressive stresses placed on the adjacent phase then act as a driving force for destabilisation schematically shown in Fig 2.3.11.

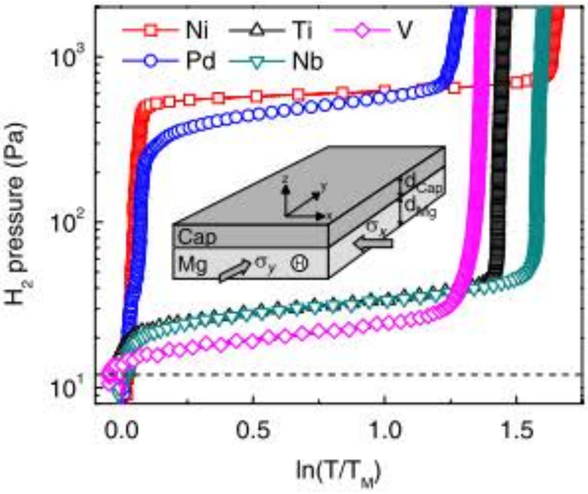

Fig 2.3.10. The effect of miscible vs immiscible alloying elements as capping layers on the plateau pressure of Mg films. The plateau pressure for the formation of MgH_2 is increased dramatically. This is suggested to be due to the effects of clamping which forms a H-H repulsive interaction [80].

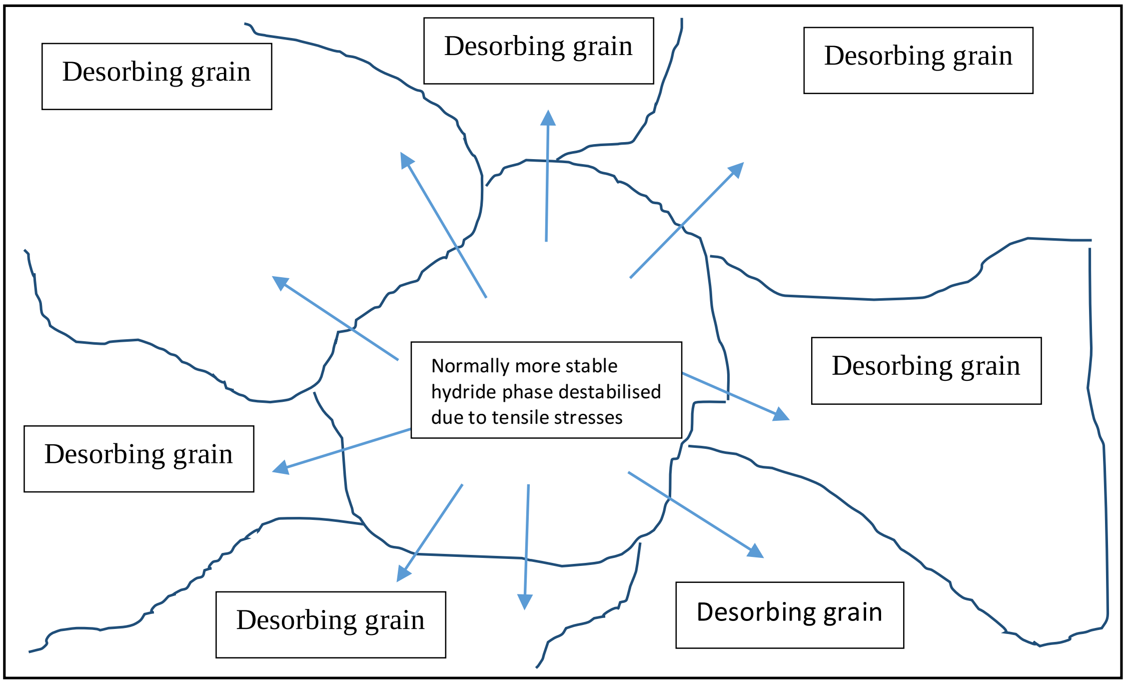

Fig 2.3.11. Author's schematic representation of the potential synergistic effects observed in multiphase powders, only recently confirmed with the use of thin film experiments.

The effect of a substrate has been investigated in Pd films[83]. It was found that an alumina substrate tended to adhere better to the film that quartz substrate. Adhesive failure in the form of buckling meant that films on quartz substrates had thermodynamic quantities very similar to bulk values. A longer activation period was required for buckling on alumina substrates to occur. Before this occurred, the plateau pressures were different to bulk, suggesting a high adhesion led to a thermodynamic modification. In a later paper, a titanium buffer layer was used to increase adhesion of the Pd film to the substrate. It can be seen that the effect of substrate clamping can adjust thermodynamic measurements in the same way as a Pd capping layer. The widening of the hysteresis is related to the amount of work done in absorption of the original host lattice, as would be expected. Fig 2.3.13 shows the difference in film stress measured on films that became delaminated from their substrate (green) and those that remained adhered to the substrate (red). The work done in this instance is the integral of the shaded area. The model proposed by Pivak in this case demonstrates that the extensive plastic work performed effectively widens the hysteresis between absorption and desorption plateau pressures by 2.7 and 1.3 kJ/mol H_2, respectively [84]. A similar effect has been observed in Fe - doped Pd films [85], Nb based films [86] and Ti films with different thicknesses [87]. The effect of mechanical properties due to preparation conditions in Pd based films prepared on a variety of substrates has also shown the combinatorial effect of both the initial microstructure and its effect on the evolving microstructure of a film during hydrogen absorption [88]. This clearly shows the importance of understanding the initial microstructural characteristics and the influence that they have on the hydrogen absorption.

The effect of substrate clamping has also been observed in Mg films, where the absorption plateau was significantly different to bulk (-61.6 kJ/mol) but there was no effect on the desorption plateau, which is similar to bulk (Fig 2.3.14). There is an extensive widening of hysteresis at low temperatures due to extra mechanical work required to hydride the film[89]. The effect of higher temperatures serves to decrease hysteresis and it likely that removal of defects is easier at higher temperatures, as well as a decrease in young's modulus. A similar effect has also been observed in Mg_2NiH_4 films (Fig 2.3.15) where an increase in absorption and decrease in desorption plateau was observed[90]. This was believed to be due to a preferential orientation between two planes, similar to orientation relationships reported in other studies of pure Mg[63,66,67,91–93]. The reduction in work required for desorption is a direct result of texture within the films and the atomic movements required. It would seem as though the effects of texture, mechanical properties due to grain size, morphology and adhesive effects can all have a large impact on thermodynamic properties of magnesium and its hydride.

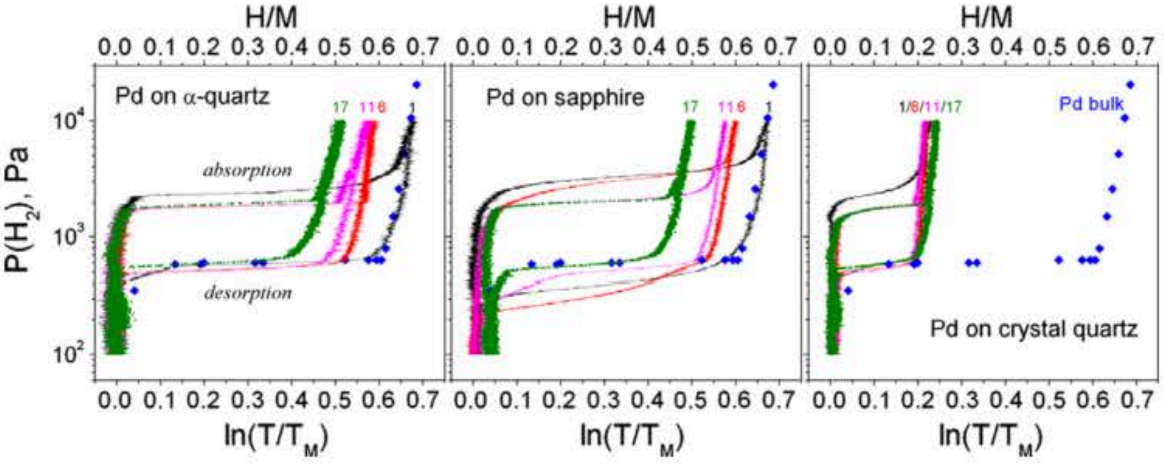

Fig 2.3.12. PCIs of Pd thin films on different substrates for a repeated number of cycles. Changes in thermodynamic behaviour are observed due to stress relaxation effects on the different substrates. Interestingly, the H/M ratio available for the film on crystal quartz would appear to show an incomplete loading – no comment was made by the authors.

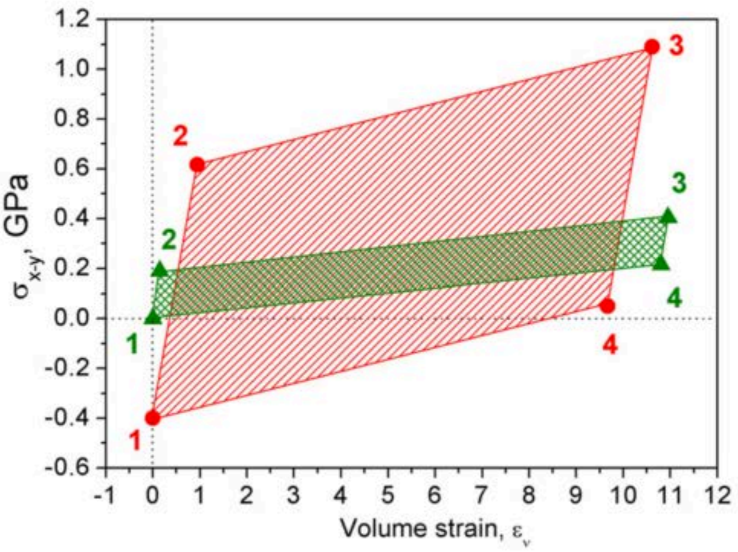

Fig 2.3.13. A stress strain analysis during hydrogen absorption/desorption for palladium films on sapphire substrates with an additional titanium ‘adhesion’ layer (red) and without an adhesion layer (green). The higher level of adhesion promotes additional storage of elastic energy and stress release via plastic deformation (material pile up) [84].

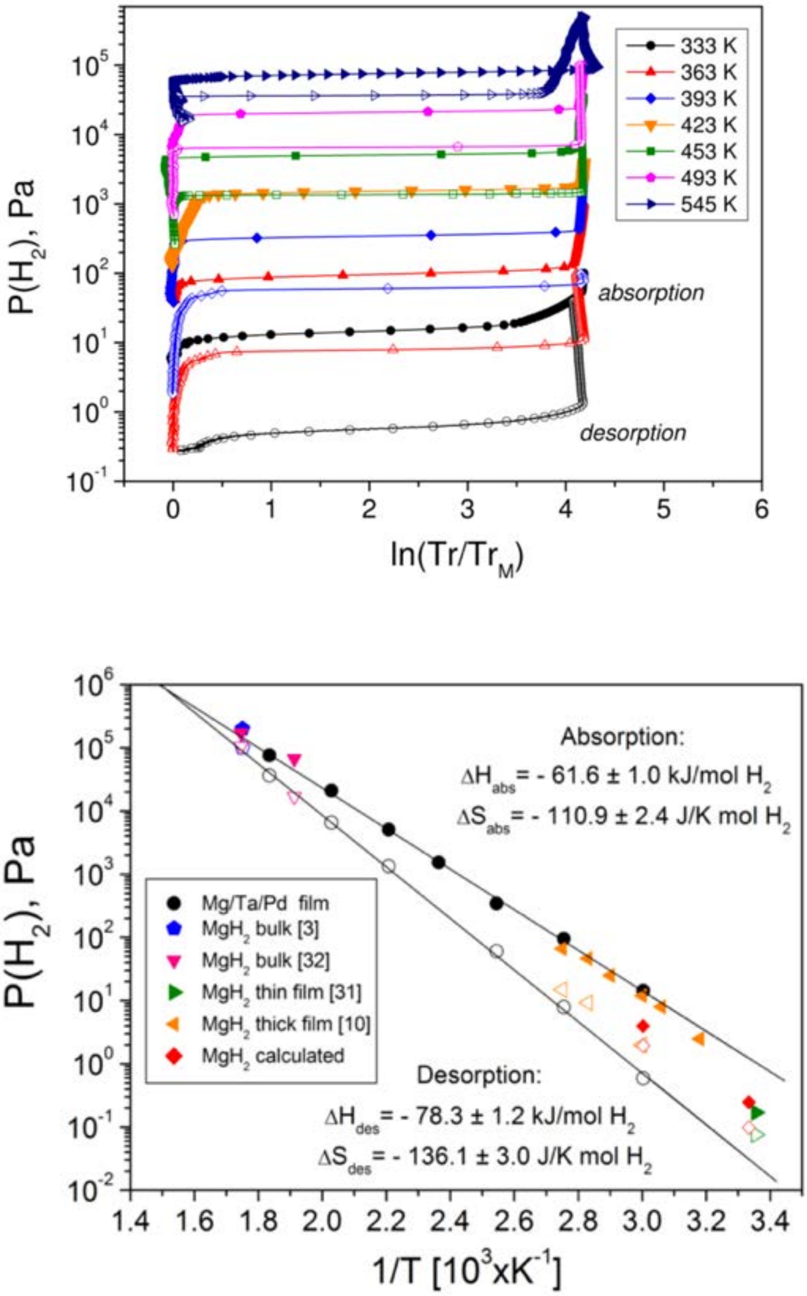

Fig 2.3.14. PCIs and corresponding van't Hoff plots of Mg/Ta/Pd films on fused glass substrates. Absorption branches show much higher plateau pressures than bulk. It is interesting to note the decrease in hysteresis with increasing temperature, suggesting a thermally activated stress release mechanism [94].

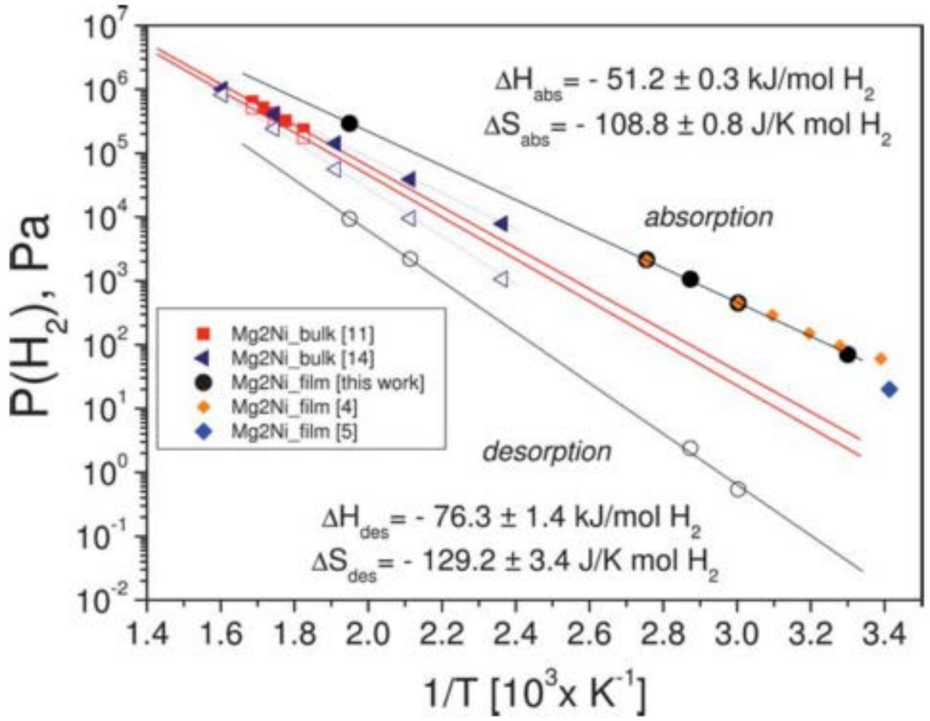

Fig 2.3.15. Van't Hoff plot of the absorption and desorption properties in a Mg_2NiH_4 thin film. A widening of the hysteresis is observed, suggested to be related to a complex mechanism involving the preferential orientation and nucleation of hydride/metallic phases within the parent phase, driving a large change in thermodynamic values [90].

2.3.5 Hysteresis

Some aspects of hysteresis have already been mentioned in the previous sections. However, it is a phenomenon that affects all metal hydrides and denotes the difference in thermodynamic behaviour between the absorption and desorption branches on a PCI. Many authors have speculated that the origin of hysteresis lies within the energy required for expansion of the host metal lattice. However, within powders, the analysis is difficult to ascertain, as the expansion must certainly exist, but it is not easily measurable. Recent work by Pickering et al showed how doping AB_2 type alloys with small amounts of niobium could affect the plateau pressure of that system by around 30 bar H_2. Furthermore, there was an asymmetric broadening of the effect in comparison to the undoped alloy and links were made to the stabilising effect of niobium on the unit cell volume [95] .

However, thin films present a simplistic model system that allows for the interpretation of mechanical constraints on the sorption behaviour. Recently, Mooij et al have demonstrated the effect that both elastic and plastic deformations can have on the thermodynamics of phase changes [79]. The changes are summarised in Fig 2.3.16 but mainly consist of a widening of the hysteresis due to plastic deformation, an upwards shift caused by some form of elastic interaction (no widening) or a combination of both, where the effect appears asymmetric in comparison to bulk, with a larger jump in absorption compared to desorption.

This type of investigation also led to the results shown in Fig 2.3.17. When investigating what happens at the nanoscale after the first hydrogenation cycle, it is shown that the films can easily absorb hydrogen at lower pressures than originally, due to the removal of the energy needed to expand the film in the original instance. This therefore proves the contribution of mechanical effects to the hysteresis in thin films, and indeed, in principle, to the rest of the metal hydride family, although those interactions may be more complex due to the nature of intermetallics.

Complementary to the practical investigations already discussed, there are a few recent density functional theory (DFT) simulations which have shown that the effect of strain changes thermodynamics but also kinetics of the reaction. A small biaxial strain is shown to change the desorption temperature in both compression and tensile regimes, with a more notable effect arising from a tensile regime [96].

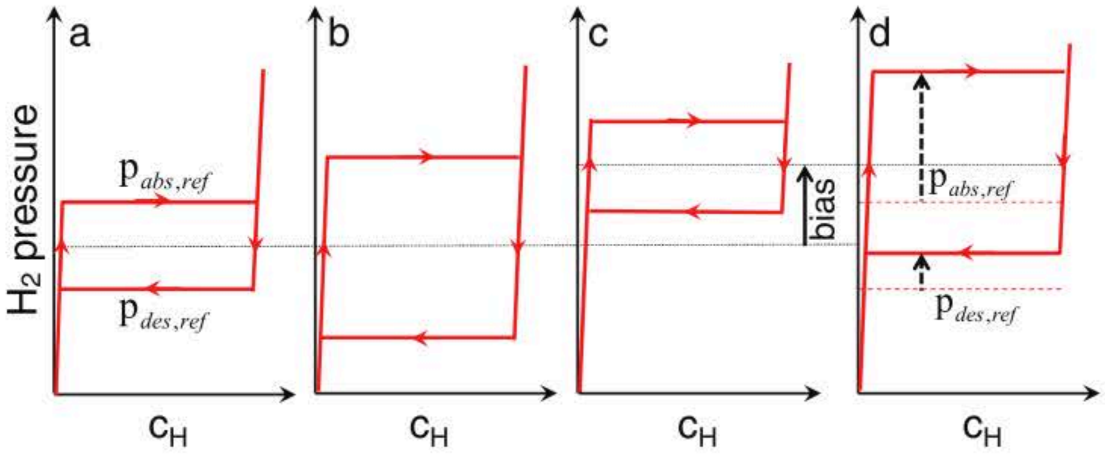

Fig 2.3.16. Hysteresis in interaction with metal hydrides [79]*. A – Reference state. B – Extra component (plastic deformation) that widens the hysteresis. C – Elastic component such as surface energy. D – A combination of B and C.*

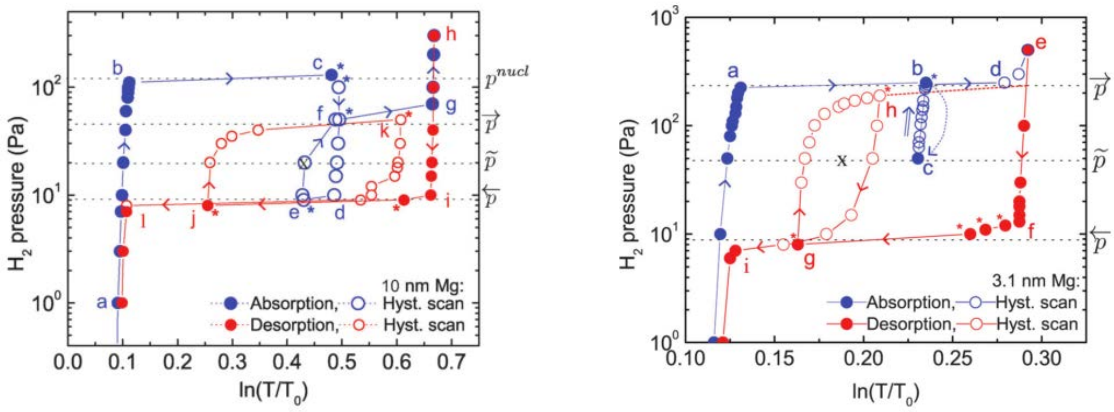

Fig 2.3.17 Hysteresis scans which show that on the second cycle (red - left), absorption pressure can be lower due to the removal of a boundary energy in a 10 nm film. However, for a 3 nm film (right) the absorption behaviour remains the same despite the removal of the boundary energy [97]*.*

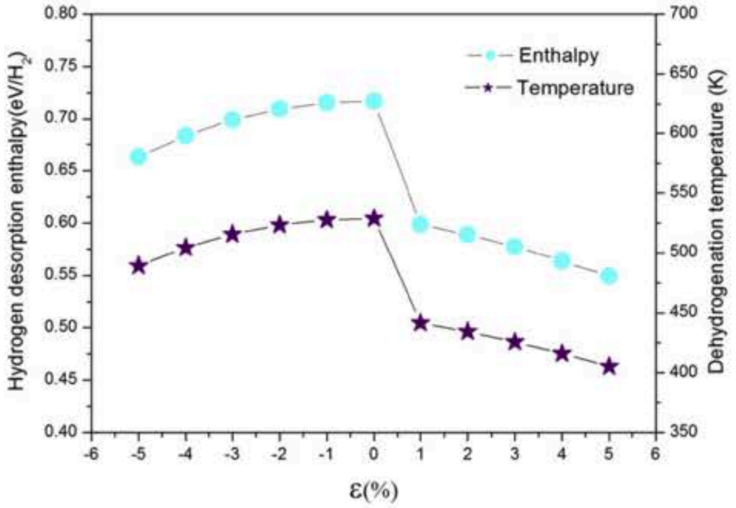

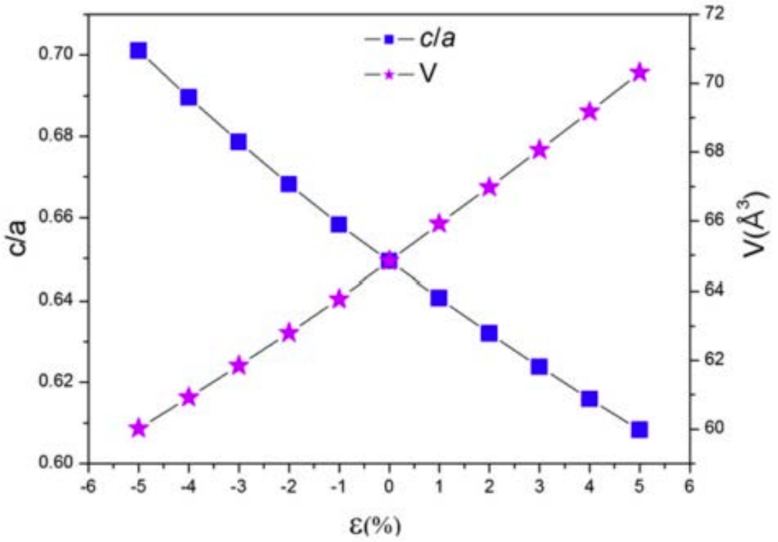

Fig 2.3.17. (Top) Calculated desorption temperatures for MgH_2 with simulated biaxial strain. Tensile strain appears to have the greater effect. (Bottom) Corresponding unit cell volume associated with the biaxial strain [96]*.*

2.3.6 Multilayers

The international union of pure and applied chemistry (IUPAC) defines a multilayer as 'a system of adjacent layers or monolayers'. In the case of this section, multilayers are defined as systems incorporating more than one layer of magnesium.

The use of multilayers has been useful to demonstrate improved sorption kinetics, by effectively catalysing the sorption reactions, often with the use of transition metals. This was demonstrated by Fry et al[98] with 4.6 wt% H_2 absorption within 10 minutes at 250 °C using Cr and Ti based films. Similar results on multi-layered Mg/Ti thin films performed at the University of Birmingham have also been observed[99]. There is no evidence in published research suggesting room temperature uptake in multilayer films of titanium.

However, there is no significant effect on thermodynamic properties within these films, as the Mg layer thickness is in the region of tens or hundreds of nanometres. In addition, the majority of interfaces are incoherent, due to the immiscibility of Mg/Ti. If a chemical coherency can be engineered, as shown in Mg/Ti systems, where layer thicknesses approaching 4nm have been fabricated, thermodynamic changes are observed[100]. This observation was attributed to potential effects of surface energy but also may have been due to non-complete Ti layers being clamped by a Pd layer. In a further paper by the same authors, the effects of interfacial surface free energy were indeed shown to be the cause of the thermodynamic change[79]. This nanoscale architecture provides a new route into the thermodynamic destabilisation of MgH_2 due to excess surface energy (Fig 2.3.18). A similar report to this effect was discussed in Mg-Ni based films where the excess grain boundary energy was estimated to effect the hydrogen absorption enthalpies by around 5 kJ/mol[101], although this was not a multi-layered structure.

Palsson et al. demonstrated switching of hydrogen site occupancy in vanadium-based superlattices because of the effects of stress [102]. This is an interesting route to take when picturing magnesium, as there may be a potential shift in the equilibrium position of the hydrogen atom when under strain, affecting the energy of the Mg-H bond.

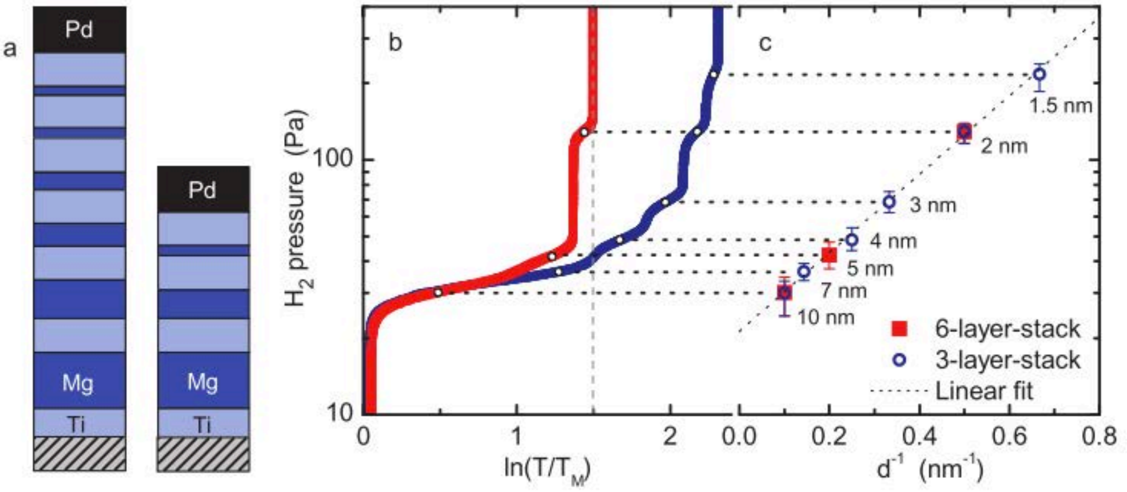

Fig 2.3.18. Demonstration of plateau pressure increase with decreasing layer thicknesses in Mg-Ti multilayer structures. A new potential method to tailor thermodynamics of MgH_2 [79].

2.3.7 Conclusions

Thin films can provide a model system in the investigation of hydrogen storage materials, as they allow for a large range of compositions to be investigated simultaneously. However, despite the obvious merits, one should be careful in treating the thermodynamic quantities as equivalent to bulk scale behaviour. Many interesting phenomena occur at such a small scale, particularly the influence of adjacent layers, microstructure and lattice strain.

Perhaps rather than being pessimistic reviewing the potential implications of the analysis tool, there could be an effort made to optimise and study these nanoscale effects. Clearly, this seems to be the case where a lot of different metal hydride systems have been investigated and there is a lot of evidence which suggests that the effect of mechanically constraining the phase transition does indeed affect the hydrogen sorption thermodynamics.

However, despite the relatively large amount of literature surrounding the subject, there is still a large amount of understanding to be gained, especially within some areas concerning MgH_2. For instance, there is no in depth study or comparison of the effect of microstructures and the influence that they may have on the diffusion of hydrogen into the film. In addition, the influence of thin film growth mechanics with increasing thickness is not taken into account apart from a study mentioned involving titanium. Indeed, the aforementioned factors can go on to influence the mechanical behaviour of magnesium. Can the substrate, microstructure and hydrogenation conditions be optimised to take advantage of this fundamental requisite of volume expansion? Can we include small amounts of dopants which could drastically alter the mechanical properties without sacrificing too much of the hydrogen storage capacity?

2.4 THIN FILM DEPOSITION SYSTEMS

A good understanding and control over deposition parameters for a given system means that the film growth mode can usually be well tailored to achieve the desired properties. Subtle changes in deposition parameters can have a large effect on the eventual properties of the film, whether in terms of adhesion, microstructure, surface roughness or intrinsic stress. This section looks at the fundamental science governing the microstructure obtained in thin films and how it can be altered for magnesium thin films. The effect of different substrates will also be discussed, which can also affect microstructure. The importance of the microstructure is important when considering applications of magnesium as a hydrogen storage material, as hydrogen sorption properties can be governed by changes in particle/grain size, as discussed in section 2.3. In addition, the effect of stress in these films will be discussed. This could be governed by the sputtering conditions used and may also affect sorption properties.

2.4.1 Nucleation and free energy considerations

The following expressions are taken from Ohring[103]. The free energy change (ΔF) to create a new spherical surface of radius, r, is given by the sum of the decrease in volume free energy (ΔF_v) and increase in the (interfacial) surface free energy (Υ_{AB}):

$$\Delta F = \tfrac{4}{3}\pi r^3 \Delta F_v + 4\pi r^2 \gamma_{AB} \qquad [1]$$

Above a critical radius (r*), the system is stable. Therefore, the change in free energy by addition of more atoms becomes zero, so:

$$\frac{d(\Delta F)}{dr} = \frac{d\left(\frac{4}{3}\pi r^3 \Delta F_v + 4\pi r^2 \gamma_{AB}\right)}{dr} = 0 \qquad [2]$$

$$\therefore 4\pi r^{*2} \Delta F_v + 8\pi r^* \gamma_{AB} = 0 \qquad [3]$$

$$\therefore \gamma_{AB} = \frac{-\Delta F_v r^*}{2} \qquad [4]$$

$$\therefore r^* = -\frac{2\gamma_{AB}}{\Delta F_v} \qquad [5]$$

Substituting r* into [1] gives the critical free energy (ΔF*) for a particle to reach critical radius:

$$\Delta F^* = \frac{16\pi {\gamma_{AB}}^3}{3(\Delta F_v)^2} \qquad [6]$$

Equation [6] describes the energy barrier for nucleation of a homogenous, spherical particle. The proportionality to Υ_{AB}^3 infers a large effect of surface energy contribution. However, dealing with heterogeneous nucleation, as in the instance of a particle on a substrate, we have to include other additional geometric factors which depend on the differential between the surface energies of film and substrate. This gives a correction factor depending on the contact angle, θ, and is denoted by:

$$\Delta F^* = \frac{16\pi {\gamma_{AB}}^3}{3(\Delta F_v)^2}\left[\frac{2-3cos\theta+cos^3\theta}{4}\right] \qquad [7]$$

Thus, the interfacial energy between adatom and substrate influences the thin film growth mode and resultant microstructure. A plot of equation 7 is shown in Fig 2.4.1.

If:

$$\theta > 0 \ \rightarrow \ \gamma_A < \gamma_{AB} + \gamma_B \qquad [8]$$

Island growth will occur, and if:

$$\theta = 0 \ \rightarrow \ \gamma_A \geq \gamma_{AB} + \gamma_B \qquad [9]$$

Then layer by layer growth will occur. Stranksi-Kranstanov growth can occur due to strain effects where θ becomes >0 and growth mode switches from layer by layer to island mode. A schematic representation of these thin film growth modes is shown in Fig 2.4.2.

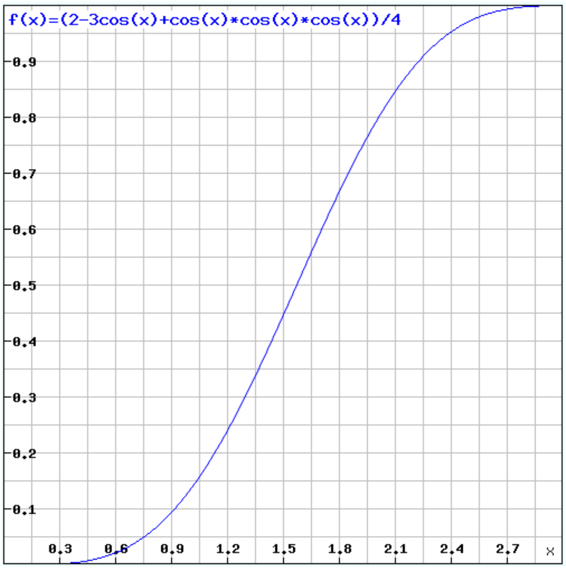

Fig 2.4.1. Graphical representation of Eq 7 showing the variability in free energy dependent on wetting angle. Y axis is free energy for nucleation and X axis is theta in radians.

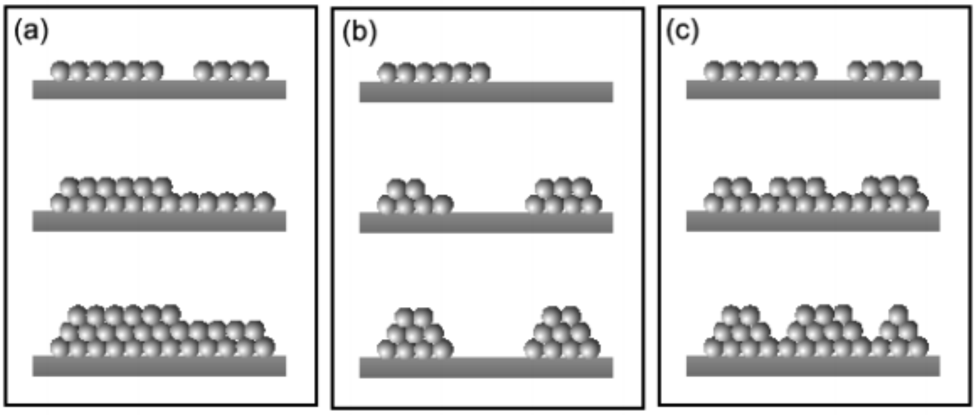

Fig 2.4.2. Thin film growth modes a) Vollmer Weber, b) Frank-van der Merve, c) Stranksi-Kranstanov.

2.4.2 Determining θ

We have defined the energy barrier for nucleation as a function of the surface energy of the film. In the case of heterogeneous nucleation, the energy barrier is also described as a function of θ. It is important to quantify θ to understand the expected thin film growth mode. A schematic diagram representing a liquid on solid interface is represented in Fig 4.2.3.

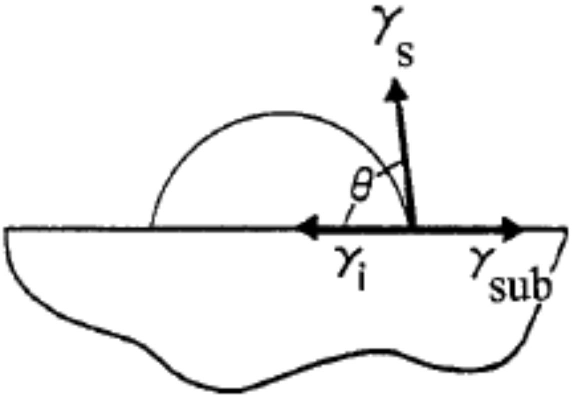

Fig 2.4.3. Schematic diagram of a water droplet on a substrate. The surface energies of λi (interface), λsub (substrate) and λs(particle surface) dictate the contact angle, θ. (Adapted from Thompson [104]).

The ability of a material to wet its substrate will depend on the surface energies (ϒ) of the substrate, material deposited, and the surrounding atmosphere. If we look at the energy required to create a new surface from an original surface, then we can see that:

$$E_{adh} = \gamma_A + \gamma_B - \gamma_{AB} \tag{10}$$

With E_{adh} as the adhesive energy, γ_A is the surface energy of material A, γ_B is the surface energy of material B and γ_{AB} is the interfacial energy between A and B. From this, and supposing that A is liquid and B is solid, we can form Young's equation where the angle subtended by the liquid-solid interface becomes a quantifiable measure of the adhesion force, which is inherently a consequence of the opposing materials surface energies.

$$cos\theta = \frac{\gamma_A \gamma_{AB}}{\gamma_B} \tag{11}$$

If we know the surface energy of both materials and the interfacial energy between them, then we can calculate the predicted wetting angle. This allows us to predict the thin film growth mode as well as relating to the energy barrier for nucleation, which affects film microstructure.

2.4.3 The effect of temperature

The rate equation for heterogeneous nucleation is:

$$\dot{N} = N^{*} A^{*}\omega \text{ (Nuclei/cm}^2\text{ sec)} \qquad [12]$$

And N* is given by:

$$N^{*} = n_s exp\left(\frac{-\Delta G^{*}}{K_B T}\right) \qquad [13]$$

Where N* is the equilibrium number of nuclei, ω is the rate of atom impingement onto the nuclei of critical area A* and K_B is the Boltzmann constant. N_s is the density of all possible nucleation sites. An increased nucleation rate is observed for a more negative value of free energy (following an exponential behaviour) and is inversely proportional to temperature, suggesting that single crystal films tend to grow at higher temperatures.

$$\left[\frac{\delta r^{*}}{\delta \dot{R}}\right]_T < 0 \qquad [14]$$

Higher temp – larger r* leads to larger ΔG*, larger, fewer grains.

$$\left[\frac{\delta \Delta F^{*}}{\delta \dot{R}}\right]_T < 0 \qquad [15]$$

Higher rate – smaller ΔG, smaller more numerous grains

Temperature is a large factor governing the grain size. Small grown islands will tend to coalesce to coarsen the grain when higher temperatures are experienced. If grain size is governed by nucleation and growth only, it follows that a small grain size will occur with increasing nucleation rate, but will increase with increasing growth rate. And, as we know, the barrier for nucleation is governed by the surface energies of the film/substrate system. In the Teer Coatings System used in this research, there is no ability to control substrate temperature. However, films were loaded at room temperature and simple temperature stickers were used to detect the range experienced by the substrate.

2.4.4 Typical microstructures

Island growth modes will occur in most deposition situations as the contact angle, θ > 0. Three typical microstructures are observed when this growth mode occurs (Fig 2.4.4). However, the control of this microstructure can somewhat be influenced by altering the energetics of the physical vapour deposition (PVD) system. Variables such as the target potential, saturation pressure and temperature are commonly used to change the coatings properties.

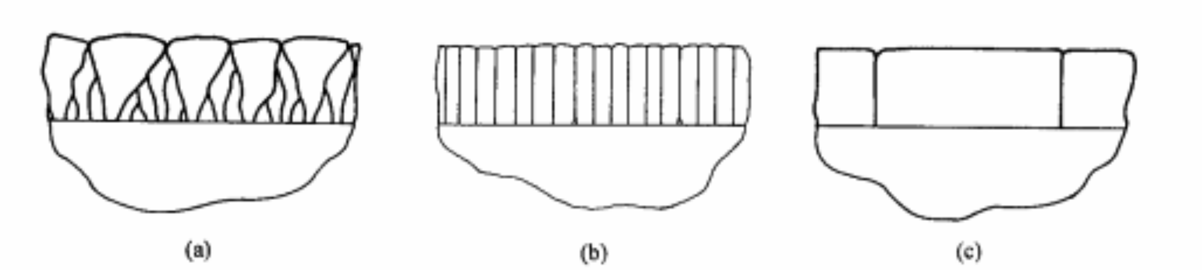

Fig 2.4.4. Potential microstructures for thin films <1 micron in thickness deposited by PVD systems. Type (a) is often seen with the highest nucleation rates. Type (b) is often seen after grain boundary motion has occurred due to coalescence. Type (c) is observed with a high degree of coalescence and film thickening. [105]

2.4.4.1 Target potential

Altering the target potential means atoms have more or less free energy for particle coalescence, yielding a different microstructure. The effect of using a substrate bias will also affect the microstructure in the same way, although the effect on deposition rate is less pronounced.

2.4.4.2 Saturation pressure

The nature of PVD ensures a large amount of nucleation sites, due to the high degree of supersaturated vapour. The volume free energy can be written as:

$$\Delta G_V = -\frac{KT}{\Omega} \ln \left(\frac{P_V}{P_S}\right) \qquad [16]$$

Where P_v and P_s are the pressures of supersaturated vapour and solid respectively and Ω is atomic volume. The degree of super saturation is dependent on the operating pressure of the system. If there is a higher operating pressure, then this suggests a more negative value of free energy change. This would suggest a finer microstructure. In the case of magnetron sputtering, control of working pressure is achieved with the flow of Argon. The density of argon influences the average distance and momentum carried by the adatoms to the film surface. The greater the density means reduced kinetic energy on collision with the substrate and so free energy to move and coalescence is reduced.

2.4.4.3 Temperature

Temperature has already been shown to affect the rate of nucleation. Therefore, we can expect that a general trend will be that nucleation rate is higher at lower temperatures and visa versa. The films tend to grow in columns of varying widths. Some may have small initial columns which then coalesce into larger ones. Others may form more equiaxed grain sizes with increasing temperature. This effect shows that the deposition temperature will greatly affect the eventual properties of the film. Moreover, any post deposition treatments can act to alter the coatings properties.

2.4.5 Intrinsic thin film stresses

When a thin film is deposited, it can inherit intrinsic (processing) stresses. This can be due to a number of factors but can vary with the sputtering conditions, film thickness, temperature and type of metal deposited.

This work will not be looking into epitaxial films, where the lattice and underlying crystal structure is preserved on the deposited film, but will be more focused on adhesive coatings. Adhesion is a relatively poorly understood phenomenon. However, it is theorised that when 2 bodies come to within intimate contact (atom radius), van der Waals forces attract them to one another. Adhesion therefore falls off as a sixth power of the separation distance. For a typical interface of 10^{15} primary bonds/cm^2 at 1 eV, the bond energy is 10^{15} eV/cm^2, which is typical for a metal. In order to improve adhesion, one can deposit an intermediate layer. This is useful in the case of glass because metals only tend to bond to sites with oxides. Deposition of a ‘glue’ like layer (oxide forming metal) can be used to improve adhesion. If the adhesion forces are stronger than the intrinsic stresses, then the film is effectively ‘clamped’ to its substrate.

2.4.5.1 Tensile Stresses

The accumulation of processing stresses can occur during film growth and can be sensitive to the deposition conditions. There are two mechanisms for this. The first is a recrystallization mechanism, where annealing during the deposition process can occur alongside shrinkage. This can be related strongly to the processing pressure, which effects the nucleation rate. The second mechanism is crystallite coalescence, which can occur when grain boundaries coalesce and form tensile stresses within the film. This is often observed in films with some porosity present, possibly due to gas entrapment. A schematic of the mechanisms is shown in Fig 2.4.5. Coalescence will be more favourable at higher temperatures. The sputter conditions can change the extent to which this occurs because adatoms with higher energies can move on the surface and effectively diffuse over the grains. For this reason, lower energy sputter will yield a more amorphous film with less opportunity for grain growth as well as lower crystallite coalescence.

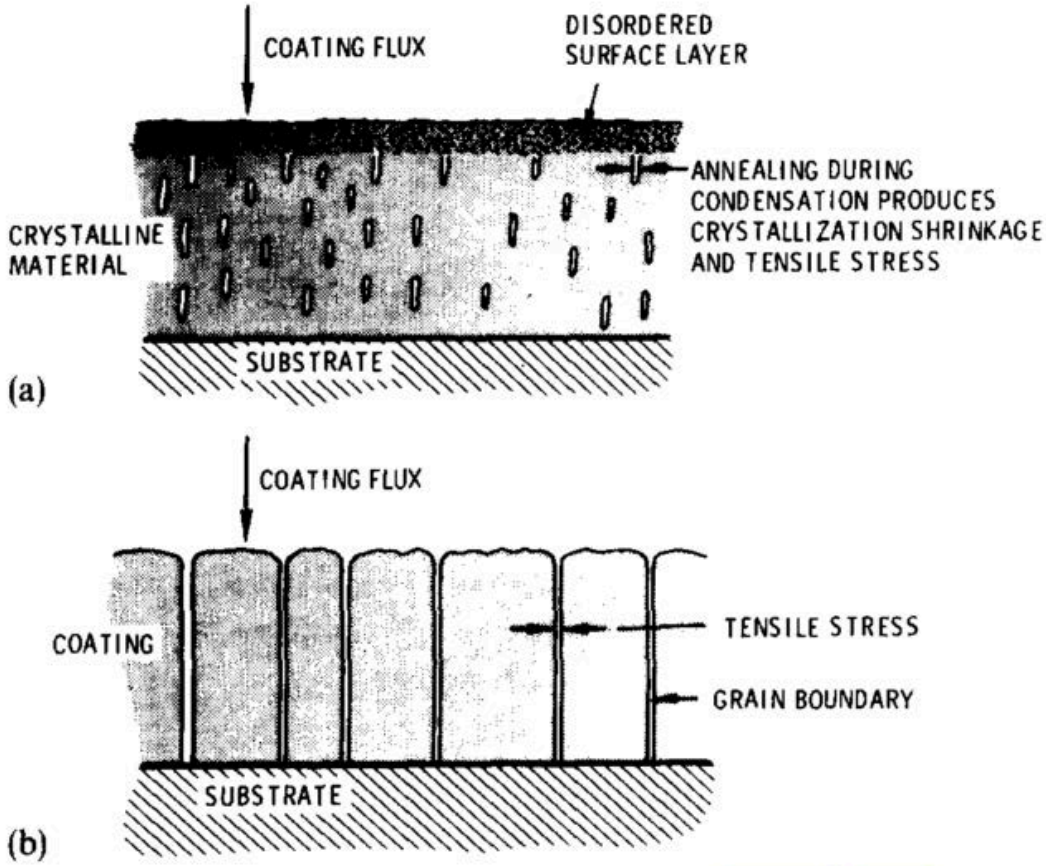

Fig 2.4.5. Mechanisms for the building of tensile stresses in a thin film (a) recrystallization mechanism (b) grain boundary coalescence.[106]

2.4.5.2 Compressive stresses

Compressive stresses can occur in thin film deposition. However, this is usually the case where there is some form of reactive gas deposition occurring. The transition to compressive stresses for purely metallic films is quite rare. However, an atomic insertion mechanism leading to grain boundary densification has been proposed to induce compressive residual stresses. [107]

2.4.5.3 Thermal Stresses

There is also an internal stress associated with thermal expansion between film and substrate. This is important to consider when processing coatings. In the case of doing experiments involving heating, then it is important to recognise that the thermal stresses will be incorporated into the experiment, which will affect results. Annealing can be used in an attempt to relieve some of these stresses, however, in the case of some films with miscible layers, there may be unwanted interdiffusion between layers.

2.5 AIMS AND OBJECTIVES

The literature review clearly highlights the importance of thin films within the context of hydrogen storage research. The use of thin film technology is advantageous in many respects, looking at new phases, microstructures, stress and hysteresis effects. All of these factors are important when looking at hydrogen storage materials. However, there are some key concepts within the area of thin film research that have not been studied in much depth. It is clear that thin films can behave much differently to bulk powders due to the fact they are mechanically constrained. The aim of the research is to build up a more complete picture of the effects of stress accumulation on the hydrogen sorption properties of magnesium films.

The research objectives are as follows:

- To investigate the relationship between deposition conditions and the resultant film microstructure for Mg films
- To investigate the hydrogen sorption properties of Mg films prepared in a variety of conditions, linking this back to their microstructural properties
- To investigate the ambiguous behaviour of films that report different sorption behaviour for Mg films of different thicknesses
- To investigate the influence of a range of substrates on the mechanical behaviour of Mg films

To investigate the use of Y in Mg multilayer systems as a potential route for destabilisation

3 EXPERIMENTAL TECHNIQUES

This chapter covers the experimental techniques used to generate the results in this thesis. The first section details the sample preparation and synthesis, whilst the second discusses methods used for characterisation.

3.1 SAMPLE PREPARATION, SYNTHESIS AND STORAGE

3.1.1 Magnetron sputtering

There are various ways to synthesise thin films depending on the coating materials required and target application of the film. The various technologies are readily divided into chemical, electrochemical and physical. Physical vapour deposition systems are generally cheaper and are more versatile in comparison to other systems. They are very clean environments and can be used with high purity elements to produce elementally pure films with low concentrations of contamination. In addition, they can easily be configured to produce precise (1 d.p) alloy compositions that may not easily form using other conventional forms of alloy production (e.g. arc melting) with a good level of homogeneity. They can also be configured to produce multilayer coatings. Both of these advantages are important in the area of hydrogen storage, as outlined in section 2.3.

The general principle of magnetron sputtering is to attract energetic ions (in the case of this work Ar^+) to a target surface with an applied potential (cathode). The flux and energy of the bombarding gaseous ion species hitting the target is determined by the applied potential. The ions interact with the target and knock out (sputter) an atom of the target material (Fig 3.1). Due to the elasticity of this process, the ejected ions are generally very energetic (>10eV). This results in high-energy bombardment of the substrate. The energy of the sputtered ions is most heavily influenced by the chamber pressure. Very low pressures allow for lower collisions with other argon ions and vice versa. This alteration of the mean free path can change the energy drastically, resulting in different morphologies and film quality.

Some of the atoms (around 1 %) have sufficiently high energy to knock out atoms from the sputtered film. This is known as re-sputtering and is a technique used to clean a substrate.

In addition to altering the system base pressure, it is possible to alter the bias applied to the substrate. The substrate bias affects the kinetic energy by which the ions are attracted to the substrate. Changes in energy can influence a films microstructure, grain size, intrinsic stress and crystallography.

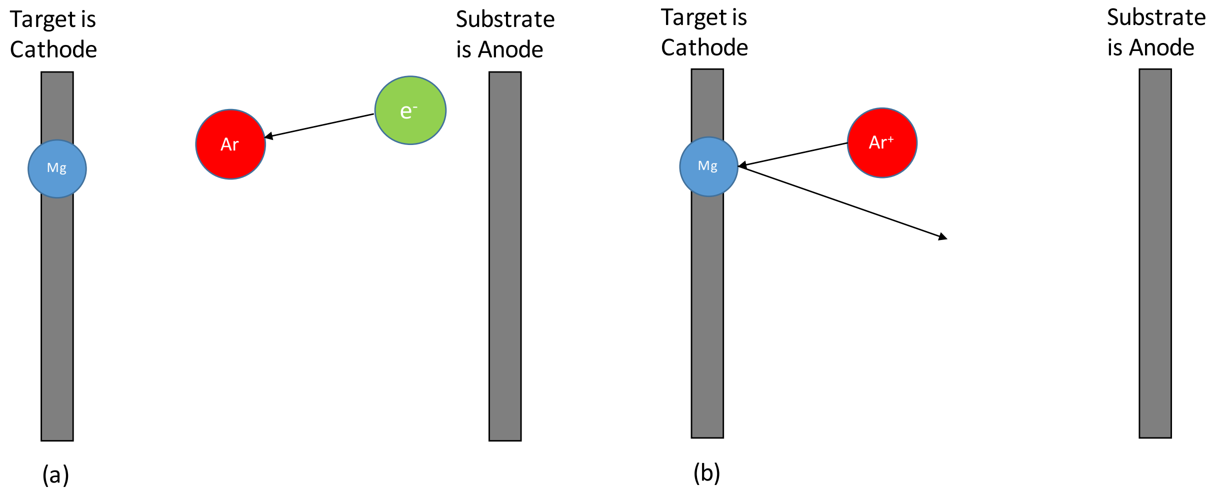

Fig 3.1. Schematic representation of the magnetron sputtering process. (a)Due to potential difference between the cathode and anode, electrons are generated which collide with argon atoms. (b) The now positively charged argon ions are accelerated towards the cathode with enough energy to knock out (sputter) an atom of the target material.

3.1.2 Teer coatings CFUBMSIP system

All of the samples used in this work were synthesised using a patented Magnetron Sputtering system manufactured by Teer Coatings [108]. The unique CFUBMSIP (Closed Field Unbalanced Magnetron Sputter Ion Plating) has multiple advantages over conventional magnetron sputtering systems. In essence, the arrangement of the magnetrons is such that alternating poles on the target materials (cathodes) within the sputtering chamber act to produce field lines that confine the plasma, enhancing its density around the workpiece (anode) – see Fig 3.2.

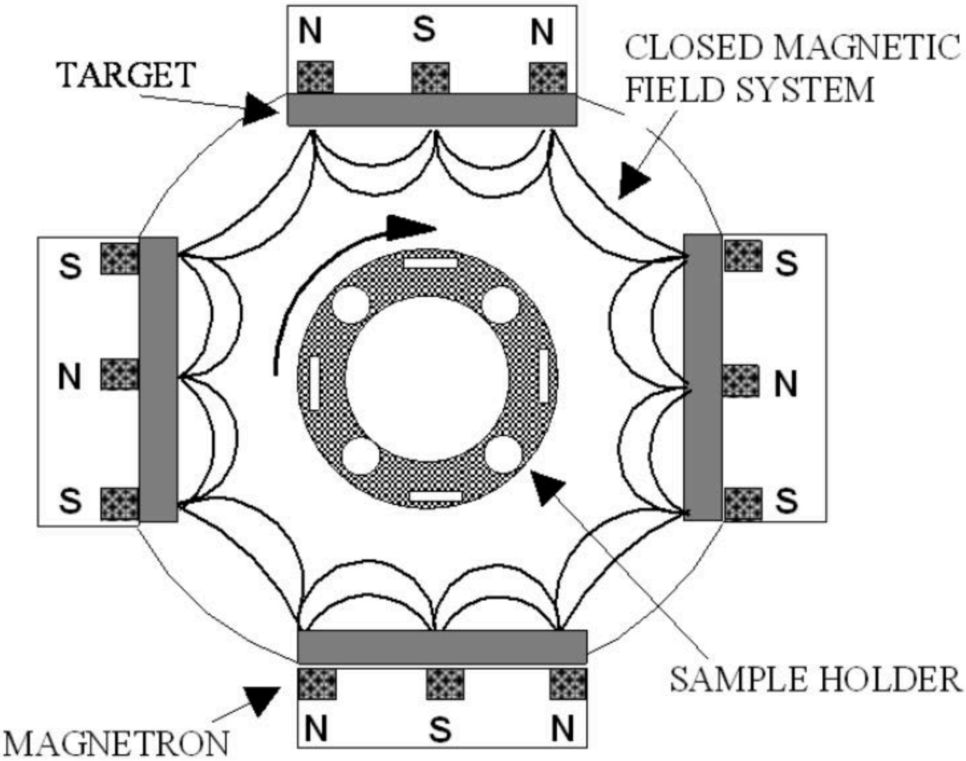

Fig 3.2. A top down schematic representation of the Teer Coatings CFUBMSIP system used in this work [108]. The polarity of the adjacent magnetrons is opposite; meaning magnetic field lines link up and plasma density is increased. This has advantages for material use, homogenous and uniform coatings.

This high density of plasma allows for bombardment of the work piece with a high number of lower energy ions. This is advantageous as it improves homogeneity, density and crystallographic perfection. In addition, the uniformity of the layers in multilayer coatings can be maintained, even if the surface is imperfect.

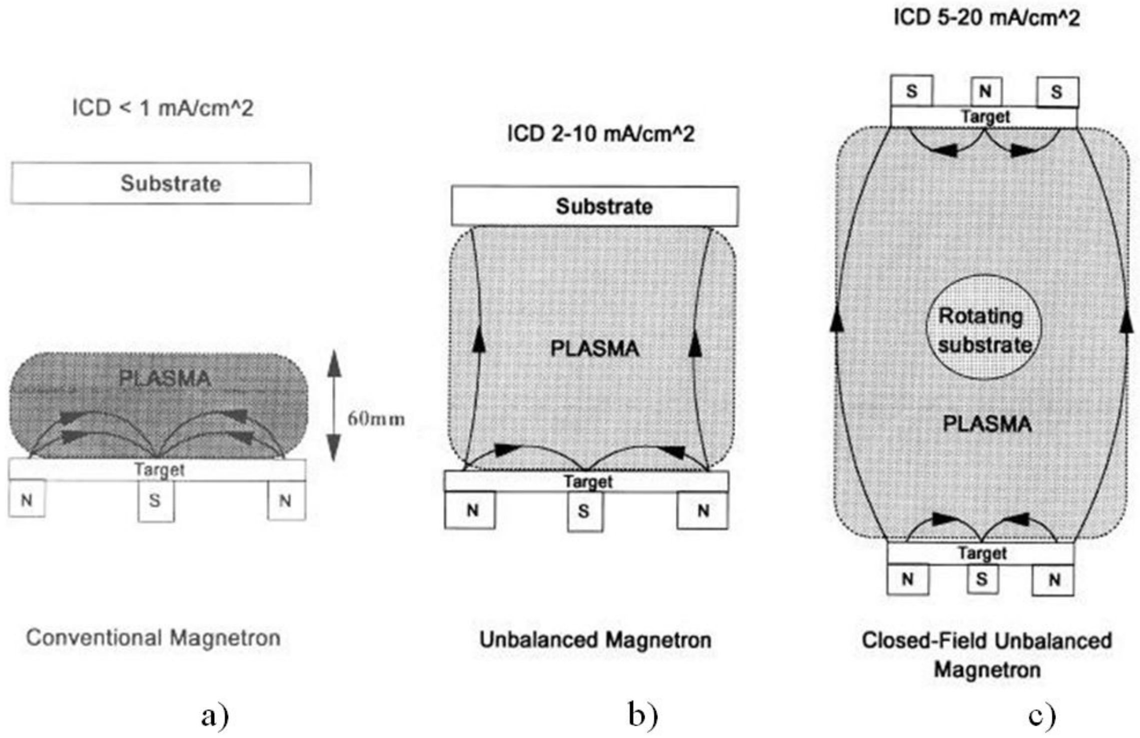

Fig 3.3. Left: Conventional magnetron sputtering with a small volume of plasma trapped in front of the target. Middle: Unbalanced magnetron with greater plasma volume and influence on the directionality of ballistic target ions. Right: A two magnetron sputtering system with a closed field arrangement further enhancing plasma confinement. A rotating substrate allows for multilayer coatings, improved homogeneity and uniformity. (ICD – incident current density)

In comparison, conventional 'balanced' and 'unbalanced' magnetron systems have significantly less confinement of plasma. In a balanced magnetron, the plasma is confined solely to the surface immediately above the target. In an unbalanced system, the confinement is loosely held, with magnetic field lines extending towards to work piece. The directionality of the ejected ions is improved with the unbalanced system. (See Fig 3.3).

3.1.3 Substrate preparation and storage

The quality of a thin film can be drastically altered by the substrate preparation involved pre deposition. (Ref). The main substrates used in this work were amorphous borosilicate glass microscope slides, single crystal polished silicon, MgO and SiO_2 and a PEEK polymer. Given that these substrates came with excellent surface roughness characteristics and already electro polished (Single Crystal specimens), it was unnecessary to polish any further. Instead, an ultrasonic bath of acetone for 5 minutes was used in order to remove any surface contamination. The samples were then allowed to dry at room temperature in a laboratory environment, before being loaded into the sputter chamber and sprayed with an anti static gun to prevent dust particles from settling. Once positioned on the substrate holder using Kapton (Polyamide) tape the chamber was evacuated for at least 2 hours until a vacuum of 1×10^{-6} mbar was reached.

In general, each deposition process followed a general recipe that involved an Ar^+ etching of the substrate surface using a very high bias voltage (typically 400 V) and low target power (material dependent). This final step aimed to remove any final impurities or oxide layers from the surface of the substrate, as well as cleaning the target material surface.

After the deposition had completed, the samples were removed from the chamber. The system has the capability to remove samples using an argon-filled glovebox and inert transfer to a permanent glovebox is possible. For pure elemental Mg samples, this was necessary due to the formation of an oxide layer. However, it was found that for samples with a Pd overlayer, samples were not affected by exposure to atmosphere for the short period of time needed for transfer into a glovebox and for even longer periods of time, if necessary. For extended periods of storage, samples were stored inside a Kilner jar inside a sealer glovebox with $O_2 < 50$ ppm and $H_20 < 1$ ppm to prevent unwanted oxidation.

For repeatability, the system allowed for a ‘recipe’ to be created. This allowed for control of various parameters including time of cleaning, coating and cooling. It also allows the control of target current, bias voltage and argon flux (affecting pressure). The affects of altering these parameters have been investigated.

3.2 MICROSCOPY

A variety a microscopic techniques were employed during this research.

3.2.1 Optical

Macroscopic photos were taken with a digital camera to describe some of the features visible to the eye and of interest.

3.2.2 SEM (Scanning electron microscopy)

To identify microstructural characteristics with a great deal of clarity, SEM was used. A combination of microscopes were used in this research, depending on availability. These included a JEOL 7000 FEG SEM and a Phillips ESEM.

The operating principle of an electron microscope is highlighted in Fig 3.4. An electron gun is used to produce electrons using a hot tungsten filament. The electrons are then emitted and accelerated through a potential difference. After this, a condenser lens and an objective lens serve to narrow and focus the electron beam onto a sample surface. These lenses are electromagnetic; the focal length is determined by altering the voltage.

Electrons can interact with a sample in several ways. Firstly, they can pass straight through the sample, not interacting at all. Alternatively, the electrons can interact with the electron cloud of the sample atoms. This creates low energy secondary electrons that can be used to create images that can show 3D features and are insensitive to elements.

Secondly, they can collide with the nucleus of the atoms in the sample, producing high energy back scattered electrons. As the size of the nucleus varies with element, this technique can be used to identify different densities and phases within a sample (heavier atoms appear lighter). This is useful in the analysis of multilayer samples.

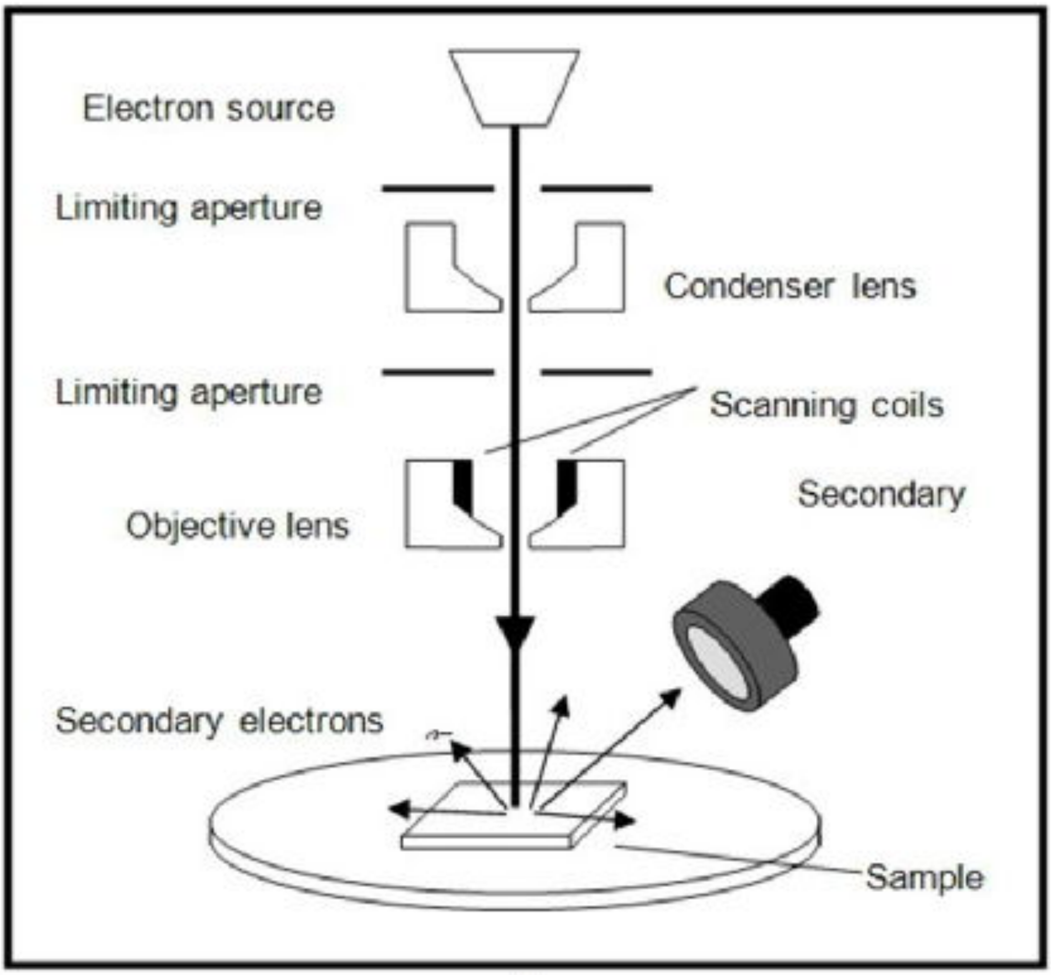

Fig 3.4. Schematic diagram showing the operating principle of a SEM[109].

In addition to the imaging features available within the SEM, it is also possible to analyse the chemical composition within the sample using energy dispersive spectroscopy (often noted EDS or EDX). This spectroscopic technique utilises the unique atomic structure of an atom. A high energy electron beam is used to eject inner shell electrons to create electron holes. The decay of a higher energy outer shell electron into the inner shell hole occurs and characteristic X-rays are emitted. The energy of the decay is detected using a semiconducting silicon detector and will be characteristic of a given element. INCA software was used for the analysis of the given spectra, which quantifies the amount of a given element in the specimen analysed. For very thin film samples, the analysis is more complex, as the volume of material available is small, especially in comparison to the substrate contribution to the spectrum. However, it was found that by taking a baseline, a reasonable approximation to the film composition could be found.

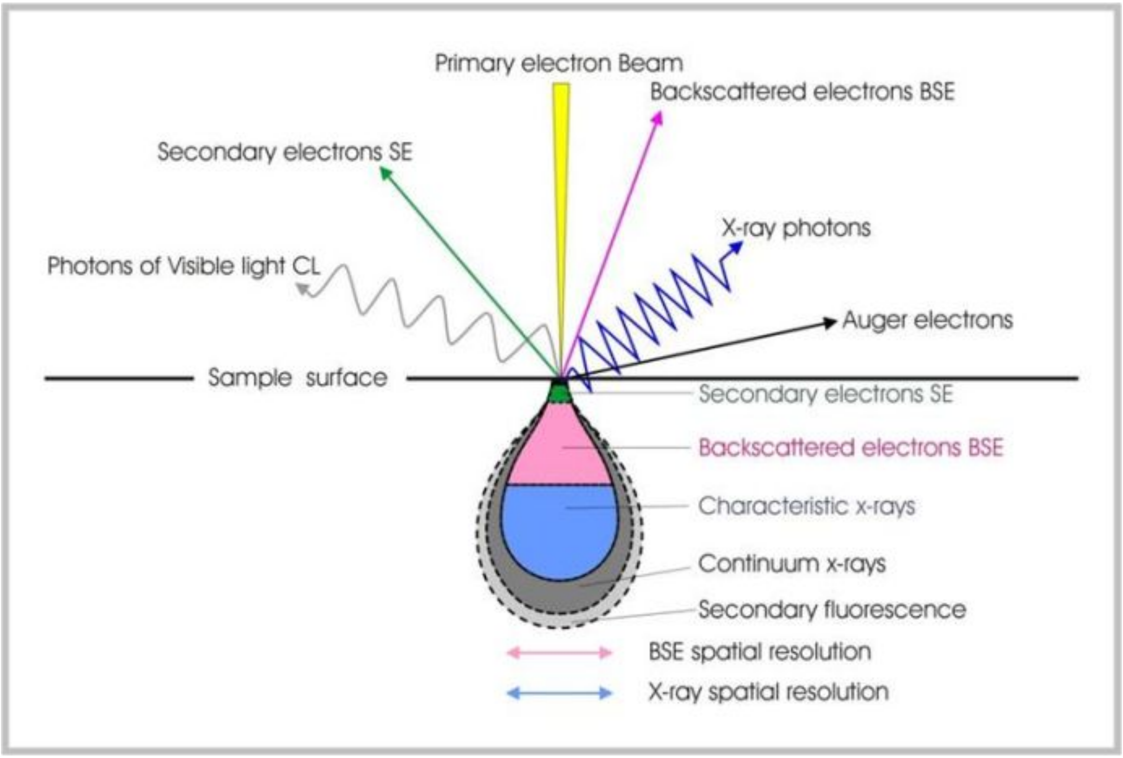

Fig 3.5. Possible interactions of an electron with the sample surface[110].

3.2.3 Confocal laser microscopy

An Olympus LEXT 3100 series laser confocal microscope was used to examine the surface topography of the films in this work. Confocal microscopes work by restricting the background light surrounding an illuminated sample to just one specific depth (Z-axis). This is done by the use of a pinhole, which is used to select just the conjugate plane of the optical lens focal plane in use. By scanning through a number of Z planes, it is possible to build up a very accurate 3D representation of sample topography. A schematic representation of the operating principles of a confocal microscope is shown in Fig 3.7.

The specific resolution of the Z-axis is determined by the focussing lens. The maximum obtainable Z resolution for this particular model was 10 nm using a 100x optical lens. However, the resolution chosen was dependent on the requirements of the area of the sample to be measured. The confocal microscope aided as a quick measure of a film deposition rate test as well as quantifying the dimensions of buckling which was seen as a resulting of hydrogen absorption in some films

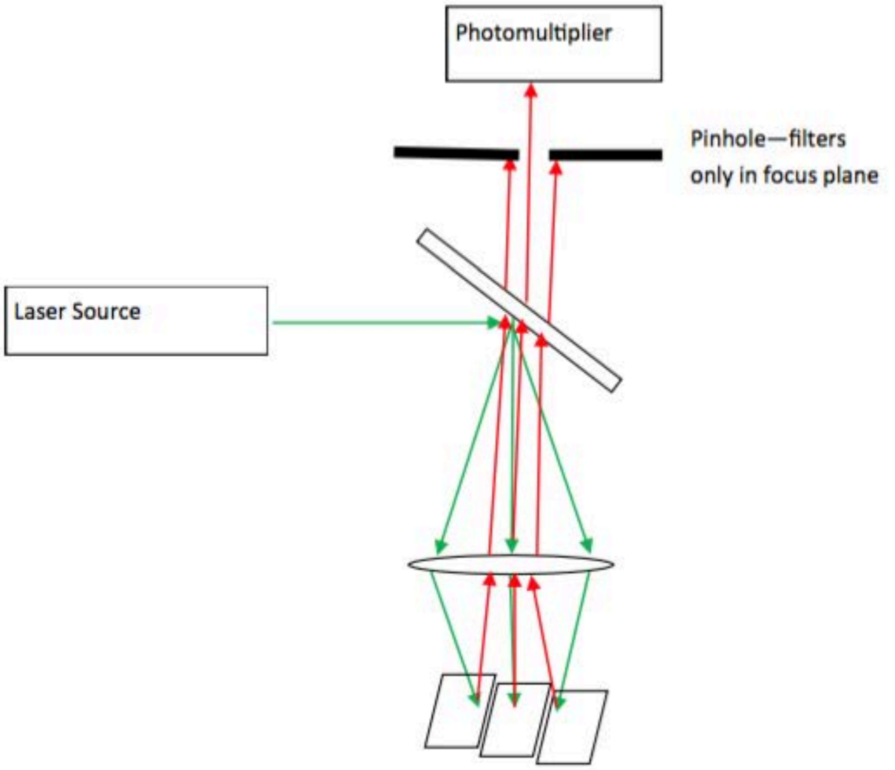

Fig 3.7. Configuration of lenses in a confocal microscope. The pinhole is used to only detect items within a very specific focal plane, allowing a 3D layered image to be built up through a variety of Z-axis scans

3.3 XRD (X-Ray Diffraction)

XRD is one of the most powerful tools for the study of crystallographic properties of a sample. As the wavelength of X-rays is similar to the lattice spacing of many common elements, diffraction can occur with the satisfaction of Bragg's law (Eq 1).

$$\mathbf{n\lambda=2d_{HKL}\sin\theta}$$

When an incident X-ray beam of given wavelength, **λ,** is incident on a crystal with a lattice spacing, **d_{HKL},** diffraction will occur at a given angle of incidence, **θ**. (**n** is the order of diffraction and must be an integer for constructive interference) The angle of incidence that produces a diffraction signal signifies coherent scattering (Fig 3.9). Assuming that the sample is powder like, there will be an infinite number of grains arranged in an infinite number of orientations. This means that there will be an infinite number of crystals lying perpendicular to the incident angle and can thus be detected. The interplanar distance varies depending on the observed plane, and thus there is a pattern of peaks that will be unique to a given material.

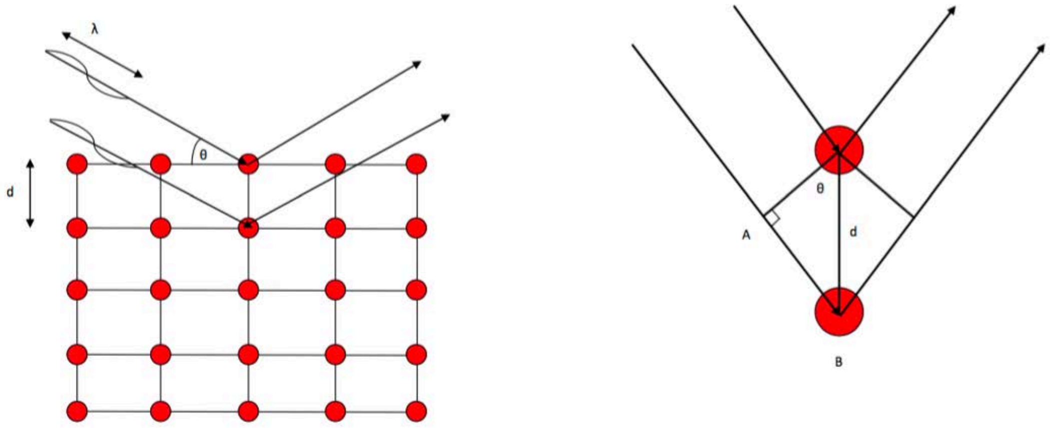

Fig 3.9. Geometric representation of Bragg's law and the assumptions required to generate a powder diffraction pattern.

A complete scan through a range of angles (usually in the order of 5 to 140°) gives a diffraction pattern, which can be referenced to a database of known materials. Given that X-rays interact with the electron cloud, the intensity of the diffraction peak is proportional to the density of electrons lying on the particular plane of interaction, as well as to the material being investigated – heavier elements generally diffract better. However, this also gives problems when trying to detect lighter elements, especially hydrogen. Neutron diffraction is a better technique to detect the position of hydrogen within a lattice, as neutrons interact with the nucleus and their detection is much easily defined. However, hydrogen sublattices have been previously detected with the use of synchotron radiation, and the nature of bonding in MgH_2 has been calculated from this [35].

Thin films often exhibit texturing, that is to say that usually only one or two of the multiple diffraction planes are observed and are perpendicular to the incident beam. This can lead to some ambiguity as to the identification of the material, as well as its exact lattice parameter. Specialised diffraction equipment is available for the analysis of thin films (techniques such as XRR, SAXS) that allow for measurements in in plane directions, giving rise to additional diffraction peaks. A typical diffraction pattern from a thin film is shown in Fig 3.10. Of course, the basic elements in the film are usually known. A lattice parameter can be calculated for the plane in question assuming the crystal structure is known.

Thin films are often deposited with a significant residual stress. XRD can be used as a tool to measure thin film strain. A homogenous strain gives rise to a peak shift, whereas an inhomogeneous strain gives rise to peak broadening. A combination of both can often be observed. It can therefore be difficult to always be certain of the strain in a given material, and other techniques are often employed in situ to measure strain build up (cantilevers). Given a bulk estimate of the Young's modulus[111], it is possible to estimate the residual stress within the layer, although given the small grain size within films, their modulus is often much higher than bulk, as is the case in many metals, due to Hall-Petch strengthening.

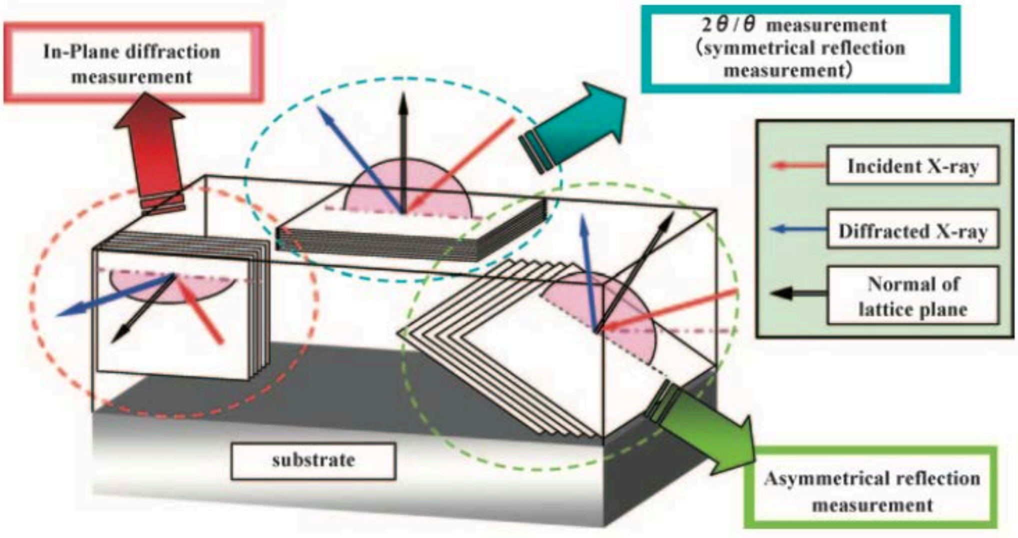

Fig 3.10. Representation of thin film x-ray diffraction techniques that can be used to probe grain orientations[112]

3.3.1 Room temperature

In this work, a Bruker D8 Advance diffractometer was used. For all measurements, a Cu source was used (λ = 0.15418 nm) which was monochromated with the use of a Göbel mirror. A divergent slit in the range of 0.1 to 0.6 mm was used for any given set of samples as a trade off between signal intensity and peak broadening. In all cases, alignment and peak breadth were calibrated with a known standard (Al_2O_3 – Corundum) prior to measurement. For ex situ measurements, it was found that the palladium capping served as an excellent oxidation barrier for the magnesium/alloy underneath and so the sample could be exposed to air. The scan time for a particular sample would vary, again depending on scanning quality.

Two types of scanning mode were employed. In the majority of cases, a θ – 2θ scan was used, so the source and detector move synchronously around the sample. In other cases, for a thin sample (<100 nm), it was often necessary to use a detector scan with an incident angle of 2°. In this mode, the angle of incidence stays fixed, while the detector scans around the range of angles. This enables a higher number of X-rays to be absorbed by the film (Fig 3.11).

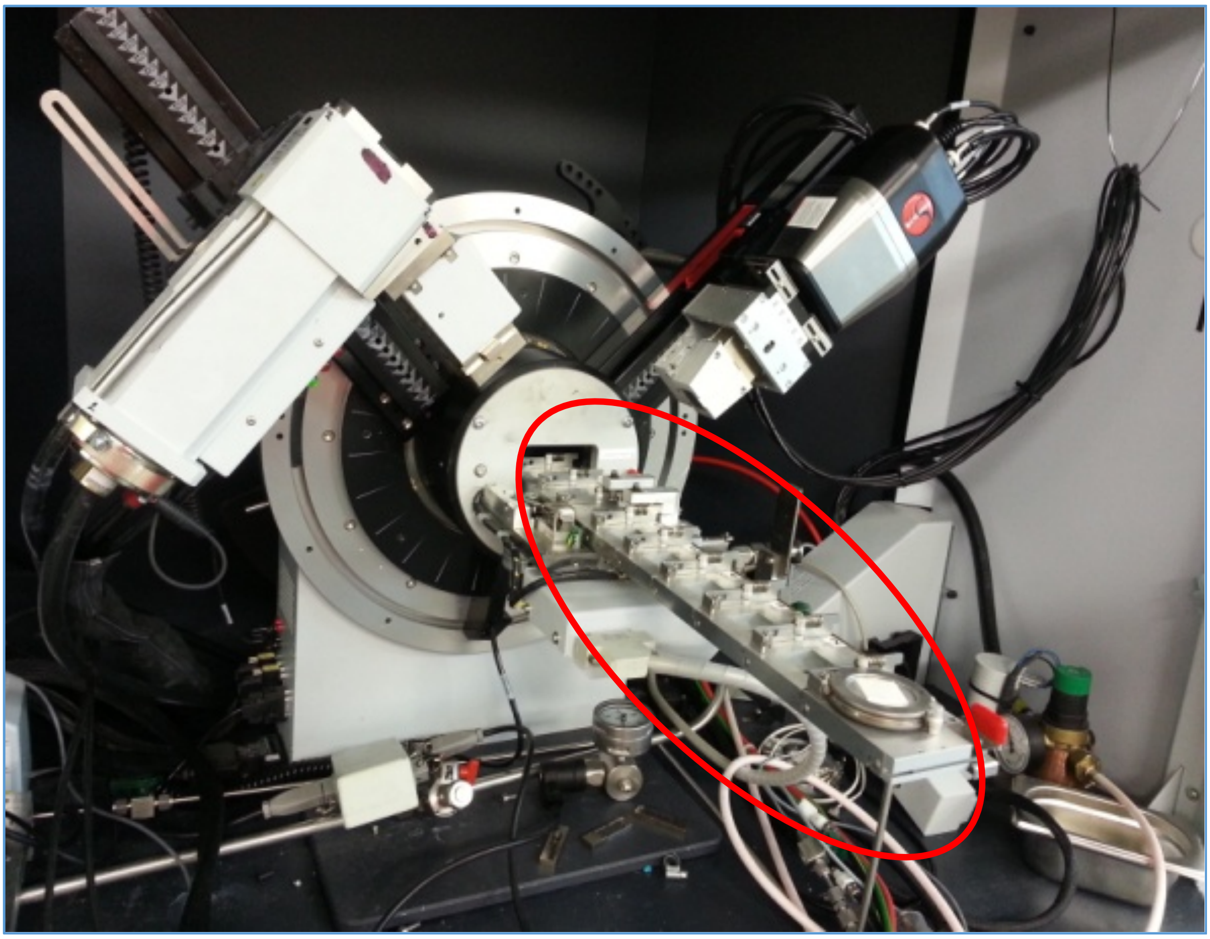

Fig 3.11. Experimental set up of the X-ray diffractometer with the multichanger unit attached (circled).

3.3.2 Variable temperature/pressure

An Anton Paar XRK 900 cell was used to obtain diffraction data in situ using a variety of different temperatures and pressures (900°C, 10 bar). This allowed novel insight into the structure and kinetic properties that thin films undergo upon (de)hydrogenation. Samples were positioned atop a macor stem and heated/cooled at a rate of 12° min^{-1} and allowed to homogenise for 5 minutes before an isothermal scan was taken. Pressure was altered by using mass flow controllers and pressure transducers, in a bespoke system manufactured by Baskerville. Flowing gas (H_2 or He) was set at 50 ml.min^{-1} for all measurements. The same parameters were used as for the ex situ measurements.

Alignment of the sample was used by movement in a vertical (Z) axis until the highest intensity of the main known peak was observed.

3.3.3 Analysis of XRD patterns

Due to the textured nature of films, it is not possible to carry out any form of structure refinement such as the Rietveld method. Instead, IGOR pro graphical software was used to fit voigt functions to peak shapes, giving peak area, intensity and position, along with the FWHM (full width at half maximum). These features are useful considering the interesting features.

FWHM can be used to calculate grain size (corrected for instrumental broadening) using the Scherrer Equation (2). Here, K is a shape factor (0.9 for spherical grains), λ is the wavelength, β the FWHM and θ the peak position. This equation assumes a spherical grain and has limitations down to 0.1 to 0.2 microns. It will be shown that the equation was a good estimator when used in conjunction with SEM.

$$D = \frac{K\lambda}{\beta sin\theta} \tag{2}$$

It is not possible to calculate lattice strain/grain size using the well known Williamson Hall method, as this depends on plotting the positions of several indexed peaks. Instead, a simple estimation of the lattice strain (ε) was obtained using the calculated lattice parameter (d_c) in comparison to a known bulk value (d_o). The precise lattice parameters were obtained from the ICSD (Inorganic crystal structure database).

$$\varepsilon = \frac{d_c - d_o}{d_o} \qquad [3]$$

3.4 HYDROGENATION CHAMBER

For ex situ/long term hydrogenation of samples, a hydrogenation chamber was used. This stainless steel reactor could be loaded to a reasonable degree of accuracy (1 d.p) with hydrogen pressure to around 1 bar H_2 (low pressure) or up to 700 bar H_2 to within 1.5 bar H_2 (high pressure). The samples were then placed inside a furnace with a thermocouple located next to the samples for accurate temperature control. Multiple samples could be loaded at one time. Given that the plateau pressure of Mg is far below the pressure used in the apparatus, the degree of accuracy for pressure did not warrant further control. Only in the regime below the α to β phase transition ($H/M < 0.1$) has there been shown to be a pressured dependence on the rate of hydrogen uptake [38,113]. Samples were placed inside borosilicate test tubes and allowed to hydrogenate for a set amount of time at temperature before being unloaded into a glovebox.

3.5 TPD (TEMPERATURE PROGRAMMED DESORPTION)

Temperature programmed desorption involves the heating of a sample at a constant rate and is a thermodynamic measure of the stability of a given compound. It is most often used for the analysis of monolayers of gas species adsorbed onto single crystals.

As with any thermal analysis method, thermodynamic equilibrium is not reached, but the onset, peak position and range of temperatures are good indicators of the thermodynamic and kinetic properties of a compound.

3.5.1 Experimental set up

A bespoke reactor was used in this thesis (Fig 3.13). The sample sits inside a borosilicate glass tube inside a furnace. The temperature of the sample environment is measured as closely as possible with a K-type thermocouple situated adjacent to the sample. The sample environment is evacuated using a rotary backed turbo molecular vacuum pump (Oerlikon TC-70) to a pressure better than 3×10^{-6} mbar. A quadrupole mass spectrometer is then used to analyse residual gases within the chamber. A period of at least 1 hour was used to allow the signal to stabilise before starting to ramp the temperature. The heating rate was standardised at 5°C min^{-1} as this temperature allowed a stable condition for the furnace.

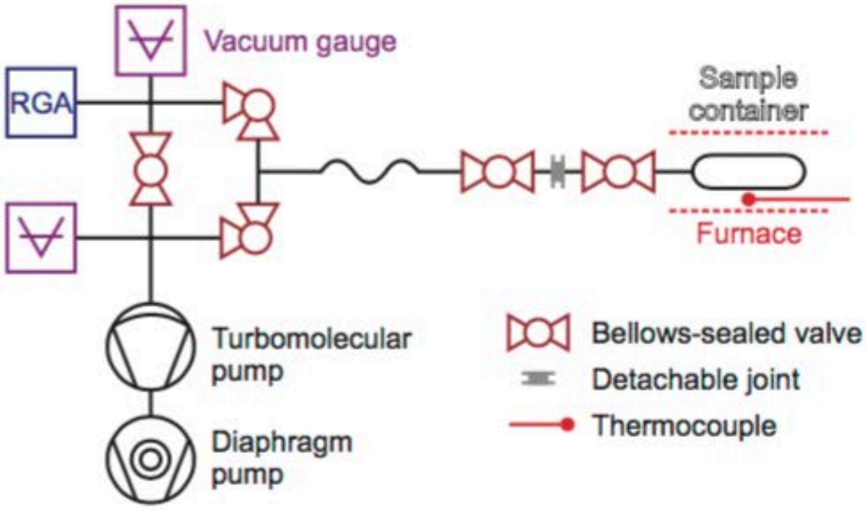

Fig 3.13. Schematic diagram of the TPD apparatus used in this work. A mass spectrometer is used to monitor the desorbed gas species from the sample which is heated at a constant rate in a UHV atmosphere generated by a rotary backed turbo molecular vacuum pump[114].

3.5.2 Mass spectrometry

As mentioned in 3.2.4.1, a mass spectrometer was used for the investigation of residual gases. The quadrupole mass spectrometer used in this work was a Microvision Plus, with the ability to detect atomic mass to charge ratios of up to M/Z=50. A schematic of a QMS (Quadrupole mass spectrometer) is shown in Fig 3.14. Gas is flown over a hot tungsten filament which acts as a high energy electron source, similar to the process in an SEM. The electrons bombard the gaseous species and ionise it. The cationic species is then accelerated with the use of an anode, towards a mass analyser. The quadrupole mass analyser has four poles, which are electrified with DC and RF currents. The RF current is selective and allows only certain ions to be detected depending on the operating frequency. The frequency can be altered, thus building a mass spectrum. For this work, only a faraday detector could be used (operating at slightly higher pressures), as the vacuum system could not sustain a sufficiently low level on the desorption of gases from the sample to operate the SEM (Secondary electron multiplier). To calibrate the TPD apparatus, a sample of MgH_2 was used (Goldschmidt, GmbH 95.5%)

with a measured mass and known quantity of hydrogen. (This was also verified using calibrated DSC and TGA methods available in the group). Integration of the resulting mass spectrum gives a total quantity of hydrogen desorbed from a given sample, assuming a mass given by the sample volume.

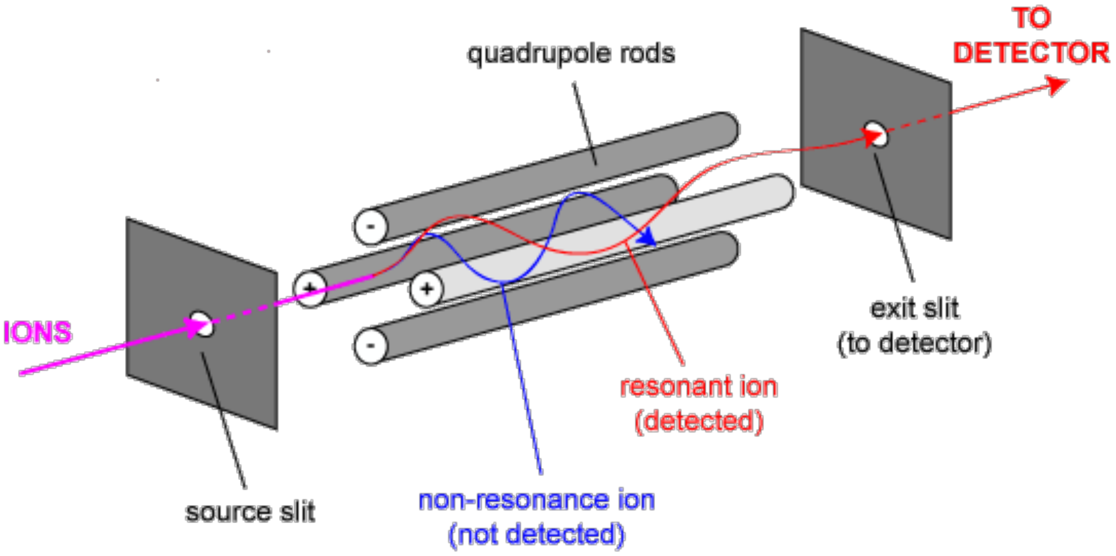

Fig 3.14. Operating schematic of a quadrupole mass spectrometer QMS. Electrons ionise a sample gas, which is then selectively filtered with the use of RF currents in a four pole configuration.[115]

4 RESULTS

4.1 EFFECT OF SPUTTERING CONDITIONS

4.1.1 CFUBMSIP sputter yield

Magnesium films were deposited onto glass substrates using a variety of preparation conditions (see Table 4.1.1), for a total of 10 minutes. Parameters investigated were magnetron current, bias voltage and base pressure (changed by argon flow).

Film thickness was measured using both confocal microscopy and SEM. The results of both techniques were compared to confirm the calibration of the confocal microscopy technique. The results from the thickness test are shown in Fig 4.1. It can be seen that sputtering yield is mostly affected by the current applied to the target, with a linear relationship observed in the conditions examined. However, factors such as bias voltage and chamber pressure also influence the sputtering rate, albeit to a lesser extent.

These results are fairly intuitive when considering the effects of the various parameters on energy of the atoms within the system. Increasing target current means Ar^+ ions are attracted to the surface with a higher energy and a larger amount of ions will have the required energy to displace a Mg atom. The same explanation can be used for the bias voltage, with the increase in applied potential promoting a greater acceleration towards the substrate and attraction to the workpiece. Even higher applied bias voltages may serve to re-sputter atoms from the substrate surface. However, given the linear relationship observed, this would suggest that these two competing mechanisms were not having a large effect on sputter yield.

In addition, the base pressure in the system (which is effectively the concentration of argon atoms/ions) has the opposite effect on sputter yield. The mean free path of an adatom is statistically reduced with the increase in argon pressure. Therefore, we would expect to observe a lower deposition rate for a higher pressure.

Given the resulting thicknesses, the range of sputtering rate could vary between 0.4 to 2 nm/s for Mg. Operation of the equipment outside of these parameters was not recommended by the manufacturer, as it may have caused either damage to the target, arcing or poor film quality. Thus, these conditions represent upper and lower boundaries for the operation of the CFUBMSIP system for this particular target.

Table 4.1.1 Sputtering conditions for films on glass substrates.

Parameter	**Sample ID**							
	A	**B**	**C**	**D**	**E**	**F**	**G**	**H**
Magnetron Current (Amps)	2	2	2	2	1.5	1	0.75	2
Base Pressure (x10^{-3} mbar)	2.6	2.6	5.6	7.9	2.6	2 .6	2.6	2.6
Bias Voltage (V)	30 (Pulsed)	100	50	50	50	50	50	50
Film thickness (+/- 0.1 µm)	1.1	1.4	1.1	1.1	0.7	0.5	0.2	1.2

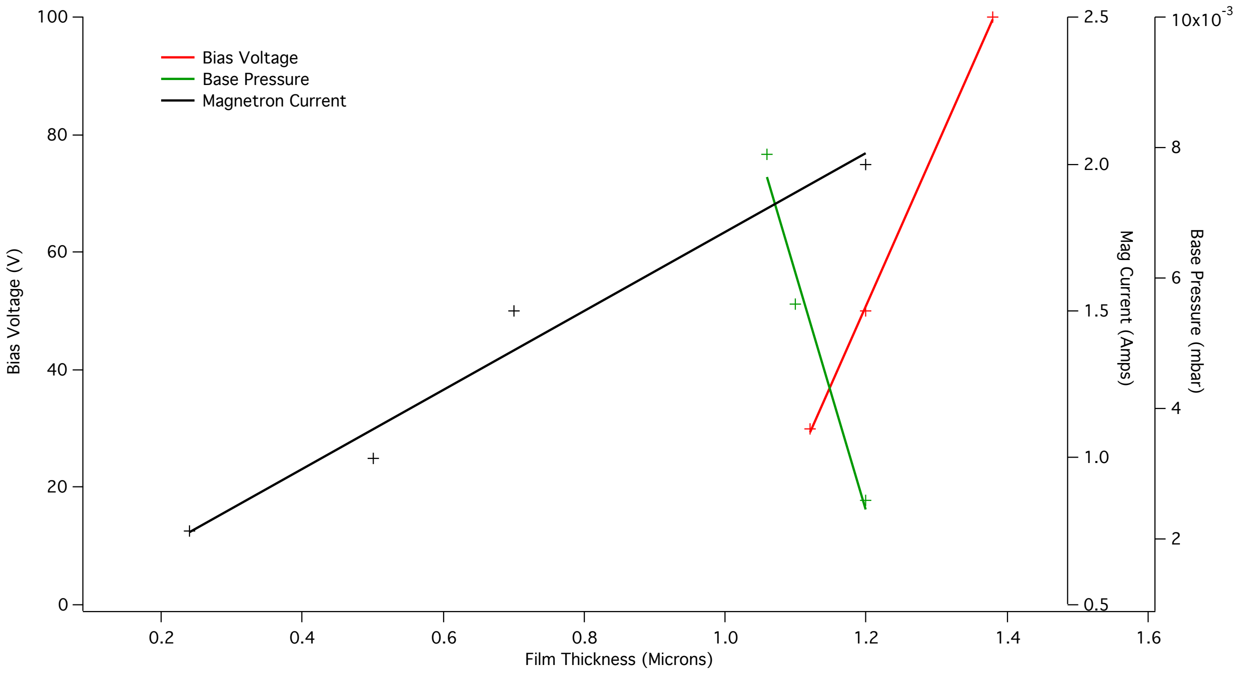

Fig 4.1. Effect of various sputtering conditions on the film thickness. Black: Magnetron Power (Left axis). Green: Base Pressure. Red: Bias Voltage. (Plotted on right axis – arbitrary). The data has been fitted using regression analysis. The factors all clearly contribute to the sputtering yield, with magnetron current having the largest effect.

4.1.2 Crystallography and intrinsic stress

Diffraction patterns for the films are shown in Fig 4.2. A strong out of plane texture is observed for all of the films with the basal plane preferred (002). This is common for thin films, in line with observations from many authors [63]. However, the 'degree' of texture varies between films. This is shown with small but noticeable peaks observed for 101, 102 and 112 reflections. The nature of the XRD set up used to produce these diffraction patterns means that only grains parallel to the substrate surface will be recognised. Therefore, the difference in the intensity of the diffraction peak is likely to show how well orientated the grains are, relative to the substrate surface. (This will be shown in section 4.1.3). Of particular note here is the sample highlighted with an orange trace (top). The diffraction intensity is around 5 times greater than all other samples. This film was deposited using a pulsed bias at 30 V. The principle of pulsed bias deposition is to allow for adatom diffusion into the growing film, promoting crystallinity. This increase in crystallinity is clearly observed with the change in intensity of the diffraction peak.

The variation of the texture observed is again due to the energy of adatoms. There are several mechanisms that can potentially play a role in the growth orientation, however these will be discussed in more detail later on in this work.

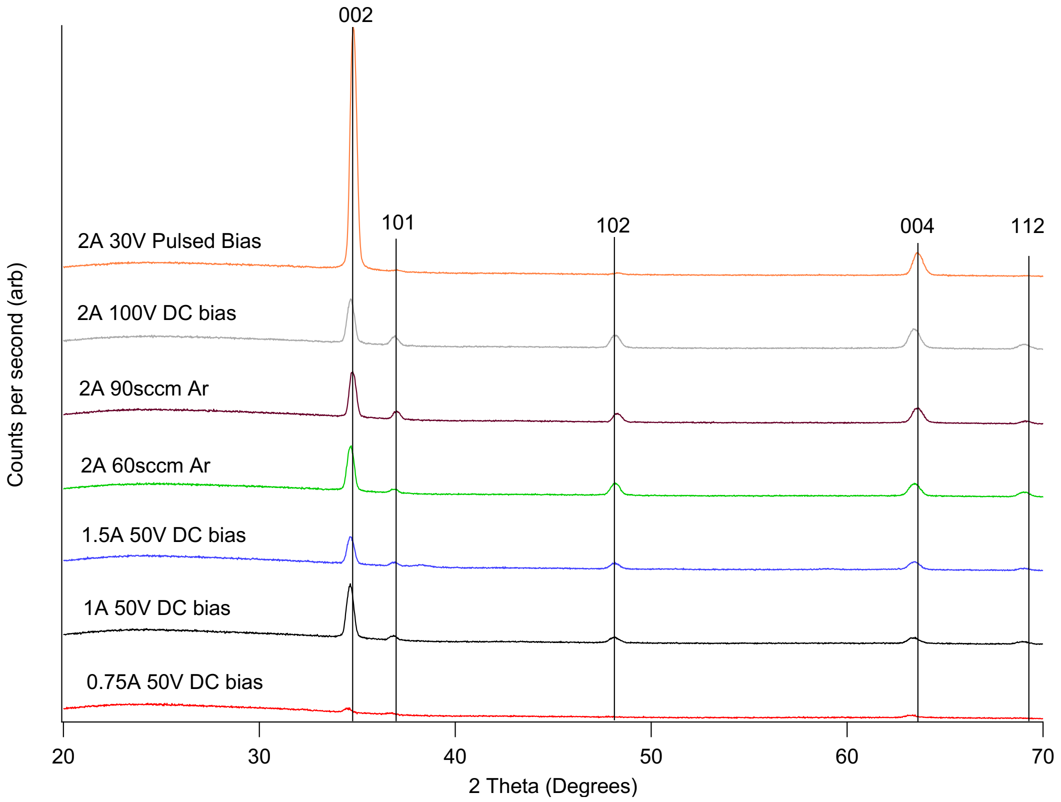

Fig 4.3. XRD patterns for the films A-G prepared in a variety of sputtering conditions. Strong texturing is observed in the basal plane, which changes depending on sputter conditions.

From the XRD patterns, the intrinsic film strain was estimated. The maximum strain calculated was 0.9 % in comparison to calculated lattice parameters from the ICSD. Using the bulk modulus for Mg of 45 GPa, this gives a stress up to around 400 MPa (Fig 4.4). However, due to Hall-Petch strengthening, it is likely that the actual stress is higher. Intrinsic deposition stresses within this range are certainly not uncommon [116–118].

The relationships shown reveal that the film stress is linearly dependent on the magnetron current, with an increase in applied current corresponding to an increase in the film stress.

Changing the bias voltage gives an interesting effect, where decreasing the bias seems to also decrease the stress, up to a point, where the stress seems to increase again. This would not be expected normally. However, an explanation would be that the film prepared with the pulsed bias at 30 V may behave differently. The principle of the pulsed bias allows for diffusion of high-energy adatoms into the surface, so it is likely that this particular mechanism skews the results in the case of the research presented here.

The effect of changing the base pressure within the system also has an effect on the observed film stress, within the conditions evaluated. It is difficult to ascertain the exact nature of the effect, whether it is linear or curvilinear. However, it appears that with increasing the base pressure, there is also an increase in the stress.

These findings are intuitive, as these deposition parameters influence the energy with which argon ions impact the target or how strongly the sputtered adatoms are attracted to the work piece. The kinetic energy of adatoms is known to influence the developed microstructure, as well as deposition stress. However, the complexity is in the interdependence between these variables, which determines how a film grows and becomes stressed.

Ohring expresses the intrinsic film stress as an outcome of various mechanisms, including gas entrapment, atomic mass of target and deposition rate. However, in contrast to other metals and coatings, the films prepared in this case did not show a transition from tensile to compressive stress[103].By combining multiple parameters one could seek to produce a film with a compressive stress using this system. However, the purpose of this particular investigation was to analyse the typical properties of this system, and not to necessarily succeed in producing a film with an intrinsic in plane compressive stress.

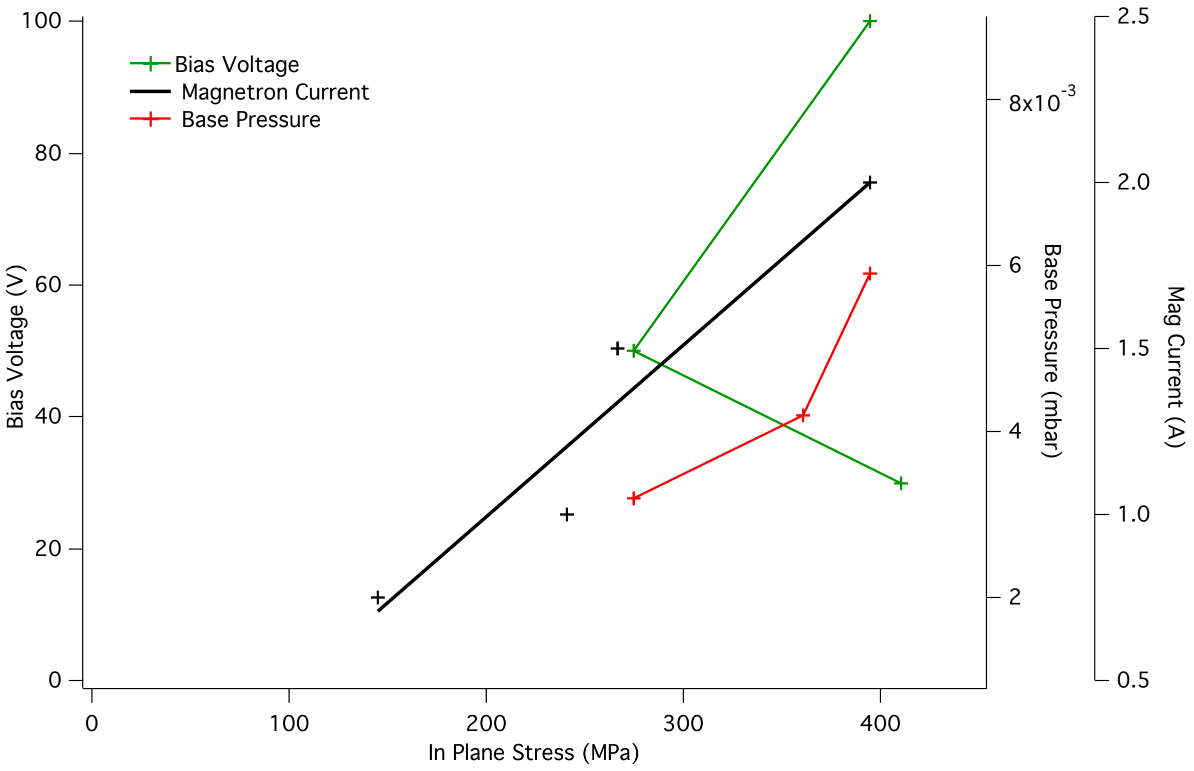

Fig 4.4. In plane stress as a function of the different preparation conditions for pure Mg films. (N.B. In plane stress is estimated using the bulk elastic modulus for Mg – 45 GPa and using generic convention – tensile stress is denoted as positive.) The black line is fitted using regression. The other two relationships are a guide to the eye for the reader. There should be a relationship identifiable, but more preparation conditions would be necessary.

4.1.3 Microscopy

Cross sectional micrographs of the surface and cross sections of a selection of the films are shown in Fig 4.5 and Fig 4.6, respectively. A range of microstructures is observed, which can be related to the variables that were altered during the deposition process. The cross sectional micrographs reveal a different growth process.

Film A does not have an obvious columnar structure in comparison to the other films. This is an effect most likely caused by the pulsed bias used, which can act to enhance crystallinity. Similar reports have been shown for Ti-C-N [119] TiO_2 [120]and YSZ[121] films by previous authors. The film appears to have high density with no evidence of microstructural porosities.

Film C initially grows with a very refined microstructure at the substrate interface, with coalescence of grains occurring further into the deposition process to form larger columns (type B microstructure in Fig 4.2.2). This suggests that some crystallite coalescence occurs throughout the film deposition process. The initial high nucleation rate is probably due to the increase in argon pressure. In addition, there is a noticeable porosity change within the films. This will be due to different argon pressures, which will affect the degree of argon entrapment within the film. Film D does not appear to suffer from the porosity present in film C, despite the increase in argon pressure. The reasons for this are unknown at this time. Gas entrapment is a known mechanism for inducing tensile stresses in physically evaporated films[117]. This is an important factor when considering hydrogen storage mechanics, as with a large volumetric phase change, porosities can provide an expansion gap for strain relief. It would therefore seem that deposition at lower argon pressures would be favourable for the following investigations. Further evidence of porosity is observed from the surface morphology shown in Fig 4.6. It is clear that there is enhanced porosity within the coatings C and E. This is important, as it may allow hydrogen penetration deeper down into the film and allow for nucleation and growth of the hydride phase from the film/substrate interface, rather than the film surface. This behaviour has been observed previously within Mg/Ni films, where the hydride phase was shown to grow backwards, controversial to what one might expect, as hydrogen enters via the top Pd surface in most cases. In this case, an excessively small grain size (10nm grains) at the film/substrate interface promoted nucleation due to excess interfacial energy [59,122].

Film F shows fairly uniaxial growth. This film is of a lower thickness to the others shown (500 nm) and at a lower target power. This may suggest that a lower growth rate lends itself to a higher grain growth.

A comparison of surface micrographs (Fig 4.6) shows that for film A, there is a very ordered and flat surface showing a uniform grain size. The pulsed bias is likely to be responsible for this effect. Films C and E tend to deposit with intrinsic porosities. In addition, there seems to be a large difference in the grain sizes observed, suggestive of abnormal grain growth. This is not uncommon in thin films and is suggestive of a competitive mechanism for grain oriented growth[105]. This phenomenon is important to recognise when considering the interaction of hydrogen with the film. Nucleation and growth of hydride at grain boundaries is preferential due to the excess in surface energy. A greater density of inhomogeneity could lead to faster reaction kinetics for the film.

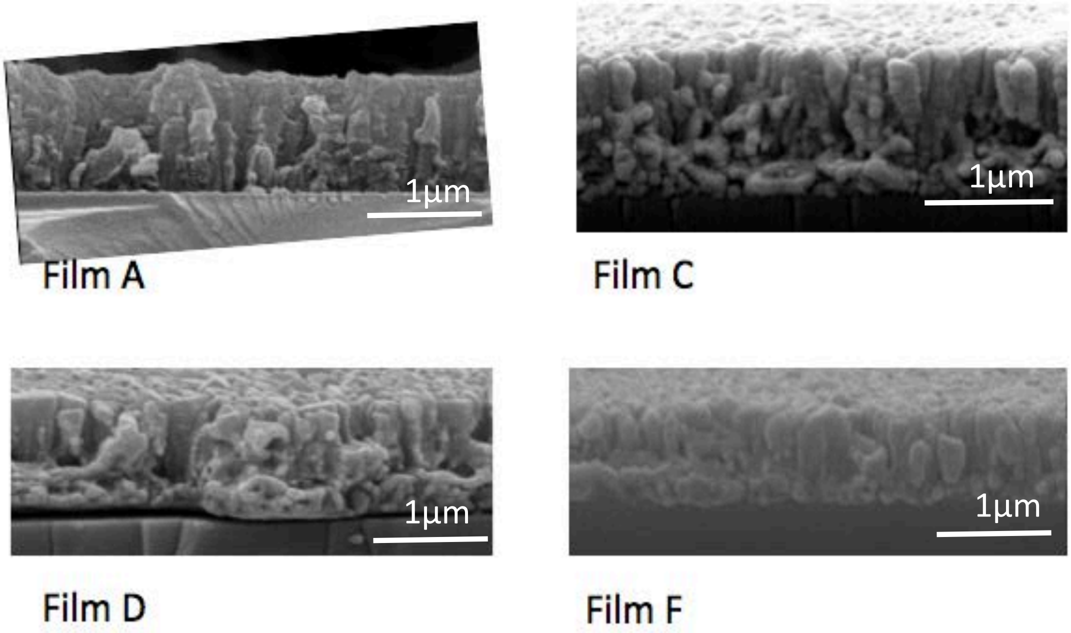

Fig 4.5. Cross sectional SEM micrographs of selected films. There is an observable difference between column width and film growth morphology, as well as film density/porosity.

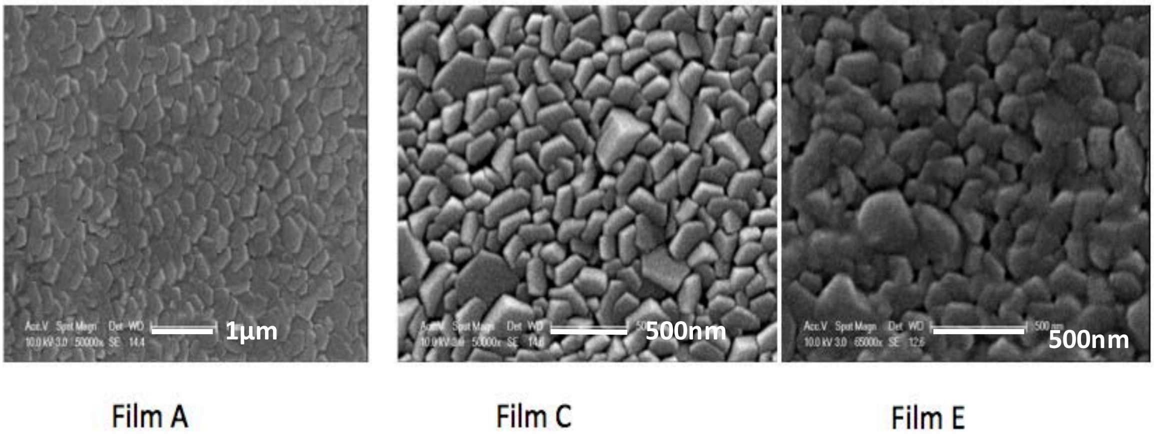

Fig 4.6. SEM images of selected film surfaces showing hexagonal Mg 'platelets'. Grain size appears more uniform moving from left to right. In addition, the texture of the grains appears more perpendicular to the substrate. The grain structure in film E is more cauliflower like. There appears to be an increase in porosity of the films from left to right.

As grain size is important for hydrogen storage characteristics as well as analysis of grain growth, it is useful to compare the grain size that can be calculated from the XRD data to that of the observation in the micrographs. Calculation of the grain sizes for these films can be fairly ambiguous. Firstly, the Scherrer formula uses a generic coefficient of 0.9 to describe the shape of a grain, which is not very applicable, as most of the grains in the samples are columnar. In addition, the sizes of the grains vary from substrate to surface, so selection of the appropriate grain size is difficult. However, as the diffractometer penetrates the entire sample and essentially provides an average grain size over a large section, the results from the Scherrer formula applied to the main Mg (002) peak are shown in Table 4.1.2.

Table 4.1.2 Calculated grain sizes for films from XRD patterns

Film	FWHM (2θ° to 2 d.p)	Grain Size (nm)
A	0.32	306
B	0.38	136
C	0.33	282
D	0.38	134
E	0.32	324
F	0.33	249
G	0.32	333
H	N/M	N/M

The results in Table 2 are suggestive of a large shift in grain size between films (130 to 320 nm). However, by image analysis using ImageJ software (an optical tool can be used to highlight grains and calculate their sizes), there is a large difference between observed and calculated grain sizes. This difference is more than likely derived from two causal factors:

(a) The averaging effect from the XRD analysis as already mentioned

(b) The difference in grain growth mechanisms

As film stress is governed by the film growth mechanism, it would seem logical that there should be some form of correlation between the grain size of films and the intrinsic stress. This is shown in Fig 4.7. In the top graph (red) we initially see a weak inverse relationship. However, considering the circled point is film A with a pulsed bias, this result can be omitted considering the vast effect it seems to have had on the film microstructure. Omitting this point gives a stronger linear dependence on stress and grain size (bottom graph). However, the inverse relationship is not what would be expected. Intrinsic stress generation is usually associated with either a recrystallisation mechanism of disordered material, or a coalescence to form larger grains. There are a number of possible explanations for the inverse phenomenon observed. Firstly, there could be some form of stress relaxation occurring via grain growth in a similar mechanism to those reported in annealed Al-Mg films[123]. If we suppose that tensile stresses are generated by porosity, then the removal of a porosity by grain growth may lead to a reduction in stress. In addition, there could be a mechanism where the adatom bombardment acts to induce compressive stresses[124]. This relatively simple set of experiments shows the complexity of the film growth process.

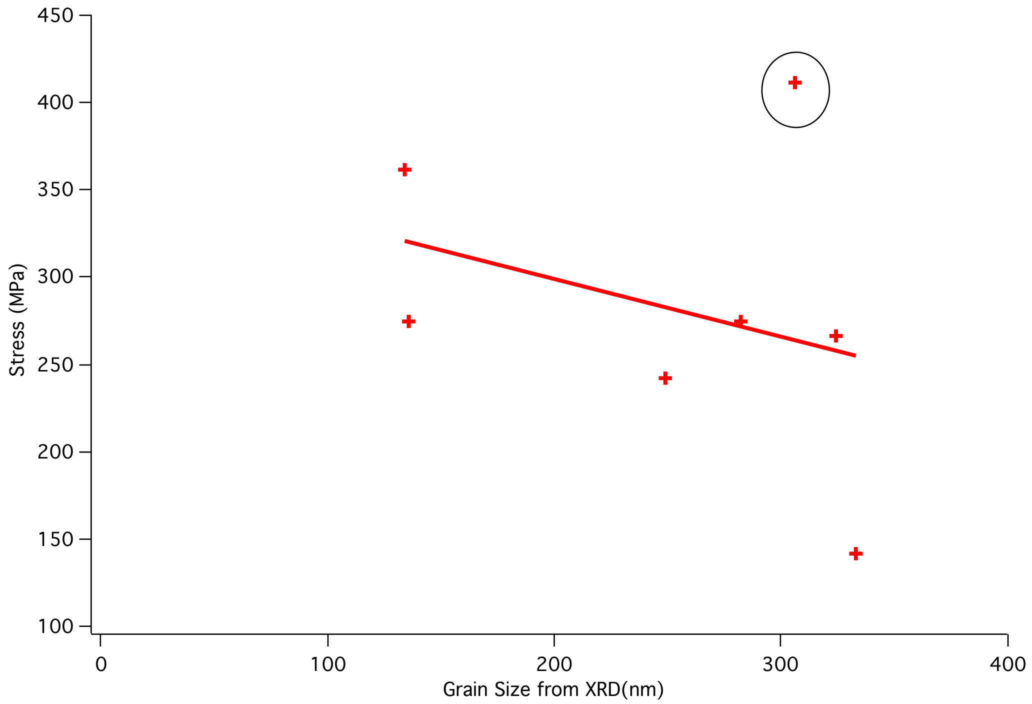

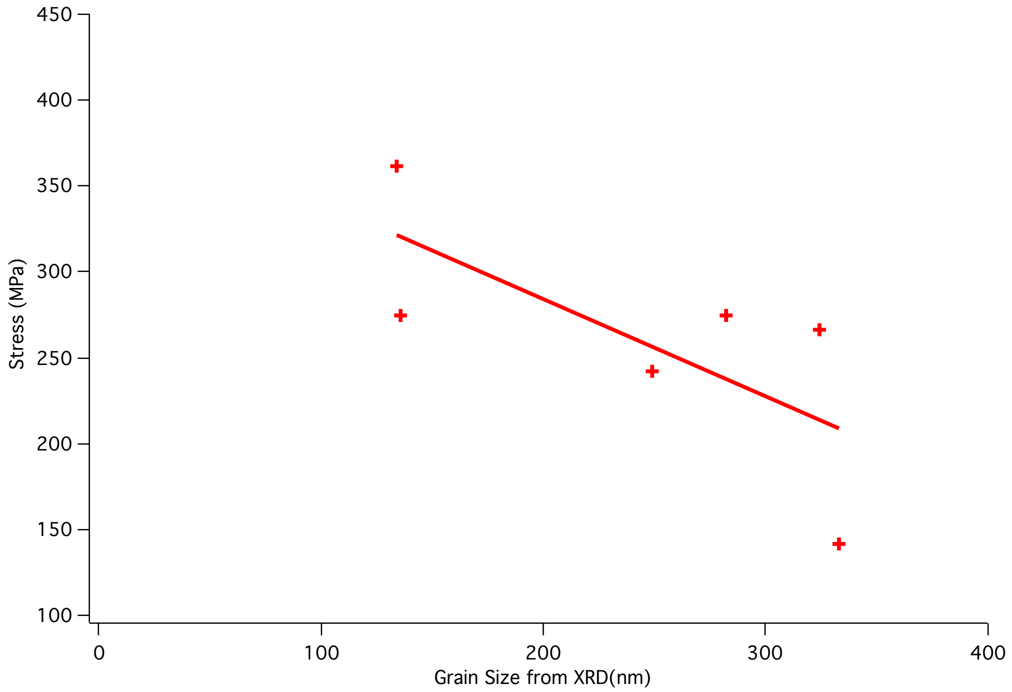

Fig 4.7. Empirical relationship between grain size and intrinsic stress. Top – with original data including pulsed bias deposition (circled). Bottom – relationship with data point ommitted showing an improved regression fit to the data. A stress relaxation mechanism such as annealing or adatom bombardment are proposed to be responsible for this effect, pointing to the removal of porosites as being the source of intrinsic tensile stress.

4.1.4 Summary

This investigation has presented a practical examination of the properites of the CFUBMSIP system. Sputter yield has been investigated, showing linear relationships amongst three different variables (Bias voltage, Magnetron Current and Argon Pressure). These variables are related to the adatom energy and clearly have different effects on yield.

In addition, the intrinsic deposition stress is variable and large (up to around 0.4 GPa), depending on the conditions used. Relationships have been shown to exist for each of the three variables examined. However, there is an interdependence between each variable which means that the overall stress is difficult to predict for any given coating. Mechanisms of argon entrapment, crystallite coalescence and ion implantation may be responsible for the observed changes. The calculations from the XRD patterns are confirmed with cross sectional SEM, which have shown evidence for the suggested mechanisms.

Finally, the grain size of the films was compared to the microscopic evidence. This showed that the Scherrer formula, despite its limitations, is in reasonable agreement with the observed micrographs. However, because the difference between calculated and observed values are different (films have a column width of between 150 – 300 nm), there is reason to be sceptical that the biaxial stress is not completely uniform, with stress concentrations around defects/impurities. This is important, as it may effect the interaction of hydrogen with the film, potentially skewing results.

Finally, the intrinsic stress mechanism is proposed to be due to porosities within the growing film. The reduction of this tensile stress is proposed to occur via an annealing or adatom bombardment mechanism.

This relatively simple set of characterisation experiments have shown the importance of thin film deposition parameters which give rise to different yields, microstructures and intrinsic stresses. This work is often neglected within many published journals regarding thin film hydrogen storage, but may be fundamental in understanding the nature of the elastic interaction and explaining the differences between authors reports on similar subjects, especially when dealing with research on films in the region of <100 nm in thickness. In addition, the importance of sputtering at low argon pressures has been shown to reduce porosities, improving film quality. The use of a pulsed DC bias has shown great improvements in film crystallinity and uniformity and will be the choice of parameters moving forward.

4.2 HYDROGEN SORPTION IN PD CAPPED THICK MG FILMS PREPARED IN A VARIETY OF CONDITIONS

4.2.1 Initial film characterisation

800 nm thick Mg films with a 40 nm Pd cap layer were deposited onto glass substrates in a variety of experimental conditions (Table 4.2.1). Substrates were cleaned and loaded at room temperature and during the deposition the bias was pulsed at 500 ns intervals at a frequency of 250 Hz. A pulsed bias was chosen based on the results in section 4.1. The greater crystallinity, as well as a reduction in the observed argon entrapment, was seen to be beneficial, and so those conditions were considered for further work.

Table 4.2.1 – Values used for the different depositions

Sample ID	Mg Current (A)	Pd Current (A)	DC bias (V) 250 Hz 500 ns pulsed	Base Pressure ($\times10^{-3}$ mbar)
A	1.5	1	50	4.2
B	1	1	50	4.2
C	0.75	1	50	4.2
D	2	1	30	4.2
E	2	1	70	4.2
F	2	1	50	4.2

XRD - As deposited Films

The diffraction patterns for each of the 800 nm films are shown in Fig 4.2.1. Mg is highly textured in the basal plane (002) and Pd is in the close packed (111) plane. No other reflections are present.

Looking into detail at the Mg (002) peak, there are differences in the amount of texturing observed (peak height) as well as the peak position. This is shown more clearly in Fig 4.2.2, with the bulk Mg lattice parameter noted for comparison. For the highest magnetron current values (D, E, F) the crystallinity seems to be generally higher. Out of these three films, the higher bias voltage gives a more crystalline film, with a fairly linear trend down to the lower bias values. This is probably due to the higher kinetic energy possessed by the ad-atoms, giving them greater energy when they hit the sputter target which aids their ability to form a more perfect crystal and grow.

For the lower applied currents, there is some evidence of a relationship, with the lower applied current generally forming a less intense peak. However, film C with an applied current on 0.75A is fairly anomalous in that it forms a fairly highly crystalline film. The reasons for this observation are unclear at this time, but it is likely due to a complex interaction of competing mechanisms of atomic interactions.

It can also be seen that the peak positions vary slightly. Using these peak positions, we calculate c axis lattice parameters for the films, which are slightly smaller than the bulk values, suggesting an out of plane compressive strain. An expansion or contraction out of plane in thin films is stress free, so we interpret this as a tensile stress in the x-y plane, in the same way as in section 4.1. These values sit well within the values expected for intrinsic deposition stresses (Table 4.2.2). A plot of intrinsic stress against both magnetron current and bias voltage is shown in Fig 4.2.3. No certain conclusion can be gained from the effects of bias voltage. However, a linear relationship is shown to exist for the relationship between magnetron current and intrinsic film stress. Film A (highlighted), may be anomalous, or there may be a competing mechanism in these conditions, that reduces tensile stress build-up.

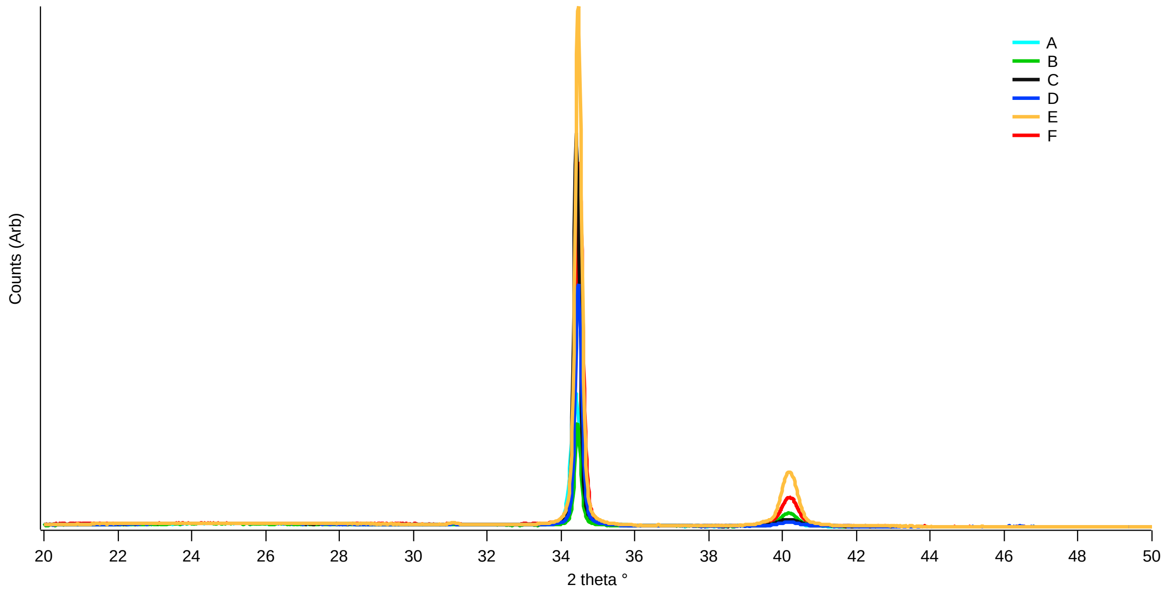

Fig 4.2.1. XRD patterns of films prepared in a variety of sputtering conditions, as referenced in Table 4.2.1. Mg out of plane texture (002) at around 34° and Pd (111) at 40°.

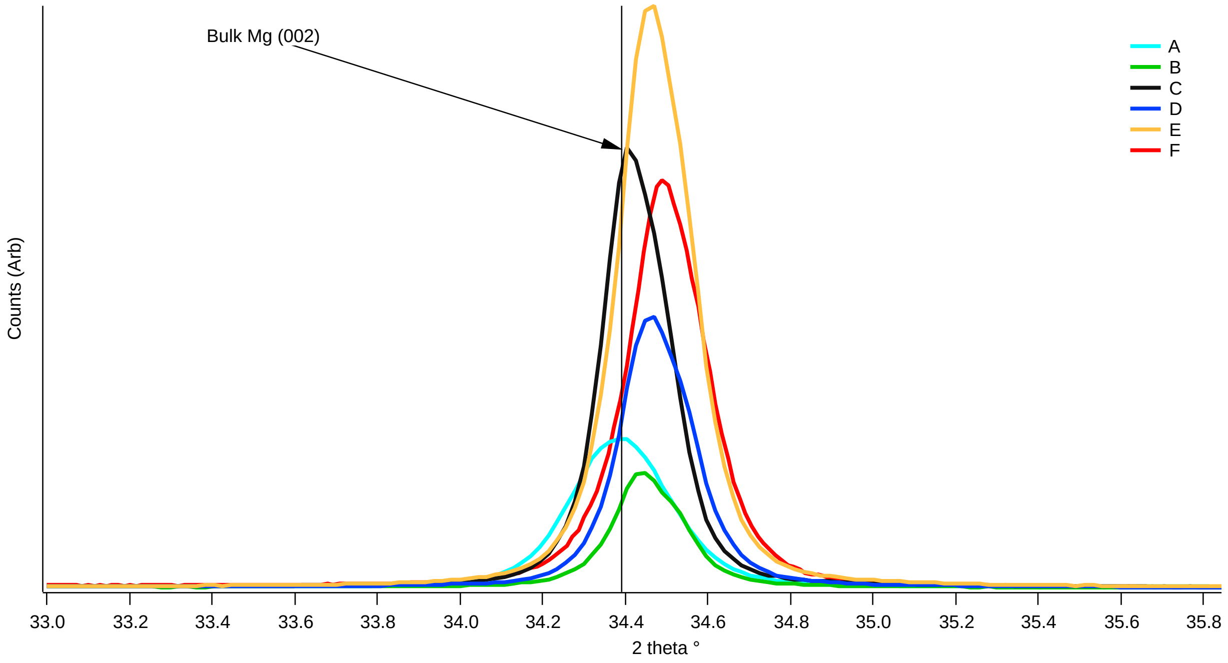

Fig 4.2.2. XRD patterns showing detail of the Mg (002) peak position in as deposited films.

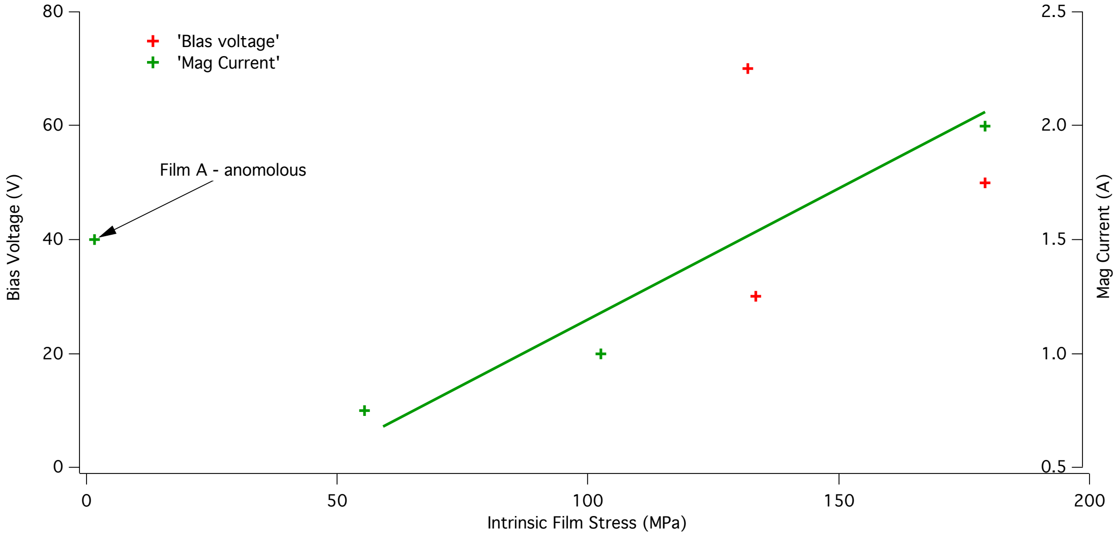

Fig 4.2.3. Analysis of the effects of magnetron current and bias voltage on intrinsic film stress. There is no apparent relationship between bias voltage and intrinsic stress. However, the increase in magnetron current seems highly correlated with an increase in film stress.

Table 4.2.2. Calculated in-plane stresses and grain sizes for films A-F.

Sample	Stress (in-plane) (MPa)	Scherrer Grain Size (nm)	Grain size SEM (nm)
A	-1.6	863	314
B	99	3000	331
C	54	4718	363
D	130	2900	350
E	128	1670	324
F	173	1433	N/A

SEM

SEM micrographs (Fig 4.2.4) reveal that the films grow with basal texture and the hexagonal platelets of Mg are clearly visible. This is consistent with the previous section, as well as reports from other authors[42,125]. A few features of interest are revealed. In film B, small inhomogeneous regions appear. These look like grains that have grouped together, which may cause areas of localised stress. Relating the smoothness of the films to the X-ray diffraction patterns, we see that films E, C and D have the smoothest looking appearance, which agrees well with the diffraction intensity (those who appear smoothest have the X-ray peak largest intensity). This would be due to perpendicular alignment of the basal plane with the substrate surface, as only this alignment gives rise to a diffraction signal.

There is a small variation in the grain size between each film, but only in the order of a few tens of nanometres. The prediction from XRD gives a much higher grain size than SEM. The reasons for this are likely due to the corrections for instrument broadening. A calibrated corundum standard was used to correct for instrument broadening, but as the films are highly crystalline, the correction is probably not accurate enough to predict an accurate grain size. In addition, the shape factor of 0.9 is set for a uniform grain size, which is an another assumption within the calculation that could lead to error.

A plot of intrinsic stress against grain size would initially yield a lack of apparent correlation (Fig 4.2.5 - top). However, considering that sample A appears anomalous in both Fig 4.2.3 as well as in this Figure, it has been omitted. After this, there appears to be a stronger correlation between the intrinsic stress and the observed grain size. This observation is consistent with those shown in section 4.1 and suggests that there is a mechanism whereby grain growth leads to a more relaxed film.

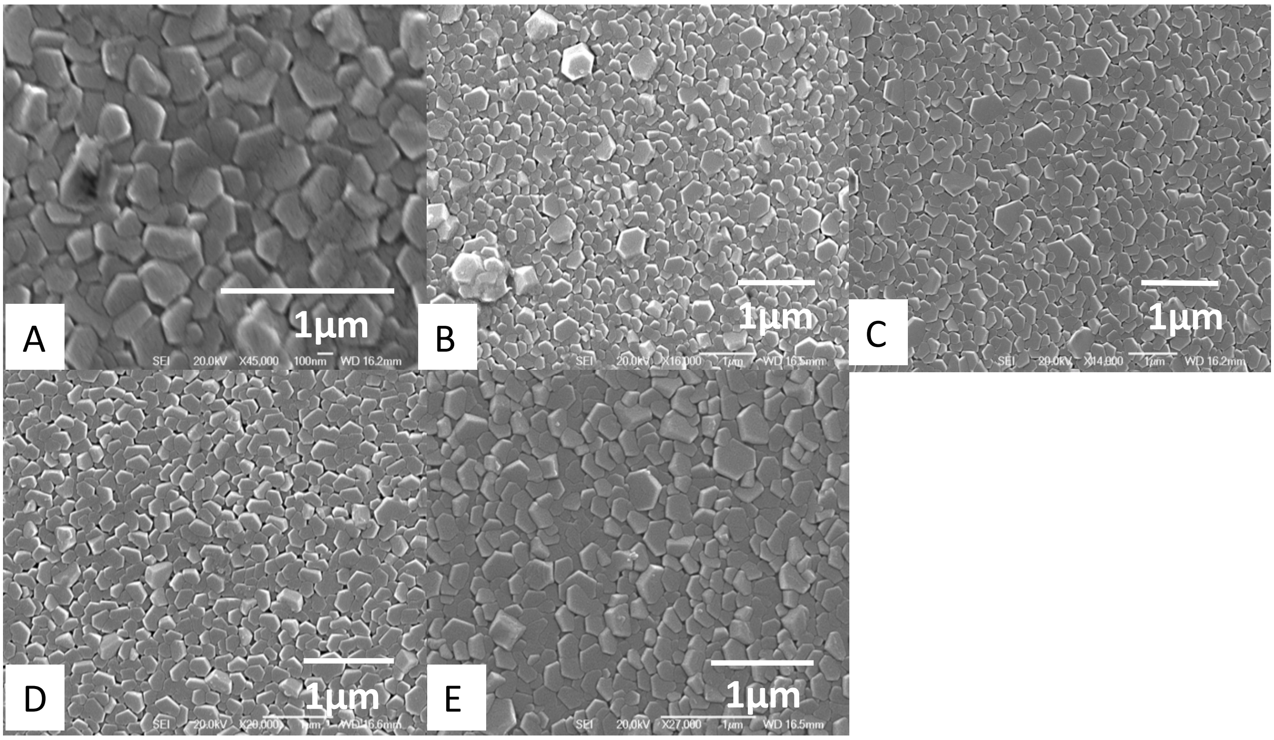

Fig 4.2.4. SEM microscopy of each of the 800nm films A-E. Inhomogeneous grain clusters can be observed, as well as surface porosities.

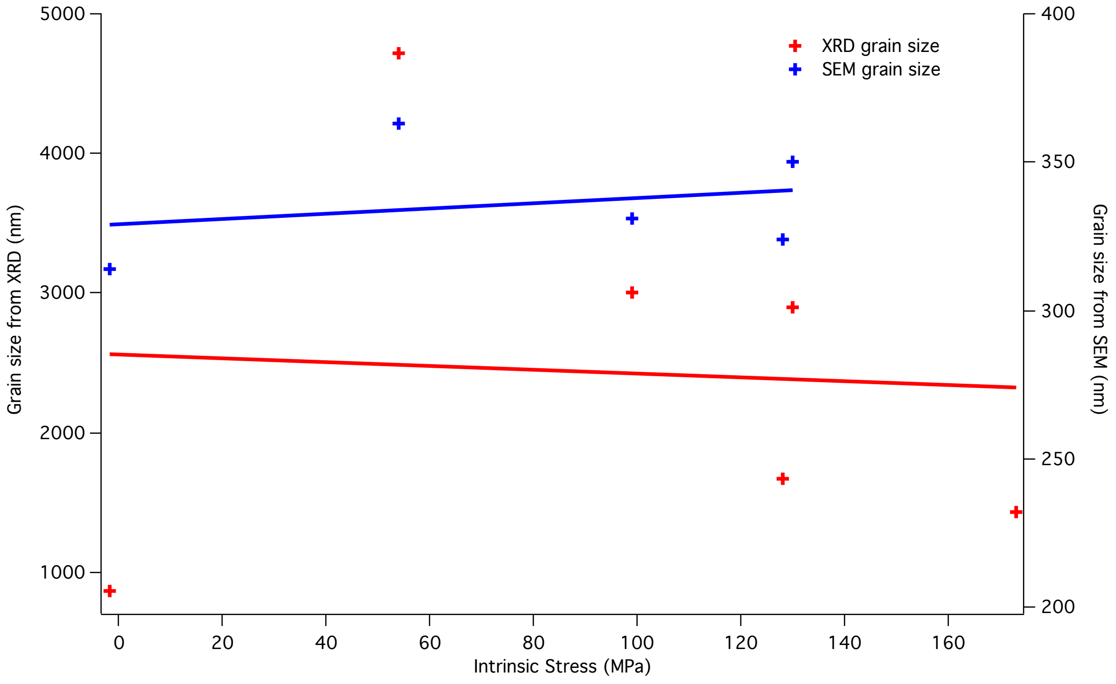

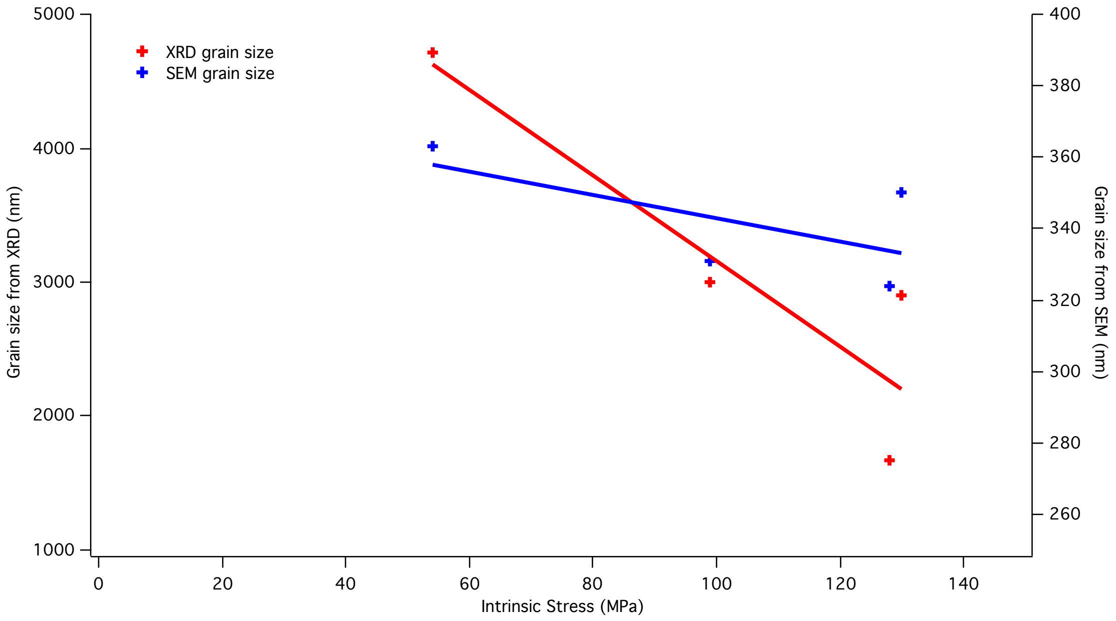

Fig 4.2.5. Comparison of calculated grain size from XRD and SEM. Top – a lack of relationship observed between grain size and intrinsic stress. Bottom – omitted anomolous result (film A) shows a stronger correlation.

4.2.2 Hydrided film characterisation

Hydrogenation was performed in a sealed reactor inside a furnace at 1 bar H_2 at 100 °C for 48 hours. XRD patterns after hydrogenation for 48 hours at 100 °C are shown in Fig 4.2.6. The films exhibit the martensitic like relationship Mg (001)//MgH_2 (110) which has been reported previously [64,66]. Quantitative phase analysis using the Reitveld method is not possible using this data due to the single peak position. It is clear that there is some residual Mg.

Comparing the integrated Mg peak area from the as-deposited films to the films after hydrogenation would suggest that all films are almost completely reacted with Mg. This method was used by Kelekar et al [91]. However, it will be shown later on in this section that the intensities of the peaks do not correspond to the hydrogen concentration.

MgH_2 grain size was estimated using the Scherrer equation (Table 4.2.3). Using this analysis it would seem as though all of the films show a decrease in grain size for the MgH_2 phase. The decrease in grain size is different to observations by other authors who report an increase in grain size and removal of defects[64]. However, there could be several explanations which include the growth behaviour of the hydride and the amount of hydride phase formed (a phase must nucleate and grow and so the grain size may reflect this).

Looking into more detail at the MgH_2 [110] peak, we observe a difference in peak position, signifying a stress build up in the phase. As the [110] peak describes both a and b lattice parameters, it is not possible to say which direction is expanding, but it is likely that the out of plane expansion is more energetically favourable. Using this analogy, it is possible to assume that the initial tensile stress in the as-deposited films is reduced by an amount proportional to the volume expansion caused by hydrogenation. Using this assumption, we can calculate the in-plane stress change caused by hydrogenation. Of course, this doesn't take into account any plasticity in the Mg and microstructural effects because XRD can not show this. Plastic deformation is known to occur due to hydrogenation, once the yield stress of Mg is exceeded and assuming good adhesion to the substrate. Plastic deformation is responsible for strain energy absorption but is irreversible[8984]. The change in stress due to hydrogenation is shown to vary between 80 - 230 MPa (Table 4.2.3). This is lower in comparison with other literature using stress measurements on Mg-based films (calculated to be 1.4 GPa), however, films aren't fully loaded with hydrogen and porosity may have an important role to play[126]. The increase in stress of the original Mg layer supports the argument that the MgH_2 phase nucleates and grows as a layer, most likely from the Mg/Pd interface, forming thinner and thinner layers of Mg. It would also explain why the thicker films are difficult to hydride, even for a prolonged period of time at a reasonably high temperature as the diffusion of hydrogen through the MgH_2 layer becomes the rate limiting reaction.

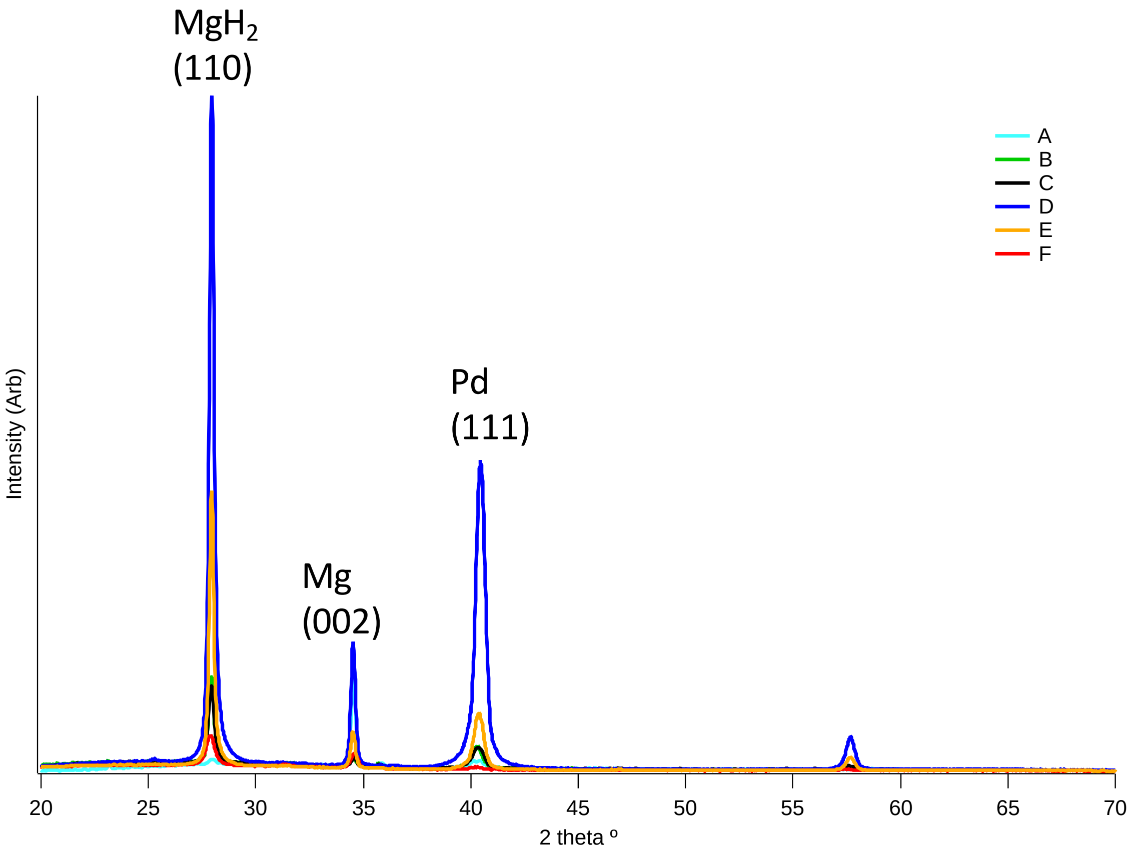

Fig 4.2.6. XRD patterns of the films after hydrogenation at 1 bar H_2 for 48 hours at 100 °C. MgH_2 peak appear at 28°. There is residual Mg in all of the films.

Table 4.2.3 – Grain size and in plane stress for MgH_2 and Mg, along with the change in stress calculated from the intrinsic state.

Sample	MgH_2 grain size (to +/- 50 nm)	MgH_2 Stress in plane (to +/- 10 MPa)	Mg in plane Stress (to +/- 10 MPa)	Change in Mg stress (to +/- 10 MPa)	Hydrogen Content (to 1 d.p wt%)
A	N/M	0	234	235	1.4
B	1160	-50	220	120	3.4
C	980	0	280	224	5.7
D	1260	-8	220	91	2.5
E	1400	-20	210	81	2.9
F	490	-130	300	128	1.7

In Situ XRD

To further validate the assumptions and further investigate the argument for stress development during hydrogen loading, in situ XRD was used. For this measurement, samples were loaded into an environmental cell (Anton Paar XRK 900) at 1 bar H_2 and heated at a rate of 0.4 °C/s to 100 °C. A scan was ran repeated every 30 minutes to track the reaction behaviour.

It is clear to see that the Mg peak shifts towards a higher 2θ value during the reaction, suggesting that there is an increased tensile stress build up in this layer. In addition, the MgH_2 (110) peak shows a small increase in d-spacing. As this plane describes the in plane lattice constants, it is reasonable to assume that the hydride layer is also experiencing a compressive stress as it grows.

This is interesting, as it shows that the two layers must be at least partially mechanically coupled at their interface.

The results obtained are for film B. The measurements show a change of stress in the Mg layer of 80 MPa. This is slightly altered in comparison to the observed ex situ experiments, but this does not take into account any lattice contraction due to thermal expansion between film and substrate.

In addition to the stress strain analysis, it was also possible to plot kinetic points of peak intensity versus time, to show how the reaction progressed (Fig 4.2.8). According to the intensity of the points, one can observe a reaction that follows a diffusion-like mechanism. This is similar in nature to the reports by Kelly and Clemens[127] and is typical of Pd capped Mg films in conditions where the hydrogen loading pressure is far above the plateau pressure[38].

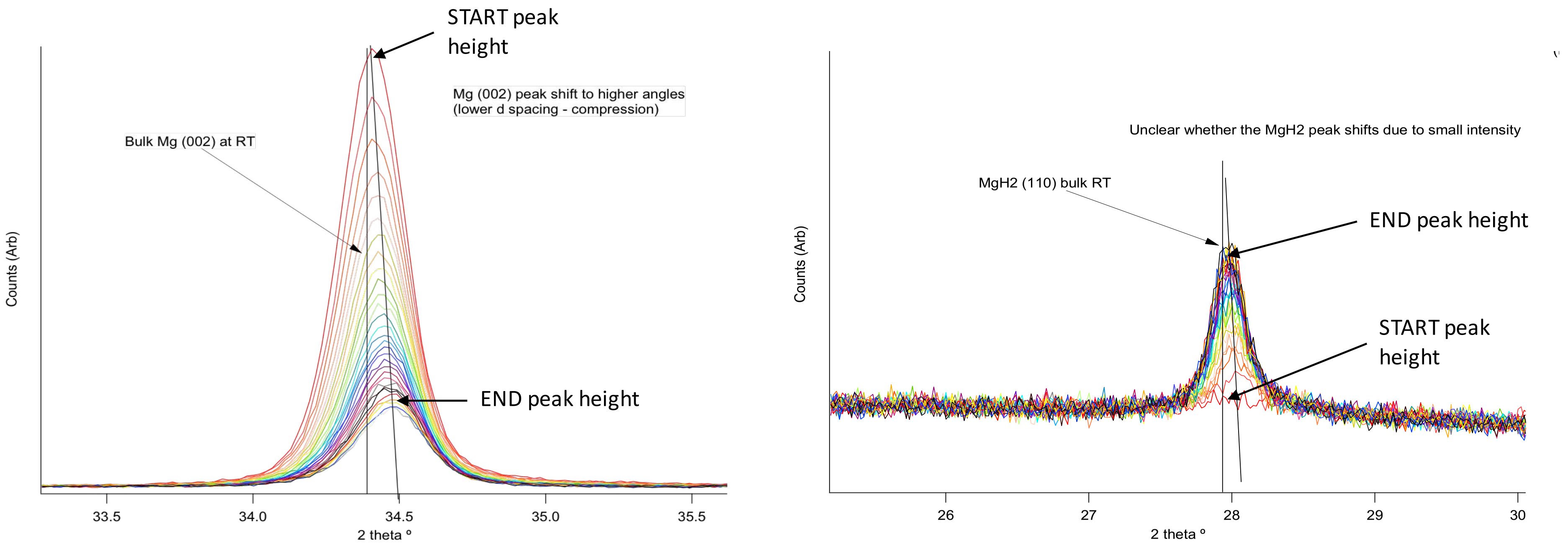

~~Fig~~Fig 4.2.7. In situ XRD patterns showing the peak height and position shift of Mg and MgH_2 peaks with time. Hydrogenated at 100 ℃ at 2 bar H_2.

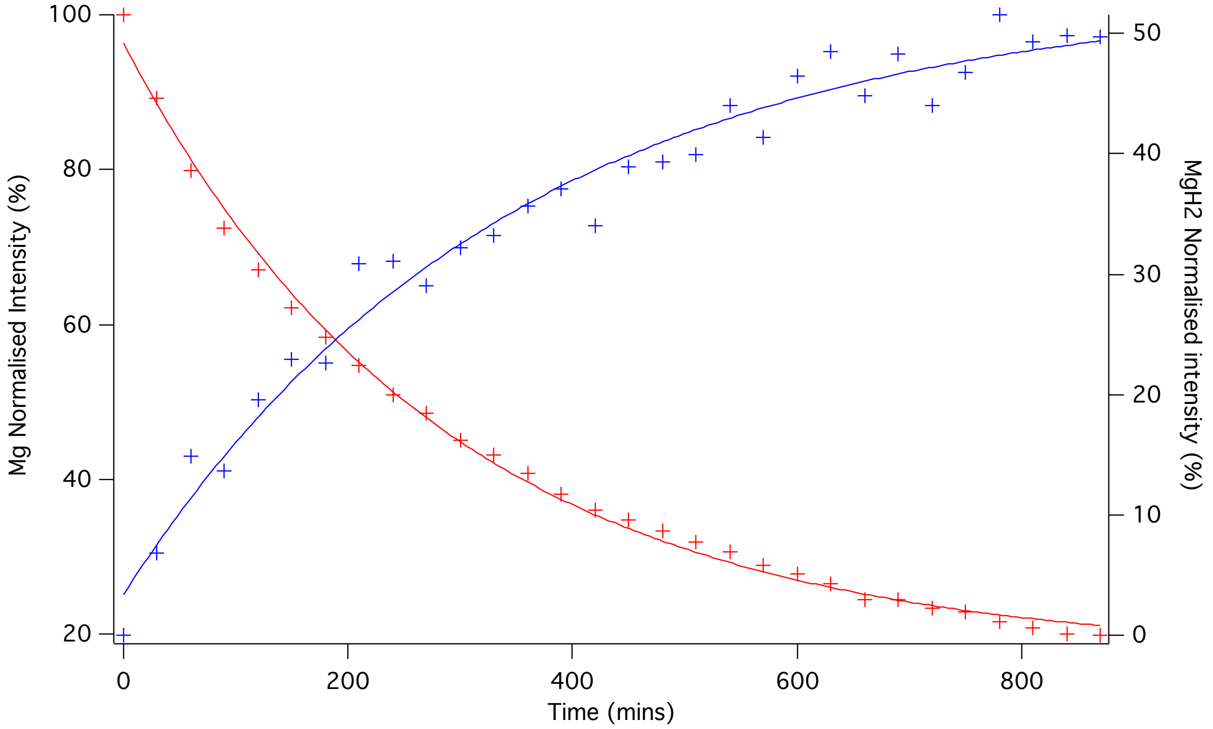

Fig 4.2.8 In situ XRD peak intensity plot versus time. The reaction appears to be first order, showing that the likely limiting factor is diffusion through the growing MgH_2 *film. (N.B. Every scan took 30 minutes – total reaction time was 15 hours. 100 ℃ at 2 bar* H_2*).*

4.2.3 TPD

Temperature programmed desorption measurements were undertaken (Fig 4.2.9). It is clear that the peak positions of the various films vary, signifying a difference in thermodynamic stability. In addition, a numerical integration of the peak area gives the total H_2 stored within each film (Table 4.2.3). This ranges from 1.4 to 5.7 wt% H_2 for films A and C, respectively.

There are shoulders visible on the peaks of films B and C. The reason for this is uncertain at this time. However, it may be attributed to some form of plastic deformation. Using the expression derived by Pivak et al [84] and other authors [79,97], we can see that the effect of plastic deformation can be to widen hysteresis behaviour. In this sense, the desorption plateau pressure of MgH_2 is decreased, effectively stabilising the phase, leading to a higher desorption temperature.

Assuming that films have a total capacity of around 90 % of the total expected hydrogen storage capacity in contrast to bulk, due to the extra defects, the expected thickness of the hydride layer expected in each case can be calculated[89]. If we assume the phase grows fairly uniformly from the surface towards the substrate, the hydride front will have reached a depth of around 600 nm. With such a large uptake, the expected volume increase may be in the order of around 24 % (compared to the known phase volume increase of 32 %). A lot of the volume increase is expected to be absorbed by plastic deformations in the form of material pile up, porosity, or buckle formation. Looking at the films after hydrogenation, it was clear that film C had undergone severe buckling and delamination from the substrate. In addition, there were areas of films around the edges of the sample that had started to form 'telephone cord' buckles (Fig 4.2.10).

This suggests that initially, the volume expansion is absorbed by plastic deformation. Without this mechanism in place, there would be no secondary peak on the TPD traces. After a critical hydrogen concentration is reached, the adhesion forces between film and substrate are overcome and the film buckles elastically.

However, this is not conventional. We would expect elastic yielding to occur before plastic deformation. Therefore, the likelihood is that the film does not grow with such a uniform layer. Instead, there must be regions of the film that nucleate and grow in 3D. This has recently been shown by Mooij et al[97]. Using this evidence, we suggest that the hydride domains nucleate and grow with localised plasticity. When the domains approach a region where elastic failure is more energetically favourable, the buckles form. This is in agreement with Pundt et al in Nb-based films[128]. In addition to this, it is known that the hydrogen solubility in Nb films is influenced by strained regions[129]. Recent mapping has shown that buckled regions tend to absorb more hydrogen than in strained regions. This also affects the thermodynamic stability of the phase. Therefore, it is most likely that the secondary shoulder peak is due to buckled regions which may have also undergone plastic deformation. The peak sizes correspond well to the buckled coverage on the film surface.

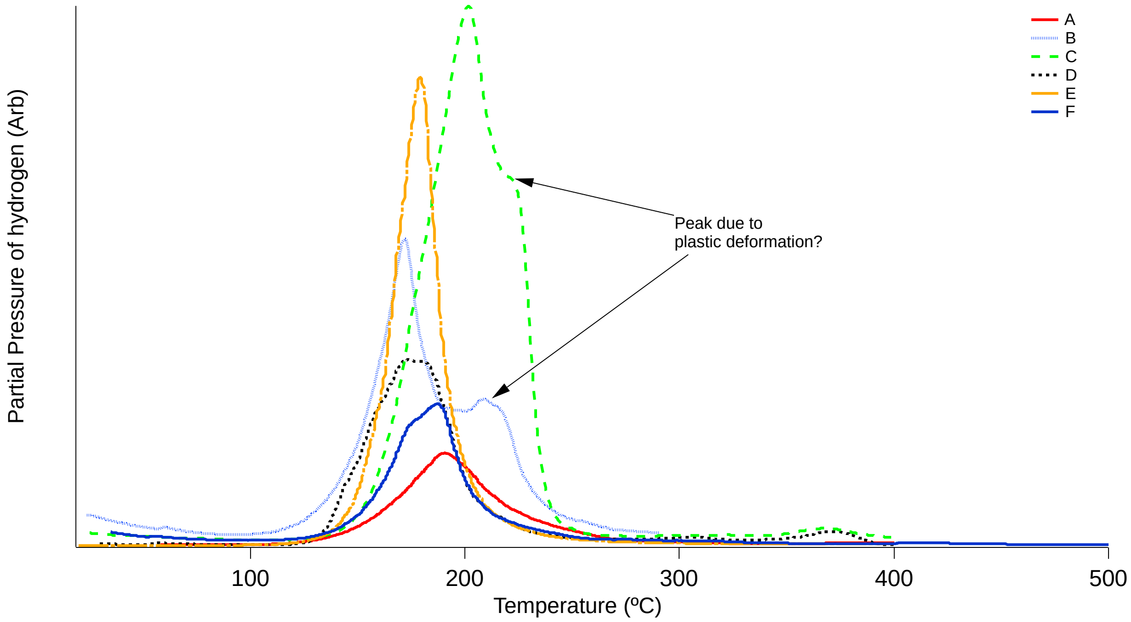

Fig 4.2.9. TPD spectrums for films A-F. A peak shift of up to 30°C is observed between the range of films investigated.

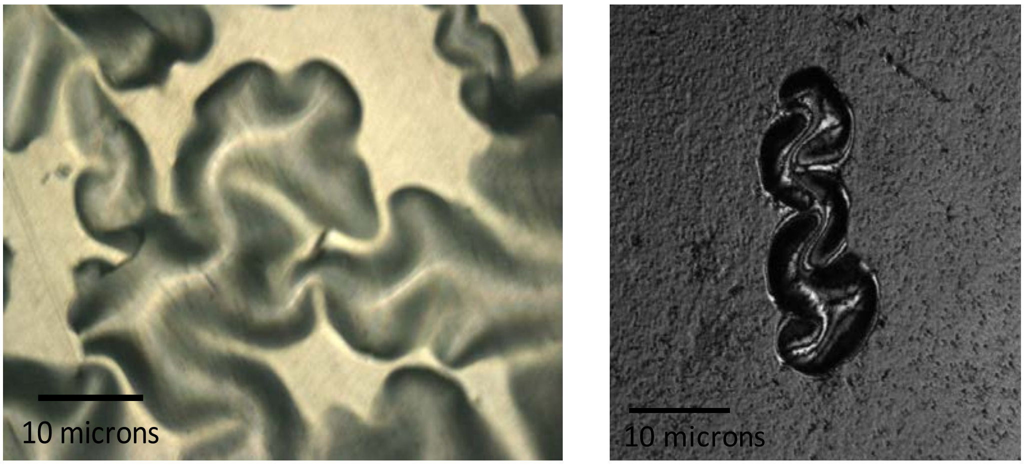

Film C – large buckles all over film

Film E – localised ‘telephone cord’ buckles

Fig 4.2.10. Confocal laser microscopy 3D images of sample C which underwent large amounts of buckling and/or plastic deformation. Some films show localised buckling with the ‘telephone cord’ appearance – film E

4.2.4 Discussion

The results presented in this chapter require a lot of interpretation. Firstly, it is clear that the deposition parameters influence a number of factors within the film deposition, including the microstructure (grain size, porosity, surface roughness) and intrinsic stress. All of these factors are dependent on one another. Essentially, they all change the energetics of the deposition process, with differing magnitudes. This is in agreement with the results presented in section 4.1.

The observed diffraction patterns are in excellent agreement with other literature on Mg-based films, with an out of plane growth preferred. Unfortunately, there was not an opportunity to investigate in-plane diffraction patterns to produce a reciprocal space map, which would identify other orientations and quantify the preferred orientation. This would have been especially useful when considering the hydrogenation characteristics, as analysis of the resultant hydride phase peak was not correlated to the observed hydrogen content of the film as seen in TPD experiments. This observation is also consistent with Fujii et al [63] who showed a different hydrogen content in comparison to the peak intensity of the MgH_2 (110) peak.

Comparing the stress analysis from diffraction data to the known hydrogen content within the film shows an interesting behaviour. Films with a lower hydrogen concentration tend to grow with a stressed MgH_2 layer, in comparison to those with a higher hydrogen concentration. The mechanism for this difference in behaviour can be explained by considering the mechanical behaviour of the film along with its microstructure.

Firstly, the observed porosity acts a stress sink for any required volume expansion. Therefore, instead of a strain increase due to hydrogen loading, as would be expected, the expansion is strain-free. After the porosity within the films is filled, the behaviour will then enter an elastic regime. This will occur until a plastic regime is energetically more favourable.

Of course, the transition to this regime is dependent upon the mechanical properties of the film. Ignoring factors such as adhesion, and purely focussing on the original diffraction patterns, we know that the diffraction intensity is dependent on the amount of grains aligned perpendicular to the substrate. Therefore, we can start to make some assumptions regarding the mechanical properties of the films. Given that there is a biaxial tensile stress being exerted on the Mg, it can start to slip along one of the 3 slip systems shown in 4.2.11. However, the energy required to activate a slip plane is dependent on the grain orientation with respect to the applied stress, according to Schmidt's Law:

$$\tau_c = \sigma_y \cos\varphi \cos\lambda$$

where τ_c is the critical resolved shear stress and σ_y is yield stress given the angle to the normal of the slip plane φ and slip direction λ. Therefore, if we have slight misorientation of grains compared to the substrate, the mechanical behaviour varies accordingly[130]. Using these mechanisms, the regime presented in Fig 4.2.12 shows why the thermodynamic properties of the films differ with respect to one another.

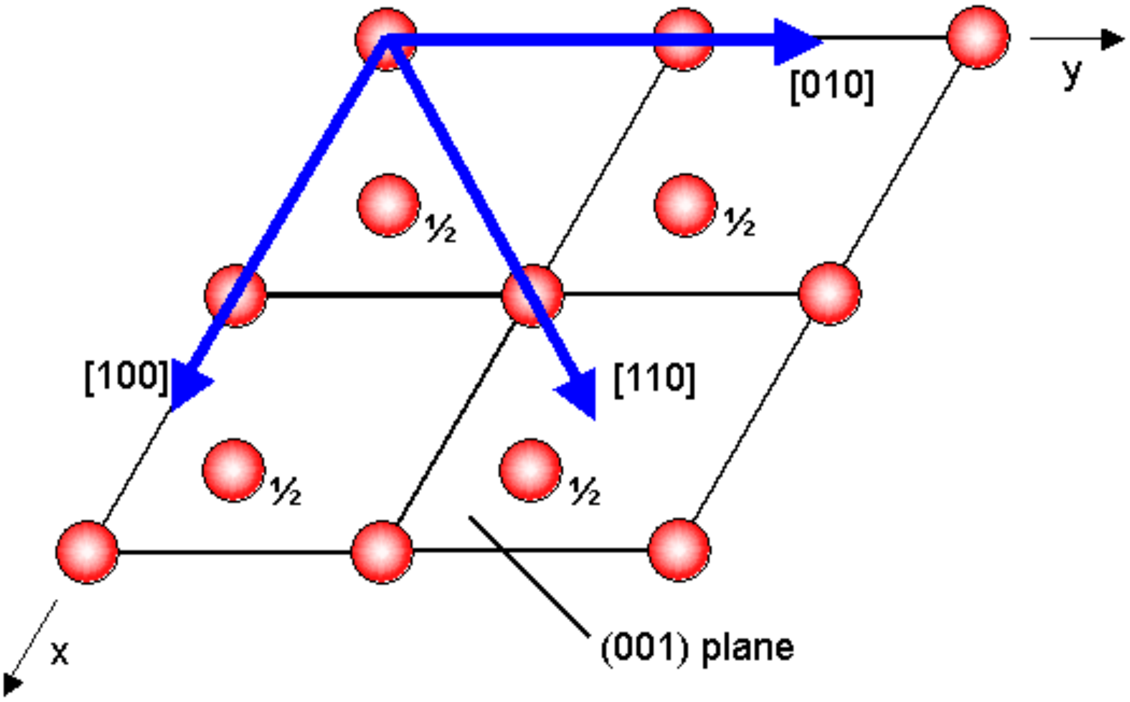

Fig 4.2.11. Slip planes in the (001) plane of HCP metals.

Moving on to microscopy of hydrided films, we see a stress release mechanism in the shape of buckling observed in the films that become most heavily hydrided. This is in common agreement with the failure modes observed by other authors[86,129]. The failure occurs when the adhesive force between the film and substrate is overcome. This suggests that the hydride layer does not grow as uniformly as one may expect, but rather it may prefer to diffuse along grain boundaries towards the substrate before diffusing through the grain itself. This would stand to reason as grain boundary diffusion is a lot faster. In addition, recent research has shown that the initial film microstructure, in particular, porosities, act to favourably enhance the kinetics of the phase transition owing to extended Mg/H_2 interfaces[131].

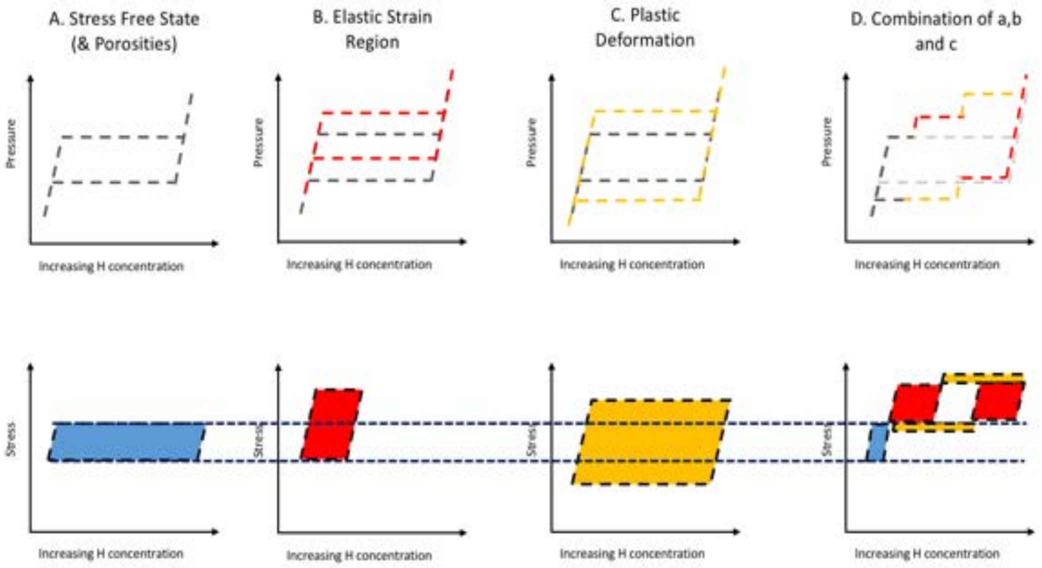

Fig 4.2.12. Proposed mechanisms for the thermodynamic behaviour of thin Mg films. Initially, voids within the film are used to accommodate volume expansion of the hydride phase. This then progresses to an elastic regime where Mg absorbs energy before moving into plastic deformation at higher strains, to accommodate further hydride phase transformation. For films with different void content as well as mechanical properties, the stress change will be different.

The desorption mechanism may not exactly replicate the absorption mechanism. It is known that the stability of the hydride phase is influenced by the both the elastic and plastic regimes of film behaviour. For the desorption behaviour, we must consider energy available for nucleation of the Mg phase. Firstly, a strained unreacted Mg layer will provide additional energy for phase nucleation. In addition, the strain energy stored within the hydride phase will also act to destabilise the hydride phase (see chapter 2). The differences in stored strain energy provide an additional thermodynamic driving force for the phase transformation[97]. As plastic deformation essentially stores a lot more strain energy, the contribution to the thermodynamics is much larger than in the elastic regime. The observed difference in thermodynamic stability is thus due to the strain energy stored within the film, which will vary with void content, mechanical properties and hydrogen uptake. Therefore, we can suggest that the desorption behaviour depends upon the initial characteristics of the originally deposited film.

However, we must also consider the vast difference in hydrogen storage capacity observed. One explanation is that the change in hydrogen flux is proportional to the thermodynamic driving force signified by Gibb's free energy. As shown by Moiij, the change in driving force depends on the strain energy associated with the formation of two phases [97]. The kinetics of hydride formation can thus be influenced if either the hydrogen pressure is changed during hydrogen loading, or if the strain energy is different for each individual film. This phenomenon is known with MgH_2 with the nucleation and growth behaviour of the hydride being different depending on loading pressure [36]. In our case, the nucleation and growth of the hydride phase is dependent on initial strain within the film. Thus, we conclude that the effect of intrinsic strain directly contributes to the kinetic properties observed in these films. A similar theoretical study has shown similar results, with strain energy reducing the activation energy for atomic diffusion [96]. Both Moiij [97]and Zhang [96] refer to transition state theory in their analysis of strain effects.

An element not discussed so far is the behaviour of the Pd top layer. A stress in this layer could also influence the rate of hydrogen uptake by the film. However, it has been shown that for film thicknesses above 60 nm, the rate limiting step is the diffusion of hydrogen through Mg, and not Pd.[132,133]

4.2.5 Conclusions

In line with observations in section 4.1, the effects of altering sputtering deposition parameters have been shown to affect the intrinsic stress of the deposited films. The mechanisms for the intrinsic in plane tensile stress accumulation are shown to be porosity inclusions. The effect of intrinsic microstructural and mechanical film properties have been shown to alter the thermodynamic properties of the films due to the strain energy

performed on hydrogen absorption and desorption. Evidence of this is shown with the shift in TPD peak position of up to 30 °C. Using the stress analysis of the MgH_2 layer formed, a difference in stress of up to 44 MPa is observed. According to Zhang, and using the bulk modulus of Mg as an estimate for the hydride strain (giving around 0.1 %), this should give a destabilisation of around 15 °C [96]. If we factor the increased modulus of the MgH_2 layer and the realisation that some plastic deformation effects may be present, the experimental data is in very good agreement with the simulation.

In addition, the kinetics of hydrogen absorption are discussed, where it can be speculated that the intrinsic strain with the film acts to alter the activation energy barrier for hydrogen diffusion, in line with transition state theory. However, there may be other mechanisms which can change the absorption kinetics, as porosity may change the sites available for phase nucleation or diffusion along grain boundaries. It is not possible to say which mechanism is most dominant in this case, but a study using in situ techniques whereby the location and surrounding chemistry of the phase change could be used to further this understanding, for example Positron annihilation spectroscopy or energy loss spectroscopy within electron microscopes.

4.3 THICKNESS EFFECT IN THIN FILMS

4.3.1 Introduction

In the previous section, the effect of sputtering conditions was shown to influence both the intrinsic stress and resulting film microstructure. These resulting features showed a contribution to the thermodynamic properties of these films and the mechanism for their effects was hypothesised to be due to their mechanical properties. In addition, the hydrogen storage properties of the films were discussed, as the films did not all absorb the same quantity of hydrogen given the same reaction conditions. This gives rise to some questions regarding the absorption mechanism of the films, namely:

- Is the absorption mechanism affected by (intrinsic) stress?
- What is the minimum film thickness required to completely hydride a film in the given conditions?

4.3.2 Films deposited using oblique angle deposition

4.3.2.1 Experimental

By using oblique angle deposition at 155° to the substrate parallel we are able to form a wedge shaped structure as the deposition rate varies with distance to the substrate, due to additional collisions with Ar+ ions. The magnesium is deposited onto a glass substrate at room temperature. Current was 1 A and the time period was varied for the three different samples, from a) 12 5 to b) 60 to c) 30 seconds deposition to give 3 wedges of different thicknesses. After this deposition, the films were coated with a Ti and then a Pd layer using a substrate rotation speed of 10 rpm. The Ti and Pd layer had been previously characterised to give a total thickness of 20-25 nm in thickness, which could be used to calculate Mg thickness from profilometry. The thickness profiles were measured using a stylus profilometer at measured points along the wedge after the removal of a kapton tape mask. This was used to calculate the gradient and total thickness of the films at various points.

The wedge structure was cut into seven sections of 1cm x 1cm and examined using GIXRD with a 10° incidence angle in a 2θ range from 20-60°. After this, the hydrogenation characteristics of the films were examined using variable temperature XRD at 1 bar H_2 up to a maximum temperature of 100 °C.

4.3.2.2 Results

Profilometry

Profilometry revealed that the wedged deposition was successful with a gradient being produced. There were three thicknesses of films used, which match the predictions made from the deposition rate and initial deposition trials. The results presented in this section are for a wedge that measures from 100 nm to around 30 nm in Mg thickness over a 7 cm long glass substrate.

As deposited films

The XRD of the as deposited films are displayed in Fig 4.3.1. It is clear that Mg has grown with basal plane texture with a peak at 34.68°. This value is 0.3° higher than would be expected than in bulk Mg. In addition to this, the peak at 40.29° can be attributed to the Pd peak. Although there is a significantly lower amount of Pd on the sample, the electron density of the Pd is much higher, increasing the structure factor. This peak is also in a similar position to the Ti peak, but their deconvolution would be highly speculative. The small peak at around 29° could possibly be associated to Mg_6Pd, but this cannot be confirmed as there is only one X-ray peak present. It could also potentially be a small amount of Mg/Ti alloy. Normally these elements are immiscible, but have been alloyed using thin film techniques. The amorphous hump centred at around 25° is due to the glass substrate.

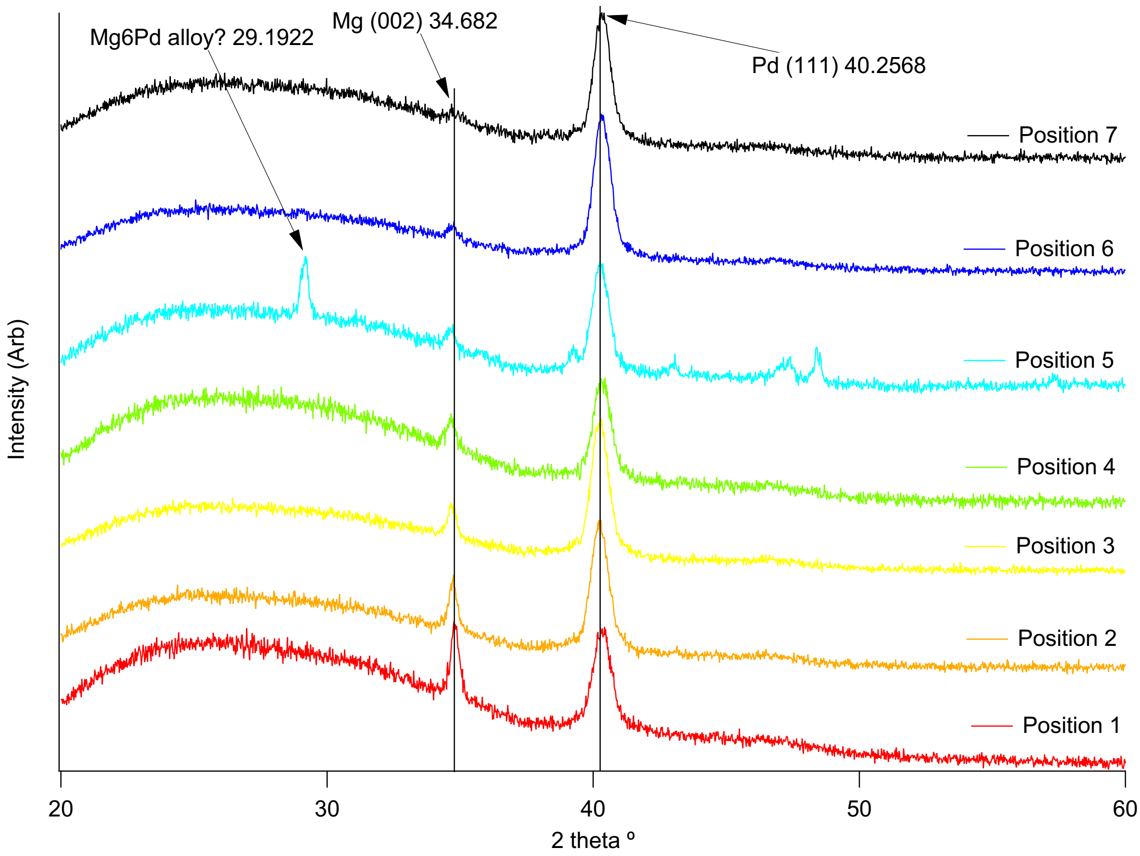

Fig 4.3.1. XRD patterns of as deposited Mg films. The bottom (red) line represents the thickest film section (predicted to be around 100 nm Mg). Moving up the traces, the film gets thinner and this is confirmed by smaller Mg peak heights. The smallest film section corresponds to around 40 nm of Mg which appears X-ray amorphous.

In situ characterisation

The same sections of film were placed inside an environmental cell (Anton Paar XRK 900) and exposed to 1 bar H_2 at room temperature. There is virtually instant formation of palladium hydride ($PdH_{0.64}$) which is seen at around 38.8°. However, the expected peaks for Mg and MgH_2 are virtually indistinguishable. This is potentially due to the slightly weaker signal due to configuration changes within the XRD apparatus but could also be an indication that the Mg has transformed to MgH_2 with a grain size that is X-ray amorphous. It is therefore not clear if complete hydrogenation at room temperature has occurred or not. Film section 1 was originally tried, as it has the thicker layer of Mg which would be more easily seen on the XRD pattern. The peak for Mg had disappeared in this case. In addition, a small hump is observed around the MgH_2 expected position. However, the signal to noise ratio meant it was not possible to either predict a peak position or even say with any confidence a peak was definitely observed. Therefore, it was decided there was no point in heating to higher temperatures to look for further hydrogenation. Section 5 was also checked to investigate the unexplained peak (29.192° 2θ) thought to be Mg_6Pd. This trace shows a very small hump around the Mg peak, suggesting that there is some residual Mg left, despite being a thinner section. This is believed to be due to the influence of the blocking layer of Mg_6Pd. As a result of this initial investigation, it was not possible to identify the formation temperatures of MgH_2 with these film thicknesses using this in situ XRD set-up.

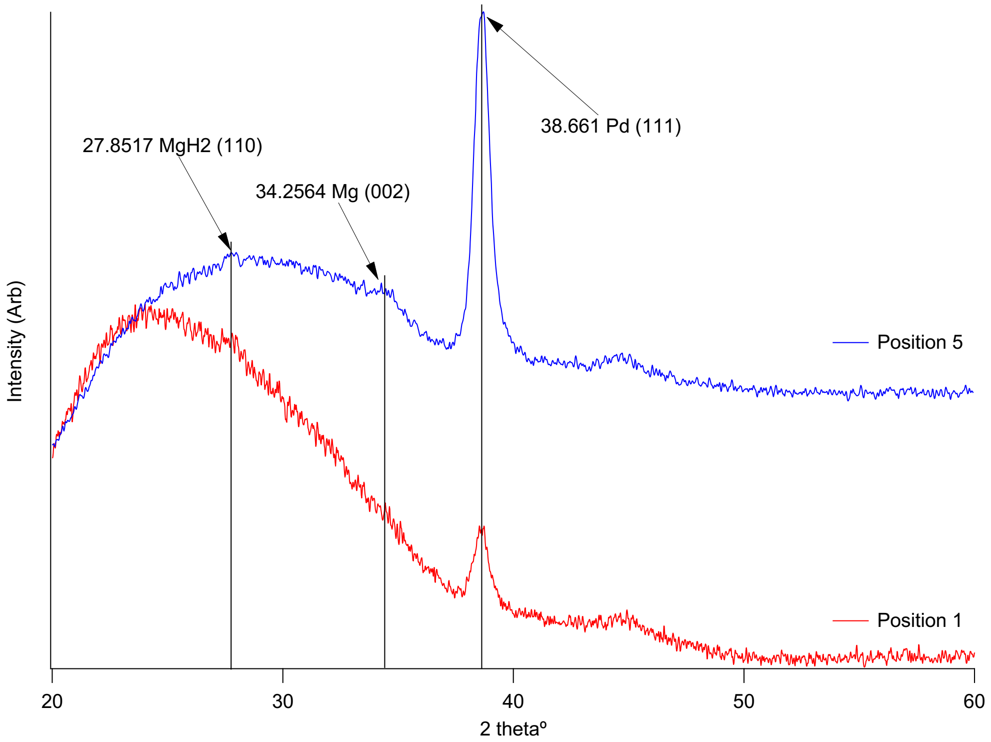

Fig 4.3.2. XRD traces of two film sections at different thicknesses after hydrogenation at 1 bar H_2 for 24 hours at 100 ℃.

A strain analysis of the films is presented in Fig 4.3.3. This shows that films initially deposit with a fairly high intrinsic stress which reduces at around 50 nm before again increasing. This is an insight into the growth mechanism of the Mg layer at the initial stages.

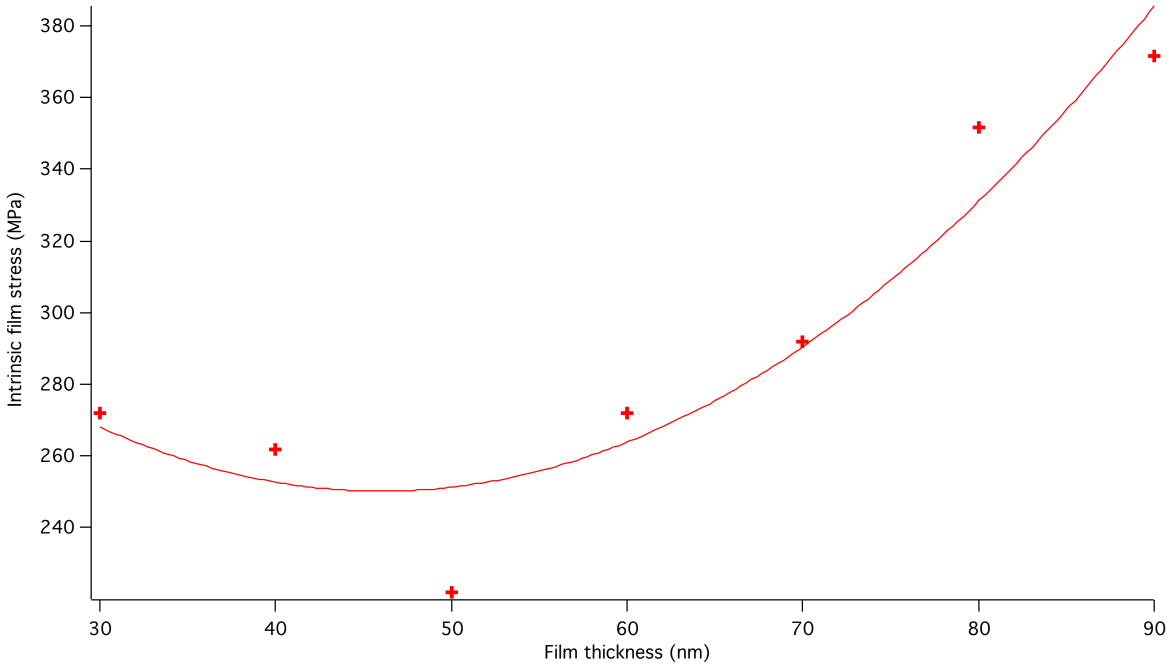

Fig 4.3.3 Film stress as a function of film thickness. A transition is observed at around 50 nm.

4.3.3 Films with different thicknesses

4.3.3.1 Experimental

Films were deposited with a variety of Magnesium layer thicknesses (20, 50, 100, 200, 400, 800 nm). The sputtering conditions (Bias Voltage - 50 V, Magnetron Current – 2 A, argon pressure – 4.2x10^{-3} mbar) were selected, as this was the condition that gave the highest intrinsic tensile stress in the previous sections.

4.3.3.2 Results

As deposited films

XRD patterns of the films are shown in Fig 4.3.4. The peak intensities of Mg do not correspond to the film thickness in a linear relationship as may be expected and according to other observations[134]. If we ignore the 100 nm film for the moment, there seems to be no significant chance in the peak intensity between the 50, 200 and 400 nm films, however there is a vast increase when looking at the 800 nm film. The 100 nm film trace is anomalous in that is has higher intensities than the surrounding films. The reasons for this are unclear.

A suggestion for the observed difference would be that there is a competition in film growth mechanisms, which manifest at different stages. Firstly, the film may nucleate and start to grow with very small grain sizes, up to around 50 nm. After this, the adatoms may have enough kinetic energy to start recrystallization within the film, which is observed at 100 nm in the form of a higher intensity X-ray peak. With further film growth, there may be a transition where the adatoms do not have enough energy to interact with the entire depth of the film and there is a region of more amorphous growth, or there could be other grain orientations within the film that XRD cannot detect. Finally, with a much higher thickness to 800 nm, there is again an increase in crystallinity. This may arise due to a temperature increase in the chamber and an annealing mechanism may play a part. This is fairly speculative and would certainly require further investigation. In addition to this, the Pd overlayers also vary in their crystallinity. This is probably due to the influence of the underlying Mg layer.

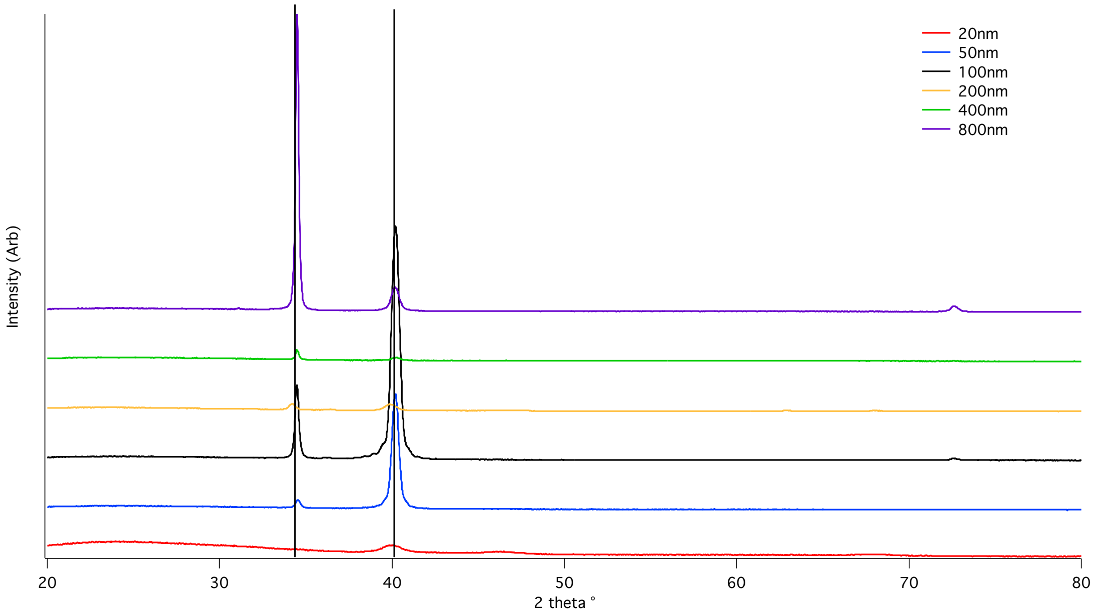

Fig 4.3.4. XRD patterns of films with different Mg layer thicknesses as deposited on glass substrates. The Mg peak at around 34.4° shifts from bulk depending on film thickness. Mg peak intensity does not correspond well to Mg thickness. The peak for 20 nm Mg is X-ray amorphous (with the XRD system used).

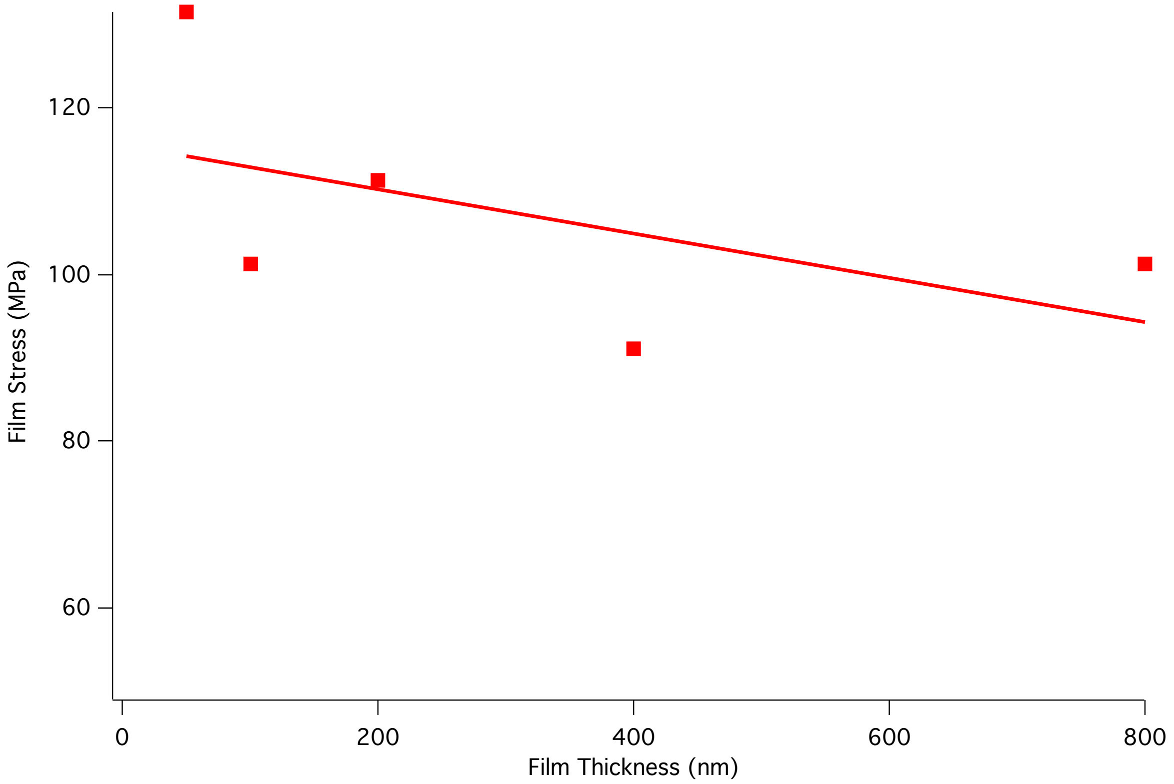

Fig 4.3.5. As deposited film stress as a function of film thickness. A least squares regression analysis shows a weak linear relationship is observed between a growing film with increasing thickness.

Hydrogen Absorption Properties

After hydrogenation for 48 hours at 100 °C there is evidence of MgH_2 formation in the majority of films (Fig 4.3.5). Films below a thickness of 50 nm did not show a peak for MgH_2 but the Mg peak had disappeared entirely, suggesting a complete transformation. The 20 nm trace is omitted as it showed no peaks at all.

Fig 4.3.6 shows the measured stress within the hydride layer as a function of thickness. Firstly, we notice that some intrinsic tensile stress still remains in the thinner films up to 100 nm. This may suggest that the films have not properly hydrided, as the volume increase due to hydrogenation would induce a compressive stress. The reason for this is unclear. However, using a similar analogy (section 4.2) it may be the case that the hydride phase nucleates and along columnar grain boundaries. If this was to occur, then there may still be a residual tensile force acting on the film. This is more likely to occur in thinner films, as the distance to the substrate is smaller and so the grain growth may be predominantly more lateral than vertical. This is similar to the results by Palsson et al.[135]. This is rather thought provoking as it demonstrates that the film thickness combined with different microstructures can influence the hydrogen diffusion direction as well as the stress related behaviour. The bottom graph in Fig 4.3.6 shows how the stress state changes from the original Mg layer to the newly formed MgH_2 phase. We can see that there is a clear transition above 100 nm to higher stresses formed within the hydride phase. This is again likely to be a consequence of the hydrogenation behaviour as the hydrogen has a preferred path towards diffusion along grain boundaries, however, it must also start to diffuse across the grain, forming a more uniform diffusion front and changing the resultant stress. This is shown in more detail in Fig 4.3.7.

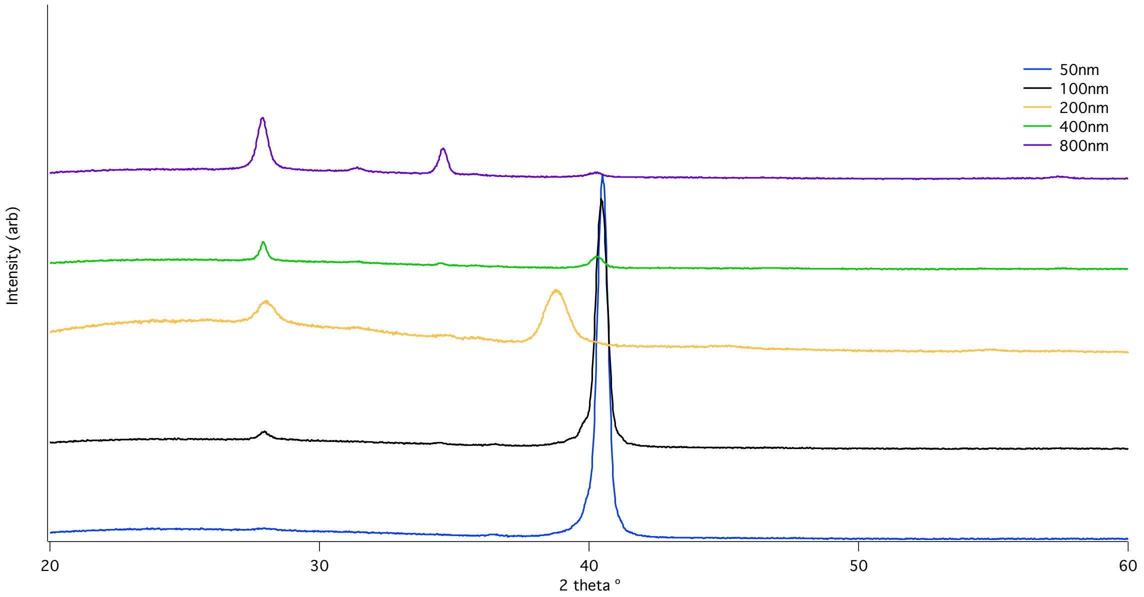

Fig 4.3.5. XRD patterns of films after hydrogenation for 48 hours at 100 ℃ 1 bar H_2*.* MgH_2 *peaks are visible at around 28°. There are very small residual Mg peaks observed for 200 and 400 nm films. No Mg peak is observable for film thicknesses below this. The 800 nm film still shows residual Mg.*

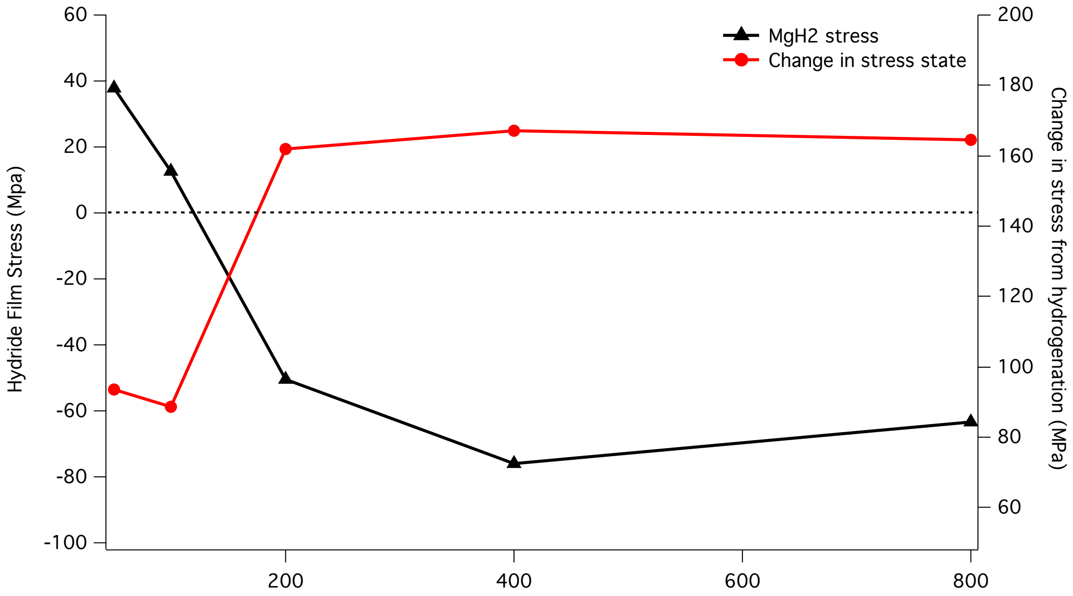

Fig 4.3.6. Hydride stress as a function of thickness and change in stress of original Mg layer to the new hydride phase formed.

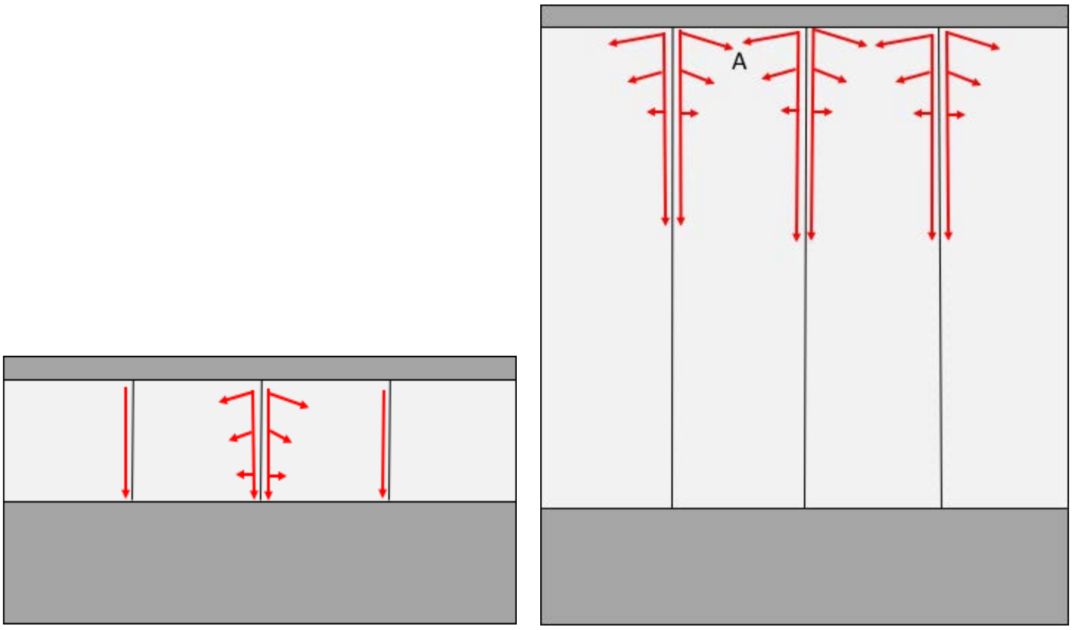

Fig 4.3.7. Potential explanation for the different mechanisms of hydrogen diffusion in thinner versus thicker films. For thinner films where the thickness approaches the column width, there could be more lateral growth of the hydride meaning a series model of stress may be applied and tensile residual stresses remain. For thicker films, the horizontal growth direction at point A means hydride grains impinge and start to form compressive strains, more like a parallel model of growth.

Hydrogen Desorption Properties

The TPD traces for these films are shown in Fig 4.3.8. There was no detectable trace for the 50 nm or 100 nm samples. It is likely that some exposure to air may have catalysed the reaction and desorption may have occurred at room temperature in transition to the apparatus[136]. Comparing the wt% for each film, we can see that the 200 nm film desorbs the most hydrogen (5.7 wt%), the 400 nm film desorbs hardly any hydrogen (0.6 wt%) and the 800 nm film desorbs 2.9 wt%. The reasons for the lack of desorption observed for the 400 nm sample are not understood, as all of the absorption analysis points to a similar amount. Potentially, a Mg-Pd alloy has formed at the interface which is known to be detrimental to the sorption behaviour.

There seems to be a destabilisation of the 200 and 400 nm films in comparison to the 800 nm film. The explanation for this behaviour cannot simply be in the stress analysis as XRD shows that the films have roughly similar stresses acting on them. We note the presence of the shoulder on the 800 nm film and this is attributed to localised buckling

However, we have already hypothesised that there is a difference in the nucleation and growth behaviour of the hydride phase between thin and thick films. Therefore, it would not be unreasonable to assume that during hydrogen unloading, the Mg phase starts to nucleate and grow differently. For both films, it is likely that the nucleation or growth of a new/existing Mg phase will start at a local defect such as a grain boundary. If we suppose that the mechanism proposed in Fig 4.3.7 is true, then for thinner films, there is a lot more opportunity for nucleation at grain boundaries, as this is where the hydride phase is concentrated. This will have two effects, which include a potentially faster desorption as well as local shrinkage. The local shrinkage exerts a residual tensile strain on the remainder of the MgH_2 phase, which will drive destabilisation. However, for a thicker film, the opposite may be considered. The opportunity for phase nucleation at grain boundaries will be similar, as the column width is not greatly affected by deposition conditions. However, as there is a more uniform hydride layer, then the local shrinkage will be absorbed into the remainder of the underlying film, potentially not affecting the remaining hydride layer.

A similar report in the differences of hydrogen behaviour in very thin films is shown by Mooij[97]. Although the films here are thicker, the importance in nucleation and growth behaviour has been shown to alter thermodynamics of the phase transformation. In addition, it is noted that using TPD does not show the potential differences between the thermodynamic and kinetic effects observed.

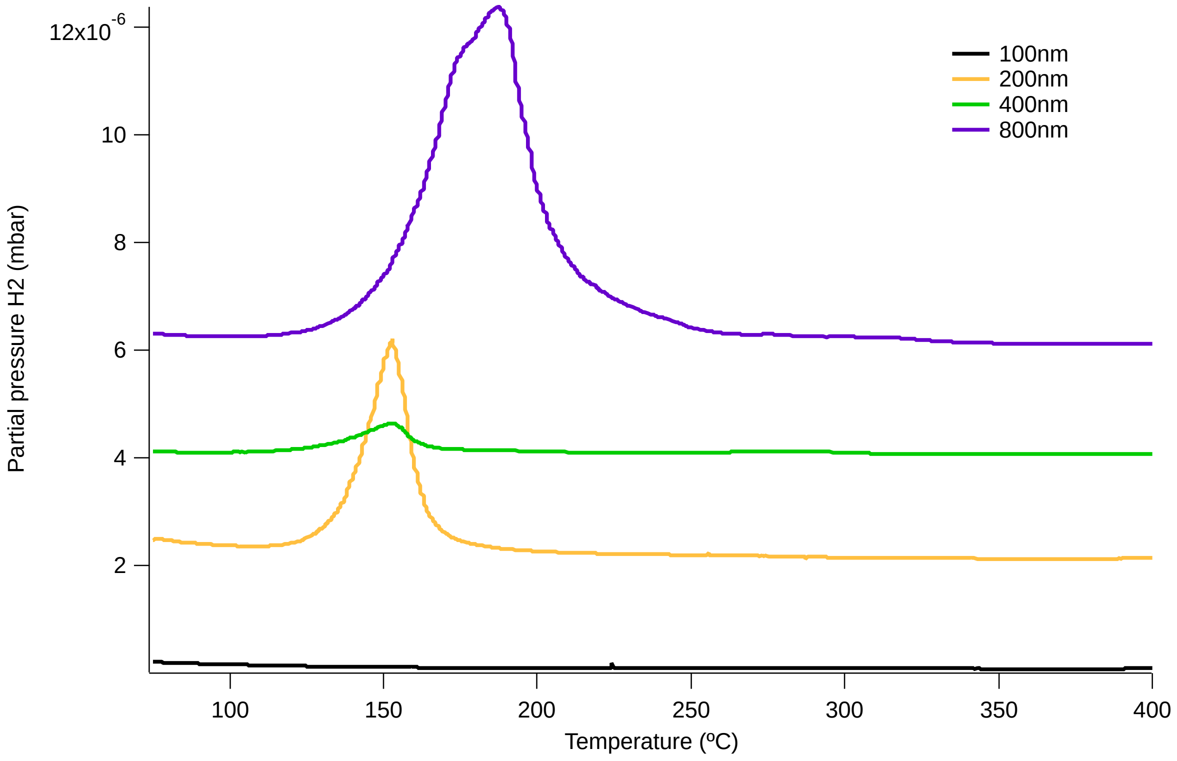

Fig 4.3.8. TPD spectra of films with different thicknesses after hydrogenation at 100 ℃ in 1 bar H_2 for 24 hours. Heating rate 5 ℃/min in vacuum. Films of lower than 100 nm did not show any hydrogen desorption and their traces are omitted.

4.3.4 Discussion and conclusions

The initial concept of this set of experiments was to determine the minimum film thickness required to achieve complete hydrogenation in a given set of hydrogenation conditions (100 °C, 1 bar H_2). Wedged films were successfully deposited using oblique angle deposition within the CFUBMSIP system, which has not been reported before to the best of the authors knowledge. However, using XRD as a methodology to determine strain in ever thinner layers showed to be impractical as the signal to noise ratio became greater and interpretative errors of peak position could have led to erroneous results.

Using thicker films proved to be more successful with the experimental approach as a much clearer signal could be observed. The deposition characteristics showed that a tensile film stress is developed over the range of thicknesses examined, with a small decrease in stress (40 MPa) with an increase in thickness from 50 to 800 nm. It is likely that this relaxation mechanism is due to atomic peening or some thermal annealing with additional growth.

After hydrogenation, the films all showed some hydrogen uptake. Films of 100 nm or less showed a complete phase transformation according to the diffraction data. Residual MgH_2 peaks were observed above this thickness with varying intensity. The resulting TPD traces showed uptakes of up to 5.7 wt% for the 200 nm film. Although it would be expected that the thinner films show higher uptake, there was no recordable trace, suggesting that desorption had already occurred.

The XRD analysis of strain within the hydride layer showed that there was some residual tensile stress remaining within the thinner films. It is proposed that due to the columnar microstructure of these films, the nucleation and growth behaviour of the hydride layer is different between thinner and thicker films. Diffusion of hydrogen along grain boundaries is much faster than through grains, suggesting that thinner films can remain in a state of tensile stress, rather than thicker films which may prefer to grow and form a more compressive state. Due to this behaviour, we may also expect that the kinetics of the phase transformation alter.

In addition to this, a significant destabilisation of the hydride layer in the thinner film is observed according to the TPD traces. This is not in accordance to the stress analysis which shows that both the films are in a similar state of stress. It could be that the mechanism proposed for the differences in absorption behaviour (Fig 4.3.7) also influences the desorption behaviour. For example, residual strain in the Mg layer can act as a driving force for nucleation or strain energy release in the form of buckles (observed locally in the thicker film). However, it is also noted that the onset of hydrogen desorption is at a similar temperature. TPD is not ideally suited to differentiate between kinetic and thermodynamic effects and the thickness effect makes conclusions from this data inconclusive in this respect. Instead, generation of PCIs could be achieved with Sievert's type apparatus. This was attempted in earlier versions of this thesis, however the sorption quantity was too small to accurately detect. Alternatively, one could use electrochemical methods or optical methods.

4.4 EFFECT OF THE SUBSTRATE IN MG FILMS

The previous sections have demonstrated that a film with thickness of around 200 nm can be almost completely hydrided under reasonable conditions (1 bar H_2 100 °C) and remain attached to the substrate. However, thicker films loaded with the same hydrogen content have tended to buckle. This section has investigated the influence of using different substrates to see if this can further affect the hydrogen sorption properties of films.

4.4.1 Characterisation of as deposited films

Structural characterisation

XRD patterns for the as deposited films are shown in Fig 4.4.1. The films all deposit as highly textured with the Mg (002) basal plane as most preferred. This is similar to other films deposited using magnetron sputtering techniques [63,67,137,138]. The Pd cap layer is also highly textured in the close packed (111) plane with other small reflections present. The relative scattering factors of Mg and Pd are very different, explaining the similarity in peak height compared to the amounts of each material present.

The peak positions for the Mg (002) peaks are slightly different for each substrate and are slightly lower than the bulk value (Table 4.4.1). This could be explained due to intrinsic growth stresses. The film deposited onto a glass substrate should, as it is amorphous, provide no influence on the crystal structure as there is no ordered lattice to grow from, and only thin film growth stresses should be formed. In addition to the intrinsic processing stresses, the substrate may induce different morphological features into the films. Differences in surface energies of the substrates alter energy required for the nucleation and growth of grains from nucleation theory[139]. It is possible that there are slightly different degrees of orientation, with columnar grains that do not grow perfectly adjacent to one another, affecting the diffracted intensity.

There is no observable evidence of Mg-Pd alloying with any of the films. However, there may be a slight region of intermixing which is <10 nm, as reported by Baldi, but this is not detected by XRD[140]. The lack of intermixing may be a result of the low temperature during sputtering.

An additional set of films were deposited on similar substrates in order to see if there is a difference in stress with growth thickness. It would appear than for thicker films there is a general increase in stress which varies between substrates. In addition, the intensity of the peak for the film deposited on MgO is around 3 order of magnitude greater than the other films (Fig 4.2.2). This suggests some influence of crystallinity from the substrate.

Table 4.4.1. Intrinsic deposition stresses for films deposited onto a variety of substrates

Substrate	Thickness (nm)	In plane stress (MPa)	Thickness (nm)	In plane stress (MPa)
Glass	200	10	800	x
Si	200	40	800	80
MgO	200	15	800	80
Si (B-doped)	x	x	800	160

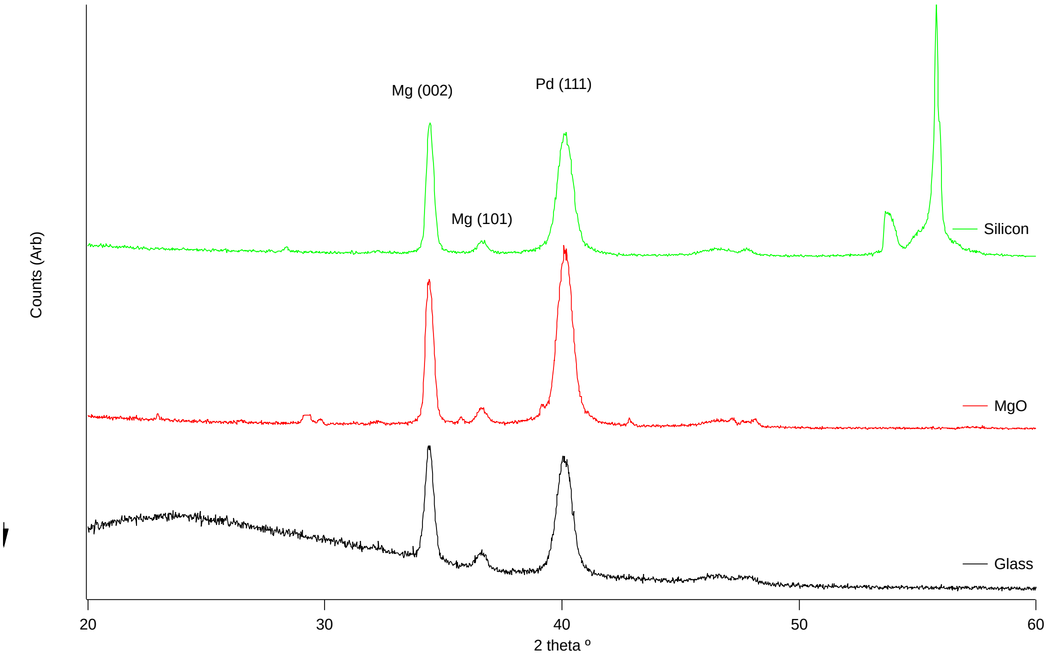

Fig 4.4.1. XRD patterns of 200 nm films as deposited on a variety of substrates. Small reflections in the film deposited on the MgO substrate are small regions of MgO that are not of the main substrate orientation.

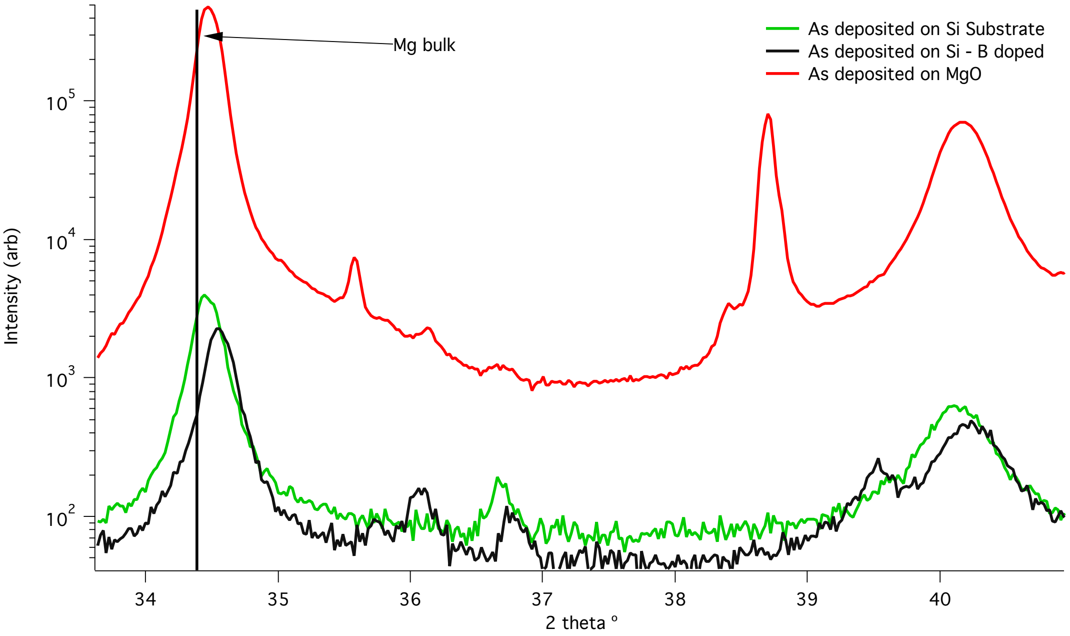

Fig 4.4.2. Local section of XRD pattern for 800 nm thick films as deposited on a variety of substrates clearly showing a peak shift. (Note the logarithmic scale)

Growth morphology

SEM micrographs of fracture surfaces of the as deposited films are shown in Fig 4.4.3.

Using SEM at this scale meant that observation of the grain structure was difficult. The film on the glass substrate seems to have a structure with columns that do not extend the whole thickness of the films such as those reported in other studies[64,66]. The film on the silicon substrate appears to nucleate with a fine grain structure at the interface, which then appears to coalesce further into film growth, with coarser grains towards the surface. This mechanism is likely to explain the higher stress observed in this film[117]. The film on the MgO substrate appears to show fairly equiaxed grains that are similar to the film on glass. Possible reasons for this are the difference in surface energy of the substrate, which influences the film growth mode. Silicon has the highest surface energy of these materials[141], which will increase the free energy for nucleation at the interface.

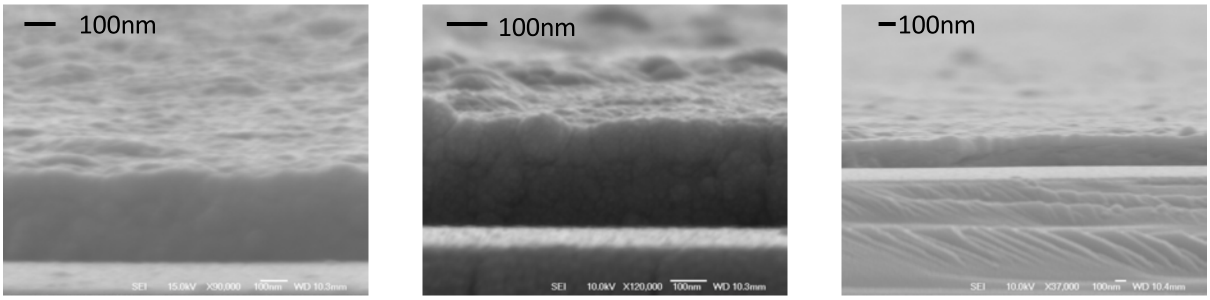

Fig 4.4.2. SEM micrographs of film cross sections. Left – Glass substrate. Middle – Silicon substrate. Right – MgO substrate.

4.4.2 Hydrogen absorption behaviour

An initial experiment at room temperature under 100 bar H_2 for 3 days was initially undertaken to see if the films could absorb hydrogen at this temperature with what could be considered an almost infinite pressure and time for the reaction to proceed. The results of this investigation showed that there was very limited uptake in these films, suggesting a diffusion-limited regime.

Therefore, in situ XRD was used to investigate the growth behaviour at increasing temperature intervals. Fig 4.4.3 shows the results of an in situ experiment where the temperature was ramped up 10 °C and a scan was then initiated. It is clear to see that at 30 °C there is some evidence of initial hydride formation. Each scan takes approximately 1 hour to complete and so scans were completed until the Mg phase was not observed. At 100 °C a complete phase transformation is observed. The peak shift of the $PdH_{0.64}$ layer at around 38.8° is due to the temperature increase during the experiment. Interestingly, the peaks do not tend to shift for Mg and MgH_2 as might be expected, showing that there must be some growth stresses in the layer, as would be expected.

In addition to this hydrogenation, the films (both thin and thick) were hydrided ex situ at 100 °C under 1 bar H_2 for 48 hours. Very similar results were observed. The resulting XRD patterns for the thicker films are shown in Fig 4.4.4 for different substrates. This clearly shows a difference in the growth stresses for the films. The smaller peaks in this Figure are assumed to be due to imperfections in the MgO single crystal substrate that still reflect with a relatively high intensity.

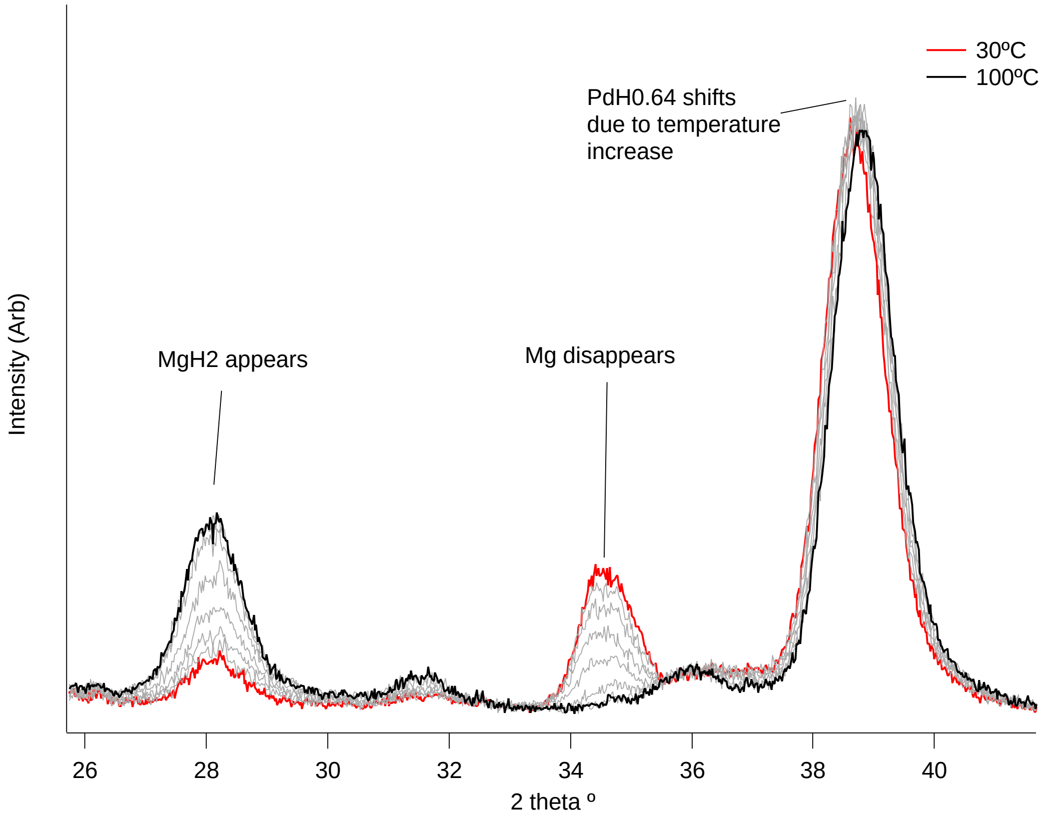

Fig 4.4.3. Example of an in situ XRD experiment with rising temperature in a constant H_2 atmosphere of 9 bar. After a temperature of 100 °C is reached, it appears that the phase transformation is complete with no further evidence of peak growth observed.

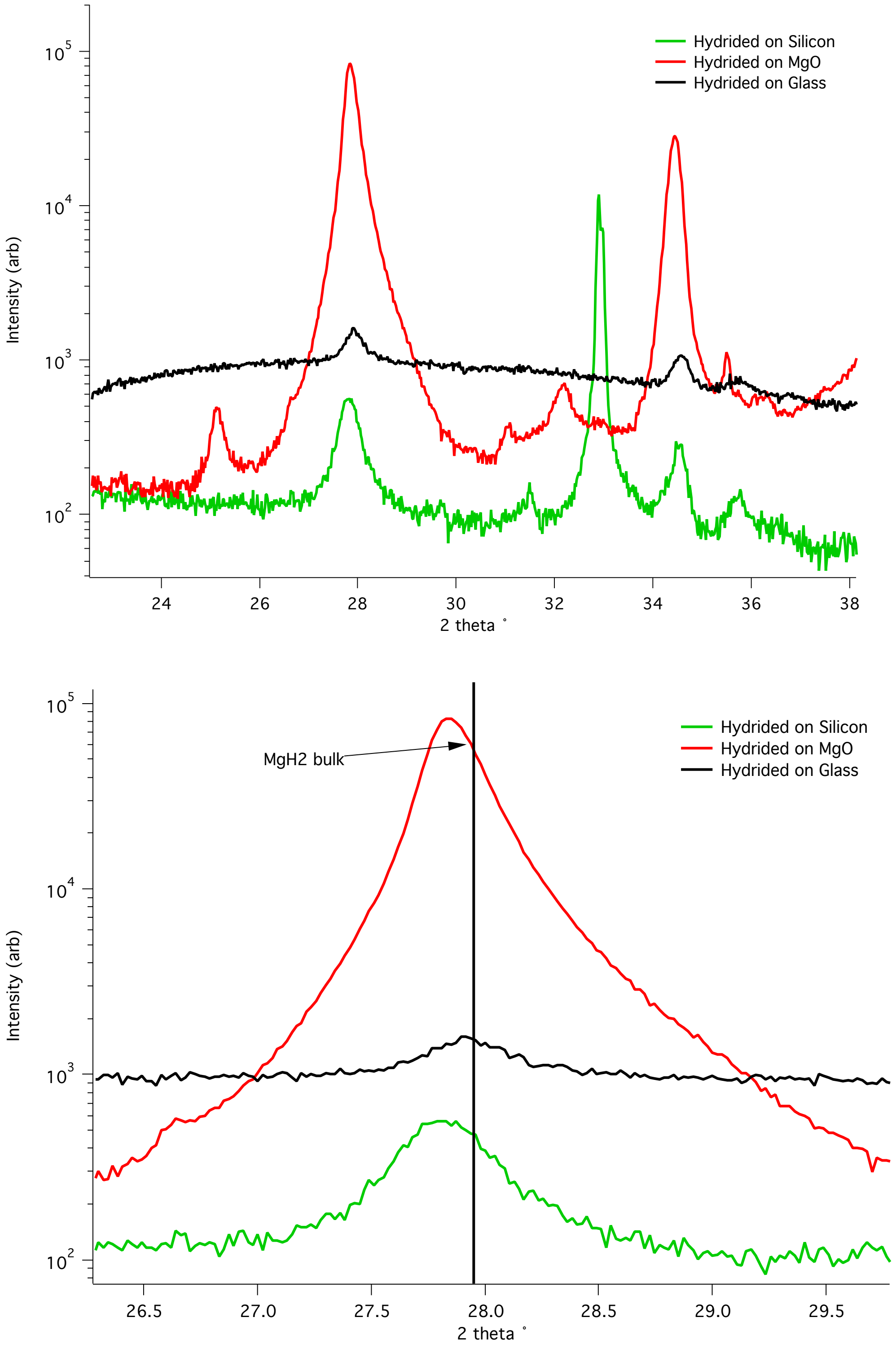

Fig 4.4.4. XRD patterns of thicker 800 nm films after hydrogen absorption at 1 bar H_2 at 100 °C for 48 hours. Note the logarthimic Y scale. (Bottom – zoomed image showing MgH_2 peak position detail).

4.4.3 Hydrogen desorption behaviour

The TPD profiles of the 200 nm films hydrogenated at 100 °C are shown in Fig 4.4.5. The highest temperature desorption is exhibited by the film on the MgO substrate, with a peak desorption temperature of 180 °C. The films prepared on glass and silicon films show very similar desorption profiles, with peak desorption temperatures at lower values of 151 °C and 148 °C, respectively. In addition, the TPD traces of the 800 nm films are shown in Fig 4.4.6. The pattern of the peaks is not the same as the thinner films, suggesting that there is a different mechanism(s) affecting the thermodynamics of the phase transition. This difference could be caused by different microstructures of the films, where thinner, high density films cause a higher in plane stress, in comparison to thicker films where evidence of porosity has been observed, leading to stress relief (See section 4.1 &2 4.2). The same observation has been made recently by Ham and colleagues[134]. This also explains why the thinner films would tend to desorb hydrogen at a lower temperature, as the elastic energy stored is greater, leading to a higher thermodynamic bias.

Confocal microscopy of the thicker films shows how the film on the MgO substrate remains smooth on the surface in comparison to the small, localised buckles observed on glass and total delamination observed in the silicon film. This leads us to believe that the MgO substrate would tend to induce a sorption behaviour dominated by plasticity, probably due to its higher modulus as well as apparently higher adhesion force. In addition, the small asymmetry of the peak may be explained by the presence of inhomogeneous regions in the film, which had not completely reacted with some of the residual Mg. In comparison, the glass substrate seems to be on the limits of adhesion, with the presence of small but noticeable buckles, suggesting that absorption is largely accommodated by plasticity, but there is some in-plane stress relief. Finally, for the film on silicon, there appears to be delamination of the film from the substrate in a lot of areas. Unlike the other films which exhibited two distinct peaks for the attached and delaminated sections, there appears to be a small release at around 110 °C followed by an asymmetric peak. This suggests that similar to the film on the MgO substrate, there are some inhomogeneous regions within the film that may affect the reaction order.

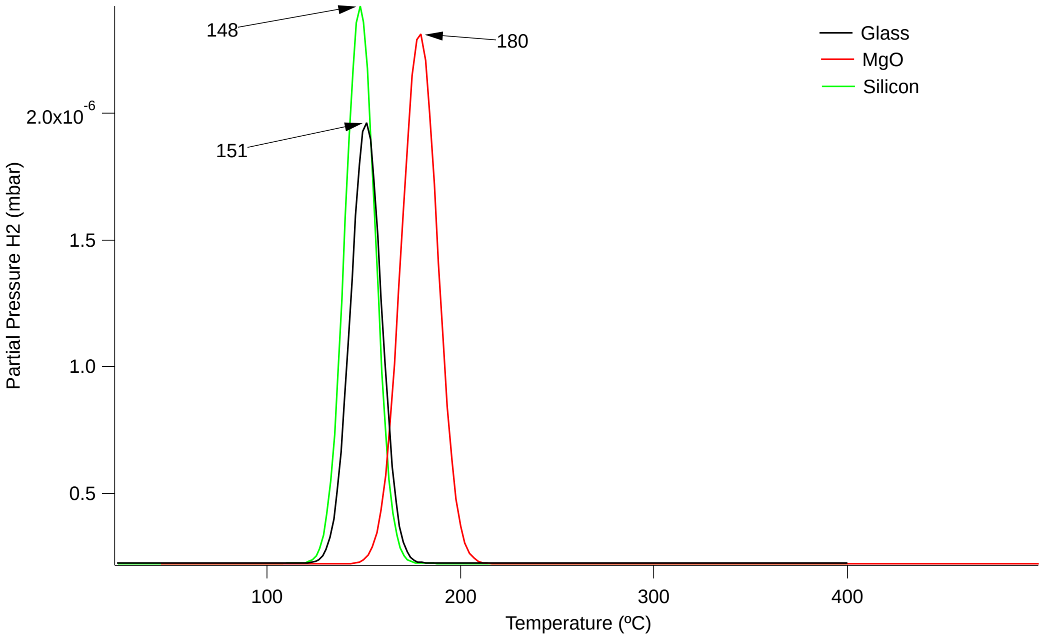

Fig 4.4.5. TPD plots of 200 nm films deposited on various substrates. A clear difference is observed between the MgO substrate and the other two silicon-based substrates.

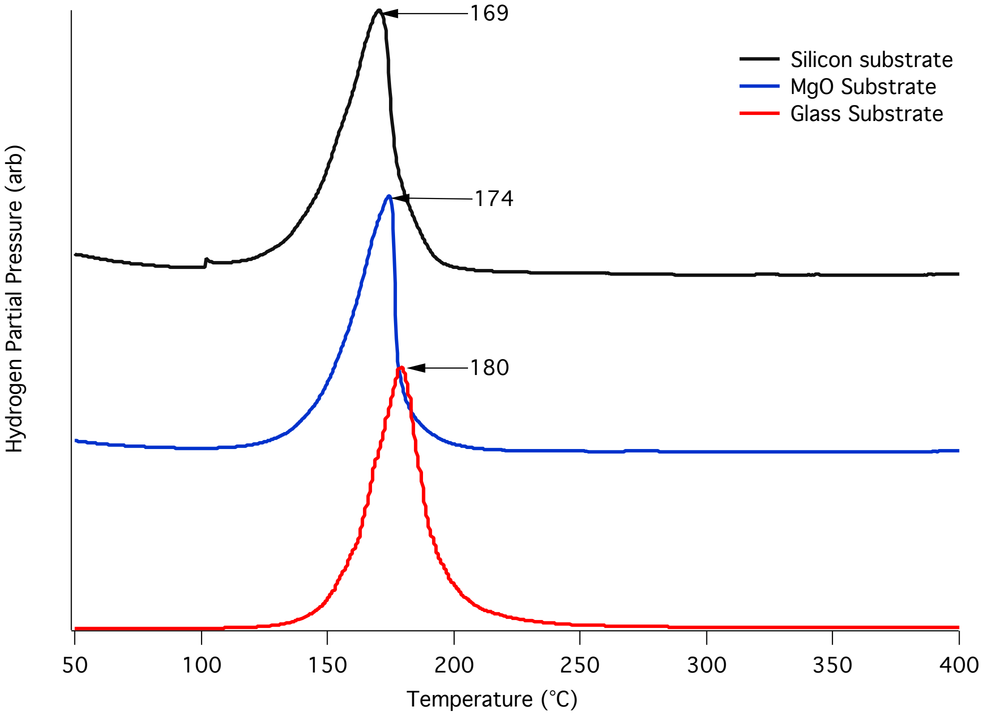

Fig 4.4.6. TPD profiles of 800nm thick films after hydrogen absorption. A small difference is noticed between the films. Film on MgO substrate absorbed 5.2 wt%, Silicon 7.2 wt% and Glass 5.75 wt%.

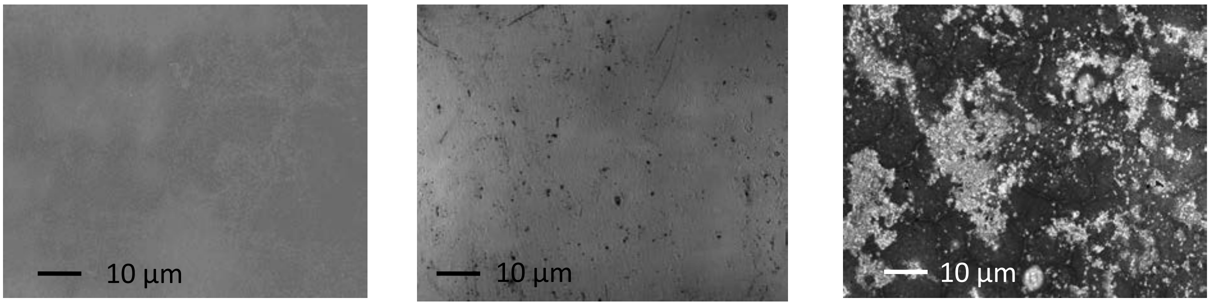

Fig 4.4.7. Sample surfaces after hydrogenation of 800 nm films obtained using confocal microscopy. Left – film on MgO substrate. Middle – glass substrate. Right – Silicon substrate.

4.4.4 Discussion

All of the thinner films exhibit a good level of adhesion to the substrate when examined using confocal laser microscopy. This suggests a material pile-up occurs and out of plane expansion of the parent phase is energetically more preferable. Therefore, a plastic deformation mechanism must be preferred in these thinner films. For each substrate, the thermal stresses have been evaluated using the formula in equation (1) where, σ_f is the in plane film stress, α_s and α_f are the linear co-efficients of thermal expansion, E_f and v_f are the Youngs modulus and Poisson ratio of the film, and ΔT is the change in temperature.

$$\sigma_f(T) = (\alpha_s - \alpha_f)\Delta T E_f/(1 - v_f) \qquad (1)$$

The results are tabulated in Table 4.4.1 using the linear thermal expansion coefficients of Mg (2.5×10^{-5} K^{-1}). This reveals that for the given onset temperature, the predicted compressive stresses are very similar. The difference in the stress values can be explained due to the simplicity of the equation, some degree of experimental error, assumptions that the substrate expands isotropically, there is zero plastic deformation, there is no large effect of the Pd cap layer at this thickness, as well as no variation in the microstructure/in plane crystal orientations.

Table 4.4.1. Thermal expansion coefficients of substrates along with the predicted stress in the MgH_2 layer at the peak desorption temperature for 200 nm films.

Substrate	Thermal Expansion Coefficient (μm/K)	Predicted stress at onset temperature (MPa)
Silicon	3	-107
Borosilicate glass	3	-109
MgO	8	-111

The approximate strain value for the transition of Mg to MgH_2 can be calculated using previosuly proposed models for the atomic movements in the martensitic like transition from Mg[0001] to MgH_2[110].

Substrate clamping effects have been reported in Pd films where thermodynamic properties were initially altered due to adhesive forces. However, these films did eventually become comparable to bulk data due to buckling mechanisms which act to release stress[83]. The addition of a Ti buffer layer improved adhesion in these films, and the buckle formation was inhibited even upon cycling, with compressive stresses estimated at around 1.5 GPa[84]. In contrast to this, the behaviour of thin films of the complex hydride Mg_2NiH_4 showed a vastly different behaviour in both absorption and desorption behaviour, attributed to the phase transition between two preferentially oriented phases[90]. This clearly highlights the importance of stress build-up and texture on the sorption behaviour of materials.

On hydrogenation, the volume change associated with the crystal structure transformation from hexagonal Mg to tetragonal MgH_2 is around 32 %. The OR of Mg(002)|MgH_2(110) in thin films has been reported previously[91,93]. This martensitic like transformation means that the phase would ideally like to form with a Z-axis expansion of around 24 % but an expansion in the x-y plane of 6-7 %. The out of plane Z-axis expansion should essentially be stress-free in thin films (although mechanical work is required to deform the film), however, the x-y plane expansion is restricted due to substrate clamping, potentially distorting the c axis lattice parameter, forcing a more distorted MgH_2 phase to form, which has been suggested by other authors previously[66]. For this reason, the tetragonal lattice is distorted in thin films and a larger out of plane expansion is observed, where the z-axis expands around 30 % (See Fig 4.4.8).

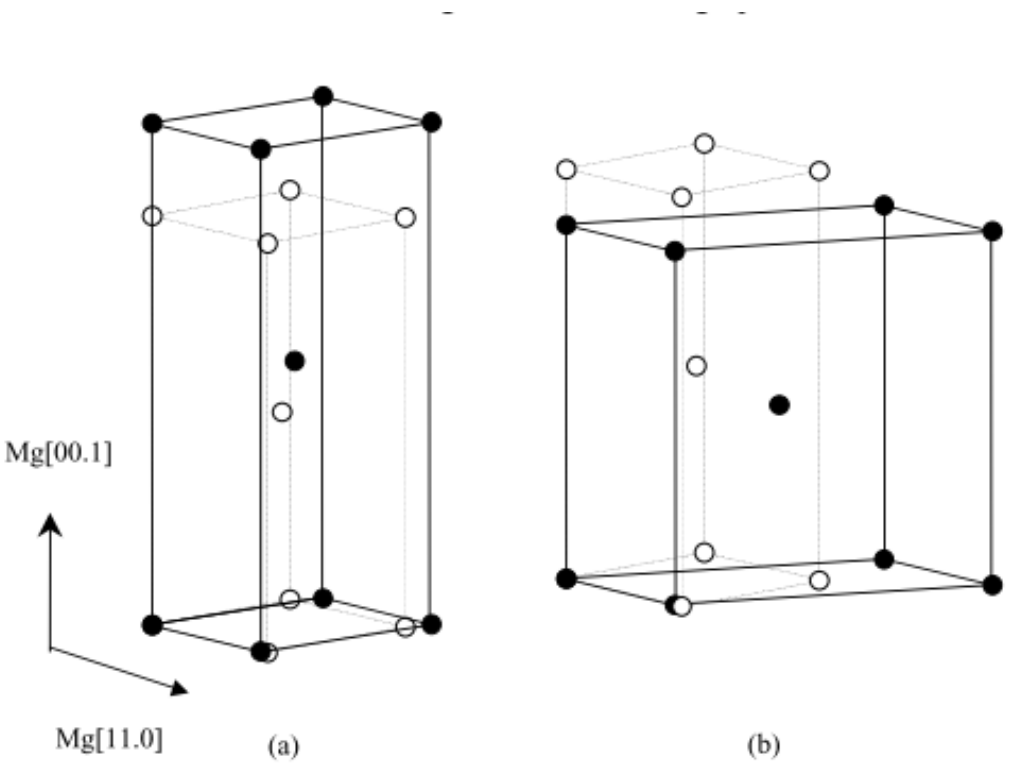

Fig 4.4.8. Left – atomic displacements in transformation of Mg to MgH_2 *in thin films in comparison the bulk (right)*[66].

4.4.5 Conclusions

Films of Mg with a Pd cap (20 nm) were deposited on glass, silicon and MgO (001) substrates using Pulsed DC magnetron sputtering. Both a thinner (200 nm) and thicker (800 nm) film were deposited to look for differences in structural development and sorption properties.

Despite the differences in crystallographic features of the substrates, XRD revealed only basal plane texture of Mg (002) and strong texture of Pd (111). For thinner films, the diffraction intensity of the Mg peak was similar. However, for the thicker films, around 5 order of magnitude in the diffraction intensity is observed for the MgO substrate. This suggests a difference in the microstructure of the films, with the MgO substrate likely to induce some pseudo epitaxial growth leading to both better adhesion and a difference in mechanical properties. Surprisingly, there was no evidence of a difference in the diffraction intensity between amorphous silica and crystalline silicon. However, their growth stresses were dissimilar. The higher surface energy of the silicon substrate appeared to alter the nucleation behaviour at the substrate interface.

Variable temperature XRD up to a temperature of 100 °C at 10 bar H_2 showed a complete transformation to textured MgH_2 (110) for all substrates. It was not possible to complete this exercise for thicker films due to time constraints and instead an ex situ hydrogenation chamber was used. Due to the higher temperature used for the in situ experiments, stresses were not estimated for the thinner films. However, for thicker films the resulting strain analysis of the MgH_2 diffraction peak suggested that both the silicon and MgO substrates exert a more compressive stress in that layer. The glass layer seems to grow with minimal strain. The resultant TPD profiles of these films show a similar behaviour, with both the silicon and MgO substrates desorbing hydrogen at slightly lower temperature. The differences in desorption is not as high as may be expected.

Given such a large difference in diffraction intensity, the mechanical response of the films is likely to be different. Transitions between elastic and plastic behaviour will affect thermodynamic stability. The appearance of slightly larger, more equiaxed grains on the MgO substrate would suggest that plastic deformation is easier in these films. Thermal mismatch will most certainly play a role in the evolution of strain within the film as it is heated.

The exact mechanism for the difference in thermodynamics cannot be attributed to one mechanism from the results contained herein. However, it is certain that the substrate does affect thin films. Further work in this area should focus on in situ techniques that allow for precise determination of the film strain with hydrogen loading. In addition, observation of hydrogen loading would be most useful, as it could reveal mechanisms for stress release and generation.

4.5 INDUCING STRESS USING FLEXIBLE SUBSTRATES

The previous chapters have shown how the influence of stress has affected hydrogen desorption behaviour. The influence of different substrates has shown the growth stresses as well as the adhesive energies differ, which allow for varying amounts of thin film stress build-up. The highest compressive stress seems to provoke the lowering of the desorption temperature.

However, with the thicker films, there was substantial stress release due to buckling from hydrogenation stresses in some films, which was due to their underlying microstructure when they were deposited using different sputter conditions. Indeed, there is a critical hydrogen content for a given film where it becomes favourable for the film to delaminate from the substrate, rather than staying adhered.

It is also important to note the differences in elastic and plastic deformation of the film. The large out of plane expansion is favourable due to the in plane restriction. The microstructure also plays a part here. Excessive void formation can be detrimental to the film quality and ductility as well as providing a means for stress release.

By the use of flexible substrates, tailoring the film stress in hydrogenation and dehydrogenation is possible. This novel concept has allowed for investigation of hydrogen sorption properties in thin films with controlled, applied stress.

4.5.1 The Stoney equation - Thin film bending stress

The Stoney equation is based on thin film curvature. The method is widely used but makes some assumptions that are important to recognise:

1. Film thickness and substrate thickness should be uniform, have the same bend radius. Film thickness << substrate thickness << bend radius
2. Strain and rotation of the plate system are negligible
3. Film and substrate are homogenous, isotropic and linear elastic

4. Film stress are in-plane isotropic or equibiaxial. Out of plane stress is zero.

For these experiments, the Stoney equation is valid.

By using a variety of bending radii, we can calculate and alter the film stress (σ_f). Because the film should be elastically connected to the substrate, the hydride phase should feel a compressive stress when bend to do so. In addition to this, it is possible to use a different film thickness to give different stresses for a given bend radius, as the stress experienced is dependent on cross sectional area.

Thin film stresses often go up into the GPa range.

$$\sigma_f = \frac{1}{6R}\frac{E_s d_s^2}{(1 - v_s)d_f}$$

Where R is the radius of curvature, E_s is the substrate modulus, d_s and d_f are the film and substrate thicknesses and v_s is the Poisson ratio for the substrate.

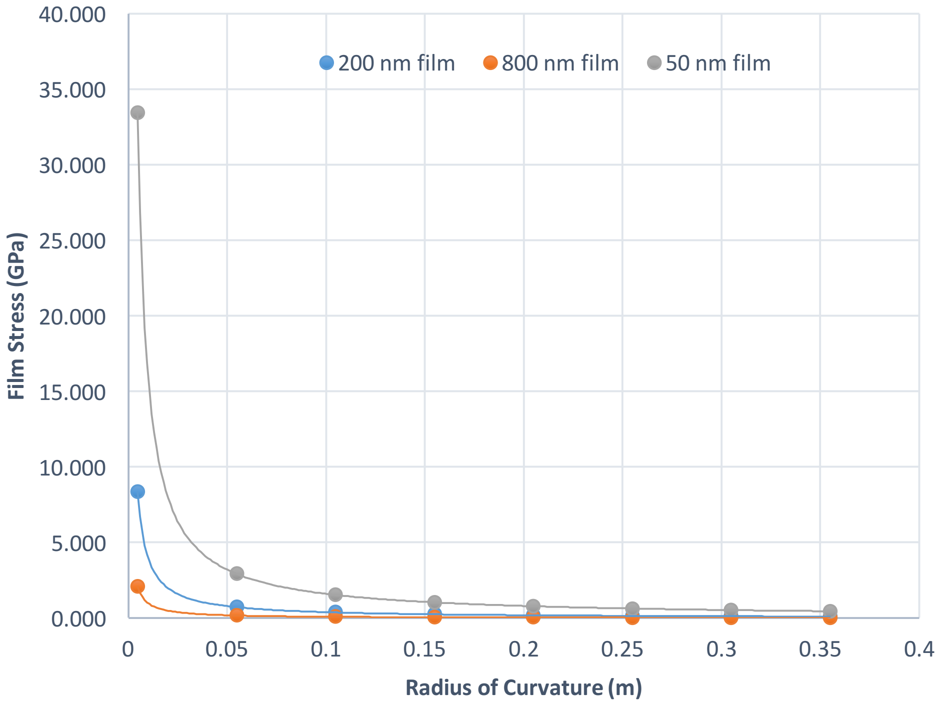

Fig 4.5.1. Predicted film stress for given thicknesses and radii of curvature as given by the stoney equation for a thin film of Mg on a PEEK substrate.

4.5.2 Characterisation of PEEK

One of the important choices in choosing a flexible substrate is to use one that can be bent to a sufficient radius so that it provides a realistic and measurable value of stress. In the particular case of the hydrogenation/dehydrogenation experiments, it also has to be non-reactive with hydrogen and be thermally stable. PEEK is a polymer that has a high thermal stability, Tg, melting point and chemical resistance. This may resolve any issues with forming Mg alloys, hydrogen embrittlement of the substrate and melting of the polymer. Dynamic mechanical thermal analysis (DMTA) was used to assess the mechanical behaviour of the film with temperature (Fig 4.5.2). We can see that the variability in Young's modulus with temperature initiates at around 130 °C and is slightly dependent on frequency. However, the drop in stiffness is around 4-5 fold, which is low in comparison to other fully amorphous polymers. This is important to consider when doing TPD measurements, as the reduction in the modulus value will affect the film stress. In addition, the thermal expansion of the polymer must also be taken into account, as this will also contribute to the effect.

In an attempt to relieve any influence from the substrate and keep the Mg layer free of other factors, a film structure of PEEK/Ti/Mg/Ti/Pd was used, as well as a more straightforward PEEK/Mg/Ti/Pd architecture. The role of the interfacial Ti layers means that the surfaces are essentially uncoupled mechanically and that the only way to apply stress is via bending. Ti layers also promote adhesion to the substrate.

Structural characterisation using XRD is complex, as the semi crystalline nature of PEEK gave a trace that could not be interpreted very well due to a large background scattering and a poor signal to noise ratio. For this reason, these particular results are omitted. A glass substrate deposited in the same batch was tested and analysed, showing expected orientation of Mg and Ti during preliminary investigations.

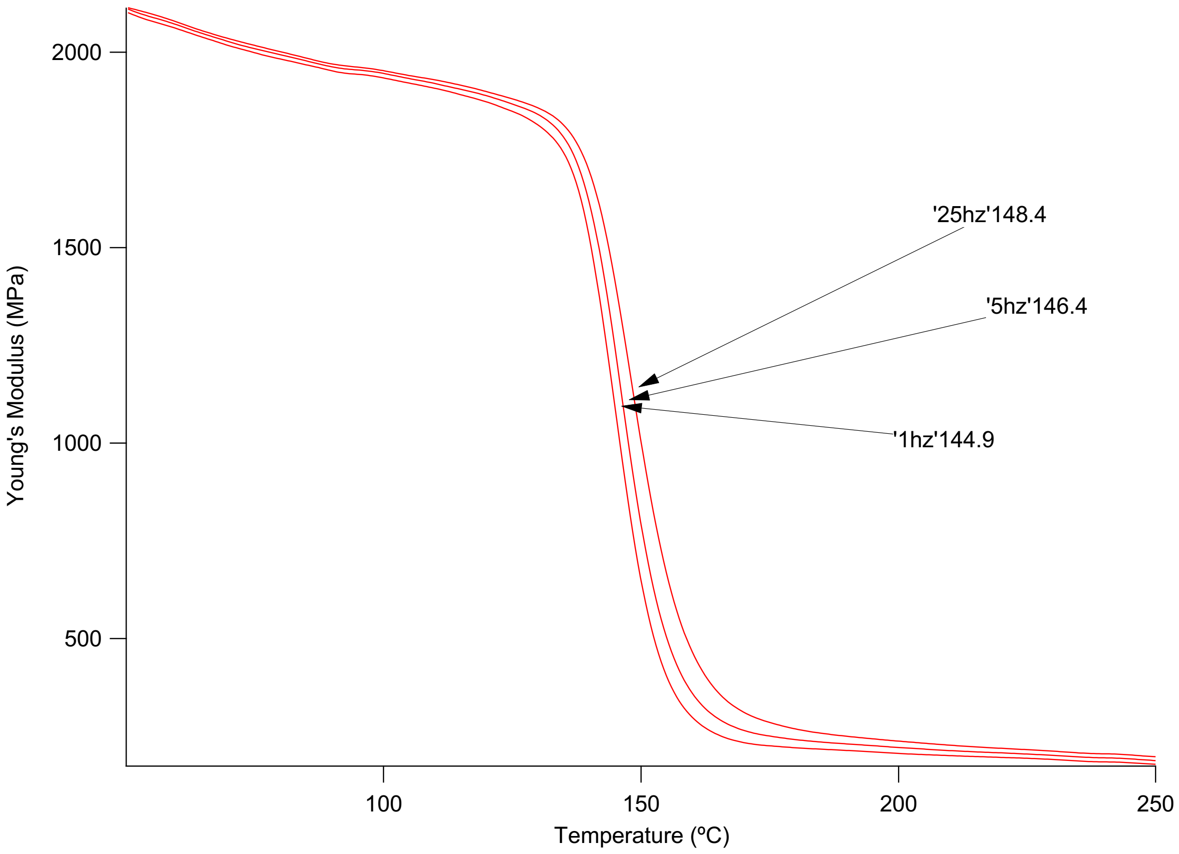

Fig 4.5.2. Drop in young's modulus through T_g for PEEK at frequencies of 1,5 and 25 Hz. Initial melting begins around 130℃ and is complete by 170℃.

4.5.3 Hydrogenation

Films on the PEEK substrates appear to adhere excellently to the substrate and are visibly curved after hydrogenation due to the lattice expansion required to form MgH_2. Using image analysis software, the radius of curvature was calculated. Using the Youngs modulus of Mg (not MgH_2) as 45 GPa and the PEEK substrate (4 GPa below Tg) and calculated curvature, the stress due to hydrogenation would be around 110 MPa. This value is remarkably similar to the values obtained when analysing the stress values calculated at the onset of hydrogen desorption due to thermal mismatch in the Mg-Pd layers. As the volume expansion has been accommodated in plane by bending of the film, the MgH_2 layer is stress-free in this bent state.

Given a stress of 110 MPa, this would correlate to around 0.2 % strain in-plane if the film were to be straightened out again. This also suggests that the largest amount of volume expansion occurs out of plane via plastic deformation. Loading in a compressed regime should therefore only slightly affect the mechanical response to hydrogenation. Loading in a tensile regime would probably have a larger effect. Loading in these regimes was attempted, but time constraints did not allow for full characterisation of the films.

Fig 4.5.4 shows XRD traces of the films that were initially characterised after hydrogenation at room temperature in a preliminary experiment. The results demonstrate the difficulty in using XRD to characterise these films as there are large substrate reflections present, even when using GIXRD. Due to the small peak intensity and the difficulty in separating the peak from the underlying substrate, it was not possible to assess any structural properties of the MgH_2 phase formed.

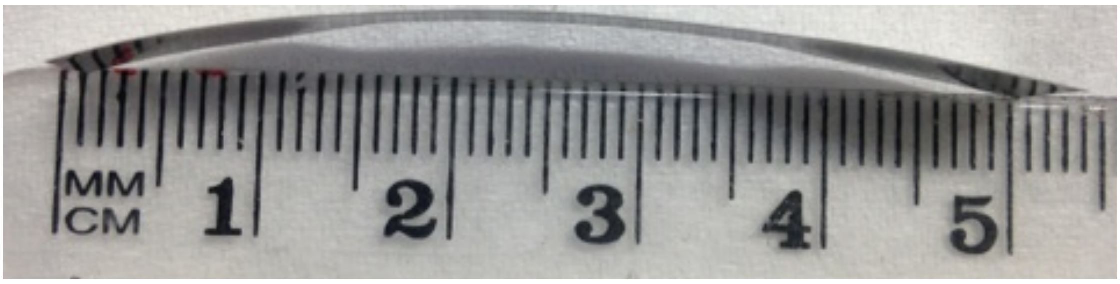

Fig 4.5.3. Photograph of film on PEEK substrate showing developed curvature from hydrogenation.

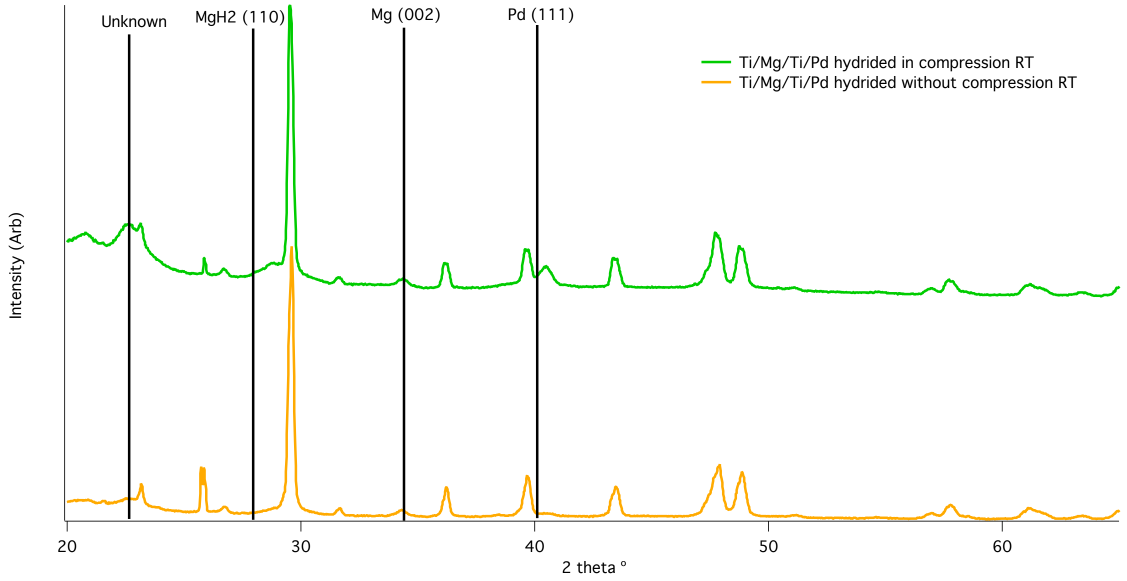

Fig 4.5.4. XRD patterns of films after hydrogenation at room temperature on flexible substrates in 'normal' conditions as opposed to compressive stress. A small MgH_2 peak is observed during the loading with a compressive stress.

4.5.4 Hydrogen desorption Behaviour

TPD traces from the investigation showed interesting behaviour. Firstly, all films reveal a trace with a multitude of desorption peaks. Other work that has not yet been shown (see section 4.6) has shown that any desorption of TiH_2 only occurs at temperatures around 350 °C. This means that the peaks must be attributed to MgH_2 desorption. There are two possible explanations for this behaviour, both of which result in changes to the mechanical properties of the film.

Firstly, the DMTA graph illustrates the modulus drop off around the desorption temperatures observed. This of course reduces the film stress and any driving force for desorption.

Secondly, the 'dog bone' shape of the samples may induce localised plastic deformation of the film during hydrogenation. It is thought that the localised plasticity within slimmer and wider regions has meant that there are inhomogeneous regions within the film surface area. Advanced plasticity in slimmer regions in comparison to wider regions will widen the hysteresis observed. We would expect to see a higher desorption temperature for these regions where the most plastic deformation has occurred. Additional hysteretic components such as plastic deformation have previously been shown to alter thermodynamics in this way[79,97]. However, this is the first time that a result using this sort of approach has led to this conclusion.

Looking into more detail at the Ti/Mg/Ti/Pd films, we can see that adding additional compressive forces would seem to stabilise the hydride phase. This seems the opposite to what could be expected. However, let us consider that the additional film stress added with this geometry is estimated to be in the region of 2-2.5 GPa. This is far above the bulk yield stress of Mg and it is likely that additional plasticity is induced to accommodate this compression. The increased plastic deformation would drive a destabilisation of the hydride phase. This is in line with the observations of the TPD experiments.

Assuming that this is the case, the slimmer regions of the dog bone would have to accommodate more plasticity than the wider regions and the effect would increase. This is seen in the Ti/Mg/Ti/Pd films which are elastically disconnected from both the substrate and Pd layers.

In the case of Mg/Ti/Pd films, the effect is a lot less pronounced. However, the same patterns of peaks are observed, although not with the same intensity. In this case, the interaction with the thermally expanding substrate may allow for some of the mitigation of the effect. The Ti buffer layer seems to play an important role in elastically disconnecting the substrate from the film.

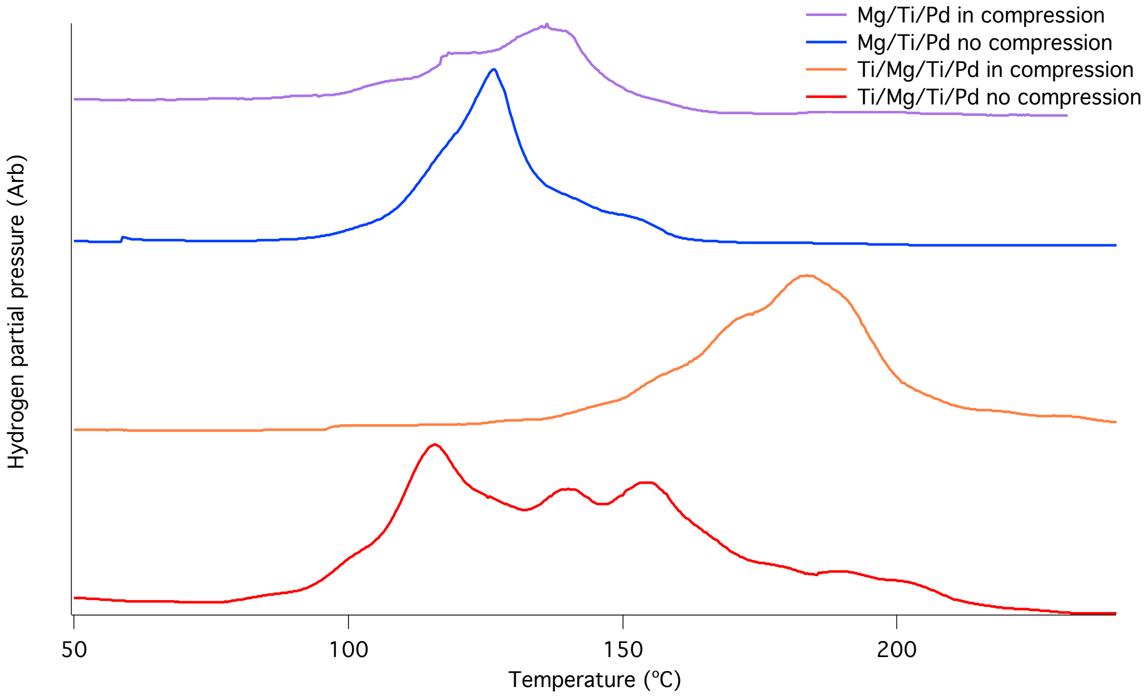

Fig 4.5.6. TPD traces of films hydrogenated on PEEK substrates. Films were dehydrogenated in 'normal' conditions with no additional force applied, as well as in compression to a radius of curvature of 10 mm.

4.5.5 Conclusions

Mg based films were successfully deposited onto PEEK substrates. The in-plane expansion of the films was observed by thin film curvature measurements. This expansion was in good agreement with other results presented in this work, showing around a 0.25 % compressive strain and suggesting that the majority of the volume expansion due to hydrogenation is accompanied by out of plane plastic deformation. Hydrogen desorption in both normal (not bent) and in-plane compressive stress showed a marked difference in the stability of the hydride phase. The increased stability of the film under compression is thought to be due to increased plastic deformation, which would manifest itself as a widening of the hysteresis observed on a PCI. The conditions examined show that it could be possible, in theory, to optimise the hydrogen loading behaviour of the films, by perhaps loading in a tensile regime and then unloading in compression. However, plastic deformation must be reduced in order for this analogy to be effective and reversible. This is the first time to the authors knowledge, that this effect has been demonstrated and this experimental approach for thin films.

4.6 MG BASED MULTILAYERS

4.6.1 Mg/Ti based multilayers

Three samples were prepared with different layer thicknesses on glass substrates, ranging from 15 to 60 nm Mg with 5 to 20 nm Ti interlayers. A schematic of the films is shown below:

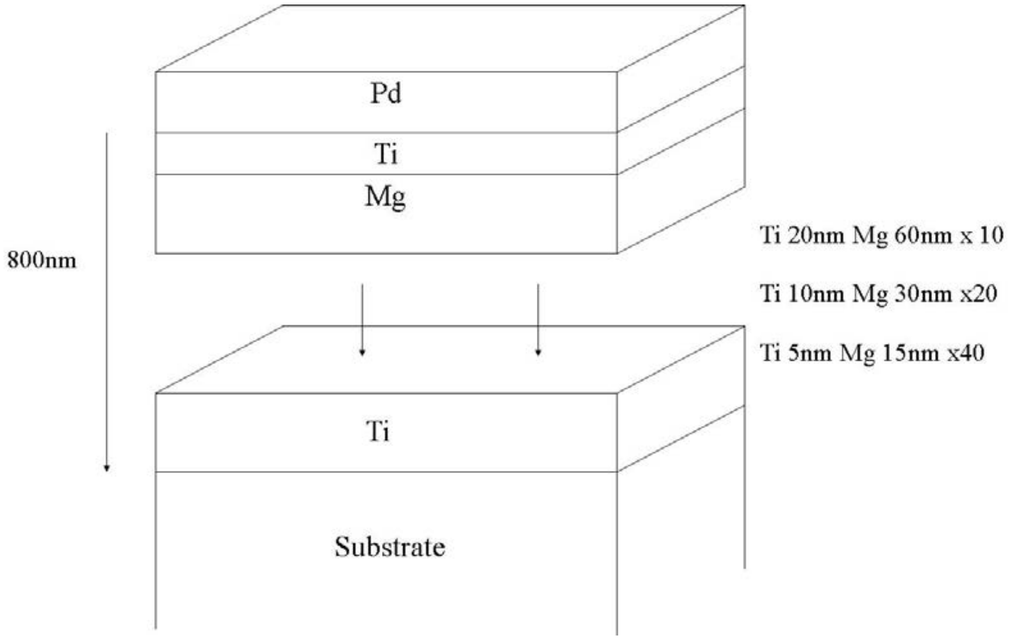

Fig 4.6.1. Schematic representation of multilayer stacks as prepared.

4.6.1.1 Structural properties

The XRD of the as prepared samples is shown in Fig 4.6.2. The films as a whole, are very crystalline. There are 3 well pronounced peaks. The first peak is due to Mg (002). However, the lattice parameters do not match well with Mg. The second peak at around 38° is attributed to the Ti (002) peak. However, in both cases, the lattice parameters do not match exactly with bulk parameters. This could be for 2 reasons, either: a stress caused by the lattice mismatch between Ti and Mg; or an incorporation of Ti into the Mg lattice. Although Mg and Ti have a positive enthalpy of mixing, the 'non equilibrium' conditions such as sputter deposition have previously shown a tendency to form a metastable alloy with stable and reversible hydrogenation. No data is given is given on the temperature required to promote phase segregation[73–75].

Using Vegard's law to calculate the lattice parameter of the MgTi alloy with the peak positions of the Mg (002) and the Ti (002) peak gives compositions of $Mg_{93}Ti_7$ and $Ti_{99.4}Mg_{0.6}$. This may be an indication of some interdiffusion at the interface layers in the sputtering process.

However, using the peak positions to estimate the stress in each layer (and the bulk modulus for Mg and Ti (45 and 100 GPa) respectively, shows a c axis compression for Mg and expansion for Ti. Mg is in around 300 MPa of c axis compression and Ti is around 500 MPa tension. This is reasonable considering that the Ti layers are thinner than the Mg layers.

It is not clear (based on this data) if the layers are stressed or if there is a small amount of solution of one element in the other. According to the phase diagram, only around 1 at% of Mg in Ti is expected although this is >400 °[142].

Considering the right-most peak at 40°, this can be attributed to the 111 reflection from Pd as well as the reflection from Ti (101). It is difficult to distinguish between them, however the change in the intensity of the diffraction peak is interesting: for smaller Ti thicknesses the peak does decrease, but it is not clear why there is a difference in peak intensity. It may be due to the rotation speed used in the magnetron sputtering system or could be a different mechanism for relaxation or that more Ti is incorporated into the Mg lattice/used at an interface.

Looking further into the Mg and Ti peaks we can see a series of superlattice peaks at the thicknesses corresponding to 10/30 and 5/15 nm which is similar to thicknesses when superlattice peaks have occurred in other films[100] (Fig 4.6.3). There are no superlattice peaks in the sample with thicker dimensions.

Using SEM, it was possible to look at the cross-section of the films (Fig 4.6.4). For thicker bilayers, individual layers could be fairly easily distinguished. It would appear that the Ti layers seem thinner than would be expected, which points to some potential alloying at the interfaces between layers, which is complimentary to the peak positions shown by XRD.

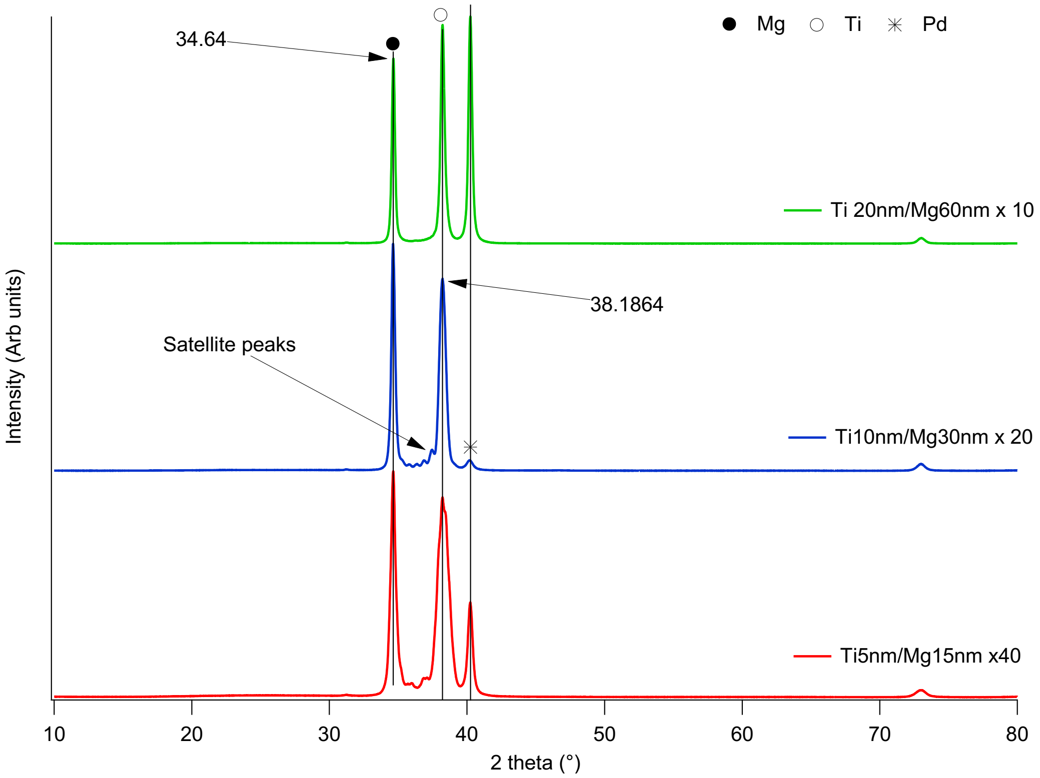

Fig 4.6.2. XRD patterns of as-deposited Mg-Ti multilayer thin films. The 2θ values of 34.64 and 38.1864 are unknowns as either highly strained layers or solid solution metastable Mg/Ti alloys.

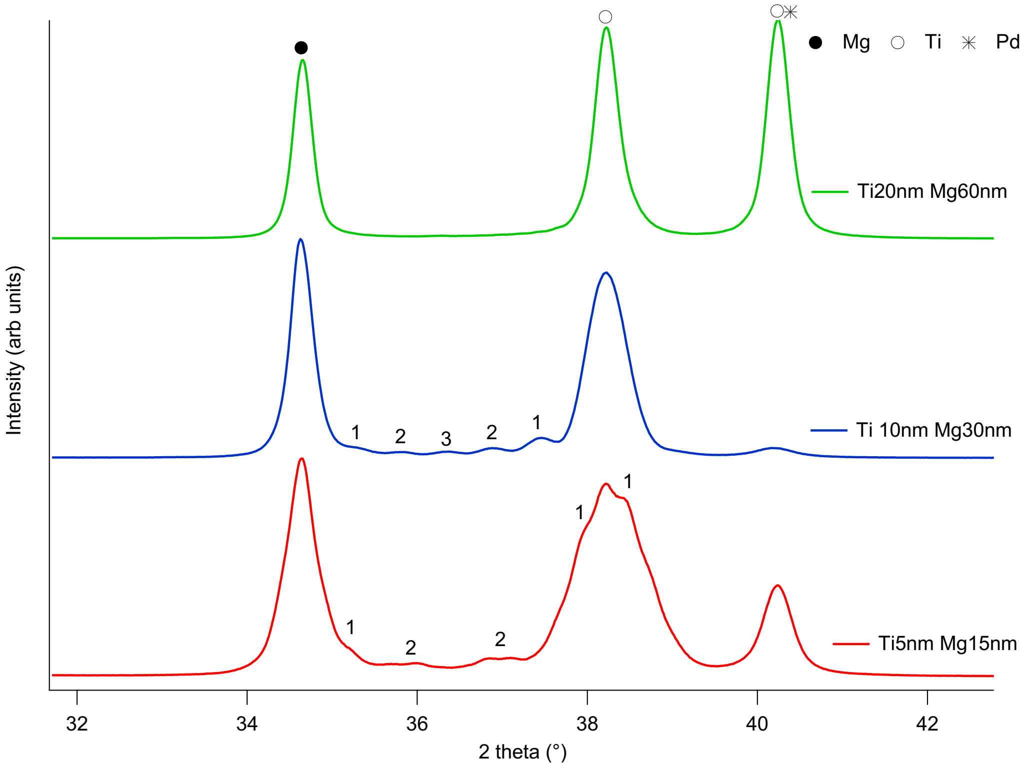

Fig 4.6.3. Magnified view of part of the XRD patterns in Fig 4.6.2: evidence of superlattice peaks is evident on closer inspection of the peak positions in the as-deposited state.

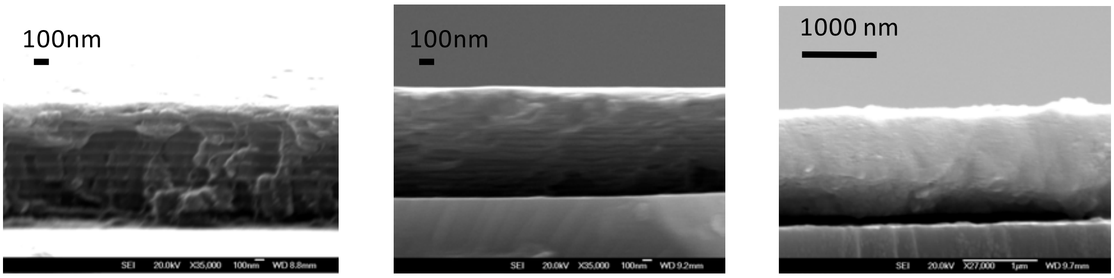

Fig 4.6.4. SEM micrographs of Mg/Ti multilayer structures in the as deposited state. Interlayers are clearly observable in the thicker specimen but due to the resolution of the SEM, they become more indistinguishable as thinner layers are produced. (Left – Ti 20nm/Mg 60nm. Middle – Ti 10nm/Mg 30nm. Right – Ti 5nm/Mg 15nm).

4.6.1.2 Hydrogenation characteristics

Films were hydrided in the same conditions that had been successful previously (100 °C, 1 bar H_2 for 48 hours). The resultant XRD patterns are shown in Fig 4.6.5. After this period of hydrogenation, it was clear that there was some formation of MgH_2 from the peak appearing at 28°. However, there was still a large reflection present at the original peak position of 34.2°. The peak at 38° which was originally attributed to Ti has completely disappeared, suggesting a complete formation to TiH_2. However, this position is very close to that of the original Mg peak.

Looking in more detail at the peak positions does show asymmetry, suggesting the presence of another phase (Fig 4.6.6). The peak at 34.25° sits closely with that of Mg/Ti films previously reported[75]. There is also evidence of residual Mg that may be highly strained within the thinner multilayers.

Therefore, in situ XRD was used to try to probe the reaction mechanisms within the film. The results of this investigation are shown in Fig 4.6.6. Initially, there is some evidence of MgH_2 growth but only a small decrease in peak height of the Mg/Ti peak (phase contributions cannot be analysed from a single peak). Above about 60 °C as the reaction progresses, the MgH_2 growth increases to a linear regime, likely due to the temperature change. The Mg/Ti peak also seems to reciprocate this, showing the same linear response. After some time, at around scan 12, the rate of increase of the MgH_2 intensity peak slows. This suggests that a mechanism of diffusion-limited growth is becoming more obvious. The Mg/Ti peak does not reciprocate this behaviour, but this could be to do with the size of the peak in comparison, and that only small amounts of phase transformation are responsible for a large decrease in this peak height. It would therefore seem that the peak at 34.2° observed in the diffraction data can be attributed to TiH_2 and that the majority of the Mg has reacted.

The desorption behaviour of the same film was examined, to see if the reaction tends to proceed in a similar way (Fig 4.6.7). Again, it is clearly visible that the Mg/Ti peak starts to appear, whilst the MgH_2 peak starts to disappear, at the same temperature. There are small differences in the Mg/Ti peak height from the initial temperature ascending upwards and this is likely due to the influence of increasing temperature acting to decrease the peak height. The MgH_2 peak was not as sensitive to this, due to the relative difference intensities between the peak heights.

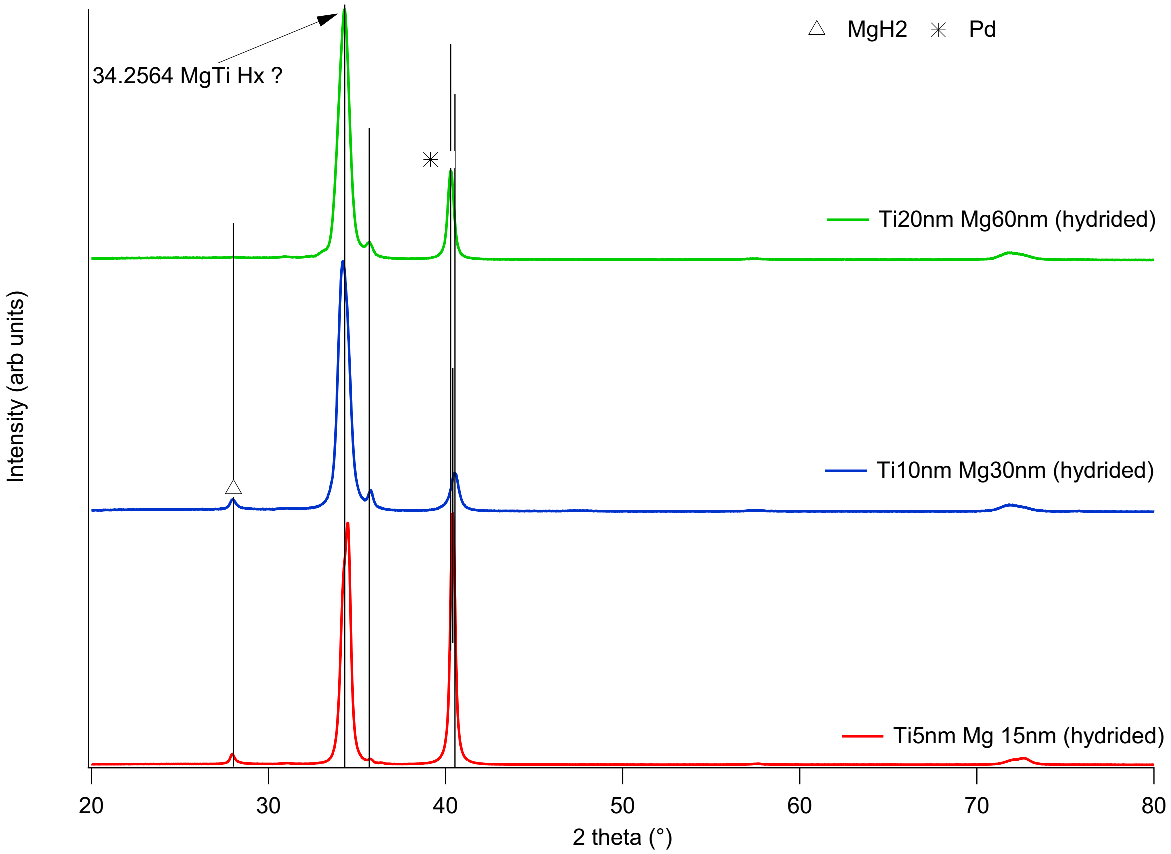

Fig 4.6.5. XRD patterns of Mg/Ti multilayer films after hydrogenation. There is clear evidence of MgH_2 formation, however the large peak remaining at around 34.2°2θ is unknown.

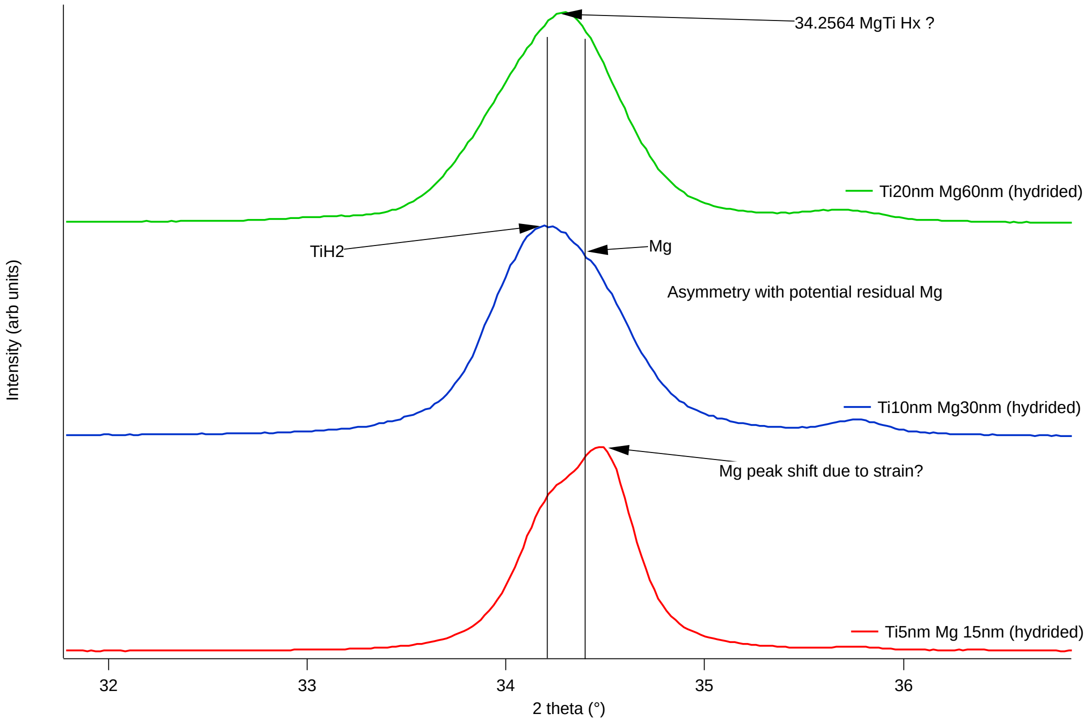

Fig 4.6.6. Magnified view of part of the XRD patterns in Fig 4.6.5: X-ray peaks surrounding Mg or TiH_2 regions.

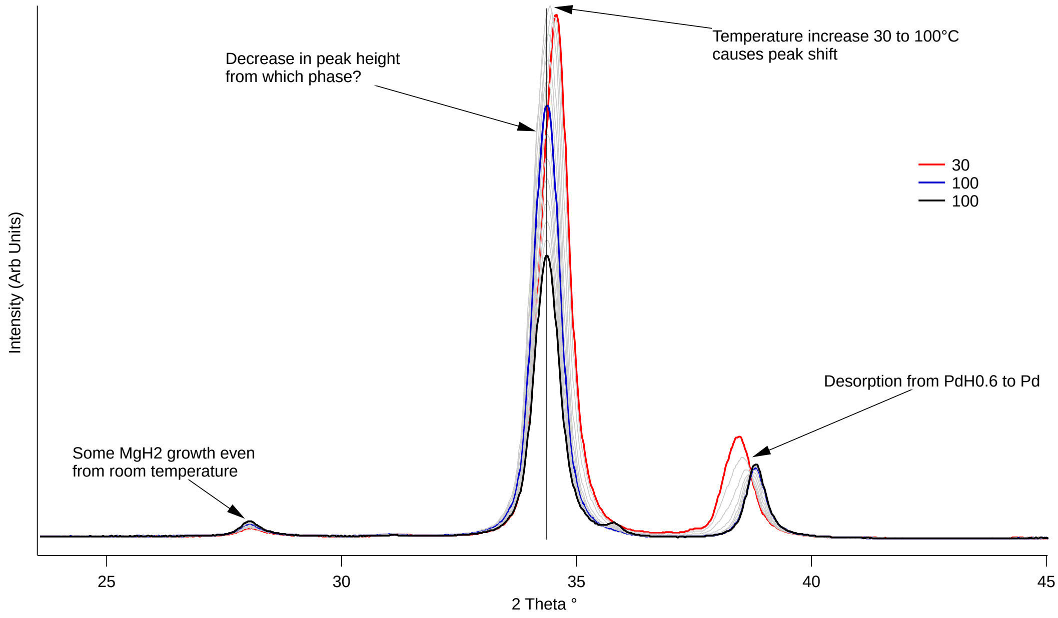

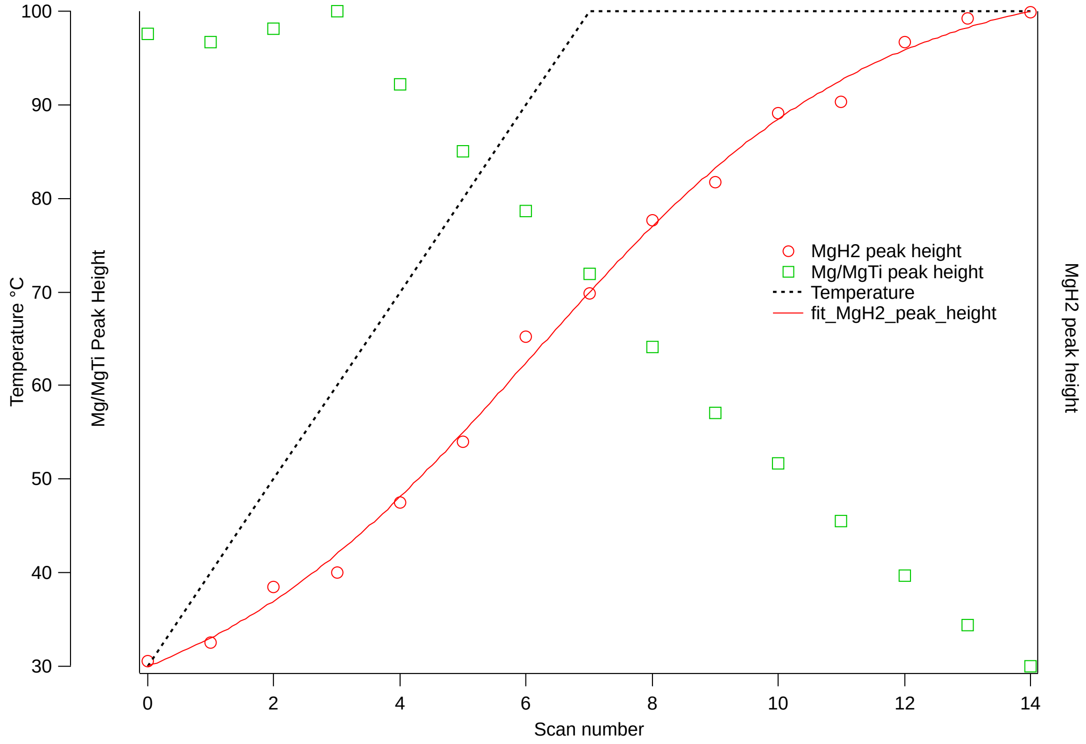

Fig 4.6.7. Top – in situ XRD showing the reaction within a multilayer sample. There is clear evidence of MgH_2 formation and a decrease in peak height of the original peak at around 34.2°. Bottom – analysis through time showing the peak height change for both the MgH_2 known peak and the unknown Mg/Ti peak.

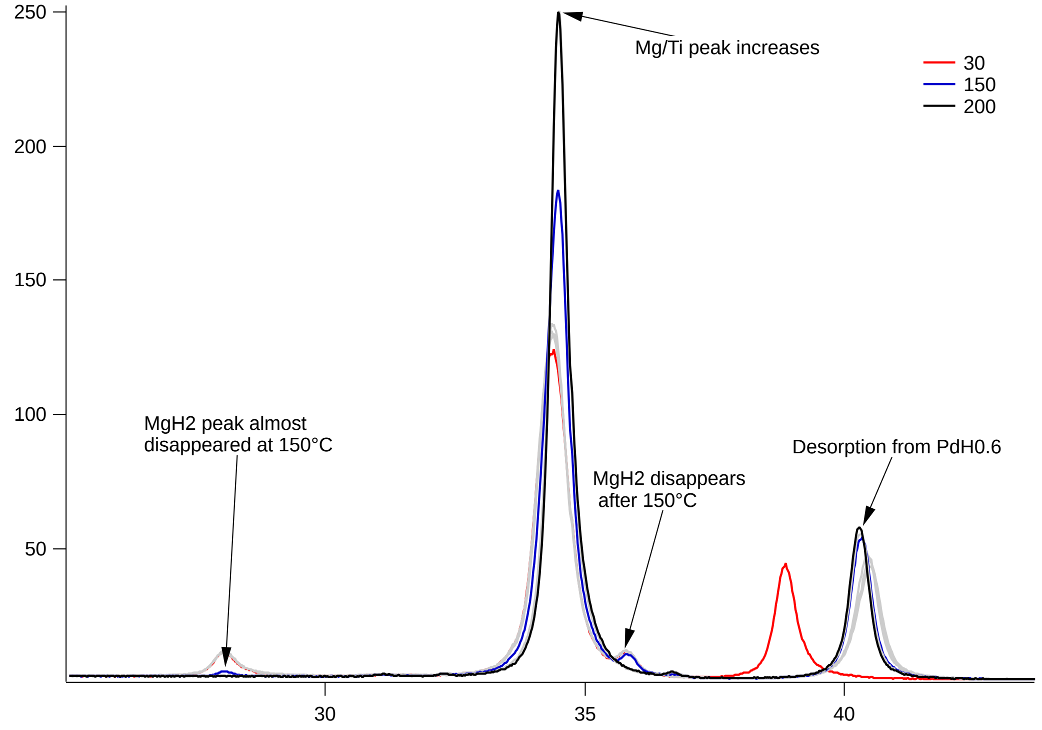

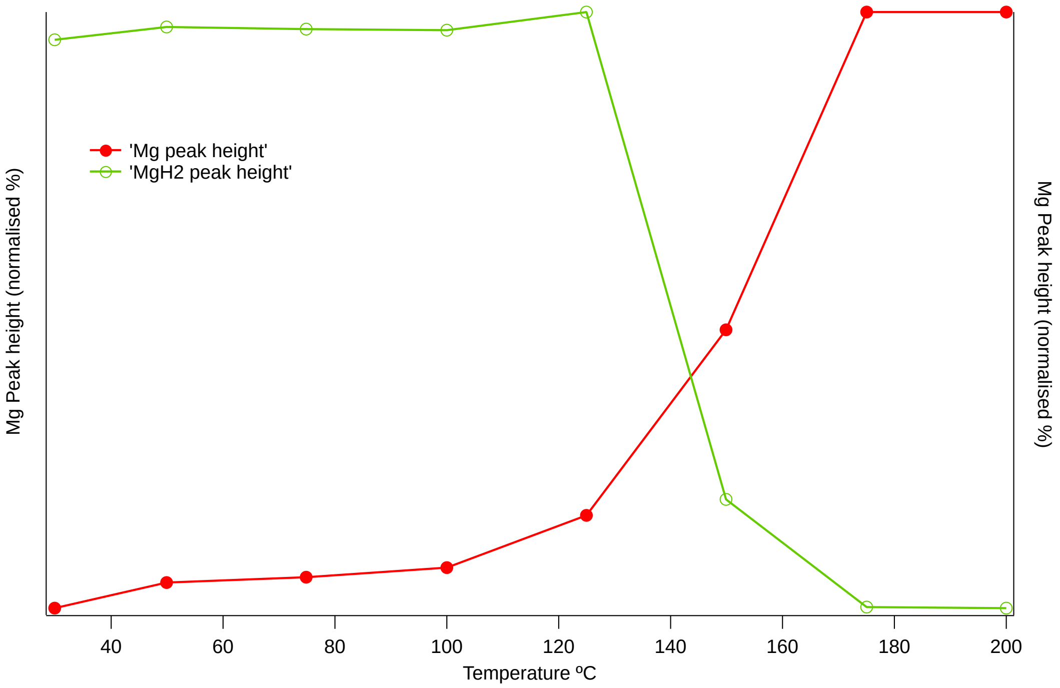

Fig 4.6.8. Top - In situ XRD showing desorption of the multilayer sample with increasing temperature.

Bottom – peak heights as a function of temperature.

4.6.1.3 Hydrogen Desorption Characteristics

The TPD traces for the respective multilayer samples are shown in Fig 4.6.8. It is clear that there is some form of destabilisation. In comparison to the 20 nm thick Mg layers, the thinner layers of Mg (10 and 5 nm) desorb hydrogen at lower temperatures. It is expected that at the lower thicknesses, there is a considerable destabilisation due to interfacial energy contributions. Mooij et al showed this to be in the region of around 0.3 Jm^{-2} in Mg/Ti films[79]. One should therefore expect that for the 5 nm Mg sample, there would be increasing destabilisation due to this interfacial energy contribution. However, it would appear that this is not the case. This may in part be due to the partial decomposition of the film before loading into the chamber. To examine whether some room temperature desorption in argon was possible, the sample was left for 3 days within the glovebox and then re-tested. This is shown as the black trace on the same graph, showing that almost all of the hydrogen has been released at room temperature in argon.

It was apparent that there were other peaks appearing, that may correspond to the desorption of some hydrogen. A more complete TPD trace is shown in Fig 4.6.9. This shows that the films appear to desorb hydrogen at around 450 °C. This is likely due to TiH_2 desorption. This was not examined using XRD in situ, as the temperatures required approached the melting point of the glass substrate and there was fear of damaging equipment.

Looking at Fig 4.6.9 there is around the same amount of desorption attributed to the TiH_2 desorption for 2 out of the 3 films. The exception being the Mg 60 / Ti 20 nm film. It has already been discussed that there is potential for some incorporation of Ti and Mg within a film structure, and it would seem that this may be the case here. This would also explain the apparently smaller hydrogen content within this film.

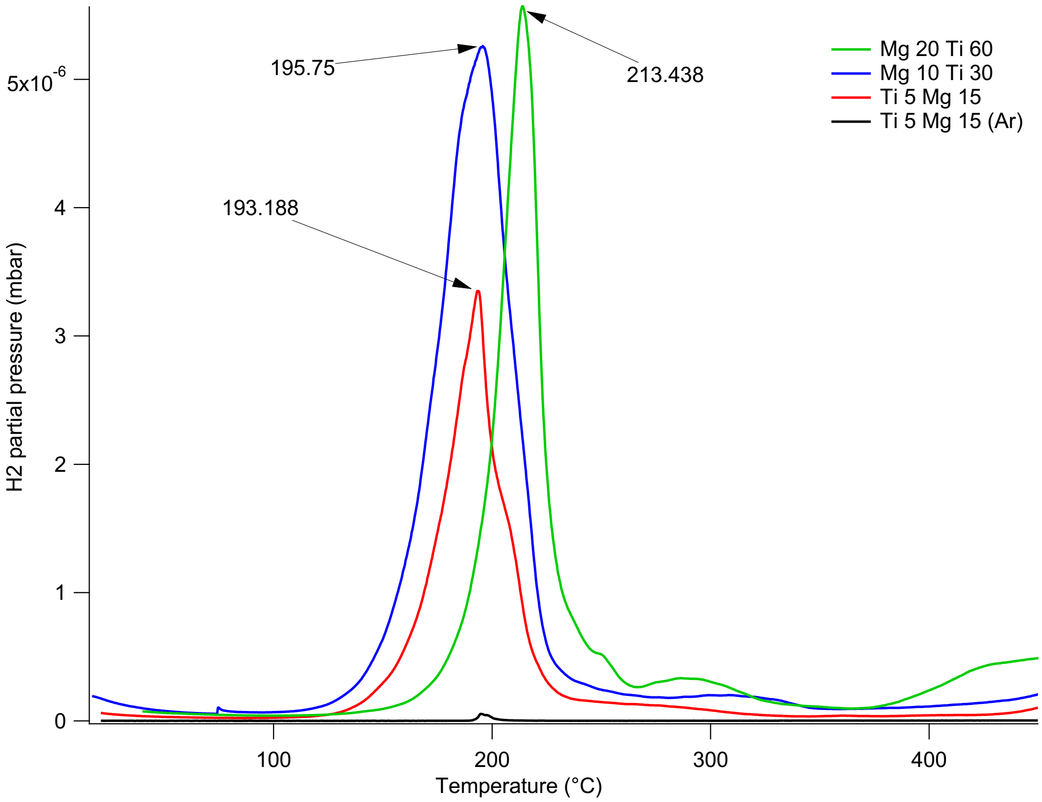

Fig 4.6.8. TPD traces of Mg/Ti multilayer films up to 450℃.

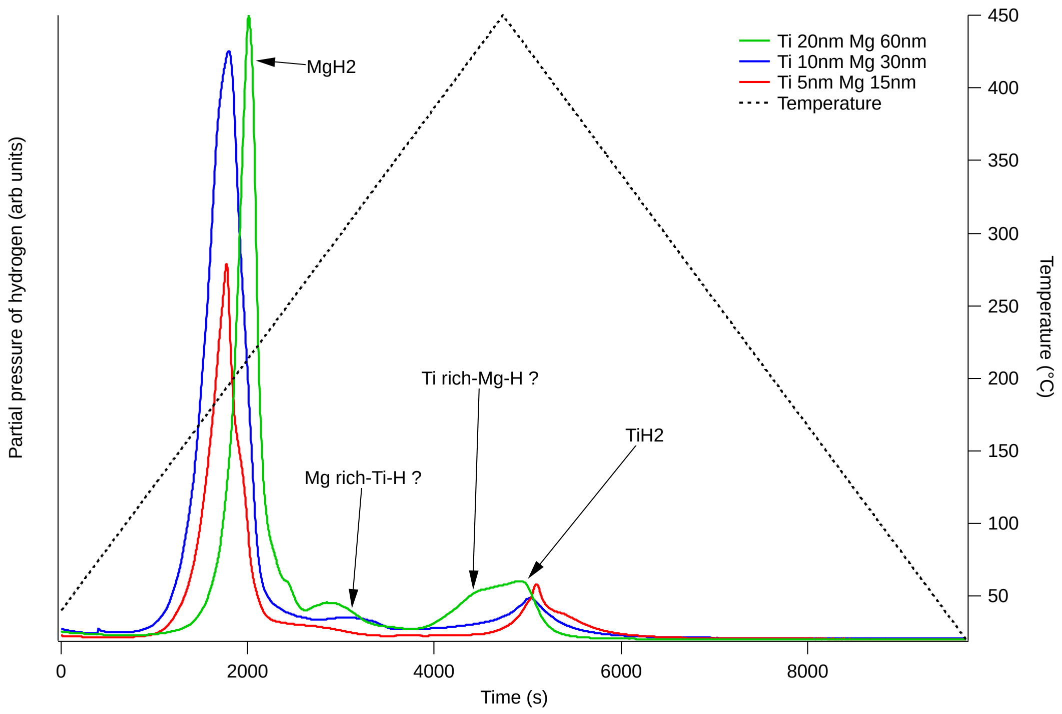

Fig 4.6.9. TPD traces of Mg/Ti multilayers versus time with temperature plotted separately (corresponding to right hand axis).

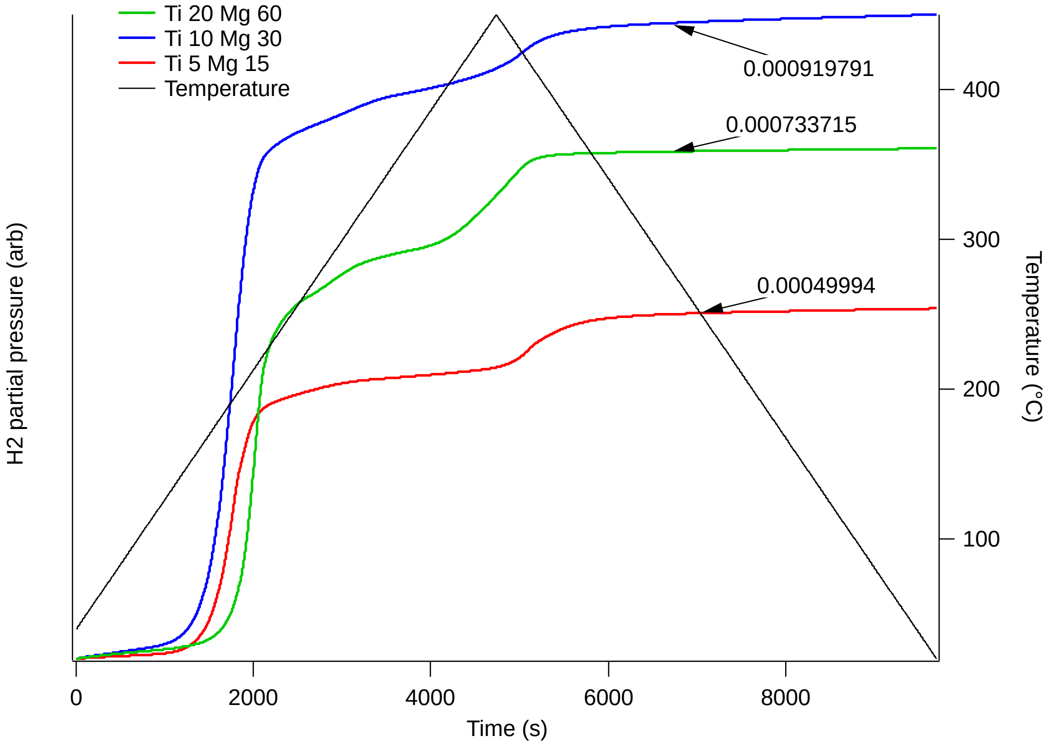

Fig 4.6.10. Integration of TPD traces shown in Fig 4.2.9. The total integrated intensity was taken at a tangent to the points labelled on the graph after subtraction of a baseline measurement.

4.6.2 Mg/Y based multilayers

Thin film multilayer structures of Mg and Y were deposited with a variety in the layer thickness ranging from 10-40 nm and having a total thickness of 850 nm with a 40 nm palladium capping layer. Schematic representations of the films are shown in Fig 4.6.11

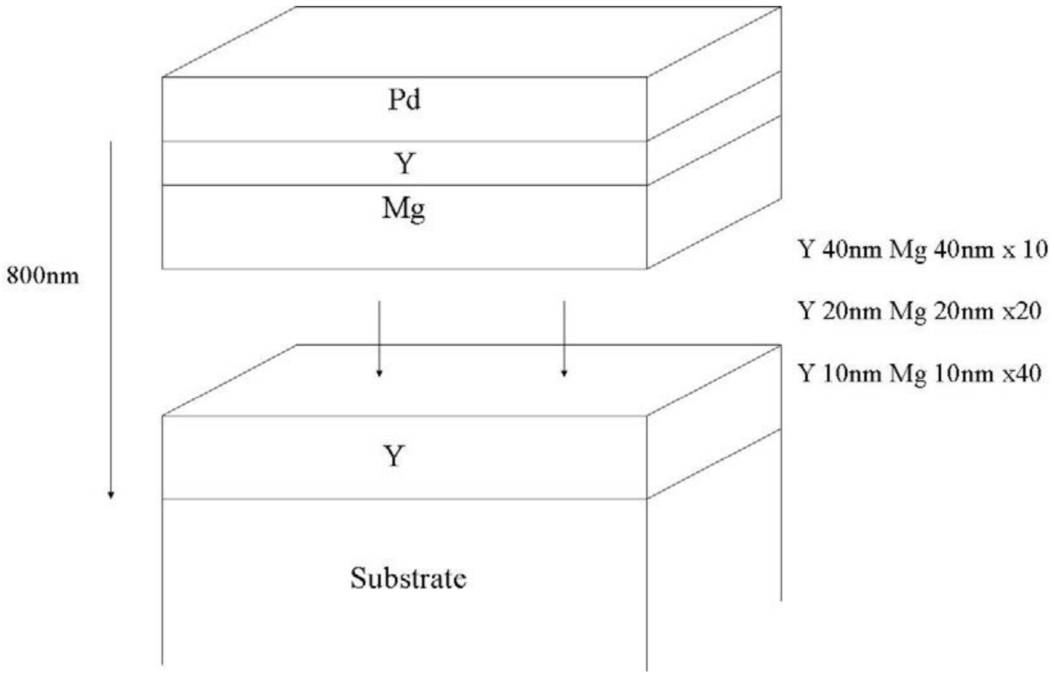

Fig 4.6.11. Schematic representations of the films with Y and Mg layers of varying thicknesses and number of layers.

4.6.1.4 Characterisation of samples as prepared

The films in the as deposited state were analysed with XRD (fog 4.6.12). Several interesting features are observed. Firstly, we observe that for the thick sample of pure yttrium (black trace) the film growth is polycrystalline but highly textured in the basal plane. Lattice parameters for this film are calculated from these three peaks to give a=0.3678 nm , c=0.5767 nm. This is in reasonable agreement with powder yttrium and other films prepared in a similar method (evaporation etc). The Pd close packed

(111) plane is also observed with a smaller intensity, which can be expected due to the small thickness of this layer.

Looking at the multilayer samples we see that the Mg layers are textured in the basal plane. The relative intensities of the Mg vary. There does not seem to be a recognisable pattern to the intensities as the thickness decreases. However, this may also be in part due to the change in crystal structure of the deposited yttrium. Previous research has demonstrated that below around 30 nm, Y tends to deposit as an FCC structure in comparison to the bulk HCP. This shift in behaviour is observed in these thin samples. The 40 nm sample still exhibits significant HCP texture but with a slight peak shift. The peak shift is further towards higher d spacings in the 20 nm sample and finally in the 10 nm sample there is not a definitive peak resembling the HCP structure and an FCC texture is developed. This is similar to the results obtained by Ferrater et al, with peaks in very similar positions[143]. Therefore, the potential for some alloying at the interface between the Mg and Y during the sputtering process, cannot be ruled-out. This hinders any further interpretation of these initial runs. The Mg basal plane intensity varies between the layer thicknesses. This may be due to a number of factors, but may be that the preferred crystal growth direction is energetically more favourable in the 20 nm layers and that the lattice mismatch can be accommodated between layers.

Lattice constants for the as deposited films are calculated (Table 4.6.1). The films tend to deposit with reasonable agreement with literature values for Y. There is a reasonable amount of strain associated with the deposition, with Y depositing with an in plane tensile stress of around 30-100 MPa depending on thickness (calculated using the 101 peak position). An out of plane tensile strain is also present, meaning that the unit cell volume seems to be larger than that of bulk Y.

In terms of Mg deposition stress, the out of plane strain is calculated which would correspond to an in plane tensile stress of 120 and 200 MPa for 40 and 20 nm films. The 10nm film is shifted to an in plane compression of around 240 MPa, although we expect that the peak position may have shifted due to some alloying with Y, so this should be noted. In addition, the peak shift to a compressive stress may be due to the increased presence of FCC yttrium, which would produce a different sort of lattice distortion and require different accommodation of lattices, assuming that the elements to alloy a small amount. This may an indication of a different growth mechanism in these very thin layers, and a potential epitaxial growth mechanism.

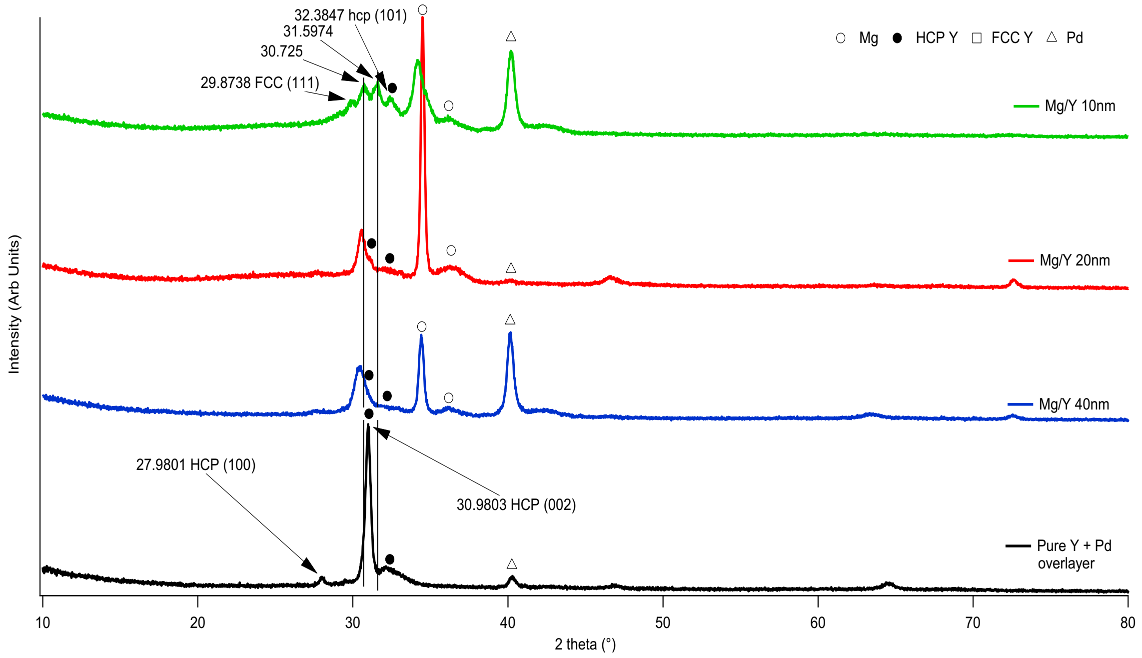

Fig 4.6.12. XRD patterns of as deposited Mg/Y multilayer films.

Table 4.6.1 Lattice parameters of as deposited Mg/Y multilayered films

Sample	**HCP - Y**		**FCC - Y**	**Mg – C axis**
	C (nm) **(+/- 0.0002)**	**A (nm)** **(+/- 0.0002)**	**A (nm)** **(+/- 0.0002)**	**C (nm)** **(+/- 0.0002)**
Y (800nm)	*5.767*	*3.678*	*N/A*	*N/A*
Mg/Y (40nm)	*5.768*	*3.734*	*N/A*	*5.2079*
Mg/Y (20nm)	*5.758*	*3.706*	*5.06*	*5.1949*
Mg/Y (10nm)	*5.814*	*3.639*	*5.18*	*5.2412*

4.6.1.5 Hydrogen Desorption Characteristics

TPD traces of the multilayer samples are shown in Fig 4.6.13. The stability of the different films varies with the bilayer thickness. Firstly, the films with a bilayer thickness of 40 nm Mg without an observed FCC Y phase desorbs with a singular peak, suggesting a singular phase with a uniform distribution of any strain.

Looking to thinner bilayer thicknesses, we see a shift towards a double peak. The reasons for this are not clear. However, given that there are different Y phases present, with different measured lattice parameters, this would suggest that there is a different degree of lattice strain between the Mg and Y interfaces. If we assume that the interfaces are coherent with FCC Y and HCP Mg, then the most destabilised film should, according to the data, be the Mg/Y 20 nm multilayer, as the c axis mismatch to the Mg would be in the order of 2.7 % whereas for the Mg/Y 10 nm sample, the mismatch would be around 0.6 %. If the interfaces are coherent and between Mg and HCP Y, then the mismatch in the c axis lattice parameter is 13 % and 11 % for the 20 nm and 10 nm layers, respectively. This difference in the likely accommodation of strain is thought to be the cause of the observed destabilisation. Unfortunately, there was no time remaining to complete the characterisation of these multilayer samples. However, the use of in situ XRD would be very useful in ascertaining the hydrogenation behaviour of these films, possibly revealing the transformation to YH_2 or YH_3 as well as the strain accommodation within these layers.

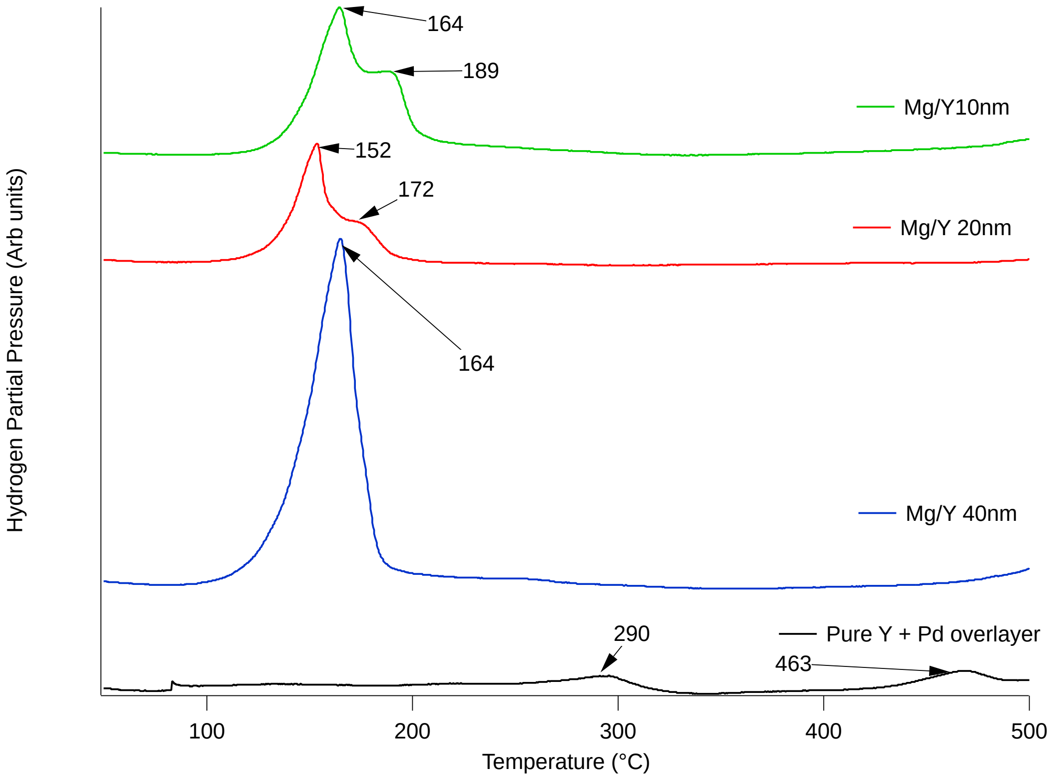

Fig 4.6.13. TPD traces of Mg/Y multilayer samples. Changes in the lattice accomodation between Mg and FCC or HCP Y are postulated to be the reasons for the observed destabilisation.

4.6.1.6 Discussion and Conclusions

Two Mg multilayer-based systems have been investigated. Ti based multilayers were used on the basis of other research which has shown a route to destabilise the MgH_2 system using interfacial energies. This initial set of films were investigated to look at the validity of the experimental approach for these types of films, as when dealing with multilayer systems, both kinetic and thermodynamic effects can be observed, leading to potential misinterpretation of results. A destabilisation of the hydride phase is observed and is attributed to the effects of extended interfaces providing additional interfacial energy to the system. With the use of in situ XRD performed for the first time on these multilayer type systems, it is shown how the reaction progresses with MgH_2 growth and decomposition being identified. Without this technique, it would not have been possible to interpret the ex situ XRD with the deconvolution of the Mg/TiH_2 peak being impossible. Unfortunately, there was not enough time to perform this sort of experiment on each individual film, however, the application of the technique has shown benefits and should be used for future investigations, potentially to show kinetic differences in the behaviour of these films at various temperatures.

Based on the success of the Mg/Ti multilayers, Y-based mulitlayers were investigated with a range of bilayer thicknesses. To the author's knowledge, this is the first time that these films have been fabricated with the use of this system in mind as a hydrogen storage material. Other research has investigated the optical properties of this system[144]. The results presented demonstrate that below a certain thickness of between 20 and 40 nm, yttrium has a tendency to deposit with an FCC structure. This is potentially observed to accommodate lattice mismatch between the Mg layers. The energetically more favourable crystal structure of Y in this multilayer arrangement shows an ability to influence the hydrogen sorption properties of these films.

5 DISCUSSION AND CONCLUSIONS

5.1 GENERAL DISCUSSION

The research presented in this thesis has been focussed primarily on the effects of stress on the hydrogen sorption properties of thin films of magnesium. The initial approach was to characterise the intrinsic features of magnesium films, which had been deposited in a variety of conditions using a CFUBMSIP system. What resulted was a difference in the observed crystallinity, microstructure and intrinsic stress within the films. The interdependence of these features is quite complex, and so the prediction of the exact resulting features can be difficult. However, the results presented demonstrate that, for this system, in the conditions examined, the magnesium films tend to grow with an in plane tensile stress, which varies with conditions.

The mechanism for the tensile stress appears to the coalescence of some of the columnar grains and/or intrinsic porosity's. This mechanism correlates well with the observed microstructures and complements the diffraction analysis.

These relatively simple results importantly explain why differences in the behaviour of hydrogen storage characteristics are observed between some research groups and the importance in understanding of the influence of microstructure and strain in the original state. For example, the observations of Fujii et al[66] show how thicker films tend to be more destabilised in comparison to thinner, whilst observations by Ham show thinner films being more unstable[134]. Recent research into observations of single grained Pd nanocubes highlights the importance of observation of single size and uniform structures, rather than an 'ensemble' of grain sizes[145].

With this understanding, an investigation was carried out with a palladium coating on top of the magnesium surface. The Pd acts as a catalyst for hydrogen absorption (achieving up to 5 wt% H_2 at 1 bar H_2 at 100 °C for 24 hours) and also prevents it from oxidation, making characterisation a lot easier. It was shown that for a number of films deposited with similar conditions to those observed in the previous chapter, an intrinsic tensile stress was again observed. This suggests that the Pd overlayer does not have an excessive influence on the underlying film, which could have been the case (for example ion implantation, shot peening or other stress related effects).

The hydrogen absorption behaviour of these films showed differences in both the XRD patterns as well as the hydrogen uptake, which were not related to each other (i.e. the intensity of the MgH_2 peak was not coincidental with the amount of hydrogen observed physically from the desorption behaviour). This behaviour has previously been reported[63] and suggests that there is most likely a difference in the absorption thermodynamics of this phase change, which would be due to a combinative mechanism of intrinsic stress release, porosity occupation, elastic and finally plastic deformation behaviour. As the films were loaded in isobaric conditions, the difference in Gibb's free energy for nucleation and growth of the phase would be different if the system plateau pressure was altered by mechanical mechanisms. This does not rule out the potential effects of stress on the diffusion coefficient of H in Mg/MgH_2 but, equally, it does not prove it. Recent research has elucidated that excessively porous structures improve kinetics, but a relationship to strain was not mentioned[131]. To support the hypothesis that the absorption branch of the isotherm would change, a stress strain analysis was developed. With this analysis and evidence from supporting literature, an example isotherm was constructed of the effects of mechanical constraints depending on hydrogen concentration. To complement this analysis, the desorption behaviour of the films also showed a thermodynamic difference. The complex addition of the absorption mechanisms must also play a role in the desorption process. This complex interplay between the intrinsic stress, microstructure and elastic/plastic behaviour will all factor into the resulting desorption plateau pressure(s). Therefore, the suggestion is made that at least on initial characterisation, there are a multitude of plateaus, associated with the sorption behaviour, when considering a thin film system. Therefore, whilst it is important to characterise the effects of initial conditions, the resultant thermal cycling for repeated ab/desorption cycles will inevitably mean that the film tends towards a more natural state of equilibrium in line with bulk thermodynamic properties, which has been reported in Pd films[83,146].

One of the key questions arising from the research on thicker films was why such films could be only partially hydrogenated, but more interestingly, why this behaviour was observed and how it can be affected, i.e. what mechanisms can be attributed to the reaction rate and can a combination of stress and microstructure be engineered to improve the hydrogen sorption behaviour. The effect of film thickness was investigated using the same sputtering conditions, but for different durations. The results indicate that for a film of around 200 nm thickness, complete hydrogenation was possible in the conditions examined (100 °C, 1 bar H_2). The TPD results from these film thicknesses indicate that the thinner film was destabilised in comparison to the thicker film. Analysis of stress change before and after hydrogenation showed an apparent difference in stress state. Therefore, a theory has been proposed that shows that due to diffusion related phenomena, the hydrogen absorption mechanism in thinner films is different to those in thicker films. The change in regime is also shown to be influenced by the: resultant microstructure, void content and intrinsic deposition stress associated with these different thicknesses.

It would be interesting to use a technique such as PAS (Positron Annihilation Spectroscopy) which would detect vacancy concentration as a function of thickness, during in situ hydrogen loading. In addition, TEM could be used to show advances in the hydride phase front and the behaviour of the underlying Mg. This might shed light into the fundamental interaction of hydrogen in stressed grain boundaries and the mechanical response of Mg. A similar approach has been used for the identification of phase transitions in Pd nano-cubes[145].

Moving further, the effect of using different substrates was also investigated. This has not been studied for thin films of magnesium. By using different crystalline orientations of different substrates, films were deposited with the same conditions as before. The results indicated some difference in the intensity of the Mg (002) diffraction peak. This suggests a different growth morphology for films on each substrate. This is unsurprising, as the free energy for nucleation is altered due to the interfacial energies on each substrate surface. A similar effect has been observed with Mg films on a Pd substrate[67].

Again, the hydrogen storage characteristics of these films showed that they could be loaded fully with hydrogen. There is a slight difference in the total absorption, but this is mainly due to both experimental error but may also be due to porosities and areas at excessively small grain boundaries. For the films on glass and quartz, the desorption temperature is some 30° lower than for the MgO. There may be an explanation here in terms of mechanical properties, but we also must take into account the thermal expansion properties of the different substrates, as this can have a significant contribution to the stress within the film. For MgO, the thermal expansion is over 200 % higher than that of glass and quartz. This would therefore lead to a lower in plane compressive stress for a given temperature. The calculated stress due to thermal mismatch between the substrates correlates well with the onset temperature for hydrogen desorption. That is to say that the substrate most certainly has an effect on the thermodynamic properties of the film, and that the difference in substrate can promote multiple effects, but the largest contributor in this case, would appear to be the thermal mismatch. This approach was also valid for thicker films, although the effect of different amounts of hydrogen uptake also seem to have more influence on the thermodynamic properties in this region.

After establishing the effects of sputtering conditions, optimising the thickness of the films and ascertaining the effect of a substrate, a system using a series of flexible substrates was engineered to try to extract all of the advantageous properties of all of the systems at once. The rationale was to have a microstructure that could allow for the inclusion of porosity's in the film and an intrinsic tensile stress. This would ideally minimise the plastic deformation effect and allow the elastic interactive effects to become dominant, and more importantly, reversible. In addition, the experiment would allow for interpretation of the effects of stress on the kinetic loading behaviour. Three trial systems were deposited onto PEEK substrates: PEEK/Mg/Pd, PEEK/Mg/Ti/Pd and PEEK/Ti/Mg/Ti/Pd. The resultant XRD patterns were inconclusive in revealing any structural properties of the films on the substrates, due to the large amorphous hump caused by the underlying PEEK substrate. In addition to this, the hydrogenated samples could not be examined using XRD due to their curved nature, bought about by the biaxial expansion due to hydrogenation. Therefore, our only interpretation of these results could only be from the TPD traces. However, they do provide an interesting insight into the desorption process. It is likely that under the conditions used, a large amount of plastic deformation was induced. The in-plane film stress calculated for the radius of curvature examined would have been in the region of 3 GPa. This would suggest that the yield point of MgH_2 would have been far surpassed.

Therefore, although the work done in absorption could have effectively been stress-free, the conclusion would be that the desorption branch of the hysteresis is far lower than normal. This is further supported by the separation of 3 TPD peaks in the desorption trace. As the specimen for the sample was a traditional dogbone tensile test size, the formation of dislocations in given regions is preferable, such as at the neck of the sample. In these regions, the distribution of biaxial force becomes uneven and the will experience more or less stress depending on its location. The interpretation is that the film is most certainly deformed plastically, but to different degrees, depending on the location within the sample.

To further improve on this set of experiments, one would try to deform only in the elastic region, to see if the thermodynamic bias could be shifted the opposite way, and that the plasticity could be avoided. However, this approach in using flexible substrates most certainly is a novel way of trying to tune the sorption thermodynamics, and most importantly, with potential reversibility.

Of course, the type of supported MgH_2 films investigated in this work could not be used in on-board hydrogen storage systems, as the thick substrates would add prohibitive mass and volume to the system. The dilution effects of the substrate would indicate a volumetric requirement of some 40 m^3 for a 200 nm film thickness. So, one must ask what is the thickest structure that can be hydrogenated that may also take advantage of being 'tuned' if it were then deposited onto a thin flexible system that could further enhance its hydrogen storage properties. The potential use of very thin substrates such as graphene, could be considered for future films. In this instance, the volumetric requirements for the storage system would be only just greater than those required for pure Mg. Apart from an application as hydrogen storage media, one may consider an application as a mechanical sensor for hydrogen. The bending of the thin film system due to sorption reactions could lend itself to a mechanical switch. Other sensor designs are based on optical or resistive methods.

A multilayer approach was undertaken to investigate the thickest structure that could be hydrogenated under reasonable conditions, using catalysts to aid the reaction, as well as probing for interfacial and crystal structure changes upon hydrogenation using in situ XRD for the first time. Both Mg/Ti- and Mg/Y-based structures were deposited. It is known that the Ti acts as an immiscible layer between Mg layers, so the only energy considerations here are from interfacial energy. However, because Y will alloy with Mg, there is potential that the interfacing layers will provide a thermodynamic bias. Using this approach, it can be seen that the films undergo a complete structural transformation and the Mg/Y film certainly appears to destabilise in comparison to the Mg/Ti. The destabilisation may be due to the difference in crystal structure to absorb strain within the Mg/Y multilayer system. The use of in situ XRD would show this effect in more detail.

5.2 CONCLUSIONS

This research has clearly identified significant factors in the behaviour of hydrogen sorption properties of magnesium based thin films:

- The intrinsic stress state can be heavily influenced by deposition conditions. This intrinsic stress is seen through characteristic microstructural features including porosities. The intrinsic stress is well correlated to grain size, where an increase in grain size accommodates a reduction in stress, suggesting that a grain growth or coalescence mechanism reduces stress build up.

- The influence of the underlying microstructure heavily influences hydrogen sorption mechanics. A model has been proposed which shows regimes dominated by porosity, elastic and plastic contributions and their likely effects on sorption thermodynamics.
- In addition, stress analysis using different thicknesses have been used to model the diffusion behaviour within the films, demonstrating how differential rates and directionality of absorption also affect both kinetic and thermodynamic properties of the films.
- A novel approach to tailor thin film stress using flexible substrates was used to investigate and tune thermodynamics. This method requires further investigation. The use of an optomechanical hydrogen sensor based on this system design.
- Y/Mg multilayer systems were investigated for the first time. The characterisation of these shows that hcp/fcc yttrium occurs at different layer thicknesses, altering the lattice spacings at coherent interfaces with Mg. This provides another potential route to destabilisation.

5.3 FURTHER WORK

This thesis has presented multiple themes related to stress within thin films and its effect on the hydrogen sorption properties of those films.

In order to improve some of this work, it would be preferential to use an alternative XRD set up that is specialised for thin films with the ability to assess other in plane crystallographic orientations and mosaicity of grains. This would aid in some of the interpretation in section 4.2 when interpreting the mechanical properties of the resultant films. It would also allow for experimentation on smaller films thicknesses down to below 100 nm.

More detailed microscopy of the same cross section could be used, using TEM as opposed to SEM, for a higher resolution. This would give a more refined picture of the thinner films that were produced, enabling further understanding to be gained.

Further developments in our understanding of the interaction of hydrogen with materials under applied stress warrants further discussion. Some authors are pursuing experimental research into interaction of hydrogen in single grains. As interesting as that is, it would also be beneficial to attempt to observe hydrogen interaction at stressed grain boundaries, both thermodynamically and kinetically. Techniques such as positron annihilation spectroscopy and other time resolved spectroscopies could be used to estimate hopping rates. In a similar way to other authors, TEM could be used to observe the hydride phase front of a growing film in applied stress conditions, proving the theories predicted in section 4.3.

For work on flexible substrate systems, a range of experiments could be attempted which load and unload hydrogen in stressed and unstressed states. It is envisioned that a system could be developed in line with other smart materials such as nitinol where application of temperature induces a transition to a different shape, which would induce a stress into the material. In addition, much thinner substrate/film combinations could be used that would make this system feasible for storage applications.

With regards to multilayers, the understanding of lattice mismatch between layers could be an effective route forwards towards destabilisation of hydrides assuming that a coherent interface can be maintained between layers. The work displayed on yttrium films can be further optimised to look at even thinner layers to reveal any relationships between HCP and FCC phases. In addition, further research using in situ methods would be more useful here, as it would show the phases of yttrium hydride produced. This would help to make a more complete conclusion regarding this chapter.

6 LIST OF PUBLICATIONS

Poster Presentations

Effect of the substrate in Magnesium based thin films

Hughes, L., Reed, D., Book, D.

MH2012 – International Symposium on Metal Hydrogen Systems, Kyoto, Japan

Hydrogen sorption properties of Mg films prepared in a variety of conditions

Hughes, L., Book, D.

Nanoenergy 2014, University College London

Hydrogen sorption properties of Mg films with different thicknesses

Hughes, L., Book, D.

MH2014 - International Symposium on Metal Hydrogen Systems, Salford, UK

Publications

The effect of deposition conditions on the microstructure, intrinsic stress and hydrogen sorption properties of Mg films deposited by CFUBMSIP

Hughes, L., Book, D.

To be submitted to the journal of thin films 2016

Thickness effects in thin films: relating the diffusion behaviour to stress analysis

Hughes, L., Book, D.

To be submitted to the International Journal of Hydrogen Energy 2016

An optomechanical hydrogen sensor based on Pd/Mg/PEEK film architectures

Hughes, L., Book, D.

To be submitted to sensors 2017

7 REFERENCES

1. Lucas, R. E. *Lectures on Economic Growth*. (Harvard UP, 2002).

2. McLamb, E. The ecological impact of the industrial revolution. at <http://www.ecology.com/2011/09/18/ecological-impact-industrial-revolution/> accessed (22/09/2016)

3. IEA. Key world energy statistics 2016. at <http://www.iea.org/publications/freepublications/publication/key-world-energy-statistics.html> accessed (22/09/2016)

4. Alesina, A., Özler, S., Roubini, N. & Swagel, P. Political instability and economic growth. *J. Econ. Growth* **1,** 189–211

5. Barsky, R. & Kilian, L. *Oil and the Macroeconomy Since the 1970s*. at http://www.nber.org/papers/w10855> accessed (22/09/2016)

6. Gupta, E. Oil vulnerability index of oil-importing countries. *Energy Policy* **36,** 1195–1211 (2008).

7. Murray, J. & King, D. Climate Change: Oil's tipping point has passed. *Nature* **481,** 433–435 (2012).

8. US EIA. EIA annual energy outlook 2014. at <http://www.eia.gov/totalenergy/> accessed (22/09/2016)

9. BP. Statistical review of world energy 2013. at <http://www.bp.com/en/global/corporate/about-bp/energy-economics/statistical-review-of-world-energy-2013.html> accessed (22/09/2016)

10. Abbott, B. D. Keeping the Energy Debate Clean : How Do We Supply the World ' s Energy Needs ? **98,** (2010).

11. SMMT. Decade’s fastest growth sees almost 32 million cars on the road. at <http://www.smmt.co.uk/2014/03/decades-fastest-growth-sees-almost-32-million-cars-road/> accessed (22/09/2016)

12. World CO2 levels. at <http://co2now.org/> accessed (22/09/2016)

13. CDIAC. Carbon Dioxide Information Analysis Centre. at <http://cdiac.ornl.gov> accessed (22/09/2016)

14. IPCC. Climate change 2013 - The Physical Science Basis. at <http://www.ipcc.ch/report/ar5/wg1/> accessed (22/09/2016)

15. Shakun, J. D. *et al.* Global warming preceded by increasing carbon dioxide concentrations during the last deglaciation. *Nature* **484,** 49–54 (2012).

16. Lenton, T. & Schellnhuber, H. Tipping the Scales. *Nat. reports Clim. Chang.* (2007).

17. Stern, N. *The Economics of Climate Change*. (Crown, 2006).

18. Nations, U. A summary of the Kyoto Protocol. at <http://unfccc.int/kyoto_protocol/background/items/2879.php> accessed (22/09/2016)

19. Climate Change Act 2008. at <http://www.legislation.gov.uk/ukpga/2008/27/contents> accessed (22/09/2016)

20. Department for Transport. Cars and Carbon Dioxide. at <http://www.dft.gov.uk/vca/fcb/cars-and-carbon-dioxide.asp> accessed (22/09/2016)

21. Zuttel, A., Remhof, A., Borgschulte, A. & Friedrichs, O. Hydrogen: the future energy carrier. *Philos. Trans. R. Soc. A Math. Phys. Eng. Sci.* **368,** 3329–3342 (2010).

22. Züttel, A. Materials for hydrogen storage. *Mater. Today* **6,** 24–33 (2003).

23. Department of Energy targets for Onboard hydrogen storage. at

<http://energy.gov/eere/fuelcells/downloads/doe-targets-onboard-hydrogen-storage-systems-light-duty-vehicles> accessed (22/09/2016)

24. DOE Hydrogen and Fuel Cells Program Record. at <http://www.hydrogen.energy.gov/pdfs/9013_energy_requirements_for_hydrogen_gas_compression.pdf> accessed (22/09/2016)

25. Refueling Station Compressor Efficiency, CDP #61. at <http://www.nrel.gov/hydrogen/docs/cdp/cdp_61.ppt> accessed (22/09/2016)

26. Thomas, K. M. Hydrogen adsorption and storage on porous materials☆. *Catal. Today* **120,** 389–398 (2007).

27. Orimo, S., Nakamori, Y., Eliseo, J. R., Züttel, A. & Jensen, C. M. Complex Hydrides for Hydrogen Storage. *Chem. Rev.* **107,** 4111–4132 (2007).

28. Severa, G., Ronnebro, E. & Jensen, C. M. Direct hydrogenation of magnesium boride to magnesium borohydride: demonstration of >11 weight percent reversible hydrogen storage. *Chem. Commun.* **46,** 421–423 (2010).

29. Chong, M. *et al.* Reversible dehydrogenation of magnesium borohydride to magnesium triborane in the solid state under moderate conditions. *Chem. Commun.* **47,** 1330–1332 (2011).

30. Mosegaard, L. *et al.* Reactivity of LiBH4: In Situ Synchrotron Radiation Powder X-ray Diffraction Study. *J. Phys. Chem. C* **112,** 1299–1303 (2008).

31. Fukai, Y. *The Metal-Hydrogen System*. (Springer Berlin / Heidelberg, 2005).

32. Schlapbach, L. & Züttel, A. Hydrogen-storage materials for mobile applications. *Nature* **414,** 353–358 (2001).

33. Lundin, C. E., Lynch, F. E. & Magee, C. B. A correlation between the interstitial hole sizes in

intermetallic compounds and the thermodynamic properties of the hydrides formed from those compounds. *J. Less Common Met.* **56,** 19–37 (1977).

34. Reilly, J. J. *et al.* The correlation between composition and electrochemical properties of metal hydride electrodes. *J. Alloys Compd.* **293–295,** 569–582 (1999).

35. Noritake, T. *et al.* Chemical bonding of hydrogen in MgH[sub 2]. *Appl. Phys. Lett.* **81,** 2008 (2002).

36. Aguey-Zinsou, K.-F. & Ares-Fernandez, J.-R. Hydrogen in magnesium: new perspectives toward functional stores. *Energy Environ. Sci.* **3,** 526–543 (2010).

37. Abdessameud, S., Mezbahul-Islam, M. & Medraj, M. Thermodynamic Modeling of Hydrogen Storage Capacity in Mg-Na Alloys. *Sci. World J.* **2014,** 190320 (2014).

38. Krozer, A. & Kasemo, B. Hydrogen uptake by Pd-coated Mg: absorption-decomposition isotherms and uptake kinetics. *J. Less Common Met.* **160,** 323–342 (1990).

39. Jain, I. P., Lal, C. & Jain, A. Hydrogen storage in Mg: A most promising material. *Int. J. Hydrogen Energy* **35,** 5133–5144 (2010).

40. Zaluska, A., Zaluski, L. & Ström–Olsen, J. O. Nanocrystalline magnesium for hydrogen storage. *J. Alloys Compd.* **288,** 217–225 (1999).

41. Hanada, N., Ichikawa, T. & Fujii, H. Catalytic effect of niobium oxide on hydrogen storage properties of mechanically ball milled MgH2. *Phys. B Condens. Matter* **383,** 49–50 (2006).

42. Hanada, N., Ichikawa, T., Hino, S. & Fujii, H. Remarkable improvement of hydrogen sorption kinetics in magnesium catalyzed with Nb2O5. *J. Alloys Compd.* **420,** 46–49 (2006).

43. Cui, J. *et al.* Remarkable enhancement in dehydrogenation of MgH2 by a nano-coating of multi-valence Ti-based catalysts. *J. Mater. Chem. A* **1,** 5603 (2013).

44. Buckley, A. C., Carter, D. J., Sheppard, D. A. & Buckley, C. E. Density functional theory

calculations of magnesium hydride: A comparison of bulk and nanoparticle thermodynamics. *J. Phys. Chem. C* **116,** 17985–17990 (2012).

45. Wagemans, R. W. P., van Lenthe, J. H., de Jongh, P. E., van Dillen, a J. & de Jong, K. P. Hydrogen storage in magnesium clusters: quantum chemical study. *J. Am. Chem. Soc.* **127,** 16675–80 (2005).

46. Jongh, P. E. de *et al.* The Preparation of Carbon-Supported Magnesium Nanoparticles using Melt Infiltration. *Chem. Mater.* **19,** 6052–6057 (2007).

47. Paskevicius, M., Sheppard, D. a & Buckley, C. E. Thermodynamic changes in mechanochemically synthesized magnesium hydride nanoparticles. *J. Am. Chem. Soc.* **132,** 5077–83 (2010).

48. Mary, Q., Kingdom, U. & Madrid, D. Synthesis of Colloidal Magnesium : A Near Room. 157–165 (2008).

49. Kooi, B. J., Palasantzas, G. & De Hosson, J. T. M. Gas-phase synthesis of magnesium nanoparticles: A high-resolution transmission electron microscopy study. *Appl. Phys. Lett.* **89,** 161914 (2006).

50. Zhang, X. *et al.* Synthesis of magnesium nanoparticles with superior hydrogen storage properties by acetylene plasma metal reaction. *Int. J. Hydrogen Energy* **36,** 4967–4975 (2011).

51. Baldi, A. & Dam, B. Thin film metal hydrides for hydrogen storage applications. *J. Mater. Chem.* **21,** 4021 (2011).

52. Slaman, M. Optimization of Mg-based fiber optic hydrogen detectors by alloying the catalyst. *Int. J. Hydrogen Energy* **33,** 1084–1089 (2008).

53. Slaman, M. *et al.* Fiber optic hydrogen detectors containing Mg-based metal hydrides. *Sensors Actuators B Chem.* **123,** 538–545 (2007).

54. Yoshimura, K. *et al.* New hydrogen sensor based on sputtered Mg–Ni alloy thin film. *Vacuum* **83,** 699–702 (2008).

55. Yoshimura, K., Yamada, Y. & Okada, M. Optical switching of Mg-rich Mg–Ni alloy thin films. *Appl. Phys. Lett.* **81,** 4709 (2002).

56. Mongstad, T. *et al.* A new thin film photochromic material: Oxygen-containing yttrium hydride. *Sol. Energy Mater. Sol. Cells* **95,** 3596–3599 (2011).

57. Selj, J. H., Mongstad, T., Hauback, B. C. & Karazhanov, S. Z. The dielectric functions and optical band gaps of thin fi lms of amorphous and cubic crystalline Mg ~ 2 NiH ~ 4. *Thin Solid Films* **520,** 6786–6792 (2012).

58. Huiberts, J., Griessen, R. & Rector, J. Yttrium and lanthanum hydride films with switchable optical properties. (1996).

59. Lohstroh, W. *et al.* Double layer formation in Mg–TM switchable mirrors (TM: Ni, Co, Fe). *J. Alloys Compd.* **404–406,** 490–493 (2005).

60. Bao, S. *et al.* Switchable mirror based on Mg–Zr–H thin films. *J. Alloys Compd.* **513,** 495–498 (2012).

61. Baldi, a *et al.* Mg–Ti–H thin films as switchable solar absorbers. *Int. J. Hydrogen Energy* **33,** 3188–3192 (2008).

62. Gremaud, R. *et al.* Hydrogenography: An Optical Combinatorial Method To Find New Light-Weight Hydrogen-Storage Materials. *Adv. Mater.* **19,** 2813–2817 (2007).

63. Higuchi, K. *et al.* In situ study of hydriding–dehydriding properties in some Pd/Mg thin films with different degree of Mg crystallization. *J. Alloys Compd.* **293–295,** 484–489 (1999).

64. Singh, S., Eijt, S. W. H., Zandbergen, M. W., Legerstee, W. J. & Svetchnikov, V. L. Nanoscale structure and the hydrogenation of Pd-capped magnesium thin films prepared by plasma

sputter and pulsed laser deposition. *J. Alloys Compd.* **441,** 344–351 (2007).

65. Norek, M. *et al.* A comparative study on the hydrogen absorption of thin films at room temperature deposited on non-porous glass substrate and nano-porous anodic aluminum oxide (AAO) template. *Int. J. Hydrogen Energy* **36,** 11777–11784 (2011).

66. Fujii, H., Higuchi, K., Yamamoto, K. & Kajioka, H. Remarkable hydrogen storage, structural and optical properties in multi-layered Pd/Mg thin films. *Mater. Trans.* **43,** 2721–2727 (2002).

67. Higuchi, K. *et al.* Remarkable hydrogen storage properties in three-layered Pd/Mg/Pd thin films. *J. Alloys Compd.* **330–332,** 526–530 (2002).

68. Highmore, R. J. & Greer, A. L. Eutectics and the formation of amorphous alloys. *Nature* **339,** 363–365 (1989).

69. Chen, J., Yang, H. & Xia, Y. Hydriding and Dehydriding Properties of Amorphous Magnesium - Nickel Films. *Chem. Mater.* 2834–2836 (2002).

70. Eliaz, N. & Eliezer, D. An Overview of Hydrogen Interaction with Amorphous Alloys. **31,** 5–31 (1999).

71. Aoki, K., Kamachi, M. & Masumoto, T. Thermodynamics of hydrogen absorption in amorphous Zr Ni alloys. *J. Non. Cryst. Solids* **62,** 679–684 (1984).

72. Thermfact. Facility for analysis of thermodynamics. at <http://www.factsage.com>

73. Vermeulen, P. *et al.* Effect of the Deposition Technique on the Metallurgy and Hydrogen Storage Characteristics of Metastable Mg[sub y]Ti[sub (1−y)] Thin Films. *Electrochem. Solid-State Lett.* **9,** A520 (2006).

74. Vermeulen, P., Niessen, R. A. H. & Notten, P. H. L. Hydrogen storage in metastable MgyTi(1 − y) thin films. *Electrochem. commun.* **8,** 27–32 (2006).

75. Vermeulen, P., Graat, P., Wondergem, H. & Notten, P. Crystal structures of MgyTi100−y thin

film alloys in the as-deposited and hydrogenated state. *Int. J. Hydrogen Energy* **33,** 5646–5650 (2008).

76. Asano, K., Enoki, H. & Akiba, E. Synthesis of HCP, FCC and BCC structure alloys in the Mg-Ti binary system by means of ball milling. *J. Alloys Compd.* **480,** 558–563 (2009).

77. Gremaud, R. *et al.* Structural and optical properties of MgyNi1–yHx gradient thin films in relation to the as-deposited metallic state. *Int. J. Hydrogen Energy* **34,** 8951–8957 (2009).

78. Zheng, Q. *et al.* EXAFS investigation of the destabilization of the Mg e Ni e Ti (H) system. *Int. J. Hydrogen Energy* **37,** 4161–4169 (2011).

79. Mooij, L. P. a. *et al.* Interface Energy Controlled Thermodynamics of Nanoscale Metal Hydrides. *Adv. Energy Mater.* **1,** 754–758 (2011).

80. Baldi, A., Gonzalez-Silveira, M. & Palmisano, V. Destabilization of the Mg-H system through elastic constraints. *Phys. Rev. …* **226102,** 1–4 (2009).

81. Chung, C.-J. *et al.* Interfacial Alloy Hydride Destabilization in Mg/Pd Thin Films. *Phys. Rev. Lett.* **108,** 1–4 (2012).

82. Zaluska, A., Zaluski, L. & Ström-Olsen, J. Synergy of hydrogen sorption in ball-milled hydrides of Mg and Mg 2 Ni. *J. Alloys Compd.* **289,** 197–206 (1999).

83. Pivak, Y. *et al.* Effect of the substrate on the thermodynamic properties of PdHx films studied by hydrogenography. *Scr. Mater.* **60,** 348–351 (2009).

84. Pivak, Y., Schreuders, H., Slaman, M., Griessen, R. & Dam, B. Thermodynamics, stress release and hysteresis behavior in highly adhesive Pd–H films. *Int. J. Hydrogen Energy* **36,** 4056–4067 (2011).

85. Wagner, S. & Pundt, A. Mechanical stress impact on thin Pd[sub 1−x]Fe[sub x] film thermodynamic properties. *Appl. Phys. Lett.* **92,** 51914 (2008).

86. Laudahn, U. *et al.* Hydrogen-induced stress in Nb single layers. *J. Alloys Compd.* **293–295,** 490–494 (1999).

87. Tal-Gutelmacher, E., Pundt, A. & Kirchheim, R. The influence of films thickness on hydrogenation behavior of titanium thin films. *J. Mater. Sci.* **45,** 6389–6394 (2010).

88. Wagner, S. & Pundt, A. Combined impact of microstructure and mechanical stress on the electrical resistivity of PdHc thin films. *Acta Mater.* **59,** 1862–1870 (2011).

89. Pivak, Y., Schreuders, H. & Dam, B. Thermodynamic Properties, Hysteresis Behavior and Stress-Strain Analysis of MgH2 Thin Films, Studied over a Wide Temperature Range. *Crystals* **2,** 710–729 (2012).

90. Pivak, Y., Palmisano, V., Schreuders, H. & Dam, B. The clamping effect in the complex hydride Mg2NiH4 thin films. *J. Mater. Chem. A* **1,** 10972 (2013).

91. Kelekar, R., Giffard, H., Kelly, S. T. & Clemens, B. M. Formation and dissociation of MgH[sub 2] in epitaxial Mg thin films. *J. Appl. Phys.* **101,** 114311 (2007).

92. Tan, X., Zahiri, B., Holt, C. M. B., Kubis, A. & Mitlin, D. A TEM based study of the microstructure during room temperature and low temperature hydrogen storage cycling in MgH2 promoted by Nb–V. *Acta Mater.* **60,** 5646–5661 (2012).

93. Paik, B. *et al.* MgH 2 → Mg phase transformation driven by a high-energy electron beam: An in situ transmission electron microscopy study. *Philos. Mag. Lett.* **90,** 1–7 (2010).

94. Pivak, Y., Schreuders, H. & Dam, B. Thermodynamic properties, hysteresis behavior and stress-strain analysis of MgH2 thin films, studied over a wide temperature range. *Crystals* 710–729 (2012). doi:10.3390/cryst2020710

95. Pickering, L. Ti-Vn-Mn based metal hydrides for hydrogen storage and compression applications. (University of Birmingham, 2014).

96. Zhang, J., Zhou, Y. C., Ma, Z. S., Sun, L. Q. & Peng, P. Strain effect on structural and dehydrogenation properties of MgH2 hydride from first-principles calculations. *Int. J. Hydrogen Energy* **38,** 3661–3669 (2013).

97. Mooij, L. & Dam, B. Hysteresis and the role of nucleation and growth in the hydrogenation of Mg nanolayers. *Phys. Chem. Chem. Phys.* **15,** 2782–92 (2013).

98. Fry, C. M. P., Grant, D. M. & Walker, G. S. Improved hydrogen cycling kinetics of nano-structured magnesium/transition metal multilayer thin films. *Int. J. Hydrogen Energy* **38,** 982–990 (2012).

99. Paloumpi, A. Nanoscale Magnesium as a hydrogen storage material. (University of Birmingham, 2010).

100. Baldi, A. *et al.* Mg/Ti multilayers: structural, optical and hydrogen absorption properties. *Phys. Rev. B* **81,** 1–10 (2009).

101. Ouyang, L. Z., Ye, S. Y., Dong, H. W. & Zhu, M. Effect of interfacial free energy on hydriding reaction of Mg–Ni thin films. *Appl. Phys. Lett.* **90,** 21917 (2007).

102. Pálsson, G. K. *et al.* Hydrogen site occupancy and strength of forces in nanosized metal hydrides. *Phys. Rev. B* **85,** 195407 (2012).

103. Ohring, M. *The Materials Science of Thin Films*. (Harcourt Brace Jovanovich, 1992).

104. Thompson, C. V. Coarsening of particles on a planar substrate: Interface energy anisotropy and application to grain growth in thin films. *Acta Metall.* **36,** 2929–2934 (1988).

105. Needleman, A. & Suresh, S. Mechanics and Physics Layered and Graded Materials. *J Mech Phys Solids* 44(5) (1996).

106. Thornton, J. a. & Hoffman, D. W. Stress-related effects in thin films. *Thin Solid Films* **171,** 5–31 (1989).

107. Magnfält, D., Abadias, G. & Sarakinos, K. Atom insertion into grain boundaries and stress generation in physically vapor deposited films. *Appl. Phys. Lett.* **103,** (2013).

108. Teer Coatings CFUBMSIP. at <http://www.teercoatings.co.uk/?page=28> accessed (22/09/2016)

109. Scanning Electron Microscopy. at <https://www2.warwick.ac.uk/fac/sci/physics/current/postgraduate/regs/mpags/ex5/techniques/structural/sem3/> accessed (22/09/2016)

110. ISAAC : Imaging spectroscopy and analysis. Scanning Electron Microscopy. at <http://www.gla.ac.uk/schools/ges/research/researchfacilities/isaac/services/scanningelectronmicroscopy/> accessed (22/09/2016)

111. Matweb. Magnesium. at <http://www.matweb.com/search/DataSheet.aspx?MatGUID=ff6d4e6d529e4b3d97c77d6538b29693&ckck=1> accessed (22/09/2016)

112. Yasaka, M. X-ray thin-film measurement techniques. *V. X-ray reflectivity Meas. Rigaku J.* **26,** 1–9 (2010).

113. Rydén, J. *et al.* Unusual kinetics of hydride formation in MgPd sandwiches, studied by hydrogen profiling and quartz crystal microbalance measurements. *J. Less-Common Met.* **152,** 295–309 (1989).

114. Chater, P. Mixed anion complex hydrides for hydrogen storage. (University of Birmingham, 2010).

115. Gates, P. Gas Chromatrography Mass Spectrometry. at <http://www.bris.ac.uk/nerclsmsf/techniques/gcms.html> accessed (22/09/2016)

116. Shen, Y. G. Effect of deposition conditions on mechanical stresses and microstructure of

sputter-deposited molybdenum and reacti v ely sputter-deposited molybdenum nitride films. **359,** 158–167 (2003).

117. Pauleau, Y. Generation and evolution of residual stresses in physical vapour-deposited thin films. *Vacuum* **61,** 175–181 (2001).

118. Rickerby, D. S., Jones, a M. & Bellamy, B. a. X-Ray Diffraction Studies of Physically Vapour-Deposited Coatings. *Surf. Coatings Technol.* **37,** 111–137 (1989).

119. Zhang, L., Ma, G., Ma, H. & Lin, G. Effect of pulsed bias voltage on the structure and mechanical properties of Ti–C–N composite films by pulsed bias arc ion plating. *Nucl. Instruments Methods Phys. Res. Sect. B Beam Interact. with Mater. Atoms* **333,** 1–5 (2014).

120. Bendavid, A., Martin, P. J. & Preston, E. W. The effect of pulsed direct current substrate bias on the properties of titanium dioxide thin films deposited by filtered cathodic vacuum arc deposition. *Thin Solid Films* **517,** 494–499 (2008).

121. Sønderby, S., Aijaz, A., Helmersson, U., Sarakinos, K. & Eklund, P. Deposition of yttria-stabilized zirconia thin films by high power impulse magnetron sputtering and pulsed magnetron sputtering. *Surf. Coatings Technol.* **240,** 1–6 (2014).

122. Westerwaal, R. J., Borgschulte, A., Lohstroh, W., Dam, B. & Griessen, R. Microstructural origin of the optical black state in Mg2NiHx thin films. *J. Alloys Compd.* **404–406,** 481–484 (2005).

123. Lee, J.-S., Kim, J.-H. & Kim, S. S. Evolution of grains to relieve additional compressive stress developed in Al–Mg alloy films during thermal annealing. *Thin Solid Films* **595,** 148–152 (2015).

124. Chason, E., Sheldon, B. W., Freund, L. B., Floro, J. A. & Hearne, S. J. Origin of Compressive Residual Stress in Polycrystalline Thin Films. *Phys. Rev. Lett.* **88,** 156103 (2002).

125. Siviero, G. *et al.* Structural evolution of Pd-capped Mg thin films under H2 absorption and

desorption cycles. *Int. J. Hydrogen Energy* **34,** 4817–4826 (2009).

126. Ludwig, A., Cao, J., Dam, B. & Gremaud, R. Opto-mechanical characterization of hydrogen storage properties of Mg – Ni thin film composition spreads. **254,** 682–686 (2007).

127. Kelly, S. T. & Clemens, B. M. Moving interface hydride formation in multilayered metal thin films. *J. Appl. Phys.* **108,** 13521 (2010).

128. Nörthemann, K. & Pundt, A. Coherent-to-semi-coherent transition of precipitates in niobium-hydrogen thin films. *Phys. Rev. B* **78,** 14105 (2008).

129. Wagner, S. *et al.* Hydrogen microscopy - Distribution of hydrogen in buckled niobium hydrogen thin films. *Int. J. Hydrogen Energy* **38,** 13822–13830 (2013).

130. Choi, Y. & Suresh, S. Size effects on the mechanical properties of thin polycrystalline metal films on substrates. *Acta Mater.* **50,** 1881–1893 (2002).

131. Xin, G. *et al.* Promising gaseous and electrochemical hydrogen storage properties of porous Mg-Pd films under mild conditions. *Phys. Chem. Chem. Phys.* **17,** 13606–13612 (2015).

132. Qu, J. *et al.* Hydrogen absorption kinetics of Mg thin films under mild conditions. *Scr. Mater.* **62,** 317–320 (2010).

133. Qu, J., Liu, Y., Xin, G., Zheng, J. & Li, X. A kinetics study on promising hydrogen storage properties of Mg-based thin films at room temperature. *Dalt. Trans.* **43,** 5908–5912 (2014).

134. Ham, B. *et al.* Size and stress dependent hydrogen desorption in metastable Mg hydride films. *Int. J. Hydrogen Energy* **39,** 2597–2607 (2014).

135. Pálsson, G. K., Bliersbach, A., Wolff, M., Zamani, A. & Hjörvarsson, B. Using light transmission to watch hydrogen diffuse. *Nat Commun* **3,** 892 (2012).

136. Qu, J. *et al.* Hydrogen desorption properties of Mg thin films at room temperature. *J. Power Sources* **195,** 1190–1194 (2010).

137. Yamamoto, K. *et al.* Optical transmission of magnesium hydride thin film with characteristic nanostructure. *J. Alloys Compd.* **330–332,** 352–356 (2002).

138. Gautam, Y. K., Chawla, A. K., Khan, S. a., Agrawal, R. D. & Chandra, R. Hydrogen absorption and optical properties of Pd/Mg thin films prepared by DC magnetron sputtering. *Int. J. Hydrogen Energy* **37,** 3772–3778 (2012).

139. Ohring, M. *Materials Science of Thin Films*. *Materials Science of Thin Films* (Elsevier, 2002).

140. Baldi, A., Gonzalez-Silveira, M., Palmisano, V., Dam, B. & Griessen, R. Destabilization of the Mg-H System through Elastic Constraints. *Phys. Rev. Lett.* **102,** 1–4 (2009).

141. Jaccodine, R. J. Surface Energy of Germanium and Silicon. *J. Electrochem. Soc.* **110,** 524 (1963).

142. Factsage. Mg-Ti phase diagram. at <http://www.crct.polymtl.ca/fact/phase_diagram.php?file=Mg-Ti.jpg&dir=FTlite> accessed (22/09/2016)

143. Ferrater, C., Lousa, A., Badia, F., Alcobé, X. & Morenza, J. L. Crystal structure of evaporated yttrium thin films. *J. Cryst. Growth* **113,** 181–185 (1991).

144. Giebels, I. A. M. E. *et al.* Highly reflecting Y/Mg?Hx multilayered switchable mirrors. *J. Alloys Compd.* **330–33,** 875–881 (2002).

145. Baldi, A., Narayan, T. C., Koh, A. L. & Dionne, J. A. In situ detection of hydrogen-induced phase transitions in individual palladium nanocrystals. *Nat. Mater.* **13,** 1143–1148 (2014).

146. Matelon, R. J. *et al.* Substrate effect on the optical response of thin palladium films exposed to hydrogen gas. *Thin Solid Films* **516,** 7797–7801 (2008).